The Development and Application of New Hyperpolarized Magnetic Resonance Spectroscopy Techniques for the Non-Invasive Assessment of Metabolism in the Rodent Heart

Michael Samuel Dodd

Department of Physiology, Anatomy and Genetics

and

Department of Cardiovascular Medicine

Submitted for the degree of Doctor of Philosophy

Trinity Term 2012

Supervisors:

Dr Damian Tyler
Dr Houman Ashrafian
Prof Barbara Casadei
Prof Hugh Watkins

The development and application of new hyperpolarized magnetic resonance spectroscopy techniques for the non-invasive assessment of metabolism in the rodent heart

Michael Samuel Dodd

Submitted for the degree of Doctor of Philosophy, Trinity Term 2012

Abstract

The aim of this thesis was to develop and apply new hyperpolarized magnetic resonance spectroscopy techniques, to assess *in vivo* metabolism in the rodent heart. Initial work using rat models of heart disease has provided key findings, such as significant increases in pyruvate dehydrogenase flux in the hypertensive rat heart and metabolic alterations in the TCA cycle during the progression into heart failure. Both could provide future non-invasive markers for the metabolic alterations associated with hypertrophy and heart failure in patients. Whilst both of these models provided useful information regarding the metabolic abnormalities of the diseased heart there is also a need to better characterize the individual metabolic pathways that are modified during heart disease. This requires the study of genetically modified animals, namely transgenic mouse models. However, the translation of the hyperpolarized technique from rat to mouse is particularly challenging, mainly due to the mouse heart being a tenth of the size of the rat heart and with a heart rate at least twice as fast. Work in this thesis details the development of mouse cardiac dynamic nuclear polarization (DNP). The development of this technique allowed interesting insights in to differences in the *in vivo* metabolic phenotype of commonly used "control" mouse strains, and of mouse models of defects associated with β-oxidation. This work also demonstrated that hyperpolarized [1-^{13}C]pyruvate could be used to monitor anaplerotic pathways in the stressed mouse heart, potentially increasing its power for clinical use. In combination with cine-MRI and ^{31}P MRS, this work has highlighted that DNP could play an important role in the diagnosis and prognosis of cardiovascular diseases.

Publications

Dodd MS, Ball DR, Schroeder MA, Le Page LM, Atherton HJ, Heather LC, Seymour A-M, Ashrafian H, Watkins H, Clarke K, Tyler DJ. "*In Vivo* Alterations in Cardiac Metabolism and Function in the Spontaneously Hypertensive Rat Heart" *Cardiovascular Research,* 2012; 95, 69-76.

Heather LC, Cole MA, Tan JJ, Ambrose LJ, Pope S, Abd-Jamil AH, Carter EE, **Dodd MS**, Yeoh KK, Schofield CJ, Clarke K "Metabolic adaptation to chronic hypoxia in cardiac mitochondria" *Basic Research in Cardiology,* 2012; 107 (3), 1-12

Ashrafian H, Czibik G, Bellahcene M, Aksentijević D, Smith AC, Mitchell SJ, **Dodd MS**, Kirwan J, Byrne JJ, Ludwig C, Isackson H, Yavari A, Støttrup NB, Contractor H, Cahill TJ, Sahgal N, Ball DR, Birkler RI, Hargreaves I, Tennant DA, Land J, Lygate CA, Johannsen M, Kharbanda RK, Neubauer S, Redwood C, de Cabo R, Ahmet I, Talan M, Günther UL, Robinson AJ, Viant MR, Pollard PJ, Tyler DJ, Watkins H. "Fumarate is cardioprotective via activation of the Nrf2 antioxidant pathway" *Cell Metabolism,* 2012; 15 (3), 361–371.

Schroeder MA, Atherton HJ, **Dodd MS**, Lee P, Cochlin LE, Radda GK, Clarke K, Tyler DJ "The Cycling of Acetyl-CoA through Acetylcarnitine Buffers Cardiac Substrate Supply: A Hyperpolarised 13C Magnetic Resonance Study."*Circ Cardiovasc Imaging.* 2012; 5 (2), 201-209.

Atherton, HJ, **Dodd, MS**, Heather, LC, Schroeder, MA, Griffin, JL, Radda, GK, Clarke, K, Tyler, DJ "Role of pyruvate dehydrogenase inhibition in the development of hypertrophy in the hyperthyroid rat heart: a combined magnetic resonance imaging and hyperpolarized magnetic resonance spectroscopy study." *Circulation*, 2011; 123(**22**), 2552-61.

Atherton, HJ, Schroeder, MA, **Dodd, MS**, Heather, LC, Carter, EE, Cochlin, LE, Nagel, S, Sibson, NR, Radda, GK, Clarke, K, Tyler, DJ "Validation of the *in vivo* assessment of pyruvate dehydrogenase activity using hyperpolarised 13C MRS." *NMR in Biomedicine*, 2011; 24(**2**), 201-8.

Papers under review

Dodd, MS. Ball, V. Bray, R. Ashrafian, H. Watkins, H. Clarke, K. and Tyler, DJ. "Optimisation of *in vivo* murine cardiac hyperpolarized magnetic resonance spectroscopy".

Papers in preparation

Michael S. Dodd, Helen J. Atherton, Carolyn A. Carr, Lisa C. Heather, Daniel J. Stuckey, James A. West, Julian L. Griffin, Kieran Clarke, George K. Radda and Damian J. Tyler "Assessing Metabolic Changes associated with Heart Failure Progression using Hyperpolarized MRS".

Acknowledgments

First and foremost I would like to thank my supervisor Dr Damian Tyler who has helped me through the last four years and read this thesis many times. I also want to thank my other supervisors, Dr Ashrafian, Prof Casadei and Prof Watkins for continuing to support me throughout these years and introducing me to Damian.

Secondly, I really want to thank everyone in CMRG for putting up with me, supporting through all the hard times and for helping me out with ideas and problems. Especially Lisa and Helen, for helping me through the first few difficult years during my DPhil. I also want to thank everyone in the DNP group, thanks for helping me with experiments, editing papers and for having fun on conference!

Finally I couldn't have done any of this without the support of my wonderful wife and family. Kimberley has had to listen to me nattering on about magnets for the past 2 years! With her constant love and support, she has helped me through my DPhil.

The most exciting phrase to hear in science, the one that heralds new discoveries, is not 'Eureka!' (I've found it!), but 'That's funny...'

Isaac Asimov

"Mutation: it is the key to our evolution. It has enabled us to evolve from a single-celled organism into the dominant species on the planet. This process is slow and normally taking thousands and thousands of years."

Professor Charles Francis Xavier, X-Men

Table of Contents

Abbreviations

^{13}C: Carbon 13

^{1}H: Proton

^{23}Na: Sodium 23

^{31}P: Phosphorous 31

^{3}H: Tritium

a.u: Arbitrary Units

AAT: Alanine Aminotransferase

ACD: Acyl-CoA Dehydrogenases

ADP: Adenosine Diphosphate

AMARES: Advanced Magnetic Resonance

AMP: Adenosine Monophosphate

AMPK: Adenosine Monophosphate-Activated Protein Kinase

ANOVA: Analysis Of Variance

ATMA: Automatic Tuning and Matching

APS: Ammonium Persulfate

ATP: Adenosine 5'Triphosphate

BCA: bicinchoninic acid

BMIPP: 123I-β-Methylp-Iodophenylpentadecanoic Acid

BSA: bovine serum albumin

Ca^{2+}: Calcium Ion

CAT: Carnitine Acetyl-Transferase

CO: Cardiac output

CoA: Coenzyme A

CPT: Carnitine Palmitoyltransferase

CS: Citrate Synthase

CT: Carnitine Acyltranslocase

CVD: Cardiovascular Disease

DCA: Dichloroacetic Acid

DI-MS: Direct Infusion Mass Spectrometry

DNP: Dynamic Nuclear Polarization

DTNB: 5,5′-Dithiobis(2-Nitrobenzoic Acid)

EBS: Electron Broadening System

ECG: Electrocardiography

EDTA: (Ethylenedinitrilo) Tetra-Acetic Acid

EDV: End Diastolic Volume

EF: Ejection Fraction

EGTA: Ethylene Glycol-bis(2-aminoethylether)-*N*,*N*,*N*′,*N*′-Tetraacetic Acid

ELISA: Enzyme-Linked Immunosorbent Assay

EPR: Electron Paramagnetic Resonance

ESV: End Systolic Volume

EZS: Electronic Zeeman System

FAD: Flavin Adenine Dinucleotide

$FADH_2$:Reduced Flavin Adenine Dinucleotide

FAT: Fatty Acid Translocase

FDG: Flurodeoxyglucose

FFA: free fatty acids

FH-KO: Fumarate Hydratase-Knockout

FLASH: Fast Low Angle Shot

FOV: Field of View

G6P: Glucose 6-Phosphate

GLUT: Glucose Transporter

GTP: Guanosine Triphosphate

GWW: Gram Wet Weight

HEPES: 2-[4-(2-hydroxyethyl)piperazin-1-yl]ethanesulfonic acid

HTR: High temporal resolution

i.p: Intraperitoneal

i.v: Intravenous

ICDH: Isocitrate Dehydrogenase

ID: Internal Diameter

IMS: Intermembrane Space

IPGTT: Intraperitoneal Glucose Tolerance Test

jMRUI: java Magnetic Resonance User Interface

K_{ATP}: Potassium ATP

LAD: Left Anterior Descending

LCAD: Long Chain Acyl-CoA Dehydrogenase

LCFAs: Long Chain Fatty Acids

LDH: Lactate Dehydrogenase

LPL: Lipoprotein Lipase

LV: Left Ventricle

LVM: Left Ventricular Mass

MCAD: Medium-Chain Acyl-CoA Dehydrogenase

MCFA: Medium Chain Fatty Acids

Mg^{2+}: Magnesium Ion

MHC: Myosin Heavy Chain

MI: Myocardial Infarction

Min: Minute

MLC2v: Myosin Light Chain Promoter

MR: Magnetic Resonance

MRI: Magnetic Resonance Imaging

MRM: Multiple Reaction Monitoring

MRS: Magnetic Resonance Spectroscopy

MS: Mass spectrometry

MVO_2: Myocardial Oxygen Volume

NAD^+: Nicotinamide Adenine Dinucleotide

NADH: Reduced NAD

NEFA: Non-Esterified Fatty Acids

NMR: Nuclear Magnetic Resonance

NTg: Non-Trangenic

NZS: Nuclear Zeeman System

OD: Outer diameter

PBS: phosphate buffered saline

PCr: Phosphocreatine

PDC: Pyruvate Dehydrogenase Complex

PDH: Pyruvate Dehydrogenase

PDK: Pyruvate Dehydrogenase Kinase

PDP: Pyruvate Dehydrogenase Phosphatase

PET: Positron Emission Tomography

pH_i: Intracellular pH

P_i: Inorganic Phosphate

PPARα: Peroxisome Proliferator-Activated Receptor α

rad: Radians

RF: Radio Frequency

ROS: Reactive Oxygen Species

s: Second

SAGE: Sigma's Advanced Genetic Engineering

SCAD: Short-Chain Acyl-CoA Dehydrogenase

SDS: Sodium Dodecyl Sulphate

SE: Solid effect

SEM: Standard Error of the Mean

SHR: Spontaneously Hypertensive Rat

SNR: Signal to Noise

SUR: Sulfonylurea Receptor

SV: Stroke Volume

T: Temperature

T3: Triiodothyronine

TBS: Tris Buffered Saline

TBS-T: TBS-Tween

TCA: Tricarboxylic Acid

TE: Echo Time

TEMED: Tetramethylethylenediamine

TM: Thermal Mixing

TMB: 3,3',5,5'-Tetramethylbenzidine

TNB: 2-Nitro-5-Thiobenzoate

TPP-HCl: Thiamine Pyrophosphate Hydrochloride

TR: Repetition Time

TSP: Sodium-3-(Tri-Methylsilyl)-2,2,3,3-Tetradeuteriopropionate

UCP: Uncoupling Proteins

UV: Ultraviolet

VLCAD: Very Long-Chain Acyl-CoA Dehydrogenase

VLCADD: Very Long-Chain Acyl-CoA Dehydrogenase Deficiency

WKY: Wistar Kyoto

ΔE: Change in Energy state

ω_e: Electron Larmor frequency

ω_n: Nuclear Larmor frequency

Chapter 1

Introduction

Overview

Cardiovascular disease (CVD) is the leading causes of death in the United Kingdom, with over 180,000 deaths per year [1]. The British Heart Foundation estimates that CVD costs the UK economy approximately £30 billion a year [1]. A greater understanding of the molecular nature of CVD is vital to help develop new therapies and treatments. The term CVD covers a host of conditions that affect the heart and the circulation, including myocardial infarction, hypertrophic cardiomyopathies and dilated cardiomyopathies [2]. The end result is often heart failure, a pathophysiological condition where the left ventricle is unable to pump sufficient blood to maintain normal arterial blood pressure [2].

Recent evidence suggests that many forms of CVD are linked to alterations in cardiac metabolism [3]. In the healthy heart, β-oxidation contributes 60-80% of energy [4,5]. The remaining 20-40% is derived from carbohydrate metabolism, principally the metabolism of glucose (via glycolysis) and lactate. β-oxidation and glycolysis are dynamically regulated to provide the most efficient energy production with the most abundant fuel [6]. This ensures that the heart can continue to function under changing metabolic environments. This balance is disturbed in the diseased heart, where there are changes to substrate supply and utilization and heart function subsequently deteriorates [3].

Non-invasive techniques for measuring cardiac function and substrate utilization are vital for diagnosis, prognosis and monitoring of treatment efficacy. Magnetic resonance (MR)

imaging and spectroscopy provide a valuable, non-invasive, toolset to answer these questions. MR provides a means of imaging *in vivo* heart structure, function and metabolism. Carbon 13 (^{13}C) MR spectroscopy (MRS) is particularly well suited to studying metabolism, due to the presence of carbon in all metabolically active molecules. ^{13}C MRS of the intact, *ex vivo* heart was first described in 1981 [7], although due to an inherently low sensitivity, limited *in vivo* studies have since been performed [8]. Through the recent advent of hyperpolarized ^{13}C MRS, which significantly increases the sensitivity of ^{13}C MRS, real time, *in vivo* measurements of cardiac metabolism have become possible in rats and pigs [9,10].

Thesis aims

The work described in this thesis aimed to provide a greater understanding of the *in vivo* metabolic alterations that occur in heart disease. This was achieved by using rat models of heart disease and through the development of mouse cardiac hyperpolarized ^{13}C MRS, to allow a greater understanding of the mechanisms underlying metabolic disorders of the heart.

Hypertension is a major risk factor for heart disease, if left untreated, hypertension can result in cardiac hypertrophy and eventually heart failure. To investigate the *in vivo* metabolic alterations that occur in the hypertensive/hypertrophic heart, the young spontaneously hypertensive rat (SHR) was studied in chapter 3. The SHR is a model that by 15 weeks of age develops hypertension and hypertrophy [11,12]. The SHR has previously been shown, *in vitro*, to display cardiac metabolic alterations and a switch in substrate preference [13].

Myocardial infarction is the leading cause of CVD related death and morbidity [1]. As such understanding the *in vivo* metabolic phenotype of this disease is vital to the further

development of treatments. Chapter 4 details a multi-timepoint study which aimed to understand the *in vivo* changes in metabolism, which lead up to the development of heart failure following a myocardial infarction.

Both of these studies provided us with a wealth of information on the major risk factors of heart failure; hypertension, hypertrophy and myocardial infarction. But to have a greater understanding of the metabolic alterations underlying CVD, we needed to probe individual metabolic pathways. This required the study of genetically modified animals. Whilst recent developments in Sigma's Advanced Genetic Engineering (SAGE) program have made it easier to produce genetically modified rats [14], the majority of existing work has been carried out on genetically modified mice. The translation of the hyperpolarized technique from rat to mouse was particularly challenging, mainly due to the mouse heart being a tenth of the size of the rat heart and with a heart rate at least twice as fast [15]. Chapter 5 discusses the development of mouse cardiac hyperpolarized MR and its first demonstration in the cardiac specific fumarate hydratase knockout (FH-KO) mouse. FH-KO mice were studied at 6 weeks and 12-14 weeks of age to attempt to understand the *in vivo* metabolic alterations which occur in response to a genetic manipulation of the tricarboxylic acid (TCA) cycle.

Finally chapter 6 investigates the *in vivo* effects on cardiac metabolism and function due to critical mutations which affect β-oxidation. Firstly a systemic knockout of a key β-oxidation enzyme, long chain acyl-CoA dehydrogenase (LCAD), which displays a phenotype similar to the human condition very long-chain acyl-CoA dehydrogenase deficiency (VLCADD) was studied [16]. Secondly, the systemic knockout of peroxisome proliferator-activated receptor α (PPARα), one of the transcription factors controlling key genes of β-oxidation was investigated [17]. Finally a type 1 diabetic model was studied using a pancreatic β-cell specific cre inducible gain of function adenosine 5'triphosphate (ATP)-sensitive potassium channel mutation. Type 1 diabetes is characterized by an increase in plasma fatty

acids [6] and a shift towards fatty acid oxidation. Hyperpolarized MRS was used to monitor disease progression and subsequent treatment with the sulphonylurea, Glibenclamide [18].

Introduction

1.1 Energy metabolism in the normal heart

Fatty acids are the major energy source for the mammalian heart [4,5]. The remaining energy is principally derived from carbohydrate metabolism, mainly glucose (glycolysis) and lactate. The human heart needs to consume at least 10 times its own weight in ATP a day to maintain function (3.5 to 5 kg of ATP) [2]. To maintain this level of ATP generation the balance between β-oxidation and glycolysis must be tightly regulated in a process known as the Randle (glucose-fatty acid) cycle [6]. Both pathways are dynamically regulated to provide the most efficient energy production with the most abundant fuel. There are several factors driving this competition, e.g. hormones and the bioavailability of oxygen, which can become a limiting factor in pathological conditions and under physiological stress [6,19]. Both glucose and fatty acid metabolic pathways converge with the production of acetyl-CoA, which is a two-carbon molecule that enters the TCA cycle.

1.2 Glucose uptake and oxidation

Glucose uptake into cardiomyocytes is facilitated by the glucose transporters (GLUT), primarily GLUT1 and GLUT4. Although both transporting glucose into the cell, each transporter plays a different role in glucose uptake. GLUT1 is responsible for basal glucose uptake [20] and expression is normally maintained at a constant level, although can be increased by recruitment of GLUT1-containing vesicles during stress [21,22]. On the other hand, GLUT4's cell surface expression is relatively low, but is dynamically regulated in response to insulin levels [23,24]. Following a meal, when blood glucose levels increase, the pancreatic beta cells release insulin to stimulate glucose uptake into cells. GLUT4 is translocated to the sarcolemmal membrane in response to this insulin stimulation, thereby increasing glucose uptake into cardiomyocytes [23,24]. Important to note is that although sarcolemmal membrane

presentation of GLUT4 increases, total cellular GLUT4 protein expression is unaltered [21]. GLUT4 translocation can also be stimulated by adenosine mono-phosphate (AMP)-activated protein kinase (AMPK), for example during exercise and ischemia [21,22,25].

Once glucose enters the cell, it is phosphorylated by glucokinase, to glucose 6-phosphate (G6P), this step consumes ATP [26]. G6P can then enter either glycolysis, for the production of energy or can be stored as glycogen. Insulin signalling stimulates glycogenesis, where by glycogen production is favoured in a time of plentiful energy supply, this stores glucose for future use. The process of glycolysis converts G6P and nicotinamide adenine dinucleotide (NAD^+) into pyruvate, reduced NAD (NADH) and a net generation of two ATP molecules, per molecule of glucose, Figure 1.1 summarises the steps [27].

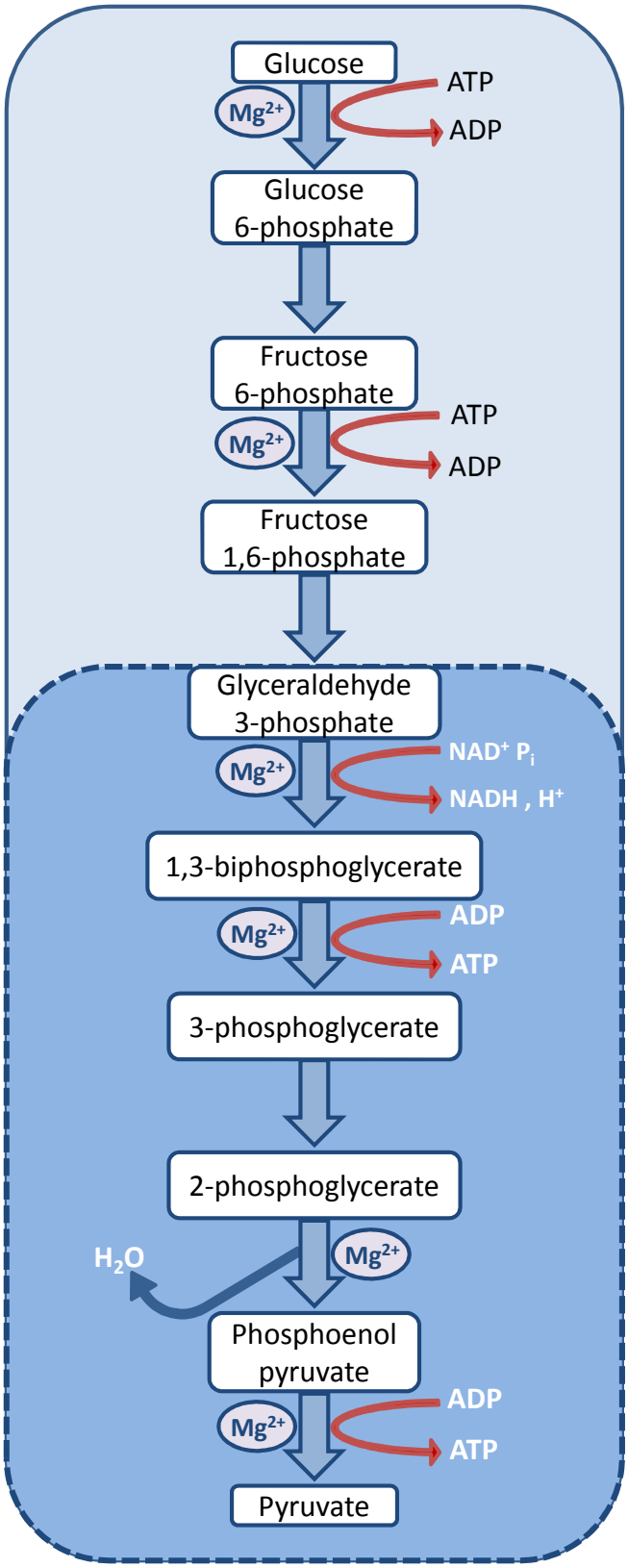

Figure 1.1 – Glycolysis – Glucose enters the cell through either GLUT1 or GLUT4. It then undergoes a series of phosphorylation steps before being cleaved in to two molecules of glyceraldehyde 3-phosphate molecules (shown as the area with a doted border). The terminal molecule in glycolysis is pyruvate. Glycolysis consumes 2 ATP molecules per glucose molecule and generates 4 ATP, giving a net product of 2 ATP per molecule of glucose.

1.3 Role of pyruvate in metabolism

Pyruvate is the terminal molecule of glycolysis, it is transported into the mitochondria and irreversibly decarboxylated to acetyl-CoA by the pyruvate dehydrogenase complex (PDC). The enzyme pyruvate dehydrogenase (PDH) is responsible for catalysing this reaction, within the PDC. The activity of PDH is tightly regulated via a kinase/phosphatase cycle, which ensures that the use of glycolytically derived carbon compounds can be rapidly controlled in response to the changing cellular environment [6,28–30] (Figure 1.2). Phosphorylation of the PDH enzyme complex by PDH kinase (PDK) results in inactivation, this is reversed by the action of PDH phosphatase (PDP).

Four PDK isoforms have been identified to date, with three being expressed within the heart, PDK1, PDK2 and PDK4 [31]. Increases in PDK activity can be stimulated by an excess of acetyl-CoA, NADH and ATP, all signs of plentiful energy supply [27,31]. Whilst NAD^+, CoA and adenosine diphosphate (ADP), all signs of energy deprivation, and pyruvate (sign of increased glycolysis) deactivate PDK, stimulate PDP and increase PDH flux [32,33]. PDP is also activated by insulin and increases in Ca^{2+} and Mg^{2+} , signals of contraction and therefore energy requirement [19,30]. There are two known PDP isoforms in mammalian tissues [34], PDP1 and PDP2, these have different tissue expression patterns, but are both found in the heart [35,36]

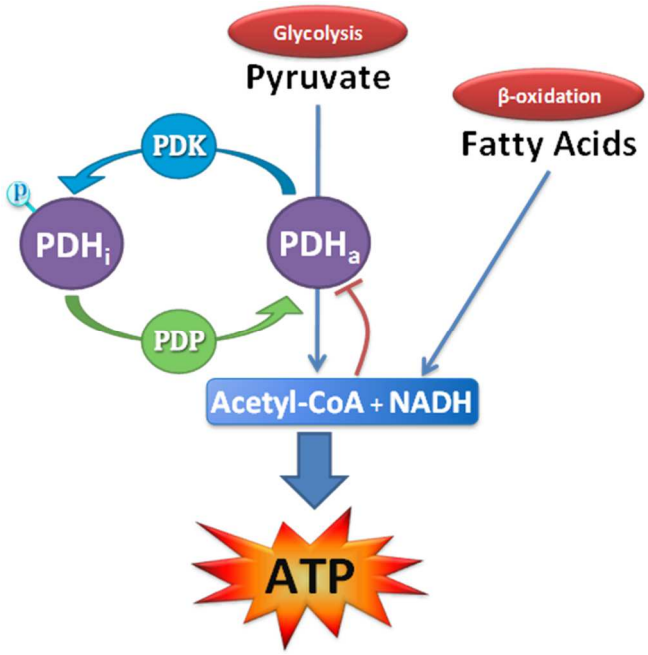

Figure 1.2 – Regulation of PDH – Diagram to illustrate the converging pathways of glycolysis and β-oxidation in the production of acetyl-CoA and NADH. PDH is found in an active (PDHa) and an inactive (PDHi) form, depending on substrate supply to the heart

During starvation or in diabetes there is a decrease in PDH activity in the heart, through both substrate alterations and transcriptional/translational changes/regulation [6,8,35,37]. Both conditions are characterized by an increase in circulating non-esterified fatty acids (NEFAs) [6]. Diabetes is a general term that refers to either type 1 or type 2 diabetes. Type 1 diabetes is characterized by a lack of insulin production due to either a defect in the pancreatic beta cells or autoimmune destruction of beta cells. Type 2 diabetes is still a disease of insulin signalling, but is characterized by a lack of host cell recognition of insulin, or insulin insensitivity. Both result in an inability of the heart to take up glucose after a meal and a subsequent reduction in glycolysis [6]. During diabetes or starvation, adipose tissues release NEFAs into the circulation [6]. These are taken up by cells and are used to supplement the loss of glucose uptake [6]. Increased cellular fatty acids stimulate their own catabolism through β-oxidation, this is achieved in part via the activation of the PPARs, a group of nuclear response elements [38]. PPARα has a high binding affinity for fatty acids and functions to transcriptionally regulate the expression of a range of β-oxidation genes [39–42]. Along with β-oxidation genes, PPARα also

regulates the expression of carbohydrate oxidation genes, decreasing the expression of GLUT4 and increasing the expression of PDK4 [36,43,44]. The consequence is reduced glucose uptake and oxidation and increased β-oxidation. The increased expression of PDK4 and the increase in β-oxidation-derived NADH and acetyl-CoA, lead to significant reductions in PDH flux/activity, thereby minimizing the use of carbohydrate derived carbon compounds [31].

1.4 Fatty acid uptake and oxidation

Fatty acid breakdown via β-oxidation comprises the major fuel source for the mammalian heart. Fatty acids are variable chain length hydrocarbon molecules with a carboxyl group on the end. Uptake of fatty acids is facilitated by cell surface transporters, for example fatty acid translocase (FAT/CD36) is responsible for the transport of long chain fatty acids. Once inside the cell, fatty acids are activated to fatty acyl-CoA, which is transported into the mitochondria through carnitine palmitoyltransferase (CPT) 1, which creates fatty acylcarnitine in the intermembrane space (IMS). Carnitine acyl-translocase (CT) then facilitates the transport of fatty acylcarnitine into the mitochondrial matrix, where CPT2 swaps carnitine for CoA, to reform fatty acyl-CoA, summarized in Figure 1.3 [2,27]. Once inside the mitochondria, β-oxidation cleaves the long chain acyl-CoA's into acetyl-CoA, with the concomitant generation of NADH and $FADH_2$ (reduced flavin adenine dinucleotide) for energy generation in the electron transport chain.

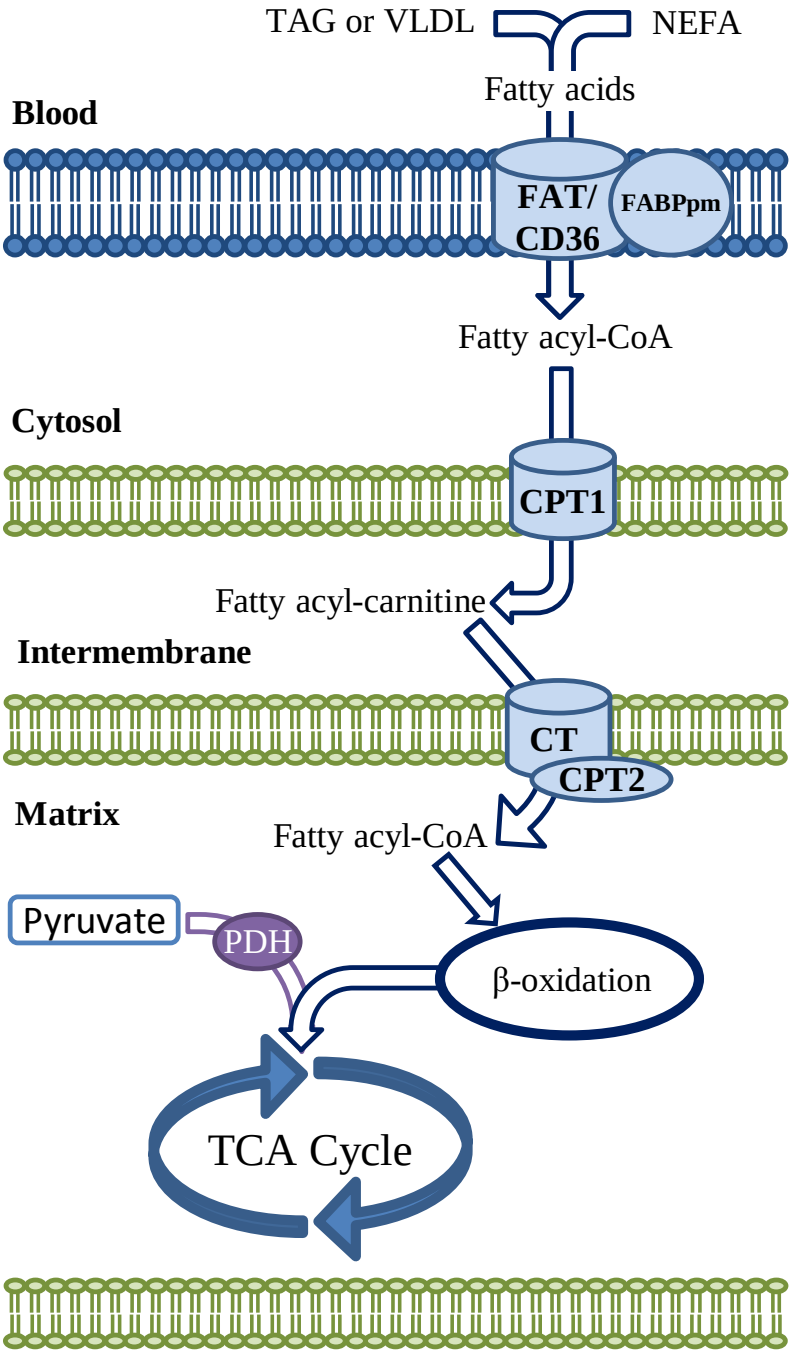

Figure 1.3 – Schematic diagram showing fatty acid transportation from the blood into the cell – From there fatty acids are transported into the mitochondrial matrix to undergo β-oxidation. CT, carnitine acyltranslocase; CPT-I, carnitine palmitoyltransferase-I; CPT-II, carnitine palmitoyltransferase-II; FABPpm, plasma membrane fatty acid binding protein; FAT, fatty acid transporter; FFA, free fatty acids; TAG, triglyceride; VLDL, very-low-density lipoproteins. Figure adapted from Stanley, Recchia, and Lopaschuk (2005)

1.5 TCA cycle

As mentioned in section 1.1, both glycolysis and β-oxidation result in the production of acetyl-CoA, which enters the TCA cycle (Figure 1.4). The ultimate aim of the TCA cycle is to reduce NAD^+ (to produce NADH), and flavin adenine dinucleotide (FAD) (to produce $FADH_2$) for the generation of ATP in oxidative phosphorylation. The first step of the TCA cycle is the condensation of acetyl-CoA with oxaloacetate to form citrate, which is performed by citrate synthase. Aconitase catalyses the next step to form the stereo-isomer of citrate, isocitrate. α-ketoglutarate's production from isocitrate leads to the reduction of NAD^+ into NADH, H^+ and the loss of a carbon molecule, via carbon dioxide (catalysed by isocitrate dehydrogenase). Further NAD^+ reduction is performed between α-ketoglutarate and succinyl-CoA, along with the loss of another carbon dioxide (catalysed by α-ketoglutarate dehydrogenase) [2,27].

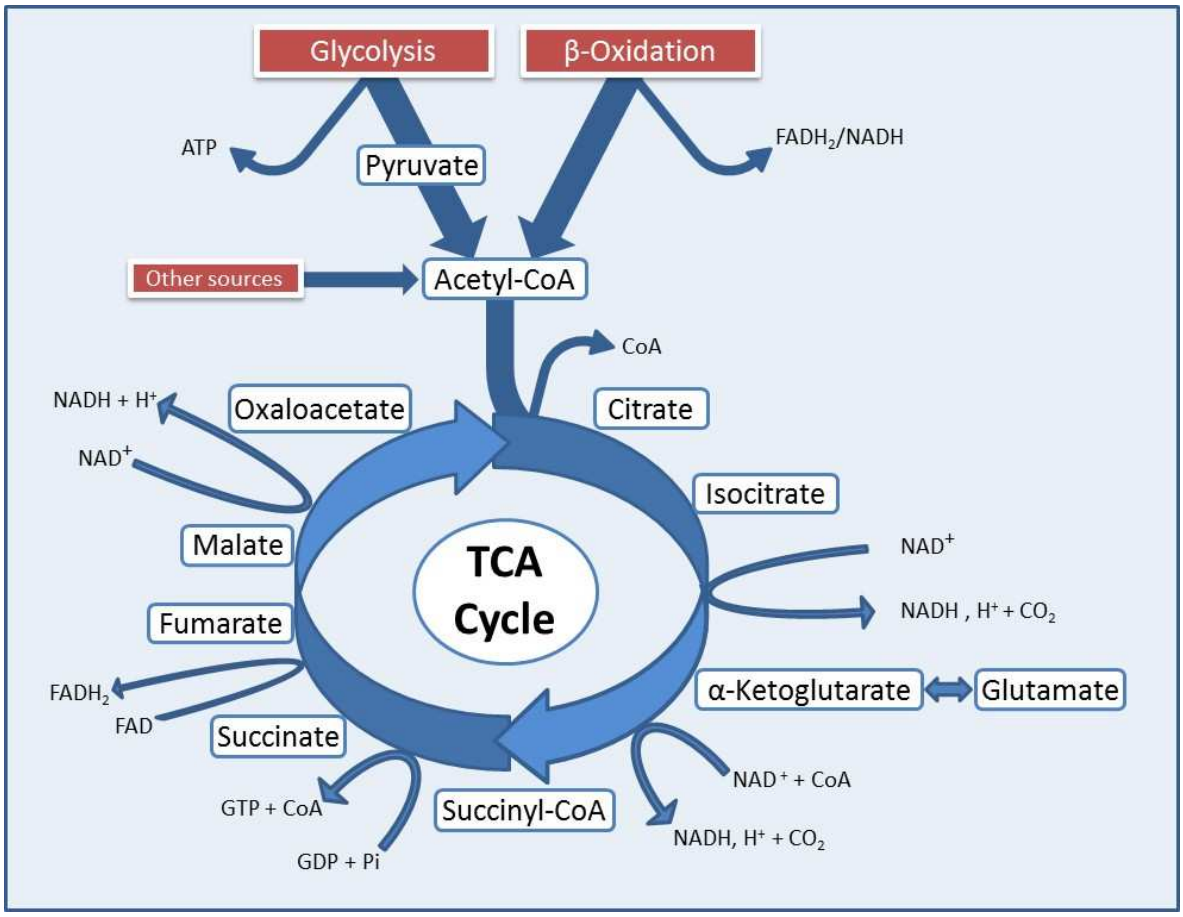

Figure 1.4 – The TCA cycle – Glycolysis and β-oxidation converge with the production of the two carbon molecule, acetyl-CoA.

The removal of the CoA group from succinyl-CoA results in the formation of succinate and a molecule of guanosine triphosphate (GTP). GTP is equivalent to an ATP molecule. The formation of a double bond in succinate produces fumarate, this reaction is catalysed by succinate dehydrogenase, which is linked to complex II in oxidative phosphorylation. This leads to the reduction of FAD to $FADH_2$. An electron is stripped from $FADH_2$ by complex II, is then passed on to coenzyme Q10 and into the electron transport chain (see Figure 1.5).

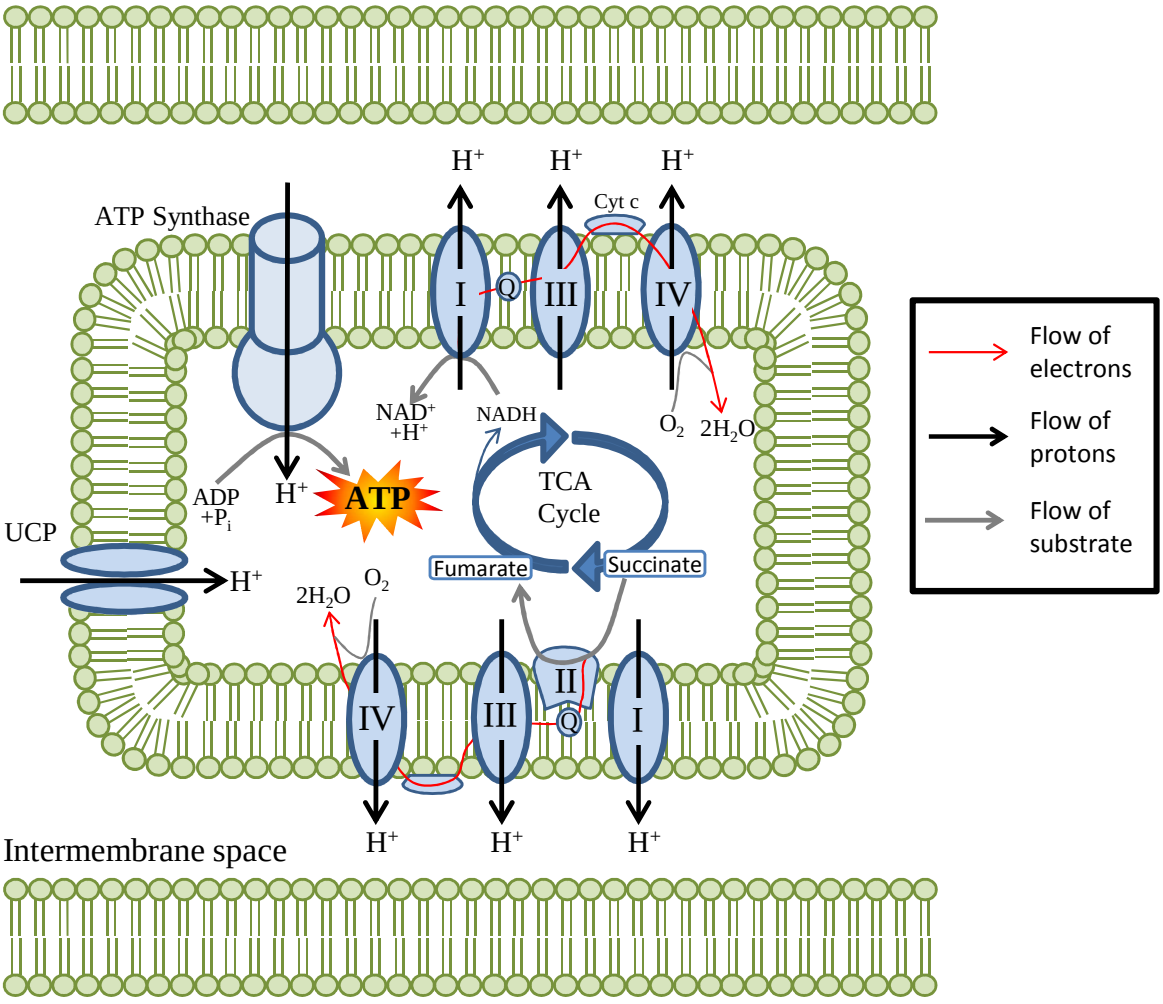

Figure 1.5 – Oxidative phosphorylation within the mitochondria – The following diagram illustrates the production of ATP, by the pumping of protons (H+) into the intermembrane space. Adapted from Stanley, Recchia, and Lopaschuk (2005)

The final NAD^+ reduction is performed by malate dehydrogenase, which means three molecules of NADH are generated per molecule of acetyl-CoA that enters the TCA cycle. Figure 1.5 illustrates the use of NADH, as an electron donor to complex I, which pumps four

protons, from the mitochondrial matrix, into the IMS. Coenzyme Q_{10} transfers electrons to complex III, which pumps four more protons in to the IMS. Cytochrome C shuttles the electrons onto complex IV, where further protons are pumped in to the IMS. The electrons transferred combine with molecular oxygen and protons to form water. The protons that are pumped into the IMS form an electrochemical gradient between the IMS and the mitochondrial matrix. The protons have two paths to re-enter the matrix, either generating heat through uncoupling proteins (UCP) or generating ATP, through the ATP synthase complex. As protons pass through ATP synthase, molecules of ATP are formed from ADP and inorganic phosphate (P_i) [2].

1.6 Techniques for the study of cardiac metabolism

Many techniques exist to assess the metabolic phenotype of a diseased animal or transgenic mouse. Ultraviolet spectroscopy has been used for over 70 years to assess metabolic concentrations or enzyme activities [45]. More recently metabolomic techniques including, ^{1}H-nuclear magnetic resonance (NMR), gas chromatography-mass spectrometry (MS) and liquid chromatography-MS have allowed a greater understanding of the range of metabolites present as they are able to detect milliimolar to sub-picomolar changes of metabolites in disease states [46,47]. As well as biochemical analysis of tissue homogenates, the intact heart can be studied in an *ex vivo* setting using Langendorf perfusion. Langendorf perfusion is a mechanism where the heart is retrograde perfused through the coronary arteries with Krebs-Henseleit buffer, a solution which aims to mimic the ionic composition of blood. This is designed to mirror the *in vivo* setting, but allows for greater control over heart function, due to the absence of hormones. Radiolabelled metabolites can be substituted into the Krebs-Henseleit buffer, to study their metabolism and understand the hearts metabolic state, at a specific time point. Of particular interest to metabolism within the heart are, ^{3}H-palmitate and ^{3}H-glucose which can be used to calculate the rates of β-oxidation and glycolysis, respectively. Heather *et al.* (2006) used ^{3}H-palmitate, to show that the rate of

palmitate oxidation correlated with ejection fraction in the infarcted rat heart, highlighting the ability of this technique to understand metabolic changes during disease [48]. However, these techniques all require the collection of tissue at specific time points. They fail to allow for serial measurements in the same animal over the progression of a disease.

1.7 *In vivo techniques in the heart*

Positron emission tomography (PET) has become an important technique in understanding metabolic processes and uptake of key compounds in both humans and animals [49]. The most extensively studied PET tracer is the fluorine-18-labeled 2-deoxyglucose, fluorodeoxyglucose (FDG) [50,51]. FDG is taken up by the same transporters as glucose and once inside the cell it goes through the first step in glycolysis, namely hexokinase. Hexokinase converts FDG into FDP-6-P, which becomes trapped inside the cell but cannot be further metabolised. FDG-6-P is a poor substrate for glycolysis or glycogen synthesis and cannot be converted back to FDG because of the relatively low abundance of the reverse enzyme (glucose-6-phophatase) [50]. FDG has therefore been used to identify areas/tissue with altered glucose uptake. This has been a particularly important tool for assessing myocardial perfusion and viability following a myocardial infarction. Following an ischemic event, the surrounding myocardium has been shown to alter its metabolic profile, moving from fatty acids to glucose utilization, this would lead to an increase in FDG uptake. PET, however, has several draw backs, the main one being the use of radioactive compounds for detection and x-ray computed tomography for anatomical imaging. This limits the ability to use the technique to monitor serial timepoints. Another major drawback, is that it is not possible to differentiate between the injected compound and it's downstream products. Both decay by the same mechanism and are therefore indistinguishable.

1.8 Magnetic Resonance Spectroscopy

Cardiac MRS offers a non-invasive technique for measuring and studying myocardial metabolism, without the radiation issues associated with PET. MRS provides chemical information of the metabolic state of the myocardium and can be performed serially to track disease progression, therapeutic intervention or as an early diagnostic tool. There are several nuclei of interest in cardiac metabolism: ^{1}H, ^{13}C, ^{23}Na and ^{31}P. ^{31}P has been extensively used to study cardiac energetics, both in the clinic and in the laboratory [52]. The first ^{31}P-MRS studies on the rat, were performed on the *ex vivo* perfused rat heart [53,54]. They showed that it was possible to detect resonances from phosphocreatine (PCr), P_i and the three phosphate groups of ATP, in the beating heart and that levels of PCr, Pi and ATP were altered during ischemia [53,54]. Subsequent studies have shown this in the human heart, where there is a shift in the PCr:ATP ratio, indicating energetic dysfunction [3,55]. ^{31}P MRS has proved to be an invaluable tool in detecting and monitoring energetics within the heart [3,52]. However, due to the relatively low sensitivity of ^{31}P nuclei compared to ^{1}H, clinical application has been limited [52].

^{1}H-MRS should offer the possibility to measure all the metabolites in the body. The physical properties of the ^{1}H nuclei, compared to ^{31}P and ^{13}C are advantageous and allow for the possibility of good signal to noise ratios (SNR). However, the dominant ^{1}H peak in the body is water, which is a very high concentration peak and requires suppression to enable the visualisation of other molecules [52]. Another issue is the need for metabolites in high concentrations, most are actually found in relatively low concentrations. Meaning that the NMR signal from these metabolites is relatively low. ^{1}H MRS has provided a wealth of information into myocardial metabolism, both in humans [56,57], dogs [58], mice [16,59] and rats [60]. It has been especially useful in measuring the content of intracellular lipid pools, a key marker of fatty acid disorders [16].

1.9 ^{13}C – Magnetic Resonance Spectroscopy

^{13}C MRS is particularly well suited to the study of cardiac metabolism. The application of ^{13}C MRS in the heart was first described by Bailey *et al*. (1981)[7], since then it has been used to assess intracellular metabolism in intact hearts to determine steady state fluxes through key metabolic pathways [61]. Due to the presence of carbon in many metabolically active molecules, the advent of ^{13}C MRS led to the possibility of exploring many physiological processes. However, traditional ^{13}C MRS suffers from relatively low sensitivity and requires long scan times. This is a result of several factors; including low natural abundance of the ^{13}C isotope (1.1%), and low metabolite concentrations (mM and below). Although low endogenous concentrations of ^{13}C can be a disadvantage, it can also offer some advantages when using isotopically enriched substrates, as there is minimal non-specific background signal [62].

Another disadvantage for ^{13}C compared to ^{1}H is related to a physical property of the ^{13}C nucleus, the gyromagnetic ratio. Whilst ^{1}H has a gyromagnetic ratio of 42.576 MHz. T^{-1}, ^{13}C is one-quarter of ^{1}H at 10.705 MHz. T^{-1}, leading to an inherently lower sensitivity.

Therefore to obtain sufficient signal in acquired data, acquisitions need to be averaged over 10's of minutes to hours, depending on the sample/experimental set up. This limits biological experiments to the study of steady state metabolism and the visualisation of equilibrium situations. These reasons have limited *in vivo* cardiac ^{13}C MRS studies [63,64] and have led to a reliance on *ex vivo* perfused heart models. This poses the same problem as the other biochemical techniques mentioned earlier, that the same animal cannot be followed through multiple timepoints, meaning the use of more animals and concomitant increases in biological variability.

The benefit of *in vivo* models is that they enable serial measurements and the study of the influence of the entire system, including hormones and the interplay between organs, such as

the liver and heart. Hyperpolarization, via dynamic nuclear polarization (DNP), solves many of the problems of thermal equilibrium ^{13}C MRS. In contrast to thermal equilibrium MRS, DNP has a >10,000-fold increase in sensitivity and thus high SNR and temporal resolution [9,65,66]. A hyperpolarized compound can be injected *in vivo* and its metabolism visualized in real time [9].

1.10 Theory of hyperpolarization via dynamic nuclear polarization

The principle of DNP was first described in the early 1950s [67] and was designed to significantly increase the polarization of nuclear spins within a sample, i.e. ^{13}C containing compound.

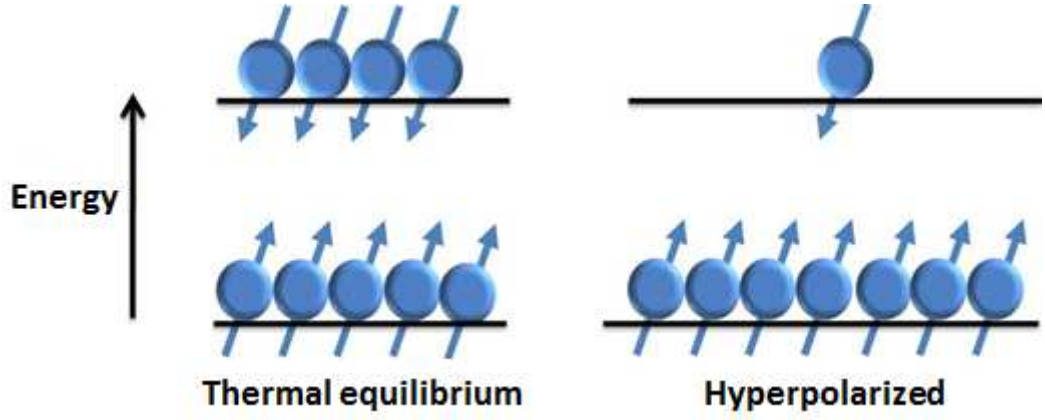

Figure 1.6 – Boltzmann distribution of nuclear spins in low and high energy levels – A) An example of nuclear spins under thermal equilibrium state. B) A hyperpolarized state, where nuclear spins are unequally distributed [66].

For nuclei with a spin number of I = ½ (i.e. ^{1}H and ^{13}C), the nuclear spins can exist in two energy states within a magnetic field, M = ±½. The spins can either align with the applied field (low energy, "up" spin) or against the field (high energy, "down" spin) the difference between energy states is known as ΔE and is determined by the Larmor frequency (ω_n) (see Figure 1.6 A) [65]. As the ΔE is low when compared to the thermal energy in standard conditions, nuclear spins distribute themselves relatively evenly between the energy states, with slightly more spins associated with the "up" state [65]. This slight difference is what is observed as the NMR signal, meaning that thermal equilibrium scans have an inherently low

sensitivity. Hyperpolarization via DNP creates an artificial disequilibrium of nuclear spins in the "up" state (Figure 1.6 B). This results in very high signal due to the increased population difference (polarization) of the nuclear spin states [9].

To achieve this artificial disequilibrium of nuclear spins, the ^{13}C sample must be subjected to low temperatures, a high magnetic field and doped with an unpaired free electron source (an organic free radial). Within this high magnetic field (3.35 T) and at temperatures approaching 1.2 K, homogenously distributed unpaired free electrons are highly polarized (~90%), whilst ^{13}C nuclear polarization is still very low (<0.1%) [66,68] ‡. The sample is subsequently irradiated with microwave radiation at a frequency close to the Larmor frequency of the electrons (ω_e), this enables transfer of polarization from the electrons to the nuclei. There are two main mechanisms by which electron polarization is transferred to nuclei, namely the Solid Effect (SE) and Thermal Mixing (TM) [68].

1.10.1 Solid Effect

As previously mentioned, within a magnetic field the nuclear spins split into two distinct energy levels determined by ω_n. The electronic spins also split into two distinct energy levels, $s = \pm½$, with a much greater ΔE than the nuclear spins. The electronic and nuclear spins couple and further divide in the homogenous DNP sample (Figure 1.7).

When microwave radiation is applied at a frequency $\omega_e - \omega_n$ a "flip-flop" transition will occur, where an electron spin will transition from $s = -½$ to $+½$ and a coupled nuclear spin

‡ To hyperpolarize a ^{13}C sample, it must readily vitrify upon freezing to enable the homogenous distribution of the electrons

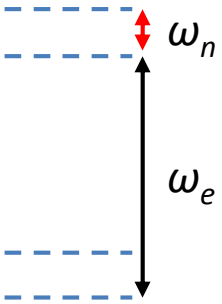

Figure 1.7 – Splitting of energy levels within a magnetic field – The electronic and nuclear energy levels couple within the DNP sample, to produce a quaternary energy state.

will also transition from M = + ½ to - ½ [69]. When microwave radiation is applied at a frequency $\omega_e + \omega_n$ then a "flip-flip" transition will occur, where an electronic spin will transition from s = - ½ to + ½ and a coupled nuclear spin will also transition from M = - ½ to + ½ (see Figure 1.8) [68,69]. These are known as "forbidden" transitions, because the likelihood of these transitions occurring in the absence of microwave radiation is low. Polarization is achieved because the electronic relaxation is significantly faster than the nuclear relaxation, allowing a single electronic spin to pump many nuclei. This produces the disequilibrium of nuclear spins in one energy level.

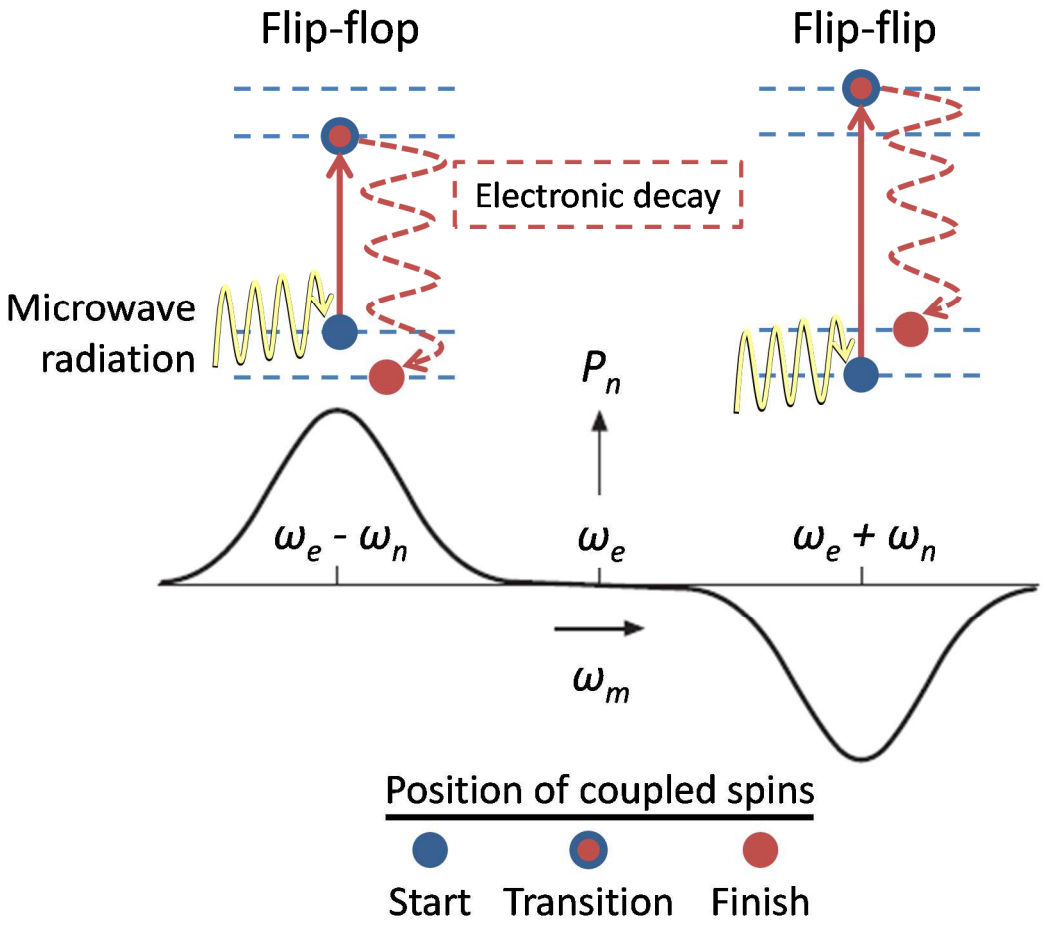

Figure 1.8 – Solid effect for polarisation of nuclear spins – Energy level diagram showing forbidden transition of the coupled spins due to microwave radiation at either $\omega_e - \omega_n$ to produce a "flip-flop" transition or at $\omega_e + \omega_n$ to produce a "flip-flip" transition. Microwave spectrum showing nuclear polarization (P_n) as a function of the microwave frequency (ω_m).

ω_e = Electronic Larmor frequency, ω_n = Nuclear Larmor frequency, P_n = Nuclear polarization, ω_m = Pumping microwave frequency. Diagram adapted from Comment *et al.* (2007)[68]

1.10.2 Thermal Mixing

Whilst the solid effect relies on "forbidden" transitions, thermal mixing works through an alternative mechanism based on allowed transitions. If we consider the electron-nuclear spin system as three "baths"; the nuclear Zeeman system (NZS; nuclear spins), the electronic Zeeman system (EZS; electron spins) and an electron broadening system (EBS; electron-electron dipolar interactions) [70,71]. The electron paramagnetic resonance (EPR) spectrum is governed by electron-electron interactions (EBS), as this interaction is large within our

sample this results in a homogenous broadening of the EPR line [70,72]. When EPR broadening becomes comparable to the nuclear larmor frequency ω_n, the NZS and EBS become thermally coupled. Microwave irradiation of the allowed EPR transitions, leads to a cooling of the EBS. As the EBS is thermally coupled to the NZS, this "bath" is also cooled, leading to nuclear spins becoming trapped in the lower energy state, creating DNP enhancement [68–70,72].

1.11 Dissolution DNP

A significant development in the use of DNP was achieved by GE healthcare with the creation of the dissolution DNP process. The dissolution DNP process allows a ^{13}C compound to be hyperpolarized in the solid state, before being rapidly transferred to the liquid state whilst maintaining relatively high polarization and signal [9,65,66]. DNP had limited biological application due to the inherent low temperatures and pressures required, but this dissolution process enabled *in vivo* applications. Ardenkjaer-Larsen *et al*, described the first dissolution process and its usage in *in vivo* experiments using hyperpolarized [^{13}C]urea, which can be seen in Figure 1.9 [9,65,66]. Urea was used for imaging the vasculature of rats, as it has relatively low toxicity within the blood and is easily polarized [9]. A further study by Golman *et al* investigated the use of [1-^{13}C]pyruvate in rodents [73]. This study showed that it was feasible to inject endogenous substances containing hyperpolarized ^{13}C into an animal and view it's metabolism in real time.

1.12 Limitations of DNP

DNP offers great benefits in terms of the observable signal but suffers from one major limitation, which is the rapid loss of the enhanced polarization due to relaxation (T_1) processes. This relaxation limits the number of subsequent downstream metabolites that are visible. The T_1 is the main determining factor in compound selection as it governs the time

taken for nuclear spins to return to thermal equilibrium, hence the time constant of signal decay. DNP should be applicable to all (small) molecules but only a limited number of compounds are actually amenable to DNP. Several key properties for DNP compounds are set out in Table 1.1.

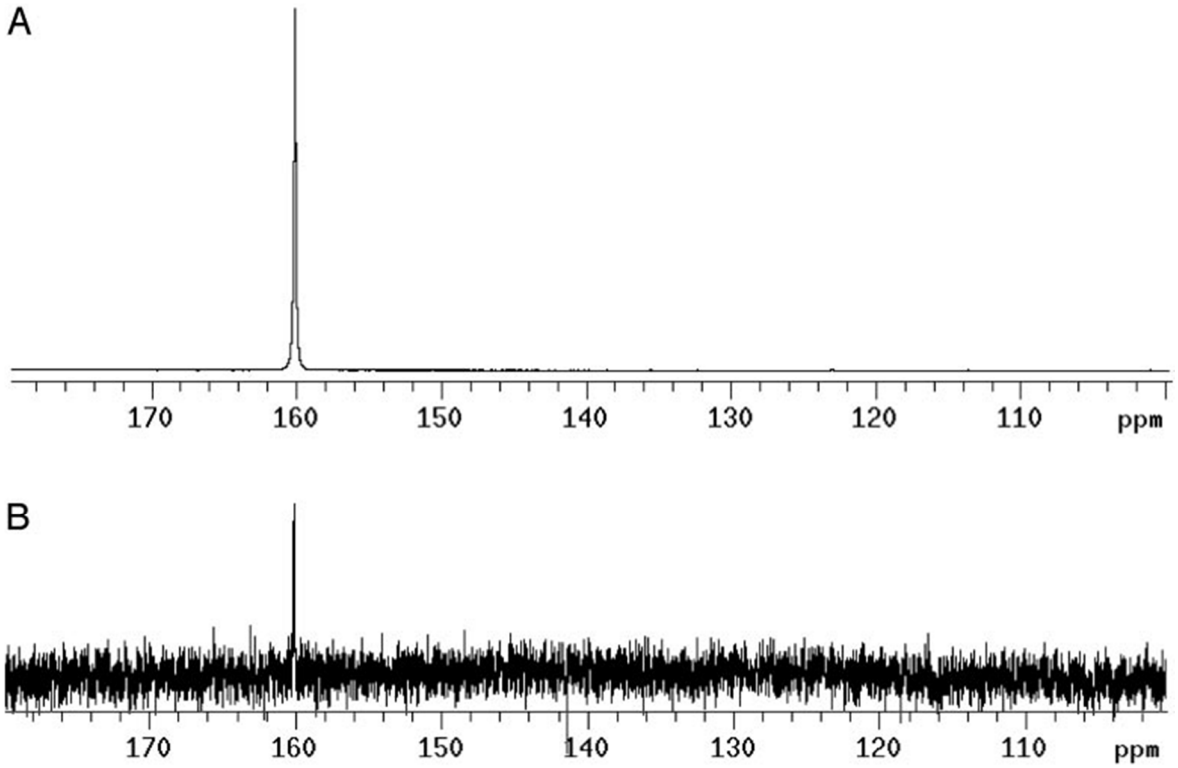

Figure 1.9- ^{13}C spectrum of urea (natural abundance ^{13}C) (*A*) hyperpolarized by the DNP-MRS method, total time for acquisition ~4 sec. (*B*) Thermal equilibrium spectrum of the same sample at 9.4 T and room temperature, total time for acquisition ~65 hours.. The concentration of urea was 59.6mM. Caption and picture are modified from Ardenkjaer-Larsen *et al*. (2003). Permission to reproduce this figure has been granted by Proceedings of the National Academy of Sciences

Table 1.1 – Key properties for a biologically relevant hyperpolarized compound and an example – Pyruvate can be labelled on the 1st or 2nd carbon using ^{13}C isotope. PDH – pyruvate dehydrogenase, LDH – lactate dehydrogenase and AAT – alanine aminotransferase.

Key properties	Example (Pyruvate)
Long T1	~60-90 seconds
Non-toxic	Oral rat LD50: 5600 mg/kg [74]
Rapid absorption	Via monocarboxylate transporter
Rapidly metabolized	Rapidly metabolised by PDH, LDH and AAT
Biological relevance	Central to many biochemical pathways
Ability to glass (vitrifies) easily	Able to glass without the need of a glassing agent

1.13 Applications of DNP

1.13.1 Cardiac DNP

Hyperpolarized [1-^{13}C]pyruvate has proved to be the most successful hyperpolarized compound to date. First described for cardiac applications by Golman and Petersson (2006), [1-^{13}C]pyruvate was injected and imaged in the pig heart [75]. [1-^{13}C]Pyruvate is processed by 3 main enzymes: pyruvate dehydrogenase (PDH), lactate dehydrogenase (LDH) and alanine aminotransferase (AAT), to form [^{13}C]bicarbonate (along with $^{13}CO_2$), [1-^{13}C]lactate and [1-^{13}C]alanine, respectively. Pyruvate was mainly seen in the ventricular lumen, where it was at high concentration due to the injection, whilst lactate, alanine and bicarbonate were seen in the ventricular walls (Figure 1.10). In this study, the pig was imaged before (pre-ischemia) and following a 15 minute occlusion and 2 hour reperfusion [75]. In the occlusion area, signal from bicarbonate was reduced [75]. This study was not quantitative, but demonstrated that pyruvate could be a useful tool in understanding cardiac metabolism.

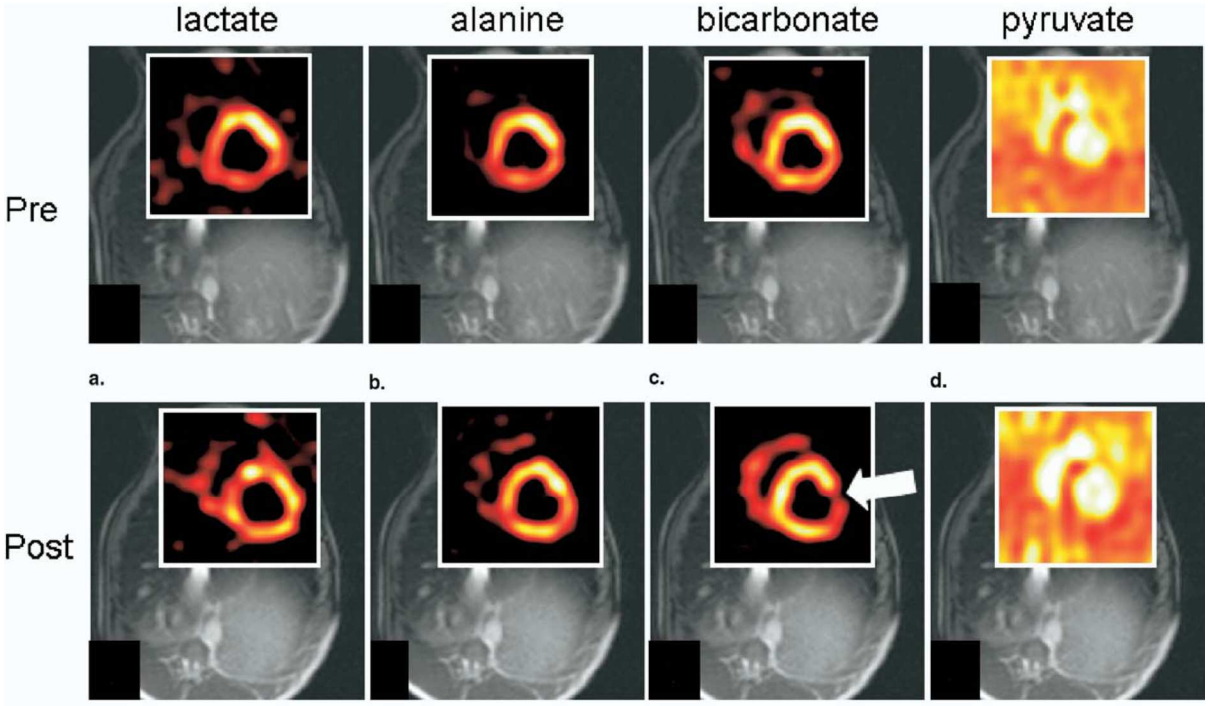

Figure 1.10 – Cardiac [1-^{13}C]pyruvate and metabolic products, pre and post-ischemic occlusion – White arrow shows area of ischemic injury. Image modified from Golman and Petersson (2006) [75]. Permission to reproduce this figure has been granted by Elsevier Ltd, UK.

Further development of imaging techniques in pigs, by Golman *et al* showed that [1-^{13}C]pyruvate could be used to detect reductions in alanine and bicarbonate in a 45 min occlusion model (Figure 1.11) [76]. Late gadolinium enhancement detected an area of severe damage in the pig myocardium. In this area there was reduction in perfusion and the delayed enhancement image overlay an area of absence in alanine and bicarbonate. This highlighted the clinical applications of DNP in understanding alterations in metabolism in the damaged myocardium [77].

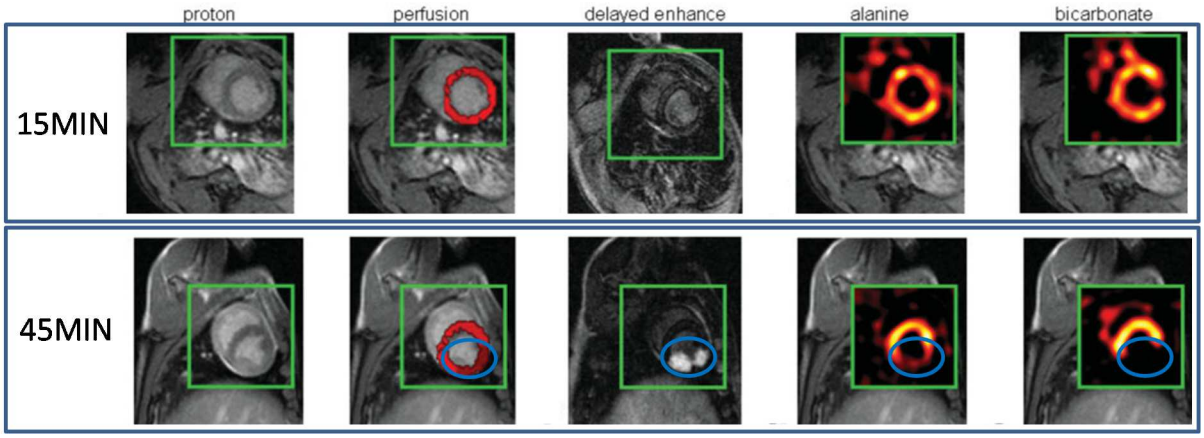

Figure 1.11 – Images from 15 and 45min occlusion of the left circumflex artery in the pig heart – Similar to previous images, the 15min occlusion shows a reduction in bicarbonate in the left ventricle. After 45min a huge perfusion deficit (Blue circle) and damage, can be seen by an increased signal enhancement in the delayed enhanced image. Alanine and bicarbonate signals are reduced in the perfusion damaged area. Image modified from Golman *et al*. (2008) [76]. Permission to reproduce this figure has been granted by John Wiley and Sons.

Further work by Merritt *et al*. (2007) showed that it was possible to measure cardiac flux of pyruvate through PDH, by monitoring the generation of $^{13}CO_2$ and [^{13}C]bicarbonate, in the perfused rat heart [78]. Adding the medium chain fatty acid octanoate to the buffer, led to a significant reduction in $^{13}CO_2$ and [^{13}C]bicarbonate production, this was accompanied by no change in O_2 consumption nor TCA cycle flux [78]. These data indicated that the production of $^{13}CO_2$ from [1-^{13}C]pyruvate, must be solely derived from PDH flux and not generated by the TCA cycle [78]. Following on, hyperpolarized [1-^{13}C]pyruvate has been used as a useful metabolic tracer to assess *in vivo* PDH flux through the progression of type-1 diabetes [8] (Figure 1.12). Here decreased PDH flux significantly correlated with increasing plasma

glucose levels. This study demonstrated the use of hyperpolarized [1-^{13}C]pyruvate in assessing *in vivo* correlations between PDH flux and disease severity [8].

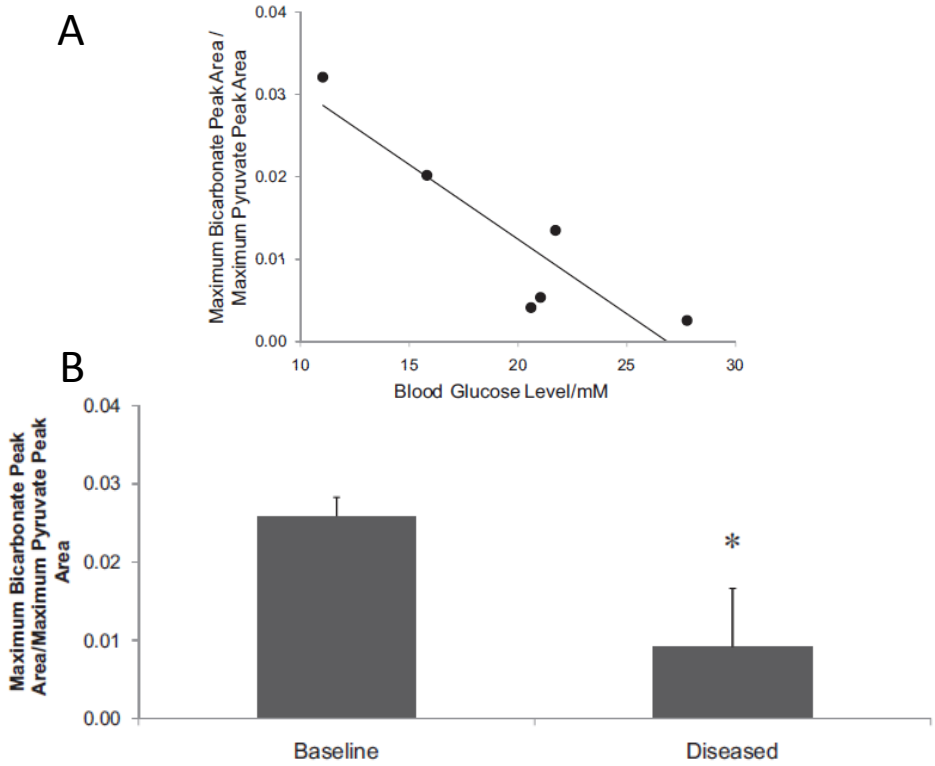

Figure 1.12 (A) Correlation between blood glucose and bicarbonate/pyruvate ratio (r^2=-0.93) – The bicarbonate/pyruvate ratio decreases with increasing disease severity (increased blood glucose concentration) (B) Diabetes induces a significant ($p<0.02$) reduction in the bicarbonate to pyruvate ratio [8]. Permission to reproduce this figure has been granted by Proceedings of the National Academy of Sciences.

Relative flux through cardiac PDH into [^{13}C]bicarbonate and $^{13}CO_2$ has recently been shown to correlate with *in vitro* PDH activity (Figure 1.13) [79]. This indicates that the measurement of *in vivo* PDH flux, reflects PDH enzyme activity. This method has recently been applied to study metabolism in the hyperthyroid rat heart. Administration of the active component of the thyroid hormone, T3 (triiodothyronine), led to significant hypertrophy, a reduction in PDH flux and increases in anaplerotic processing of pyruvate [80]. Co-administration of T3 with dichloroacetate (DCA), a potent PDK inhibitor, in drinking water prevented the changes in PDH flux and reduced the level of hypertrophy. This indicated that the metabolic disorder in PDH was tied to the hypertrophy. The use of hyperpolarized ^{13}C

MRS allowed the same animals to be studied serially throughout the course of the study, before and after T3 and DCA administration [80].

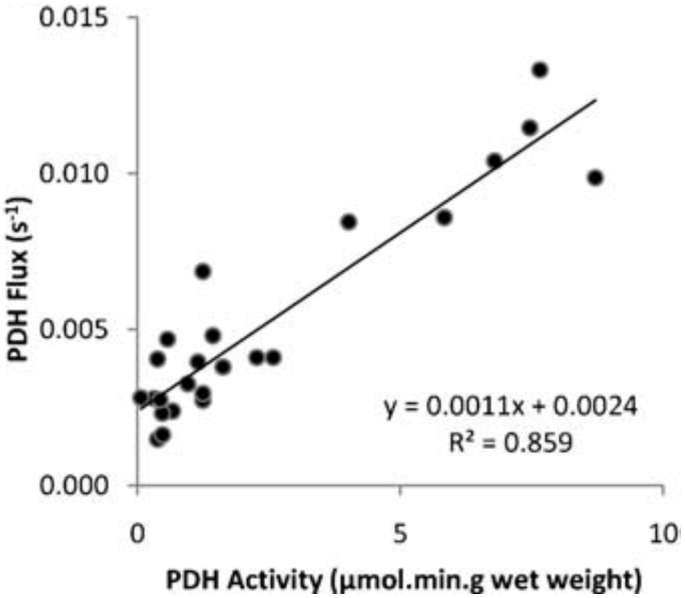

Figure 1.13 – Correlation between PDH flux, as measured by DNP and *in vitro* PDH activity [79]. Permission to reproduce this figure has been granted by John Wiley and Sons.

1.13.2 DNP in oncology

As well as understanding alterations during heart disease, DNP has played a vital role in understanding metabolic changes during cancer. One such example is the conversion of [1-^{13}C]pyruvate into [1-^{13}C]lactate, which has provided a very useful tool for assessing the efficacy of chemotherapy in animal models of cancer [81,82]. Tumour development is characterized by increased anaerobic glycolysis and lactate production, in a process known as the Warburg effect [83,84]. In this process cancerous cells reduce mitochondrial oxidative phosphorylation and produce ATP mainly from glucose. This leads to an increase in the lactate levels within the cell and in the intra-tissue space. Using an injection of [1-^{13}C]pyruvate, a large increase in [1-^{13}C]lactate can be seen in the tumour, compared to normal tissue [82,85]. Following 24 hours of chemotherapy a huge reduction in [1-^{13}C]lactate was detected in the tumour [82]. This provided a useful marker in the detection of chemotherapy efficiency.

Another potentially useful marker which has been used in combination with [1-^{13}C]pyruvate, is [1,4-$^{13}C_2$]fumarate [81,86,87]. Fumarate is a TCA cycle intermediate, which is hydrated by fumarate hydratase into malate. In healthy cells/tissue, hyperpolarized [1,4-$^{13}C_2$]fumarate is not converted rapidly enough into [1,4-$^{13}C_2$]malate, to be visible in the time frame of the experiment [87]. This is due to the relatively long time for fumarate uptake into cells, compared to pyruvate. However, treatment with chemotherapy leads to necrotic tumour cells, which release fumarate hydratase into the extratumour space. This fumarate hydratase will rapidly convert [1,4-$^{13}C_2$]fumarate into [1,4-$^{13}C_2$]malate, leading to a significant correlation between [1,4-$^{13}C_2$]malate production and tumour cell necrosis [87].

Another product of [1-^{13}C]pyruvate, [1-^{13}C]alanine has also formed a crucial role in understanding metabolic alterations in tumour formation. Hu *et al* [88] found that consistent with previous studies, alanine production was low within tumours. However, comparing three key timepoints (healthy, pretumour and tumour) in liver tumour development, highlighted a key finding on alanine production [85]. Alanine levels were unaltered in the healthy and tumourous livers, however there was a significant increase in alanine production in the pretumourous liver. This preceded primary tumour formation and areas of most abundant alanine signal, generally correlated with areas where tumour nodules would eventually form. Conversion of [1-^{13}C]pyruvate into [1-^{13}C]alanine represented the earliest metabolic change they could detect, even before an increase in [1-^{13}C]lactate [85].

Hyperpolarized [1-^{13}C]pyruvate has proved to be a vital marker in understanding tumour metabolism. Injection of [1-^{13}C]pyruvate, provides a diagnostic tool in tumour formation through appearance of increased alanine signals in pretumourous livers [85]. Alternatively, increased [1-^{13}C]lactate signals highlight tumourous tissue which have switched to a glycolytic phenotype [82,85]. Decreases in this [1-^{13}C]lactate signal provide a good prognostic marker of chemotherapy efficacy, coupled with the application of hyperpolarized [1,4-

$^{13}C_2$]fumarate, they allow the visualisation of cancer cell death and switching back to normal metabolic pathways [81,85–87]. These developments have led to the first human trials of the technique, which are currently reaching completion at the University of California, San Francisco [89]. This study aimed to image changes in [1-^{13}C]lactate signal following hyperpolarized [1-^{13}C]pyruvate injection in the prostate, to detect alterations in tumour metabolism (Figure 1.14, Clinical trial identifier:NCT01229618 [89,90]).

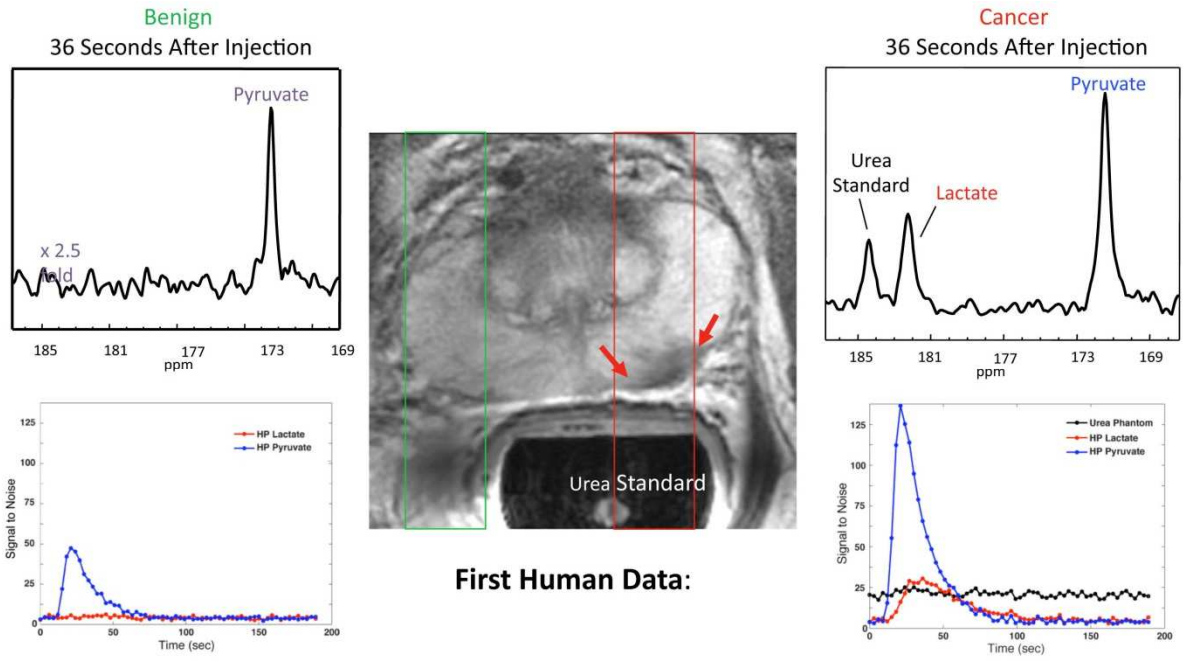

Figure 1.14 – First patient data from phase 1 trail of DNP in University of California: San Fransico.

1.13.3 In vivo pH measurements in the heart and cancer

Finally, as well as measuring PDH flux, the production of $^{13}CO_2$ and [^{13}C]bicarbonate can be used as a marker of intracellular pH (pH_i) [91,92]. During myocardial ischemia or tumour development, there is a rapid onset of acidosis due to a switch to anaerobic glycolysis [93]. Lactic acid and protons accumulate in the intra- and extracellular space, which lowers the intracellular pH in the ischemic heart and tumour. Gallagher *et al.* (2008) used hyperpolarized [^{13}C]bicarbonate to measure the extracellular pH within a tumour [92]. To test the protocol, test tubes were loaded with carbonic anhydrase (CA) (except pH 7.1) and each

had a pH ranging between 6.7 and 7.7. This was measured following the injection of labelled bicarbonate by a pH electrode (Figure 1.15). Labelled bicarbonate was injected into the test tubes and an image was produced to map the production of CO_2. The Henderson-Hasselbalch equation was then applied to (Equation 1.1) and a pH map was obtained (using a pKa of 6.17 for CO_2).

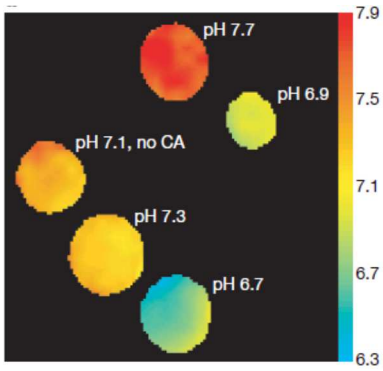

Figure 1.15 –I*n vitro* pH maps – Test tubes were loaded with CA (except pH 7.1) and each had a pH range of 6.7 to 7.7, as measured by a pH electrode. [^{13}C]Bicarbonate and $^{13}CO_2$ were imaged and a pH map was created using the method described in the text. Image taken from [92]**.** Permission to reproduce this figure has been granted by Nature Publishing Group.

$$pH = pK_a + \log_{10}\left(\frac{[HCO_3^-]}{[CO_2]}\right)$$

Equation 1.1 – Henderson-Hasselbalch equation for the calculation of pH from ^{13}C MRS.

The pH calculated using [^{13}C]bicarbonate correlated with the *in vitro* pH measured using the pH electrode. This led to the first use of hyperpolarized [^{13}C]bicarbonate for detecting *in vivo* pH in a tumour. An EL4 tumour (lymphoma) was implanted subcutaneously into mice, hyperpolarized [^{13}C]bicarbonate was injected and the distribution of $^{13}CO_2$ and [^{13}C]bicarbonate was imaged. Applying the Henderson-Hasselbalch equation (Equation 1.1), produced a composite pH map over the tumour (Figure 1.16). The pH within the tumour was measured to be lower than the surrounding tissue [92]. This provided a valuable tool to enable the measurement of tissue pH in a non-invasive technique, both experimentally and potentially in the clinic.

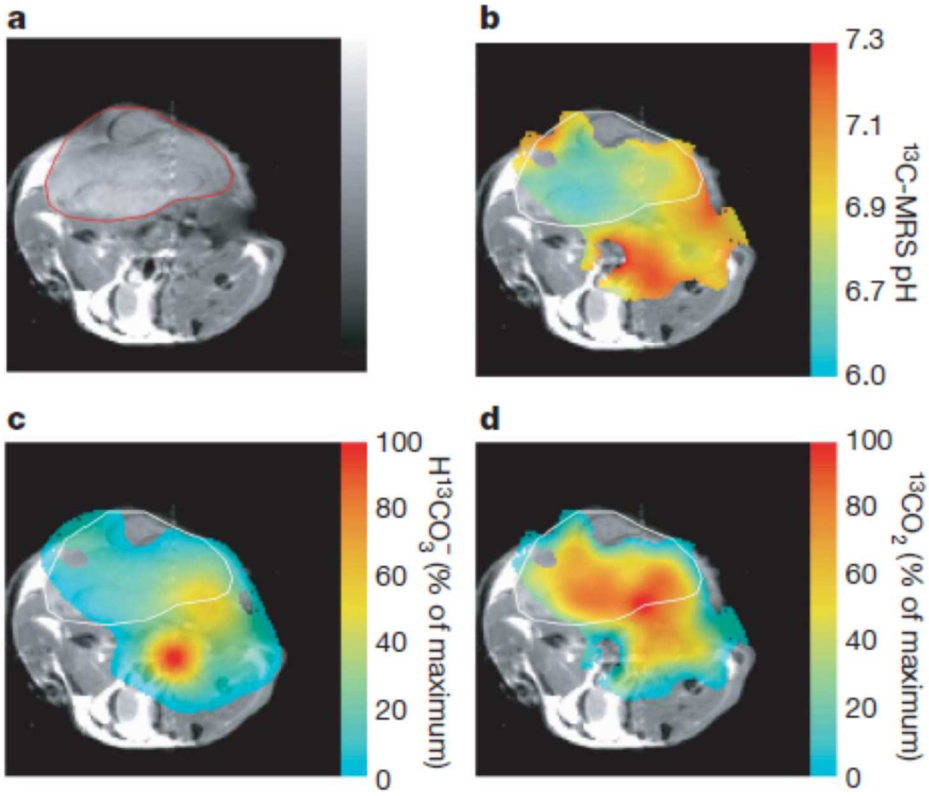

Figure 1.16 - *In vivo* imaging of tumour pH – a) Transverse proton magnetic resonance image of a mouse with a subcutaneously implanted EL4 tumour (outlined in red and white). b) pH map of the same animal calculated using [^{13}C]bicarbonate and $^{13}CO_2$. c) [^{13}C]bicarbonate map and d) $^{13}CO_2$ map. Image taken from [92]. Permission to reproduce this figure has been granted by Nature Publishing Group.

This technique is not just limited to tumours, Schroeder *et al*. (2010) showed that by using the ratio of $^{13}CO_2$ to [^{13}C]bicarbonate, produced by injecting [1-^{13}C]pyruvate, changes in intracellular pH could be detected in the heart, during ischemia [91]. Their results were able to detect a decrease in intracellular pH, which mirrored the gold standard technique of ^{31}P MRS [91].

1.13.4 TCA cycle intermediates

In addition to labelling the 1st-carbon in pyruvate, a second metabolic tracer, [2-^{13}C]pyruvate, has been used to examine TCA cycle metabolism [94,95]. [2-^{13}C]pyruvate was used in the healthy and ischemic perfused heart to study metabolic changes. [2-^{13}C]pyruvate is converted to [2-^{13}C]lactate, [2-^{13}C]alanine, [1-^{13}C]acetylcarnitine, [1-^{13}C]citrate and [5-^{13}C]glutamate (Figure 1.17) [94]. Post-ischemia there was a significant decrease in both citrate

and glutamate production and an increase in lactate. These results showed that the control and fluxes of the TCA cycle could be studied using hyperpolarized [2-^{13}C]pyruvate [94], and led to *in vivo* studies into the use of [2-^{13}C]pyruvate in understanding metabolic fluxes [95].

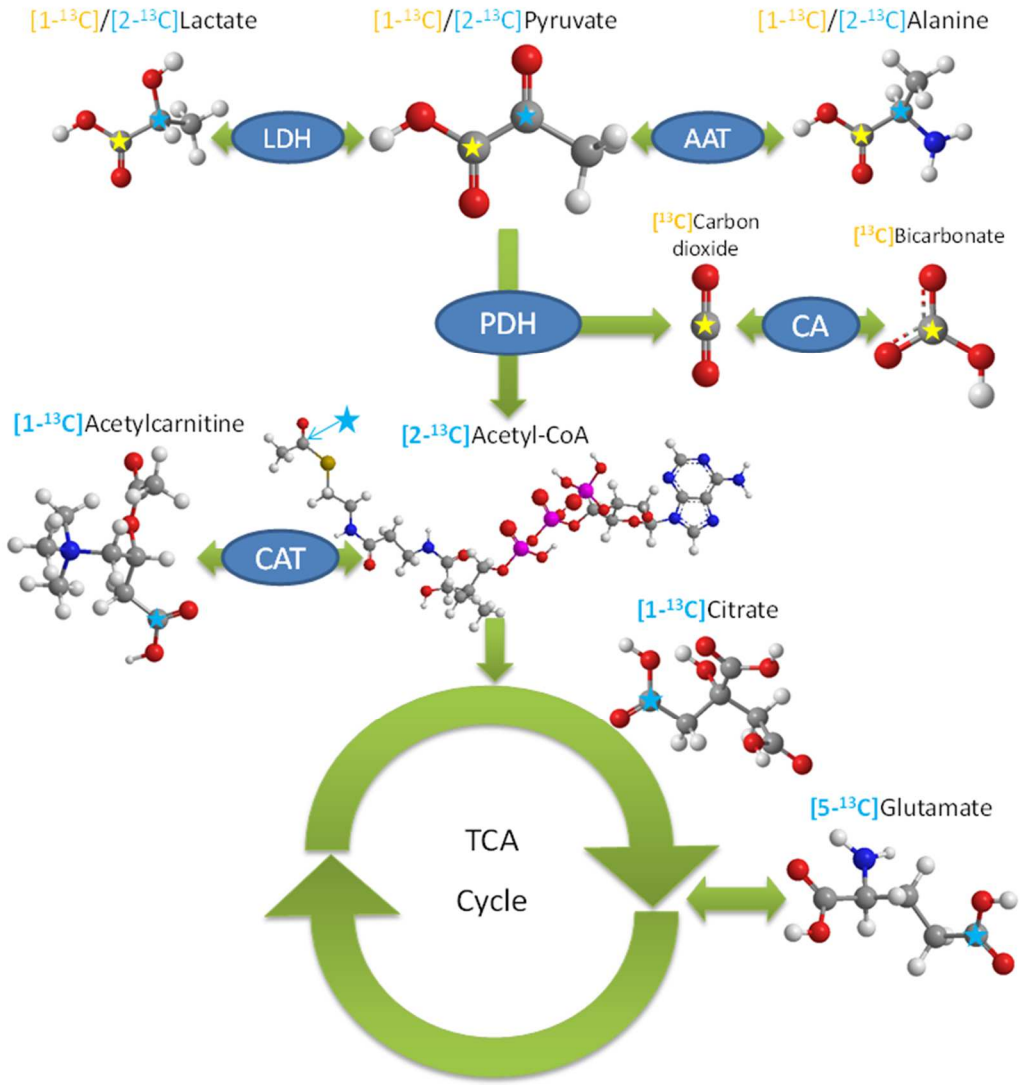

Figure 1.17 – Hyperpolarized pyruvate metabolism – The yellow stars refer to [1-^{13}C]pyruvate usage through the PDH enzyme. The blue stars refer to [2-^{13}C]pyruvate and the transfer of the label through the TCA cycle. AAT- Alanine aminotransferase, CA- carbonic anhydrase, CAT- Carnitine acetyl-transferase, LDH- Lactate dehydrogenase and PDH- Pyruvate dehydrogenase.

1.13.5 Clinical applications

As mentioned previously, the first human trial into the use of [1-^{13}C]pyruvate in prostate cancer is nearing completion [89,90]. As recently discussed by Schroeder *et al.* (2011) human applications for the study of cardiovascular medicine have yet to be started, although work in Oxford is underway to start trials in the near future [77].

Chapter 2

General Methods

The general methods used repeatedly within the thesis are collected here to minimise repetition. Any specific methods or deviations from these methods are set out in the methods sections of individual experimental chapters.

Chemicals

All chemicals were purchased from Sigma-Aldrich, Gillingham UK, unless otherwise stated.

2.1 Animal handling

All animals were housed on a 12:12-h light–dark cycle (lights on 7 a.m. and lights off at 7 p.m.) in animal facilities at the University of Oxford. All hyperpolarized scans were performed between 7 a.m. and 1 p.m., during the animal's early absorptive (fed) state, unless otherwise indicated. All investigations conformed to Home Office Guidance on the Operation of the Animals (Scientific Procedures) Act (HMSO) of 1986 and to institutional guidelines.

Anaesthesia was induced by 2.5-3% isoflurane in oxygen and nitrous oxide (4:1, total of 2 l/min). Anaesthesia was maintained by means of 2% isoflurane delivered during the experiment (O_2:N_2O 4:1, total of 2 l/min). A tail vein cannulation for intravenous administration of hyperpolarized solutions was performed on the animals, which were subsequently placed in a home-built MR animal-handling system [96]. ECG, respiration rate and body temperature were monitored throughout experiments and air heating was provided to maintain body temperature at 37°C as previously described [8].

2.2 Magnetic resonance techniques

2.2.1 Pyruvate polarization and dissolution

Approximately 40 mg of [1-^{13}C]pyruvic acid or [2-^{13}C]pyruvic acid, doped with 15 mM trityl radical (OXO63, GE Healthcare) and 3 µl 2% Dotarem (Guerbet, Birmingham, UK), was hyperpolarized in a polarizer at 1.2 K, 1 mbar, with 45 min of microwave irradiation according to the protocol of Ardenkjaer-Larsen *et al* [9]. Following irradiation, the sample was dissolved in a pressurized and heated alkaline solution (31 mM Tris base , 60 mM sodium hydroxide, 0.25 mM (ethylenedinitrilo) tetra-acetic acid (EDTA) dipotassium salt, to yield a solution of 80 mM hyperpolarized sodium [1-^{13}C]pyruvate or [2-^{13}C]pyruvate with a polarization of ~30 % or ~20 % respectively, at physiological temperature and pH [8,94].

2.2.2 Rat hyperpolarized ^{13}C MR protocol

Rats received either a [1-^{13}C] or [2-^{13}C]pyruvate scan. A home-built ^{13}C butterfly coil (loop diameter, 20 mm, see Figure 2.1) was placed over the rat chest, localizing signal from the heart [8]. Rats were positioned in a 7 T horizontal bore MR scanner interfaced to an Inova console (Varian Inc, Yarnton, UK). Correct positioning was confirmed by the acquisition of an axial proton FLASH image (TE/TR, 1.17/2.33 ms; matrix size, 64 x 64; FOV, 60 x 60 mm; slice thickness, 2.5 mm; excitation flip angle, 15°). An ECG-gated shim was used to reduce the proton linewidth to ~120 Hz. One ml of hyperpolarized pyruvate was injected over 10 s into the anesthetised rat. Sixty individual ECG-gated ^{13}C MR pulse-acquire cardiac spectra were acquired over 1 min after injection (TR, 1 s; approximate excitation flip angle, 5°; sweep width, 13,593 Hz; acquired points, 2,048; frequency centred on the C1 pyruvate resonance).

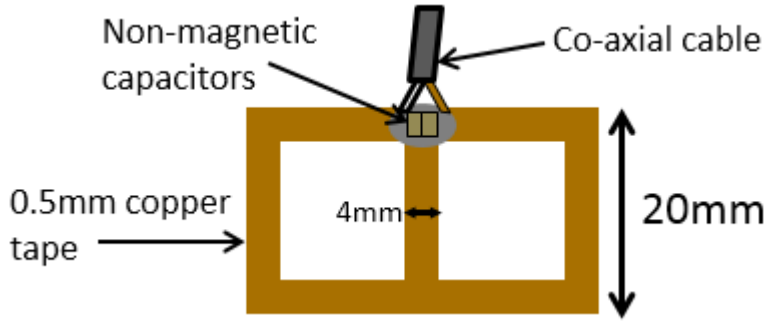

Figure 2.1 – Coil schematic for the rat ^{13}C RF coil – The coil is held on a semi-rigid curved plastic surface to manipulate it around the rat chest.

2.2.3 Mouse hyperpolarized ^{13}C MR protocol

A home-built circular ^{13}C surface coil was used for all mouse studies (10 mm radius) (testing and creation of this coil is described fully in Chapter 5). The coil was placed over the mouse chest, localizing signal from the heart. Mice were positioned in a 7 T horizontal bore MR scanner interfaced to a direct-drive console (Varian Inc, Yarnton, UK). Using a ^{1}H volume radio frequency (RF) coil (Rapid Biomedical, Rimpar Germany), sagittal and axial FLASH localizer images were obtained to confirm the location of the heart at the magnet isocentre (TR/TE, 3.67/1.63 ms; flip angle, 24°; Averages, 16; slice thickness, 2 mm; matrix, 256 x 256; field of view, 51.2 x 51.2 mm). A point phantom containing water was positioned in the centre, on top of the coil and was used to accurately localize the coil above the heart. Using the ^{1}H volume coil, an ECG-gated shim was used to reduce the proton linewidth to ~150 Hz. Following dissolution 200 µl of hyperpolarized pyruvate was injected over 10 s into the anesthetised mouse. Sixty individual ECG-gated ^{13}C MR pulse-acquire cardiac spectra were acquired over 1 min after injection. For [1-^{13}C]pyruvate (TR, 1 s; approximate excitation flip angle, 15°; sweep width, 8,012 Hz; acquired points, 2,048; frequency centred on the C1 pyruvate resonance) and [2-^{13}C]pyruvate (TR, 1 s; excitation flip angle, 15°; sweep width, 13,593 Hz; acquired points, 4096; frequency centred 2000 Hz down field of C1 pyruvate resonance).

2.2.4 MR data analysis

All cardiac ^{13}C spectra were analysed using the AMARES algorithm in the jMRUI software package [97]. Spectra were DC offset-corrected based on the last half of acquired points. The peak areas of *in vivo* [1-^{13}C]pyruvate, [1-^{13}C] lactate, [1-^{13}C]alanine, [^{13}C]carbon dioxide and [^{13}C]bicarbonate (for [1-^{13}C]pyruvate [8]), [1-^{13}C]acetylcarnitine, [1-^{13}C]citrate and [5-^{13}C]glutamate (for [2-^{13}C]pyruvate [94]) at each time point were quantified and used as input data for a kinetic model. The kinetic model developed for the analysis of hyperpolarized [1-^{13}C] and [2-^{13}C]pyruvate MRS data is based on a model initially developed by Zierhut *et al* (2010)[98] and further developed by Atherton *et al* (2011) [79]. Firstly the change in labeled pyruvate signal over the 60 s acquisition time was fit to the integrated labeled pyruvate peak area data using equation [2.1]:

$$2.1 \qquad M_{pyr}(t) = \begin{cases} \dfrac{rate_{inj}}{k_{pyr}}\left(1-e^{-k_{pyr}(t-t_{arrival})}\right) & t_{arrival} \le t < t_{end} \\ M_{pyr}(t_{end})e^{-k_{pyr}(t-t_{end})} & t \ge t_{end} \end{cases}$$

In this equation, $M_{pyr}(t)$ represents the [1-^{13}C] or [2-^{13}C]pyruvate peak area as a function of time. This equation fits the parameters k_{pyr}, the rate constant for pyruvate signal decay (s^{-1}), $rate_{inj}$, the pyruvate arrival rate (a.u. s^{-1}), $t_{arrival}$, the pyruvate arrival time (s) and t_{end}, the time correlating with the end of the injection (s). These parameters were subsequently used in equation [2.2] along with the dynamic metabolite data to calculate $k_{pyr \to X}$, the rate of ^{13}C label incorporation into each metabolite pool from pyruvate (s^{-1}) and k_X, the rate constant for signal decay of each metabolite (s^{-1}) which was assumed to consist of metabolite T_1 decay and signal loss from the 5° RF pulses.

$$2.2 \quad M_x(t') = \begin{cases} \frac{k_{pyr\to x} rate_{inj}}{k_{pyr} - k_x}\left(\frac{1-e^{-k_x(t'-t'arrival)}}{k_x} - \frac{1-e^{-k_{pyr}(t'-t'arrival)}}{k_{pyr}}\right) & t'_{arrival} \le t' < t'_{end} \\ \frac{M_{pyr}(t'_{end})k_{pyr\to x}}{k_{pyr} - k_x}\left(e^{-k_x(t'-t'_{end})} - e^{-k_{pyr}(t'-t'_{end})}\right) + M_x(t'_{end})e^{-k_x(t'-t'_{end})} & t' \ge t'_{end} \end{cases}$$

Where t' is t - t_{delay}, and accounts for delay in the circulation of hyperpolarized pyruvate through the cardiopulmonary system.

2.2.5 To determine intracellular pH using [1-^{13}C]pyruvate

The peak areas of *in vivo* $^{13}CO_2$ and [^{13}C]bicarbonate were also used to estimate pH_i in the heart. Using the method described by Schroeder *et al.* (2010) [91], two single 1 s spectra were summed to increase signal to noise. The first 16 time points were then plotted to estimate pH_i. The peak area of each of these 16 points for bicarbonate ([HCO_3^-]) and CO_2 ([CO_2]) were input into the Henderson-Hasselbalch equation (Equation 2.3), using the pKa of 6.17 for CO_2. They were then plotted on a graph of pH against time, the initial data points show an increase in pH, due to the appearance of label. After that time, there is a stable pH over 20 seconds, this plateau is used as the intracellular pH in the heart (Figure 2.2).

$$[2.3] \quad pH = pK_a + log\left(\frac{[HCO_3^-]}{[CO_2]}\right)$$

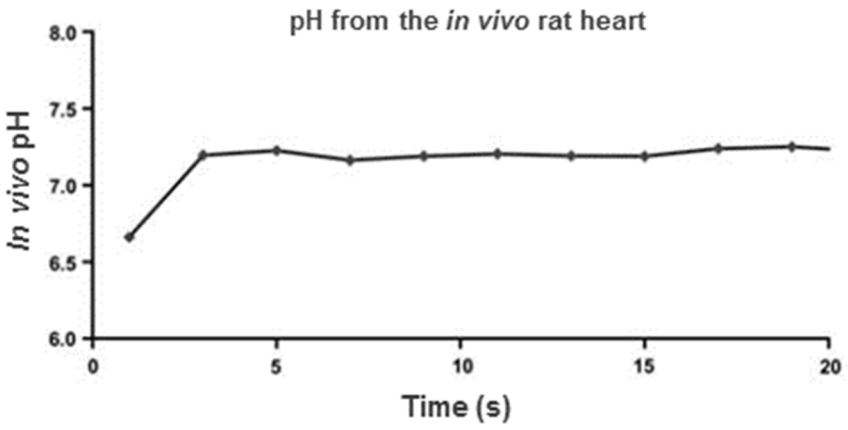

Figure 2.2 – Trace of pH (*in vivo* pH) in the rat heart. Adapted from Schroeder *et al* [91]

2.2.6 *Rat cine MRI*

Cine MRI was used to assess left ventricular mass and cardiac function. Rats were positioned in an 11.7 T (500 MHz) vertical bore MR scanner (Magnex Scientific, Oxon, UK) interfaced to a Bruker Avance console (Bruker Medical, Ettlingen, Germany) and a shielded gradient system (Magnex Scientific, Oxon, UK). A 60 mm birdcage transmit/receive RF coil was used to obtain MR signals (Rapid Biomedical, Rimpar, Germany). Experiments were carried out according to the protocol of Tyler *et al* [99] (TE/TR = 1.43/4.6 ms; Gaussian RF excitation pulse = 17.5°; matrix size = 256 x 256; FOV = 51.2 x 51.2 mm; averages = 4; slice thickness = 1.5 mm, between 10 and 12 slices were required to cover the whole heart). Sequences were ECG-triggered and 28 – 40 frames were collected per heart cycle. Left ventricular volumes were derived using the free-hand draw function in ImageJ (NIH, Bethesda, USA). For each slice, end-diastolic and end-systolic frames were selected according to maximal and minimal ventricular volumes. Left ventricular mass (LVM) was calculated by multiplying the left ventricular wall volume by the specific gravity of the myocardium (1.05 g/cm^3) [99]. Stroke volume (SV = end diastolic volume (EDV) – end systolic volume (ESV)), ejection fraction (EF = SV/EDV) and cardiac output (CO = SV × heart rate) were calculated from the end-diastolic and end-systolic volumes.

2.2.7 *Rat high temporal resolution cine-MRI*

A high temporal resolution (HTR) cine-MRI sequence was used to measure diastolic peak ejection and filling rates in rats [100]. Following the conventional cine-MRI sequences, a mid-papillary slice was selected and imaged using HTR cine-MRI over two consecutive cardiac cycles (TE/TR = 0.86/2.4 ms; Gaussian RF excitation pulse = 60°; matrix size = 128 x 128; FOV = 51.2 x 51.2 mm; averages = 4; slice thickness = 1.5 mm; ~128 frames). The high flip angle RF pulse was designed to increase contrast between blood and myocardium. Chamber

volumes were measured in every frame after threshold adjustment, using ImageJ. This was then plotted as a function of time and early and late peak filling rates were calculated [100].

2.2.8 Mouse cine MRI within hyperpolarized session

Cine MRI was used to assess left ventricular mass and cardiac function. The method was the same as described for 2.2.5 *Rat cine MRI* except for the following alterations. Mice were positioned in a 7 T horizontal bore MR scanner interfaced to a direct-drive console (Varian Inc, Yarnton, UK). Imaging was performed using a ^{1}H volume RF coil (Rapid Biomedical, Rimpar, Germany). Slice thickness was set to 1.2mm and matrix size was set to 128 x 128.

2.2.9 Mouse cine MRI

Cine MRI was used to assess left ventricular mass and cardiac function. The method was the same as described for 2.2.5 *Rat cine MRI* except slice thickness was set to 1 mm.

2.2.10 Mouse HTR cine-MRI

The HTR cine-MRI sequence was also used to measure diastolic peak ejection and filling rates in mice. The method was the same as 2.2.7 *Rat high temporal resolution cine* except that the slice thickness was set to 1 mm.

2.2.11 Tissue collection

At least 1 day post hyperpolarized scans, animals were given an overdose by anaesthetic, using 5 % isofluorane in O_2 (2 L/min). When pedal and corneal reflexes ceased, a thoracotomy was performed and the beating heart quickly removed and arrested in ice cold phosphate buffered saline (PBS). For biochemical analysis hearts were blotted (to remove

liquid), freeze clamped and stored at -80 °C. Otherwise for the assessment of cardiac energetics using ^{31}P MRS, hearts were arrested in ice cold Krebs-Henseleit buffer, instead of PBS.

2.2.12 Phosphorus MRS

The hearts arrested in Krebs-Henseleit buffer (see above) were perfused using a retrograde Langendorff perfusion mode at 85 mmHg [48]. A dual tune ^{1}H/^{31}P volume coil was used for ^{31}P MRS on a 11.7 T vertical bore MR scanner. Fully relaxed scans were performed to assess phosphocreatine (PCr), ATP, P_i and pH_i (TR = 15 s; Gaussian RF excitation pulse = 90°; acquired points, 1024; frequency centred on the PCr resonance; averages = 40). Cardiac ^{31}P MR spectra were analysed using the AMARES algorithm in the jMRUI software package [97]. Absolute ^{31}P metabolite concentrations were calculated by assigning ATP concentrations ([ATP]) of 10.6 mmol/L to the initial γ-ATP peak area for Wistar control hearts [101] and expressing all other ATP, PCr and P_i peak areas relative to this area [91,102]. pH_i was calculated from the P_i chemical shift [102], this was compared with the in vivo pH_i derived from the ratio of $^{13}CO_2$ and [^{13}C]bicarbonate [91]

2.2.12.1 Preparation of Krebs-Henseleit buffer

Oxygen was bubbled throughout the procedure and the compounds added in the order detailed in the Table 2.1, with each being fully dissolved before the next was added. A 5 minute period was left between the calcium chloride dihydrate appearing to have dissolved and the disodium EDTA being added to prevent precipitation. The buffer was then made up to the total volume with ddH_2O, before being filtered (Prefilter, 0.45 μm, 5.0 μm filters).

Table 2.1 – Composition of the Krebs-Henseleit buffer

Compound	*For glucose buffer (g) in 12 l*	*Concentration (mM)*
Sodium chloride	82.764	118
Potassium chloride	4.2	4.7
Magnesium sulphate heptahydrate	3.54	1.2
Calcium chloride dihydrate	3.09	1.8
Disodium EDTA	2.24	0.5
Glucose	23.76	11.0
Sodium bicarbonate	25.2	25.0
Sodium pyruvate	5.94	4.5

2.3 Biochemical analysis

2.3.1 Pyruvate dehydrogenase activity

The activity of the active and total fractions of PDH (PDHa and PDHt) were determined spectrophotometrically by the method of Seymour & Chatham (1997) [103]. The assay required the preparation of cardiac tissue with one of two homogenisation buffers for either PDHa or PDHt measurement. PDHa was assessed when PDH was extracted under conditions where both PDP and PDK were inhibited (25 mM 2-[4-(2-hydroxyethyl)piperazin-1-yl]ethanesulfonic acid (HEPES), 25 mM monopotassium phosphate, 25 mM potassium fluoride, 1 mM dichloroacetatic acid (DCA), 3 mM EDTA, 1 mM ADP, 1 mM dithiothreitol, 0.05 mM leupeptin, 1 % Triton X-100; pH = 7.2 and made up to 50 ml in double distilled water). PDHt was assessed under conditions were PDP was stimulated by Mg^{2+}, and PDK inhibited by DCA and ADP (75 mM HEPES, 5 mM DCA, 5 mM $MgCl_2$, 1 mM ADP, 1 mM dithiothreitol, 0.05 mM leupeptin, 1 % Triton X-100; pH = 7.2 and made up to 50 ml in double distilled water).

Frozen cardiac tissue was powdered and 0.2 g was homogenized in 1 ml of the appropriate homogenization buffer using a polytron (30 s). The sample was snap frozen in liquid nitrogen, thawed and re-homogenized 3 times. The sample was centrifuged (375 x g

for 7 min at 4 °C) and the supernatant removed for analysis. 950 µl of assay buffer (50 mM HEPES, 1 mM $MgCl_2$, 0.08 mM ethylene glycol-bis(2-aminoethylether)-*N*,*N*,*N′*,*N′*-tetraacetic acid (EGTA), 1 mM dithiothreitol, 4 µM rotenone, 1.7 mM NAD, 0.1 mM coenzyme-A, 0.2 mM thiamine pyrophosphate hydrochloride (TPP-HCl), and 16.7 mM lactate; pH = 7.2 and made up to 50 ml in double distilled water) was incubated with 2 µl lactate dehydrogenase at 30 °C for 5 min. PDH activity was determined by adding and mixing a 25 µl aliquot of either PDHa or PDHt extract to the assay buffer and immediately following the reaction at 340 nm using the kinetic program on a Shimadzu UV-1700 spectrophotometer (Shimadzu, Milton Keynes, UK) (2 min for both PDHa and PDHt samples). The rate of NADH production over the first 30 s was used to determine activity in units of $\mu mol.min^{-1}.g\ wet\ weight^{-1}$.

2.3.2 Glycogen content assay

Tissue glycogen content was determined by first destroying endogenous glucose, breaking glycogen down to glucose and measuring the glucose content using an ABX Pentra 4000 (Horiba Medical, Northampton, UK). The method was modified from Bergmeyer (1983) [104] and Cross *et al*. (1996) [105]. 50 mg of frozen powered cardiac tissue was added to 100 µl of 5.4 M potassium hydroxide and vortexed in a fumehood. Samples were then heated at 105 °C for 1 hour, before being cooled on ice for 5 min. To the samples, 50 µl of 140.8 mM sodium sulphate was added and mixed. 600 µl of ethanol was added and samples were left covered at 4 °C overnight.

The following day the samples were spun for 5 min (16,000 x g at 4 °C) and the supernatant was discarded. The pellet was then resuspended using 500 µl of 80% ethanol, sonicated for 1 hour and briefly vortexed. Samples were then re-spun for 5 min (16,000 x g at 4 °C), before being dried at 40 °C overnight.

On the final day, the pellet was resuspended using 375 µl ddH_2O and was added to 125 µl of arcyloglucosidase buffer (5.7 ml of 1 M acetic acid, 8.2 g sodium acetate to 100 ml with ddH_2O. Ten ml of the buffer was added to a 5 mg vial of amyloglucosidase and mixed) was added and samples mixed and incubated for 1 hour at 37 ^oC. To the samples, 100 µl ddH_2O was added, spun for 5 min (16,000 x g at 4 ^oC) and the supernatant collected. Samples were then assayed in triplicate on an ABX Pentra 4000 (Horiba Medical, Northampton, UK) for glucose content. Results are expressed as glucosyl units (µmol.g.w.w.$^{-1}$).

2.4 Western blotting techniques

2.4.1 Tissue lysate preparation for western blotting

Tissue was crushed under liquid nitrogen using a pestle and mortar. Samples (10 mg) were added to 100 ml lysis buffer (75 mM Tris HCl (pH 6.8), 121.5 mM sodium dodecyl sulphate (SDS), 4 M urea, 2.7 mM glycerol and 1.7 ml ddH_2O) in Nunc tubes and homogenized on ice. The samples were then heated at 95˚C for 5 mins and then centrifuged at 375 x g at 4˚C, for a 5 mins. Then samples (30 µl) were extracted and a bicinchoninic acid (BCA) protein assay was run to ensure standard protein loading (detailed below).

2.4.2 BCA protein assay

A standard curve was produced using a range of concentrations of bovine serum albumin (BSA) (0 mg/ml, 0.025 mg/ml, 0.125 mg/ml, 0.25 mg/ml, 0.5 mg/ml, 0.75 mg/ml, 1.0 mg/ml, 1.5 mg/ml and 2.0 mg/ml,). Each sample (5 µl) was diluted with 95 µl ddH_2O, then 200 µl of working reagent buffer (50 reagent A : 1 reagent B (Thermo-scientific, Hemel Hempstead UK)), was added to a 96 well plate with 25 µl of either sample or standard. The plate was incubated at 37 ^oC for 30 minutes before spectrophotometric absorbance was measured (λ = 550 nm) in a 96 well plate reader. All samples were run in duplicate.

2.4.3 Western blotting

Mercaptoethanol (5%), sample buffer (187.5 mM Tris-base, 208 mM SDS, 4.1 mM glycerol, 3 mg Brilliant blue; pH = 6.8 and made up to 50 ml with ddH_2O) and lysis buffer were added to each sample. Set sample concentrations, as determined by the protein assay, were loaded onto 10% SDS–polyacrylamide 15-well gels (detailed below) and separated by electrophoresis at 120 V before being transferred to nitrocellulose membranes. Protein loading and transfer was confirmed using Ponceau staining. All samples were run in duplicate on separate gels. The membrane was blocked in tris-buffered saline-Tween (TBS-T) with 5% milk, incubated with the primary antibody and washed with TBS-T. Then the membranes were incubated with the secondary antibody which was conjugated to horseradish peroxidase and developed using either ECL or ECL prime (GE-helathcare, Amersham, UK) and autoradiograph film (Fisher Scientific UK Limited, Loughborough, UK). The intensity of the bands was analyzed using the UN-SCAN-IT program (Silk Scientific Inc., Utah, USA). Using control animals, protein expression was standardized to equal one arbitrary unit and the relative intensity of the bands was calculated [48].

2.4.4 SDS-PAGE Gel preparation

2.4.4.1 Resolving gel buffer:

Concentrations to make up resolving gel buffer: 1.5 M Tris base and 13.9 mM SDS; pH = 8.8 and made up to 500 ml with ddH_2O

10% concentration gel	***Volume***
Acrylamide	12.5 ml
Resolving gel buffer	12.5 ml
ddH_2O	12.5 ml
TEMED	60 µl
10% Ammonium persulfate (APS)	250 µl

2.4.4.2 Stacking gel buffer

Concentrations to make up stacking gel buffer: 0.5 mM Tris base and 13.9 mM SDS; pH = 6.8 and made up to 500 ml with ddH_2O

10% concentration gel	***Volume***
Acrylamide	2.6 ml
Resolving gel buffer	5 ml
ddH_2O	2 ml
TEMED	25 µl
10% Ammonium persulfate (APS)	125 µl

Chapter 3

In Vivo Cardiac Metabolism and Functional Alterations in the Spontaneously Hypertensive Rat Heart

3.1 Overview

Spontaneously hypertensive rats are a model of hypertension and develop pressure-overload concentric hypertrophy after 15 weeks. One of the cellular responses to hypertrophy is a reduction in β-oxidation and it is hypothesised that in response the SHR heart switches to a glycolytic phenotype. The aim of this work was to assess *in vivo* metabolism in the hypertensive rat heart by performing MRS using hyperpolarized [1-^{13}C] and [2-^{13}C]pyruvate. Cine-MR imaging was also used to assess the degree of cardiac hypertrophy and alterations to cardiac function.

At 15 weeks of age SHRs displayed functional changes in stroke volume, heart rate and diastolic filling related to the hypertension and displayed significant hypertrophy with an increase in left ventricular mass of 56%. Further, an 85% increase in ^{13}C label flux through PDH was seen in the 15 week old SHR heart and ^{13}C label incorporation into citrate, acetylcarnitine and glutamate pools was elevated in proportion to this increase in PDH flux. This would indicate increased ^{13}C labelling of acetyl-CoA, but normal flux through the TCA cycle. ^{13}C label incorporation into lactate was unchanged indicating no classical switch to a glycolytic, anaerobic phenotype, but rather an increased reliance on glucose oxidation through PDH in the SHR heart.

3.2 Introduction

The World Health Organisation estimates that in 2004, 7.2 million people died worldwide from coronary heart disease [106]. A major risk factor for coronary heart disease is hypertension, which in 2006 cost the UK alone £1bn in clinical management [107]. Hypertension is characterized by an increase in arterial blood pressure and a subsequent increase in LV wall stress. A patient presenting with a blood pressure measurement of 140/90 mmHg or greater, is hypertensive and at greater risk of developing coronary heart disease [107].

On the cellular level, a mechanism to protect the hypertensive heart is the induction of pro-hypertrophic factors, which increase LV wall thickness and equalize LV wall stress via the LaPlace law (Equation 3.1 and Figure 3.1) [2]. The hypertensive heart subsequently develops (pressure-overload) concentric LV hypertrophy, where cardiomyocyte diameter increases but length remains constant (Figure 3.1). Whilst this hypertrophy is initially beneficial, if left untreated the heart will ultimately fail due to an inability to maintain normal cardiac output [2].

It has been suggested that in the hypertrophied heart there are changes in the profile of substrate utilization, limiting energy provision and eventually leading to a deterioration in heart function [3,108]. However the exact mechanism of this switch is poorly understand and the exact profile is a contentious issue. Depending on the source of hypertrophy (i.e. pressure-overload, volume-overload, post-infarction or genetic), glycolysis can be increased, decreased or unaltered [109–111]. Whilst fatty acid oxidation appears to inversely correlate with glycolysis, due to the Randle-cycle effect [6], hypertrophy also seems to produce contradictory alterations in PDH activity, with data showing both increases [111–113] and decreases in PDH activity [80,103]. These results could be contradictory because of the complicated nature of hypertrophy, the

variety of models and the different timepoints during disease progression that have been studied.

$$\sigma = \frac{(P \times r)}{2m}$$

Equation 3.1 – LaPlace law - The LaPlace law states that pressure positively correlates with wall stress. The law shows the relationship between wall stress (σ), pressure (P), ventricular radius (r) and wall thickness (m).

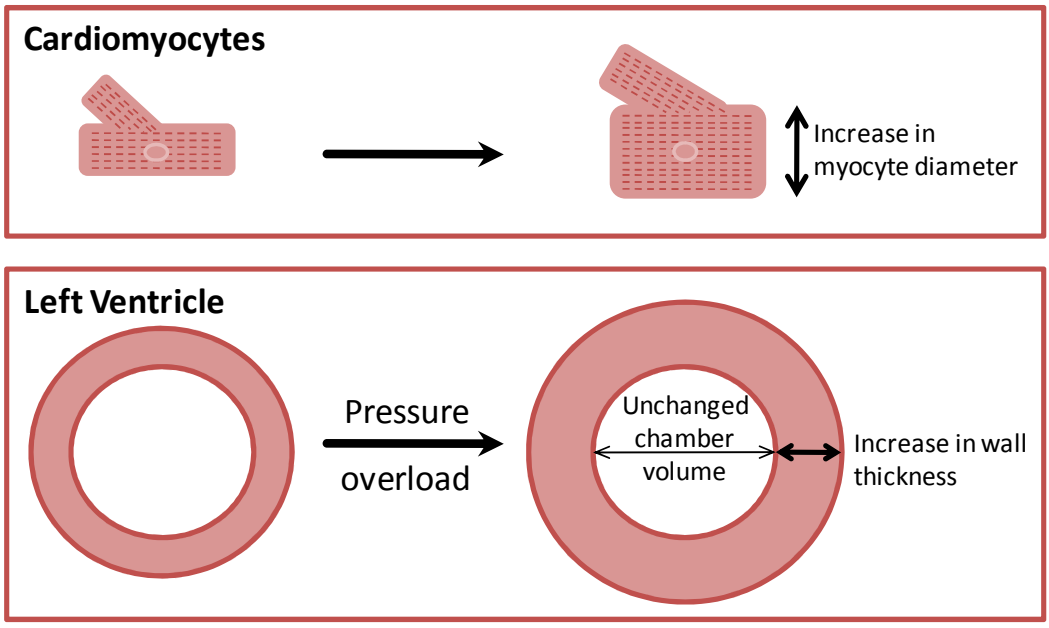

Figure 3.1 – Hypertrophy in the SHR – Hypertension leads to increase in wall stress and due to the Laplace law this corresponds to an increase in wall thickness. Chamber volume remains the same, meaning the heart still ejects the same volume of blood. Pressure overload hypertrophy results in increased myocyte diameter, while length remains relatively constant.

A commonly used model to understand the metabolic alterations underlying hypertension induced hypertrophy is surgical constriction of the aorta. This is performed by either placing a band over the descending aorta, between the right and left kidney (abdominal aortic banding) [103], or constricting the aorta at the aortic arch between the right and left carotid arteries (transaortic constriction) [114]. These methods produce varying degrees of hypertension and hypertrophy and a large cohort of animals is required to perform studies, due to the large intra-group variability in banding.

Another model that has been used historically is the SHR [11,12]. The SHR was generated naturally through the inbreeding of Wistar-Kyoto rats with elevated blood pressure. Subsequently a stable line of consistently hypertensive animals was generated. By 15 weeks of age, the SHR has a mean blood pressure of 182/126 mmHg, compared to a control value of 129/91 [115]. In terms of patients, this level of hypertension would constitute a considerable risk for the development of cardiac complications [1,107,116]. Cardiac structure and function in the SHR has been well characterised and is said to closely parallel the human hypertensive phenotype, with similar hemodynamic, endocrine and end-organ (i.e. heart) alterations [117].

The combination of hypertension and hypertrophy result in continuing adaptation of cardiac metabolism [11,12]. During early development of hypertension (5-10 weeks), the SHR heart displays compensated alterations in glycolytic intermediates and high energy phosphates, which lead to a normalized myocardial energy state [12]. At 15 weeks of age SHRs represent an early compensatory disease model of hypertrophy with elevated blood pressure and concentric hypertrophy [118].

The SHR has a number of genetic mutations which contribute to the hypertensive phenotype. A major mutation is a loss of function of FAT/CD36, a sarcolemmal fatty acid transporter [119]. FAT/CD36 is crucial for the transport of long chain fatty acids (LCFAs) across the plasma membrane. Studies in the CD36-deficient mouse have revealed a significant increase in basal glycolysis and glucose uptake in the heart [120]. Fatty acid uptake and oxidation are also severely impaired in these mice, resulting in elevated plasma free fatty acids (FFA) and triglycerides [120]. This is mimicked in the SHR rat at 15 weeks. ^{13}C MRS on the perfused *ex vivo* SHR heart has been used to track a reduction in ^{13}C label incorporation into the TCA cycle from fatty acids [13]. Furthermore, using the radioactive fatty acid analogue, BMIPP (^{123}I-β-methylp-iodophenylpentadecanoic acid), a significant reduction in fatty acid uptake and oxidation was observed in the SHR, similar to the CD36$^{-/-}$ mouse [121]. This *in vitro*

evidence demonstrates a major shift in cardiac metabolism away from fatty acid oxidation in the 15 week old SHR heart [13,121].

At this 15 week timepoint, the SHR heart also shows a significant 60% reduction in the mRNA expression of the inducible PDK isoform, PDK4 [122]. PDK4 is one of the key regulatory enzymes of PDH in the heart. In type-1 diabetes and high fat feeding, elevated mRNA and protein expression of PDK4 has been shown to decrease both *in vitro* PDH activity and *in vivo* PDH flux [8,37,79,103]. Thus, given the decrease in PDK4 in the SHR heart, we would hypothesise that *in vivo* PDH flux would be increased.

Progression into sustained hypertension and hypertrophy shows that by 25 weeks the SHR heart has a reduced lactate/pyruvate ratio and altered high energy phosphate levels, indicative of perturbed energy homeostasis [12]. As the SHR heart ages to 16-18 months, the animals display severe insulin resistance and increasingly compromised cardiac energetics [123].

The nature of hypertension and hypertrophy mean that there are a multitude of factors affecting disease progression and severity. This is particularly difficult to mimic using *ex vivo* models. Only the *in vivo* setting provides the correct balance of hormonal, functional and regulatory responses to fully characterize the disease. ^{13}C MRS is particularly suited to the study of metabolism in the heart due to the extensive range of metabolites that can be observed [13]. Therefore we utilized hyperpolarized [1-^{13}C]pyruvate to probe *in vivo* flux through PDH into [^{13}C]bicarbonate and $^{13}CO_2$, which has been shown to accurately reflect PDH activity [79]. Hyperpolarized [1-^{13}C]pyruvate was also used as it is processed into [1-^{13}C]lactate and [1-^{13}C]alanine, via LDH and AAT, respectively giving an assessment of alterative fates of carbohydrate metabolism. Hyperpolarized [2-^{13}C]pyruvate was also

studied as it is able to probe the entry of pyruvate derived acetyl-CoA into the TCA cycle via visualization of [1-^{13}C]acetylcarnitine, [1-^{13}C]citrate and [5-^{13}C]glutamate [94,95].

In this study our aim was to determine *in vivo* flux through PDH in the SHR heart at a compensated stage of hypertrophy to investigate the balance between anaerobic glycolytic metabolism and glucose oxidation *in vivo*. The findings of this work were supported by *in vivo* cine-MRI measurements of heart function and mass, and *in vitro* biochemical assays of enzyme activity and protein expression.

3.3 Methods

3.3.1 Animal handling

Fifteen week old SHR (~300 g, n = 13) and Wistar (275-325g, n = 11) control rats were obtained from Harlan UK. All rats were housed on a 12:12-h light–dark cycle and studies were performed between 7 a.m. and 1 p.m., during the early absorptive (fed) state. All investigations conformed to Home Office Guidance on the Operation of the Animals (Scientific Procedures) Act (HMSO) of 1986 and to institutional guidelines. Animal handling was carried out as described in section 2.1.

3.3.2 Hyperpolarized ^{13}C MRS protocol

On two separate days animals received either a [1-^{13}C] or [2-^{13}C]pyruvate scan. The hyperpolarized protocol and pyruvate dissolution were as set out in sections 2.2.1 and 2.2.2.

3.3.3 MRS data analysis

MRS data analysis was carried out as described in sections 2.2.4 and 2.2.5.

3.3.4 Cine magnetic resonance imaging

On a separate day, all animals were imaged to assess left ventricular mass and cardiac function. Cine MRI and HTR cine-MRI were performed as set out in sections 2.2.6 and 2.2.7.

3.3.5 Tissue collection

Between one and three days post hyperpolarized scans, the rats were anaesthetized using a 0.7 ml i.p. injection of pentobarbital sodium (200 mg/ml Euthatal). The beating heart was rapidly removed and placed in ice cold phosphate buffered saline (PBS). A subset of hearts were used to assess energetics using ^{31}P MRS and were arrested in ice cold Krebs-

Henseleit buffer, instead of PBS (n = 6). The remaining hearts were blotted (to remove liquid), freeze clamped and stored at -80°C for subsequent biochemical analysis (Section 2.2.11).

3.3.6 ^{31}P MRS

^{31}P MRS was carried out as set out in section 2.2.12.

3.3.7 Western blotting

Protein expression levels of key metabolic enzymes were assessed in total heart homogenates using SDS-PAGE western blotting (section 2.4). The primary and secondary antibodies used are set out in Table 3.1. All samples were run in duplicate on separate gels to confirm results.

Table 3.1 – Antibodies used to probe key metabolic pathways in the SHR heart.
N.B. Cell Signalling Technology (Hertfordshire, UK), Abgent (Berkshire, UK) and Abcam (Cambridge, UK)

Protein	***Antibody***	***Dilution***	***Company***	***Secondary***	***Dilution***
PDK 1	Rabbit anti-PDK1	1:2000	Cell Signalling Technology	Goat anti-rabbit	1:3000
PDK 2	Rabbit anti-PDK2	1:10000	Abgent	Goat anti-rabbit	1:3000
PDK 4	Rabbit anti-PDK4	1:500	Abgent	Goat anti-rabbit	1:2000
PDP 1	Mouse anti-PDP1	1:1000	Abcam	Goat anti-mouse	1:2000
PDP 2	Mouse anti-PDP2	1:1000	Abcam	Goat anti-mouse	1:2000
GLUT1	Rabbit anti-GLUT1	1:1000	Abcam	Goat anti-rabbit	1:2000
GLUT4	Rabbit anti-GLUT4	1:4000	Gift from Dr G. Holman, Bath University	Goat anti-rabbit	1:3500

3.3.8 Pyruvate dehydrogenase activity

To assess *in vitro* PDH activity, a PDH activity assay was employed using the method set out in section 2.3.1.

3.3.9 Glycogen content assay

The glycogen content of the heart was determined using the method set out in section 2.3.2.

3.3.10 Statistics

All results are expressed as the mean ± SEM. Analysis for statistical significance was performed using an unpaired two-tailed Student's t-test assuming equal variance (SPSS, IBM, USA). Significance was taken at $p<0.05$.

3.4 Results

3.4.1 Hypertrophy and adaptive changes in cardiac function in the SHR heart

Cine-MRI was used to confirm the hypertrophic phenotype of the SHR heart. LVM was significantly increased by 56% in the SHR versus control (Figure 3.2). This translated to a significant increase in the LVM to body weight ratio (53%), indicative of hypertrophy (Table 3.2). Cine-MRI was also used to assess *in vivo* cardiac function. Stroke volume and end diastolic volume were significantly increased by 19% and 18%, respectively, whilst heart rate was reduced by 18% in the SHR. This resulted in no overall change in cardiac output or ejection fraction indicative of compensated hypertrophy (Table 3.2).

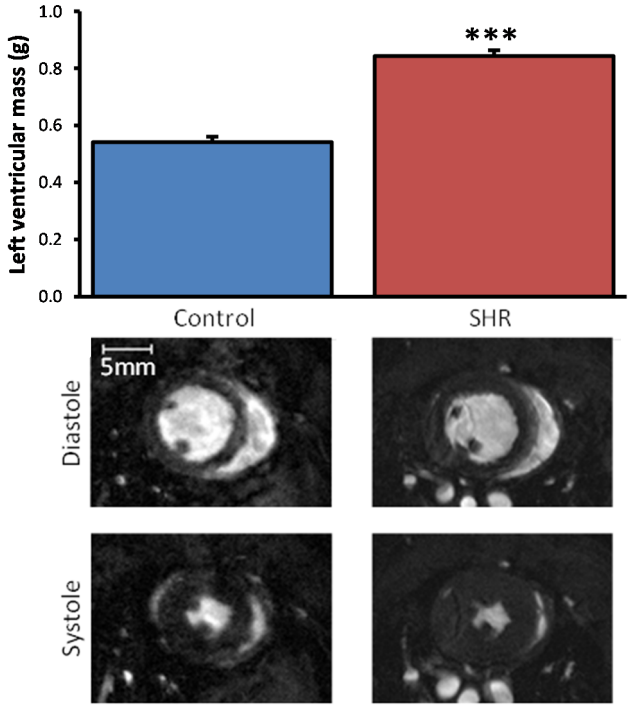

Figure 3.2 - Summary of cine-MRI data from control and SHR hearts. Calculated left ventricular mass (g) shows a significant increase in mass in the SHR heart. Representative images of diastole and systole in the control and SHR heart. (*** $p < 0.001$). Permission to reproduce this figure has been granted by Oxford University Press.

Table 3.2 – Function data from cine-MRI

	LVM (mg)	Body weight (g)	LVM/BW (mg.g^{-1})	Heart Rate (BPM)	Stroke Volume (µl)	End diastolic volume (µl)	Cardiac Output (ml.min^{-1})	Ejection fraction (%)
Control	540 ± 20	310 ± 10	1.77 ± 0.04	419 ± 7	260 ± 20	330 ± 20	105 ± 6	81 ± 1
SHR	**840 ± 20 *** **	312 ± 5	**2.71 ± 0.06 *** **	**343 ± 14 *** **	**310 ± 10 ***	**380 ± 20 ***	104 ± 5	81 ± 2

A significant decrease in heart rate was observed in the SHR, with an increase in stroke volume. Ejection fraction and cardiac output were unchanged between the SHR and control hearts. Values are mean data with S.E.M. Two-tailed Student t-test *: $p < 0.05$, ***: $p < 0.001$. Permission to reproduce this table has been granted by Oxford University Press.

A mid-papillary slice was selected to assess diastolic function using HTR-cine MRI. HTR-cine is able to assess filling of the LV following end systole [100]. In the 15 week old SHR heart, peak early filling rate was unaltered between groups (Figure 3.3 A), whilst peak late filling rate, which represents atrial filling of the LV, was significantly reduced by ~0.3 ml/s ($p < 0.05$, Figure 3.3 B).

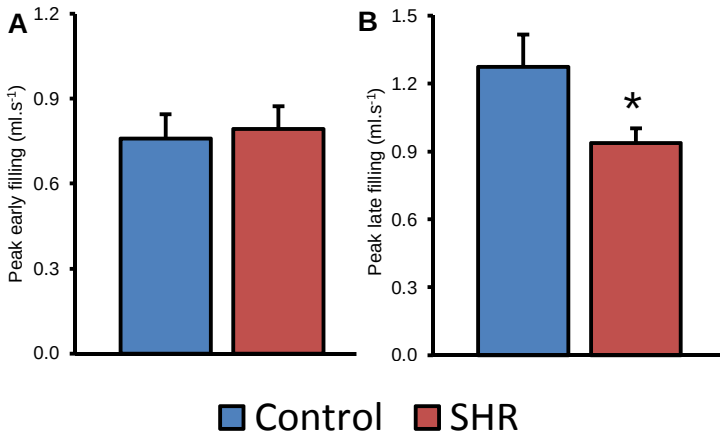

Figure 3.3 – High Temporal Resolution cine-MRI was used to assess diastolic function – A) No change was seen in the peak early filling rate. B) A significant decrease in peak late filling rate (panel B) was seen in SHRs. * : $p < 0.05$

3.4.2 In vivo PDH flux was altered in the SHR heart

^{13}C label incorporation into CO_2 and bicarbonate pools (PDH flux) was significantly increased by 85% in the SHR heart compared to control (Figure 3.4 A). ^{13}C label incorporation into alanine was also significantly increased by 28%, whilst lactate labelling was unchanged between groups.

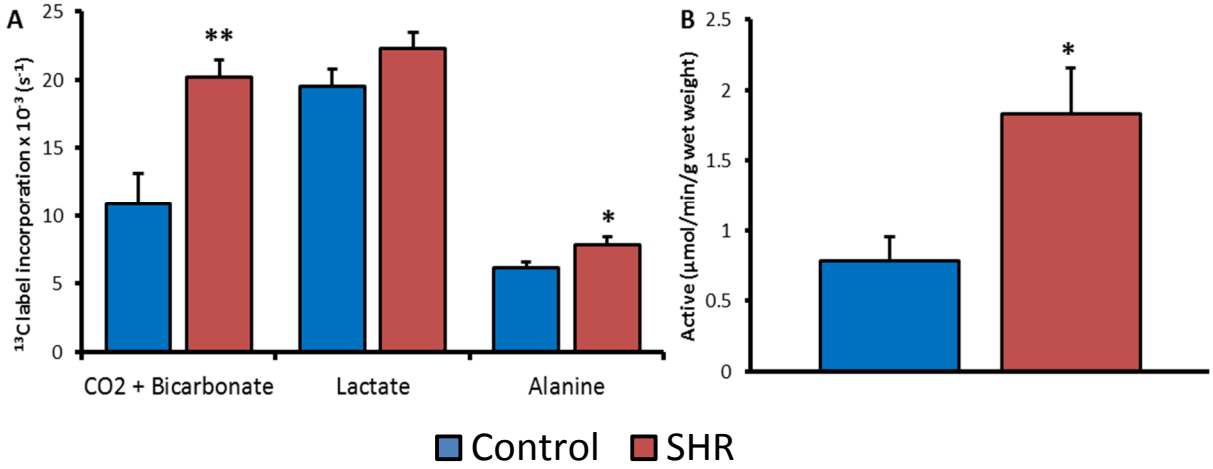

Figure 3.4 – Assessed flux using [1-^{13}C]pyruvate and PDH activity – A) Hypertensive rats show an increase in ^{13}C label incorporation through PDH (CO_2 + bicarbonate) and through AAT , whilst there is no change to LDH. PDH activity assay data normalized to citrate synthase. B) A significant increase was seen in the ratio between active and total PDH in the SHR heart. *: $p < 0.05$, **: $p < 0.01$

To confirm the increase in ^{13}C label incorporation into CO_2 and bicarbonate, an *in vitro* biochemical assay was performed to measure PDH activity. Activity of the active PDH fraction in the SHR heart was significantly elevated from 0.8 ± 0.2 to 1.8 ± 0.3 µmol.min^{-1}.g.w.w.$^{-1}$, an increase of 135% compared to controls (Figure 3.4 B). Total PDH activity was unchanged between groups (3.6 ± 0.8 and 5.5 ± 1.0 µmol.min^{-1}.g.w.w.$^{-1}$, for controls and SHR hearts, respectively). This indicates PDH flux was increased in the SHR heart *in vivo* and that changes to ^{13}C label incorporation into CO_2 and bicarbonate were due to increased enzyme activity rather than an increase in maximal PDH activity and content.

3.4.3 In vivo assessment of TCA cycle intermediates in the SHR heart

In the SHR heart, [2-^{13}C]pyruvate incorporation was significantly increased by 72% into citrate, 118% into acetylcarnitine and 81% into glutamate compared to control (Figure 3.5 A). As there was a significant increase in PDH flux, this increased ^{13}C label incorporation may be a result of more labelled acetyl-CoA being processed in to the TCA cycle. To correct for this increase in ^{13}C label flux, [2-^{13}C]pyruvate data was normalized to [1-^{13}C]pyruvate incorporation into bicarbonate + CO_2. Following normalization, no change to ^{13}C label incorporation was detected into either acetylcarnitine, glutamate or citrate pools (Figure 3.5

B). Therefore the observed increase in [2-^{13}C]pyruvate label incorporation was relative to increased PDH flux and not greater flux in the TCA cycle.

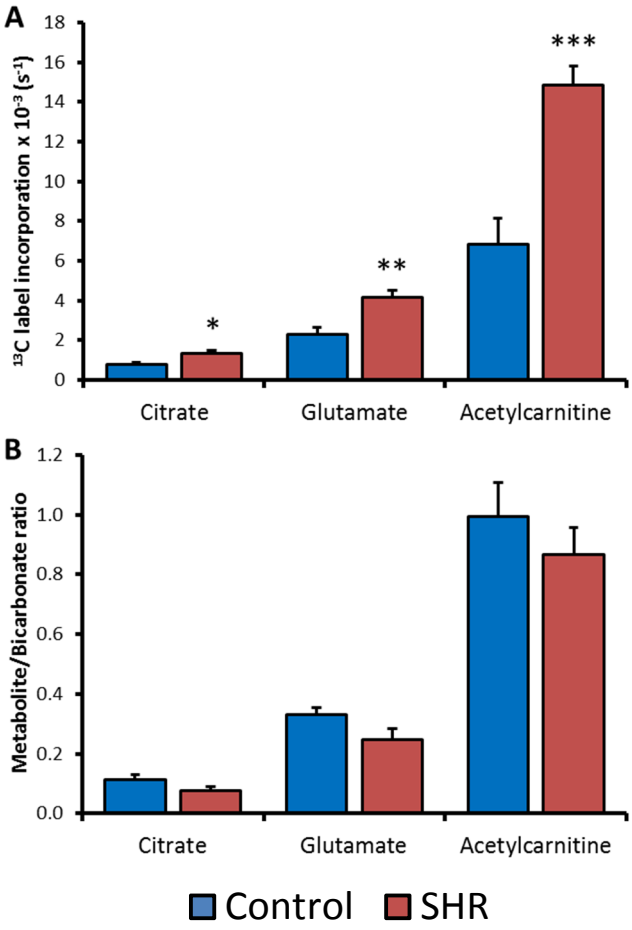

Figure 3.5 - Assessed flux using [2-^{13}C]pyruvate – A) Hypertensive rats show an increase in label incorporation into the citrate, glutamate and acetylcarnitine pools. *: $p < 0.05$, **: $p < 0.01$, ***: $p < 0.001$. B) [2-^{13}C]pyruvate data normalized to label flux through PDH.

3.4.4 Normal phosphorous energetics and pH_i in the in vitro SHR heart

To assess high energy phosphate energetics in the SHR heart, ^{31}P MRS was performed on Langendorff perfused control and SHR hearts. Figure 3.6 shows an example spectrum highlighting intracellular P_i, PCr, γ-ATP, α-ATP and β-ATP. [ATP], [PCr] and [P_i] were not significantly different between groups. This led to an average PCr/ATP ratio of 1.8 ± 0.1 and 1.6 ± 0.1, for control and SHR hearts respectively

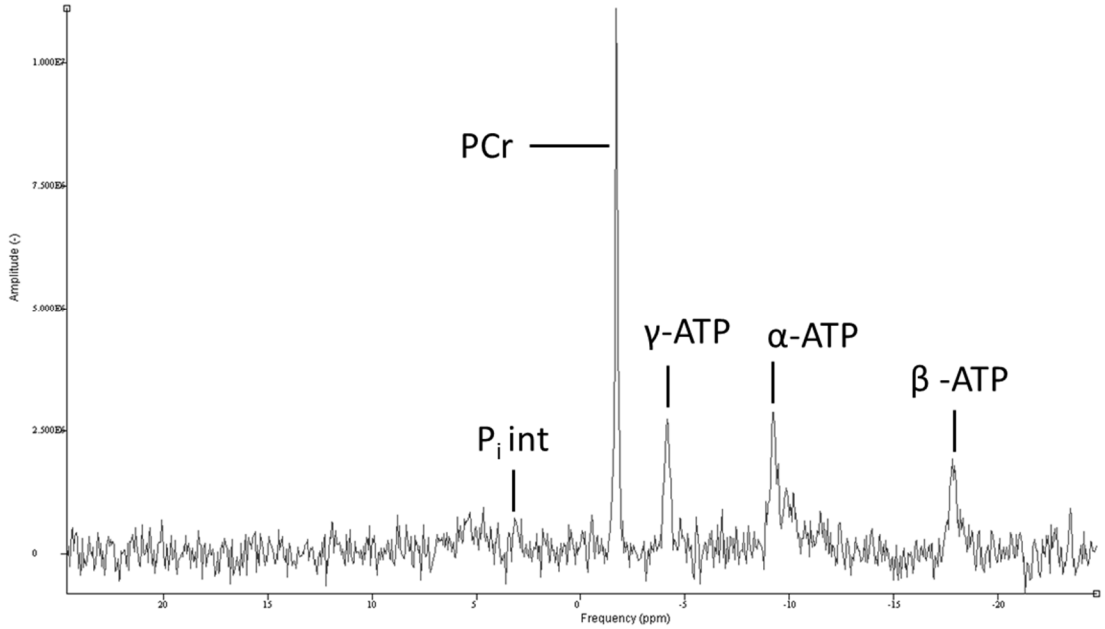

Figure 3.6 – **An example fully relaxed spectra from the perfused SHR heart –** TR = 15s; Gaussian RF excitation pulse = 90°; acquired points, 1024; frequency centred on the PCr resonance; averages = 40

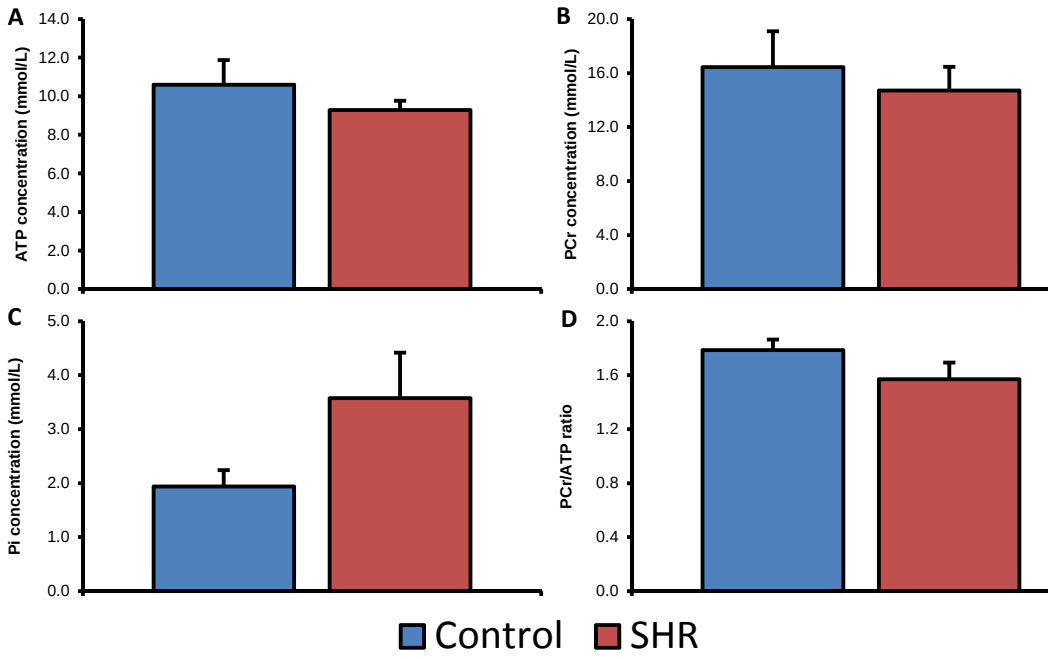

Figure 3.7 – ^{31}P magnetic resonance spectroscopy of the *in vitro* heart – High energy phosphate energetics in the SHR and control heart are unaltered as represented by a normal [ATP], [PCr], [P_i] and PCr/ATP ratio

The pH_i measured from ^{31}P MRS was 7.06 ± 0.01 and 7.06 ± 0.02 for control and SHR, respectively, these data showed that there was no significant difference in cardiac intracellular pH between groups. This was confirmed using the [1-^{13}C]pyruvate data, where it was estimated that the *in vivo* pH_i was 7.12 ± 0.02 and 7.14 ± 0.02 for control and SHR, respectively.

3.4.5 Increases in PDH flux were linked to changes in regulatory enzymes

To assess the regulatory state of PDH, western blots were performed on the key regulators of PDH in the heart: PDP (1 and 2) and PDK (1, 2 and 4). Assessment of PDK1 and 4 protein levels, showed that in the SHR heart there was a 26 and 25% reduction in expression, respectively, compared to control hearts (Figure 3.8). PDK2 was also reduced but not significantly ($p = 0.15$). PDP1 expression showed a non-significant decrease ($p = 0.07$), whilst PDP2 was significantly reduced by 29% between controls and SHR hearts (Figure 3.8).

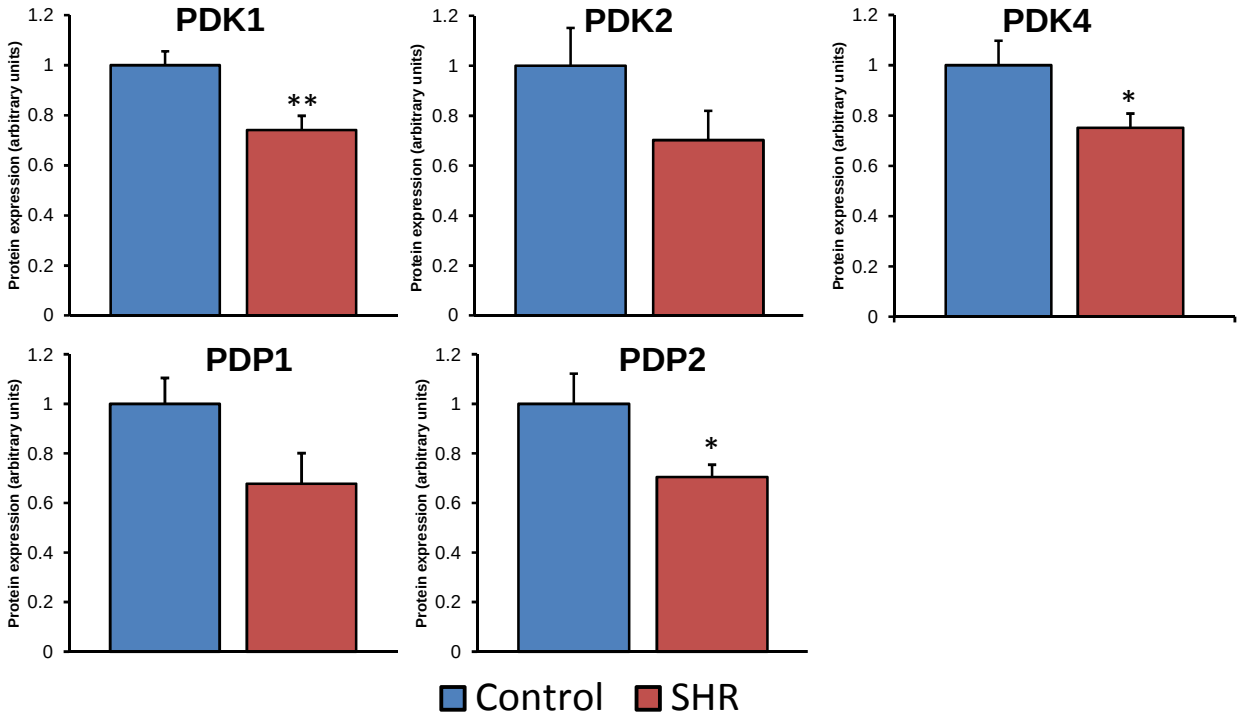

Figure 3.8 – To assess regulatory state of PDH, PDKs and PDPs protein expression was measured – PDK1 and PDK4 expression was significantly reduced in the SHR heart compared to control. No significant alteration in protein expression was observed in PDP1 ($p = 0.07$), however PDP2 was significantly decreased. *: $p < 0.05$ **: $p < 0.01$, data displayed as relative expression compared to control (arbitrary units).

3.4.6 Increased reliance on glucose oxidation was not driven by increased glycogenolysis

The glycogen content of the SHR and control hearts was assessed using an *in vitro* biochemical assay. Glycogen content was not significantly altered between SHR and control hearts, 17 ± 2 and 20 ± 3 μmol.g.w.w.$^{-1}$ respectively (Figure 3.9).

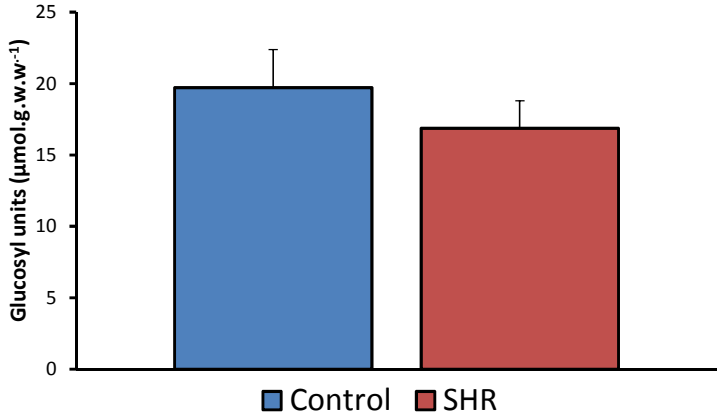

Figure 3.9 – Glycogen content was not altered in the SHR heart – Glycogen content was measured using a biochemical assay, which breaks glycogen down to glucose units, and the resulting glucose was analysed spectrophotometrically.

3.4.7 Glucose transporter protein expression was unaltered in the SHR

To investigate whether there were alterations in the uptake of glucose in the SHR heart, the protein expression of GLUT1 and GLUT4 were assessed. GLUT1 and GLUT4 protein expression levels were unaltered between groups as indicated by western blotting (Figure 3.10). This was a measure of total GLUT4 protein expression and does not discriminate between vesicle and cell surface GLUT4, which may be altered in the SHR heart.

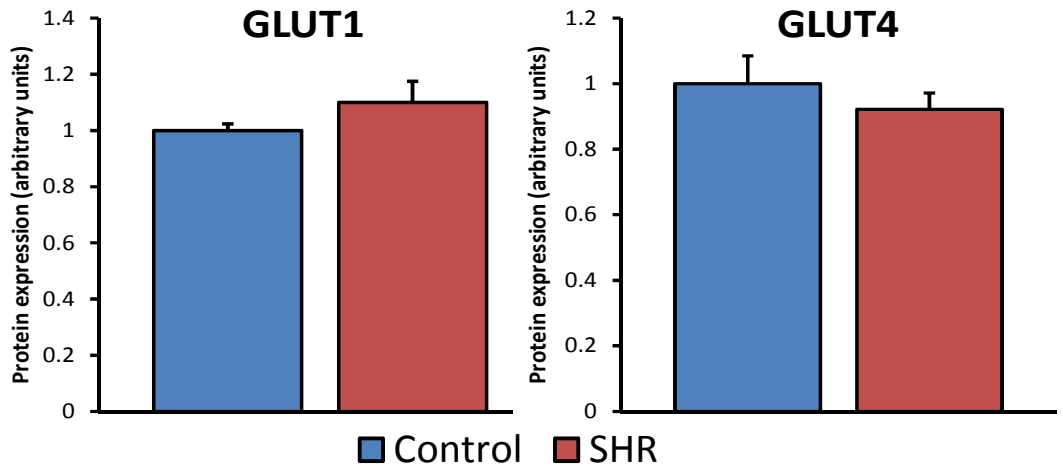

Figure 3.10 – To assess glucose transporter protein expression GLUT1 and GLUT4 were measured – Neither was altered in the SHR compared to control.

3.5 Discussion

Extensive studies of the SHR heart have shown that after 15 weeks of age, they develop concentric hypertrophy due to systemic pressure overload [122,124]. *In vivo* measurements in this study using cine-MRI, have confirmed a 56% increase in LVM and 53% increase in LVM to body weight ratio. Also *in vivo* cardiac functional data indicates that the 15 week SHR is an early disease model with hyperfunctional compensatory remodelling [125]. There were several key compensatory changes in function in the SHR heart compared with controls. Heart rate was significantly lower in the SHR, whilst stroke volume and end diastolic volume were significantly elevated. The result was that cardiac output and ejection fraction remained unchanged between groups, indicative of compensatory remodelling in response to the hypertension [125]. To accompany this, HTR cine-MRI showed that there was a significant reduction in peak late filling rate. This measure is hypothesised to be the rate of filling of the LV from the left atrium [100]. These data indicate a compensated hypertrophy disease stage in the 15 week SHR, with normalized cardiac function.

The degree of hypertrophy was greater than previously reported (53% versus 10%) but this may be due to differences in control strains [12,122]. The difference between this work and previous studies was the choice of control, as previous studies have been performed on Wistar Kyoto (WKY) rats. The WKY rat is derived from the same line as the SHR and shares several mutations in common [126,127]. However, these animals have previously been shown to display a degree of hypertrophy, whilst remaining normotensive [128]. This means that any comparison between heart/LV mass might be underestimated. Therefore to study the effects of hypertension and hypertrophy, the Wistar rat was chosen as a suitable control in this work.

Other models of pressure overload have noted high levels of hypertension induced hypertrophy, e.g. banding of the aorta lead to a significant 25% elevation in the heart to tibial

length [103]. As the body weight was unaltered in our study, it should be possible to relate these data to our study.

Further to compensated functional changes in the SHR, there were also several metabolic alterations which maintained normal energetics. *In vivo* assessment of SHR cardiac metabolism was performed using hyperpolarized ^{13}C MRS and highlighted several alterations. Firstly we have demonstrated that the SHR heart has a significant modulation of both *in vivo* PDH flux and AAT. This was detected as a significant increase in ^{13}C label incorporation between [1-^{13}C]pyruvate and [^{13}C]bicarbonate + $^{13}CO_2$ (PDH) and [1-^{13}C]alanine (AAT) in the *in vivo* hypertensive heart. An *in vitro* PDH activity assay was also employed to determine PDH activity, which was significantly elevated in the SHR heart, confirming our *in vivo* hyperpolarized PDH flux data.

The study of Seymour and Chatham also looked at the relationship between hypertrophy and PDH activity [103] and they found an opposite effect to that reported here. Whilst in the 15 week old SHR heart, we saw a significant elevation in PDH flux, they reported a decrease in PDH activity. It is possible that their model of hypertrophy was more developed in terms of disease progression as they discuss PDH activity potentially becoming a limiting factor leading to the progression of hypertrophy into decompensated heart failure [103]. This idea is further supported by data from the older SHR rat (25 weeks), which showed an increased ventricular lactate/pyruvate level compared to 15 weeks, possibly indicating a depression in PDH activity following disease progression [12].

^{13}C label incorporation was also significantly increased into alanine, via AAT. These data suggest that in the SHR heart there was either a larger pool of free alanine in the tissue or an increase in AAT activity. There are several possible explanations for this increased ^{13}C label incorporation into alanine, which include increased export of cardiac alanine to the liver for

the glucose-alanine cycle[129] or increased alanine production as would be required for the increase in protein synthesis characteristic of hypertrophy. Also, several papers have linked the presence of alanine in the blood/urine to increases in blood pressure, so the observed increase here could be a consequence of the underlying hypertension [130,131].

The observed increase in PDH flux was coupled with an increase in ^{13}C label incorporation into citrate, acetylcarnitine and glutamate pools. No change was observed in ^{13}C label incorporation into the TCA cycle when label flux was normalized to flux through PDH. This implies that the apparent increases in citrate, acetylcarnitine and glutamate are derived from increased production of [2-^{13}C]acetyl-CoA, consistent with an increase in glucose oxidation. Furthermore, it was expected that the label incorporation from [1-^{13}C]pyruvate to [1-^{13}C]lactate would increase in the SHR heart, which would have implied a shift to an anaerobic glycolytic phenotype, however this was not the case. Both these pieces of evidence highlight that the SHR has compensated cardiac metabolism, with a switch to greater glucose oxidation.

A defect in the LCFA transporter (FAT/CD36) has previously been identified in the SHR [119], which leads to a reduction in β-oxidation. Labarthe *et al.* (2005) have shown a significant reduction in ^{13}C label incorporation from [1-^{13}C]oleate, a LCFA, into the TCA cycle in the SHR heart [13]. They also stressed the importance of medium chain fatty acids (MCFA) in the SHR to compensate for the reduced contribution of LCFAs to β-oxidation [13,132]. The defect in FAT/CD36 does not however, lead to a change in energetics in the heart. ^{31}P MRS can be used to determine cardiac energetics where significant alterations in [ATP] or/and [PCr] can indicate a mismatch in energy production in the heart. As *in vivo* cardiac ^{31}P MRS is particularly difficult due to sensitivity issues and cross contamination from other organs, the perfused heart was used to assess high energy phosphate energetics. Within the SHR heart [ATP] and [PCr] were not significantly different from control hearts. This resulted in no

significant difference in the PCr/ATP ratio, a measure of cardiac energetics within the heart. ^{31}P and ^{13}C MRS were also used here to determine the intracellular pH in the *in vitro* and *in vivo* heart, respectively [91]. These results indicate that the intracellular pH was unaltered between the SHR and control heart and the pH_i measurements were consistent with previously published data from the control Wistar heart [91]. This would imply normal aerobic metabolism and fits with no significant alteration in the [1-^{13}C]lactate production.

To further understand the mechanism behind the increase in PDH activity several key regulatory proteins were probed. PDKs are one of the major regulatory factors of PDH activity in the heart [31,37]. The PDK isoforms are activated by several mechanisms including hypoxia, increases in the end-products acetyl-CoA and NADH, and increases in fatty acid oxidation [31,43,133]. PDKs can be activated short term by these factors or long term by transcriptional up regulation [37,133]. Here we observed a significant reduction in protein expression of PDK1 and PDK4 in the SHR heart compared to controls. Bowker-Kinley and colleagues (1998) have previously shown that PDK1 displays the highest specific activity and is highly sensitive to changes in the NAD^+:NADH ratio, which will be disturbed in the SHR heart, due to the reduction in LCFA oxidation [119]. Our data would suggest that the reduction in PDK1 and 4 protein expression may be sufficient to elicit the large increase in PDH flux and activity demonstrated by our *in vivo* hyperpolarized MRS data.

Other mechanisms for PDH modulation also exist including increased PDP activity and end product inhibition. Interestingly, protein expression data here show that PDP1 content did not increase but rather there was potentially a reduction, although not significant ($p = 0.07$). This was accompanied by a significant decrease in the calcium insensitive PDP2 isoform in the SHR heart. Whilst it seems counter intuitive that PDP1 and PDP2 protein expression would be decreased in the SHR heart, there may be compensatory alterations in activity. Elevated intracellular calcium ($[Ca^{2+}]_i$) and other cofactors (i.e. magnesium) have

been shown to activate PDP, concurrently increasing PDH flux and the proportion of PDH in the active fraction [30]. Previous data from the left ventricle of SHRs, have shown a significantly elevated concentration of $[Ca^{2+}]_i$ compared to Wistar rats [124].

The final mechanism to consider is that the PDH increase is mediated by a reduction in end product inhibition. In the SHR heart there would be a reduction in acetyl-CoA and NADH derived from LCFAs [13], which would reduce end product inhibition on PDH, resulting in an increase in PDH flux. The current evidence suggests that increased PDH activity in the SHR heart is modulated by changes to PDK1 and 4 expression as well as a reduction in acetyl-CoA end product inhibition due to the reduced oxidation of LCFAs.

Interestingly, although glycolysis was not measured in this study, we attempted to understand whether the increase in glucose oxidation was coupled to either depletion in intracellular glycogen levels or increased glucose transport. To assess this, the glycogen content was measured using a biochemical assay and highlighted that there was no difference between the SHR and control heart. Furthermore, protein expression of the glucose transporters GLUT1 and GLUT4 were measured. Protein expression was unaltered, but in this case we were measuring the total expression of glucose transporters and not cell surface expression. As mentioned previously, GLUT1 and GLUT4 can be found at the cell surface and in vesicles within the cytoplasm [24,134]. Upon recruitment by insulin, and under stress conditions, these vesicles combine with the plasma membrane and increase cell surface presentation and therefore overall activity of GLUT1 and 4 [24,134]. The western blot technique performed here would be unable to distinguish a situation where there was an increase in cell surface expression.

3.6 Conclusion

This study showed that *in vivo,* there was a significant increase in ^{13}C label incorporation through PDH into [^{13}C]bicarbonate + $^{13}CO_2$ and into the TCA cycle. As expected, 15 week old SHRs had significant hypertrophy, which was accompanied by compensatory remodelling. Functional alterations in stroke volume, heart rate and the late filling rate were consistent with compensated hypertrophy. [1-^{13}C]lactate data provides no evidence of an increase in anaerobic glycolysis, therefore our *in vivo* work indicates a switch towards glucose oxidation, through PDH in the SHR heart. This supports a move away from the classical, predominantly fatty acid oxidation driven cardiac metabolism, matching evidence from previous *in vitro* data [13].

Chapter 4

Assessing Metabolic Changes Associated with Heart Failure Progression using Hyperpolarized Magnetic Resonance Spectroscopy

4.1 Overview

Alterations in the profile of metabolic substrate selection following myocardial infarction (MI) and during the progression into heart failure have previously been reported, but the exact nature of these changes is poorly defined. In this work, using a surgically induced rat model of MI, hyperpolarized DNP was used to follow the *in vivo* metabolic alterations associated with the development of heart failure.

MI surgery induced a heterogeneous degree of contractile dysfunction and one week following MI, no significant differences were seen in *in vivo* cardiac metabolism. By six weeks post-MI, there were significant alterations in TCA cycle flux. There was a positive correlation between ^{13}C label flux into citrate, glutamate and acetylcarnitine and ejection fraction, indicative of impaired TCA cycle flux in the infarcted heart. However, this was not accompanied by changes in PDH flux.

At twenty two weeks post-MI, there were significant correlations between PDH flux and ejection fraction, in addition to the previously observed changes in label incorporation into the TCA cycle. Combined with these *in vivo* changes, *in vitro* biochemical analysis showed that significant (positive) correlations between PDH, citrate synthase (CS), CAT and isocitrate dehydrogenase (ICDH) activities and ejection fraction. A significant negative correlation was established between the content of acylcarnitine: free carnitine and ejection fraction,

whereas a positive correlation between free carnitine: total carnitine and ejection fraction was observed. The reduction in free carnitine in the infarcted heart might reflect a “trapping” of carnitine in acyl derivatives, which has been observed previously in heart failure. The earlier six week changes in flux into acetylcarnitine likely suggest a reduction in carnitine consistent with onset of metabolic alterations. The combination of changes in flux into citrate and acetylcarnitine could be used as *in vivo* marker of cardiac metabolism during the progression of heart failure.

In conclusion, there appears to be decreased glucose oxidation and a reduction in TCA cycle efficiency during progression into heart failure, proportional to the degree of contractile impairment.

4.2 Background

Myocardial infarction is the leading cause of heart disease in the developed world and results in high levels of mortality and morbidity in patients [106]. MI is caused by a blockage or partial obstruction of a coronary artery, leading to a significant reduction in coronary blood flow. This, in turn leads to impaired myocardial oxygen delivery and consequently myocardial ischemia. During this ischemic event, myocardial tissue is starved of nutrients and partially relies on intracellular energy stores to enable the survival of cells [2,135].

If the obstruction is removed, either by passive breakdown or via active thrombolysis in the clinic, the tissue can be still further damaged by reperfusion of the myocardium [2,135]. This effect, known as reperfusion injury, is caused by the return of blood, which leads to oxidative damage through the development of reactive oxygen species (ROS) [136,137]. In the infarcted region there is rapid cardiomyocyte death, through both apoptotic and necrotic pathways [138]. This forms the central oxygen paradox of ischemia-reperfusion injury [139], where reoxygenation of the ischemic myocardium generates injury greater than ischemia alone [140]. This damage will occur within the first 24 hours but cellular death can continue for longer [2,135].

As a consequence, the infarcted region eventually forms a tough, dead, collagen rich scar [135]. Due to the rigid nature of collagen, this scar is relatively inflexible and impedes normal cardiac contraction. To maintain normal cardiac function, due to the law of LaPlace (See Chapter 3: Equation 3.1) [2], the heart increases the wall thickness of the remaining "healthy" myocardium (hypertrophy). This remodelled state is however, unsustainable, and the heart eventually fails. At this point, the myocardial wall thins, the LV cavity dilates and cardiac output decreases [2].

The progression into heart failure can be characterised by profound changes in myocardial energy metabolism [3]. The tightly regulated reciprocal relationship between glucose oxidation and fatty acid β-oxidation breaks down, leading to perturbations in the profile of cardiac substrate selection and energy metabolism [2,3,27,48,141,142]. These can further impair myocardial function, either accelerating progression to heart failure or worsening the prognosis [3,143]. Powerful non-invasive analytical tools including MRI and PET, used in conjunction with animal models of heart failure, have enabled better characterisation of the metabolic derangements associated with heart failure [144–147]. However, experiments conducted to date have yielded conflicting results. For example, studies of substrate utilisation in the failing heart have observed both increased and decreased glucose utilisation as a consequence of severe/end-stage heart failure [148,149]. Descriptions of the metabolic effects of early-stage heart failure reveal further contradictions with evidence of both elevated and unchanged fatty acid utilisation [27,150–152]. Some of the inconsistencies described here may be due to differences in time points investigated post myocardial infarction. Also these experiments were performed in *ex vivo* perfused heart models, at selected time points, resulting in studies of varying heart failure severity [48,151,153]. A major tool that has allowed a greater understanding of the metabolic alterations underlying myocardial infarction and the progression to heart failure is ^{31}P MRS. Its application has been demonstrated both clinically and experimentally in patients and animal models of heart failure, there are decreases in high energy phosphorus energetics in the failing heart. The failing heart is effectively starved of energy, which severely affects cardiac function [3].

Whilst ^{31}P MRS provides an important insight into the energetics of the failing heart, the use of hyperpolarized ^{13}C MRS could provide information on the *in vivo* mechanisms underlying the changes in substrate utilization [9,66,153]. Due to the non-invasive nature of ^{13}C MRS, animals can be scanned serially, thereby tracking the temporal metabolic effects associated with ischemia-reperfusion injury and heart failure progression, *in vivo*.

4.2.1 Aims

The aim of this study was to assess alterations in the profile of cardiac substrate selection *in vivo* following a myocardial infarction. Rats were scanned using hyperpolarized [1-^{13}C] and [2-^{13}C]pyruvate at one, six and twenty two weeks post induction of myocardial infarction during the progression to heart failure. To monitor cardiac function, animals were scanned at each time point using echocardiography. The ejection fraction measured was used to correlate *in vivo* metabolic data with the severity of cardiac functional impairment. *In vivo* data were supported at the 22 week timepoint, using *ex vivo* metabolomics and biochemical analysis of enzyme activities.

4.3 Methods

The [1-^{13}C]pyruvic acid, [2-^{13}C]pyruvic acid and OX063 trityl radical used were obtained from GE Healthcare (Amersham, UK). Fifteen female Wistar rats (200-250g) (Harlan, UK) were housed on a 12:12-h light/dark cycle in animal facilities at the University of Oxford. All animal studies were performed between 7AM and 1PM with the animals in the fed state. All investigations conformed to Home Office Guidance on the Operations of the Animals (Scientific Procedures) Act 1986 and to institutional guidelines.

4.3.1 Myocardial infarction surgery

Surgical procedures were carried out by Dr Carolyn Carr, University of Oxford [154,155]. The left anterior descending (LAD) coronary artery was occluded approximately 2 mm from its origin. Following isoflurane anaesthesia induction (2% in O_2) and intubation, a thoracotomy was performed in the 4th intercostal space to access the heart. The pericardium was removed and a 5-0 prolene suture placed under the LAD. The suture was tied around a small piece of polyethylene tubing, occluding the LAD and the chest closed. After 50 minutes, the chest was re-opened and the tubing removed to allow reperfusion. Eleven female Wistar rats underwent MI surgery. Four sham animals operated were included in the study in an attempt to ensure a range of ejection fractions post MI. These underwent the same procedure but without ligation of the LAD.

4.3.2 Echocardiography

Animals were lightly anaesthetized with isoflurane and 2D-echocardiography was performed as described in [154]. Images were acquired from a short axis mid-papillary slice using a Philips SONOS 5500 system (Philips Healthcare UK Ltd, Guildford, UK) with a 12 MHz transducer giving one image every 8.3 ms (18 images per cardiac cycle at a heart rate of 400

beats/min). The end-diastolic and end-systolic frames from three consecutive heart cycles were analysed. Measurements of end-diastolic and end-systolic areas and diameter were used to determine ejection fractions (end-diastolic area – end-systolic area/end-diastolic area) at 1, 6 and 22 weeks post MI [154].

4.3.3 MRI measurements of cardiac function

At week 22, post hyperpolarized MRS analysis, cardiac structure and function were assessed using cine MRI. Cine MRI was performed as set out in section 2.3.3.

4.3.4 Hyperpolarized ^{13}C-magnetic resonance spectroscopy protocol

At 1, 6, and 22 weeks post MI, animals were scanned with both [1-^{13}C]pyruvate and [2-^{13}C]pyruvate, as described in sections 2.2.1 and 2.2.2. The [1-^{13}C]pyruvate and [2-^{13}C]pyruvate infusions were conducted ~1 hour apart in all animals at each time point. The sequence of [1-^{13}C]pyruvate and [2-^{13}C]pyruvate infusions into each animal was randomised.

4.3.5 MRS data analysis

Cardiac ^{13}C MR spectra were analysed using the methods set out in section 2.2.4. The acquired [2-^{13}C]pyruvate spectra were summed for the first 30 seconds following appearance of [2-^{13}C]pyruvate, to increase the reproducibility of measurements because of low SNR during collection of data.

4.3.6 Tissue collection

One-day after the 22 week hyperpolarized scan, tissue was harvested as described in section 2.2.11.

4.3.7 Metabolomic Analysis of Cardiac Tissue

Metabolomic analysis was performed in collaboration with Dr Helen Atherton at the University of Cambridge [156].

4.3.7.1 NMR metabolomic analysis

Metabolites were extracted from heart tissue using methanol/chloroform/water [156]. Frozen tissue (~100 mg) was placed in methanol-chloroform (2:1, 600 µl) and homogenised. Samples were then sonicated for 5 min before 400 µl chloroform-water (1:1) was added. Samples were centrifuged (16,000 x g, 20 min), and the aqueous layer was removed and the resultant dried overnight in an evacuated centrifuge (Eppendorf, Hamburg, Germany).

Extracts were then rehydrated in 600 µl of D_2O and buffered in 0.24 M sodium phosphate (pH 7.0) containing 1 mM sodium-3-(tri-methylsilyl)-2,2,3,3-tetradeuteriopropionate (TSP; Cambridge Isotope Laboratories, Andover, MA) as an internal standard. The samples were analysed using an Avance II+ spectrometer operating at 500 MHz for the ^1H frequency (Bruker) equipped with a 5 mm Broadband TXI Automatic Tuning and Matching (ATMA) probe. Spectra were collected using a solvent suppression pulse sequence based on a 1D-nuclear Overhauser effect spectroscopy pulse sequence to saturate the residual [^1H] water proton signal (relaxation delay = 2 s, t_1 = 3 µs, mixing time = 150 ms, solvent pre-saturation applied during the relaxation time and the mixing time). One hundred and twenty-eight transients were collected into 16 K data points over a spectral width of 12 ppm at 37 °C.

NMR spectra were processed using the ACD SpecManager 1D NMR processor (version 8; ACD, Toronto, Canada). Spectra were Fourier transformed after multiplication by a line broadening of 1 Hz and referenced to TSP at 0.0 ppm. Spectra were phased and baseline corrected manually. Each spectrum was integrated using 0.04 ppm integral regions between

0.5–4.5 and 4.7–9.5 ppm. Each 0.04 ppm region was treated as an independent variable during analysis. To account for differences in concentration between samples, each spectral region was normalised to total integral area. Resonances in the NMR spectra were assigned with reference to the literature or through the analysis of standard compounds [156].

4.3.7.2 Acylcarnitine : free carnitine assay

Cardiac tissue (50 mg) was pulverised and extracted using methanol/chloroform/water as described above. The dried organic and aqueous fractions were butylated with hydrogen chloride-1-butanol (50 µl, 3 M) at 60 °C for 15 min, dried under nitrogen and reconstituted in 200 µl acetonitrile containing 8 isotopically-labelled carnitine derivatives of known concentration as an internal standard (Cambridge Isotope Laboratories Ltd., USA). Samples were injected (10 µl) into a Quattro Premiere XE Triple Quadrupolar Mass Spectrometer (Waters Ltd, UK) coupled with an ESI source in positive ion mode. The source temperature was 110 °C and the capillary voltage used was 3.5 kV. The acylcarnitines were analysed by multiple reaction monitoring (MRM) in positive ion mode. The cone voltage was 35 V, collision energy was 15 eV and the MRM transitions used incorporated a common loss of *m/z* = +85 corresponding to loss of the carnitine head group. Samples were introduced by direct infusion (analysis time = 2 min, flow rate = 10 µl/min, increased linearly by 100 µl/min during the final min, mobile phase = 1:1 acetonitrile: isopropanol + 0.2% formic acid). Data were processed using the Neolynx software package (Waters Ltd, UK).

4.3.8 Tissue homogenisation

Tissue was homogenised using the following method for all assays unless stated otherwise. Frozen powered cardiac tissue (15 mg) was homogenized in 1 ml of ice-cold homogenisation buffer using a polytron homogeniser (Kinematic, Switzerland) for 30 seconds (100 mM imidazole, 1 mM EGTA, 5 mM $MgCl_2$ pH 7.0). To each sample 10 µl of triton

X-100 was added before being briefly vortexed and incubated on ice for 10 minutes. Samples were then centrifuged (375 x g for 10 min at 4 °C), and used for assays as described below.

4.3.9 Citrate synthase activity assay

The activity of citrate synthase was determined spectrophotometrically in a reaction that monitored the increase in absorbance at 412 nm due to the conversion of 5,5'-Dithiobis(2-nitrobenzoic acid) (DTNB) to 2-nitro-5-thiobenzoate (TNB) [157].

Buffers were prepared as follows: **Assay buffer**: 1 M tris HCl and 1 mM DTNB, were neutralized to pH 8.1 with sodium hydroxide and made up to 100 ml in double distilled water. **Acetyl-CoA**: 1 ml of ice cold dd H_2O was added to 10 mg Coenzyme A hydrate, and then added to 100 µl 1 M potassium bicarbonate and 2 µl acetic anhydride, before being mixed and incubated on ice for 10 min. A further 2 µl acetic anhydride was added, mixed and incubated for another 10 min and then diluted with 4.416 ml of dd H_2O.

To assess citrate synthase activity, 100 µl assay buffer, 50 µl acetyl-CoA, 750 µl dd H_2O and 50 µl of homogenised sample were mixed in a micro-cuvette, incubated at 30 °C for 5 minutes and used to zero the UV spectrophotometer at 412 nm. The reaction was initiated by the addition of 50 µl of 10 mM oxaloacetate and the increase in absorbance recorded at 412 mm and 30 °C for 240 seconds, using a Shimadzu UV-1700 spectrophotometer (Shimadzu, Milton Keynes, UK) and the UV probe chart reader software (using an extinction coefficient for TNB of 13,600 $M.cm^{-1}$). Each sample was analysed in duplicate and the average change in absorbance was used to calculate the activity in (µmol. $min.^{-1}$ g wet $weight^{-1}$).

4.3.10 Pyruvate dehydrogenase activity assay

To assess *in vitro* PDH activity the method set out in section 2.3.1 was used.

4.3.11 Carnitine acetyl-transferase activity assay

The activity of carnitine acetyl-transferase was determined spectrophotometrically in a coupled reaction monitoring the production of NADH using previously developed methods [158–160].

Assay Buffer: 100 mM tris base, 10 mM L-malic acid sodium salt, 1.25 mM EDTA, (pH 7.4) 0.5 mM β-NAD and 0.125 mM Coenzyme A hydrate, 4 µM rotenone, 35 U citrate synthase (porcine heart) and 275 U malate dehydrogenase (pigeon heart), made up to 50 ml in double distilled water

Ten µl of O-acetyl-L-carnitine hydrochloride (30 µM) was added to 840 µl assay buffer and incubated for 10 minutes at 37 °C. Homogenized tissue (150 µl) was added to the assay buffer/acetylcarnitine and incubated for a further 30 seconds at 37 °C. The subsequent increase in absorbance was recorded for 100 seconds using a Shimadzu UV-1700 spectrophotometer (Shimadzu, Milton Keynes, UK) (extinction coefficient for NADH = 6270 $M.cm^{-1}$). Each sample was analysed in duplicate and the average change in absorbance was used to calculate the activity (µmol. min^{-1}. g wet $weight^{-1}$).

4.3.12 Isocitrate dehydrogenase activity assay

The activity of isocitrate dehydrogenase was determined spectrophotometrically in a reaction monitoring the increase in absorbance at 340 nm due to the conversion of NAD to NADH. Tissue was homogenized in a different buffer than the other assays, but still followed the same protocol for extraction. **Homogenization buffer:** 100 mM Imidazole, 1 mM EGTA and made up to 100 ml with double distilled water

Assay Buffer: 30 ml phosphate buffer (33.3 mM dipotassium phosphate, 22.2 mM potassium phosphate; pH 7.0), 2.8 mM isocitrate, 20 mM citrate, 19.7 mM magnesium

chloride, 5 mM adenosine diphosphate, 2.2 mM NADH, 0.05 % bovine serum albumin and 0.18 % triton X-100 in ddH_2O

The UV spectrophotometer was set to zero at 340 nm with 900 µl of assay buffer. The assay buffer was then incubated in a heat block at 30 °C for 2 minutes before 100 µl of sample was added, mixed and the increase in absorbance recorded using a Shimadzu UV-1700 spectrophotometer (Shimadzu, Milton Keynes, UK) for 60 seconds (37 °C; NADH extinction coefficient = 6270 $M.cm^{-1}$). Each experiment was run in duplicate and the average change in absorbance was used to calculate the activity (µmol. min^{-1}. g wet $weight^{-1}$)..

4.3.13 Western blotting

Protein expression levels of key metabolic pathways were assessed in total heart homogenates using SDS-PAGE western blotting (section 2.4). Proteins, primary and secondary antibodies are set out in Table 4.1. All samples were run in duplicate on separate gels to confirm results.

Table 4.1 – Antibodies used to probe key metabolic pathways in the infarcted heart.

Protein	***Antibody***	***Dilution***	***Company***	***Secondary***	***Dilution***
PDK 4	Rabbit anti-PDK4	1:500	Abgent	Goat anti-rabbit	1:2000

4.3.14 Statistics

All results were expressed as correlations against the assessed ejection fraction. Significant correlations were determined by the Pearson correlation coefficient, where significance was considered if $p \leq 0.05$.

4.4 Results

4.4.1 *Alterations in cardiac structure and function following myocardial function*

One week following surgery, animals displayed a range of ejection fractions (from 28-81%) compared to sham animals (72-84%). Ejection fraction remained relatively constant over the 22 weeks following MI (Figure 4.1 A). To complement the echocardiography results, cardiac function was also assessed by cine MRI at 22 weeks post-surgery. Data from both modalities correlated tightly, however cine MRI gave consistently higher values, as has been previously observed [154] (Figure 4.1 B). The advantage of performing cine MRI at the 22 week timepoint, was that it allowed a more in-depth analysis of the structural and functional remodelling in these animals (Figure 4.2). Cine-MRI confirmed that animals analysed post MI exhibited ejection fractions ranging from 34–90%, the difference being attributed to the increased accuracy in measurement of cardiac function with cine-MRI [154]. Scar size significantly increased in the failing heart, ranging from 4-37% of the left ventricle. While end diastolic volume negatively correlated with ejection fraction, cardiac output correlated positively with ejection fraction. The dilation of the LV and decrease in cardiac output are consistent with functional abnormalities associated with the progression into heart failure.

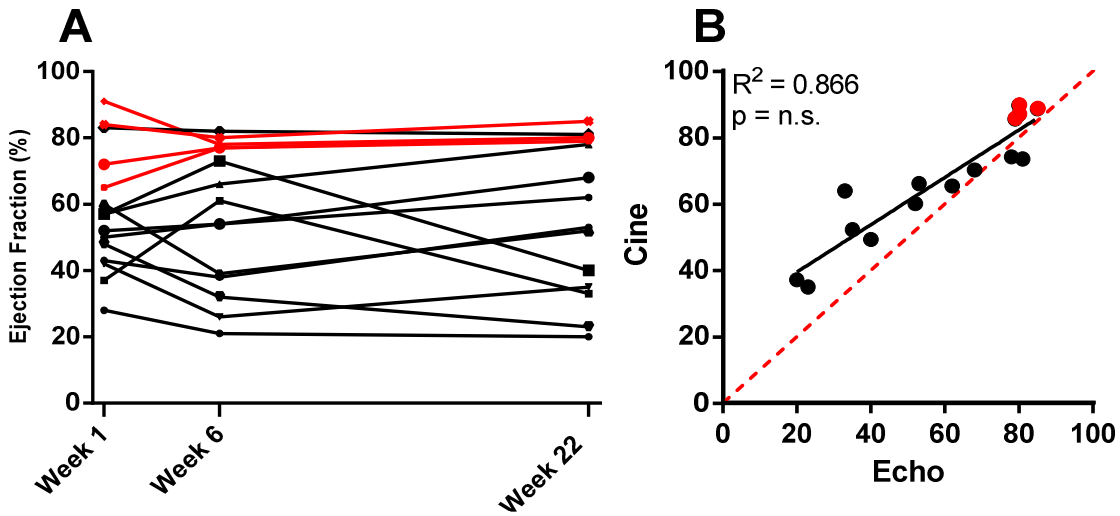

Figure 4.1 – Ejection fraction– A) Ejection fraction as a function of time over the experiment. Red lines show sham animals. B) The difference in measurements made by cine-MRI and echo at week 22 are shown here. The red dotted line shows the idealised line of regression, compared to the black line. Shams are highlighted in red.

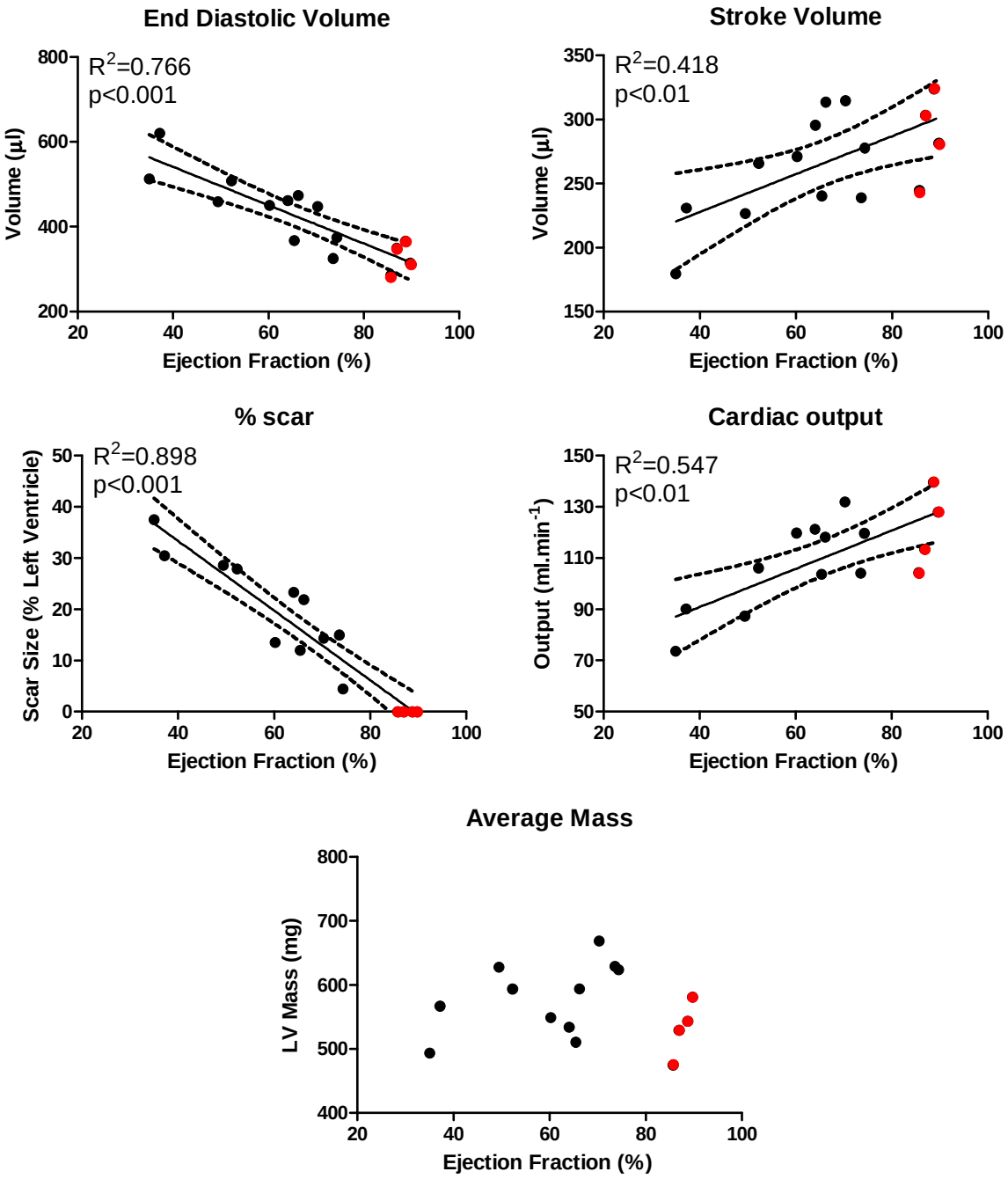

Figure 4.2 – Cine-MR images at the 22 week timepoint – As ejection fraction decreases, cardiac output and stroke volume also decrease, whilst end diastolic volume increases. No change in average mass is seen over ejection fractions. Red dots highlight sham operated animals.

4.4.2 Assessing metabolism in the infarcted heart

Hyperpolarized ^{13}C MRS was used to measure the real time conversion of [1-^{13}C]pyruvate into both [^{13}C]bicarbonate and $^{13}CO_2$, which was able to directly assess flux through PDH. At 1 and 6 weeks post induction of MI, there was no correlation between ejection fraction and

PDH flux (Figure 4.3, left column), despite several animals demonstrating severely reduced ejection fractions (Figure 4.1, left column). This would imply that energy generation from glucose was unaltered in infarcted hearts despite observed functional deficits early after MI. However, by 22 weeks post-surgery a significant positive correlation between ejection fraction and PDH flux was observed (Figure 4.3). This therefore indicated that by 22 weeks, the utilisation of glycolytically derived pyruvate for acetyl-CoA generation, and subsequent acetyl-CoA processing via the TCA cycle, was reduced in infarcted hearts.

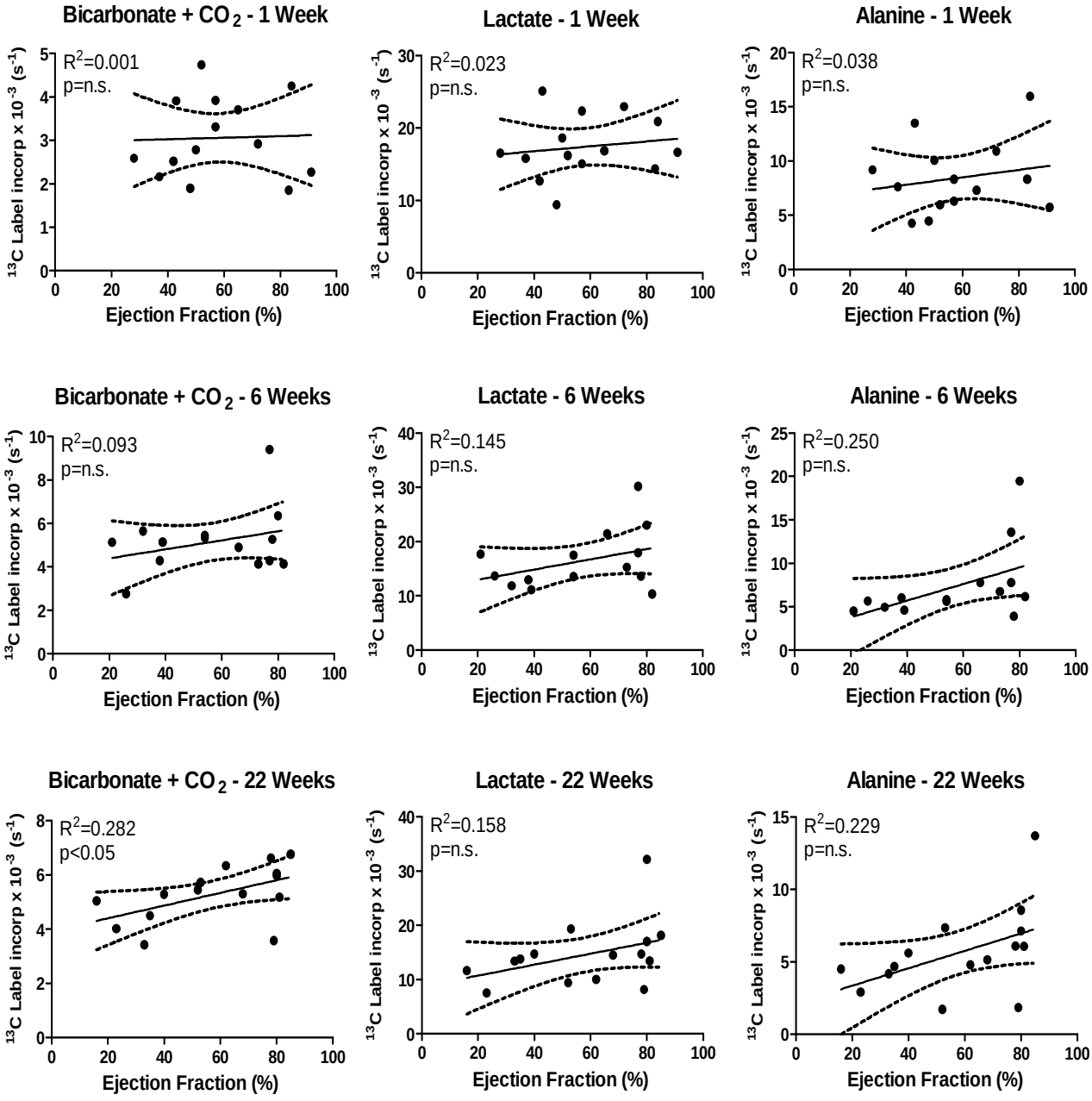

Figure 4.3 – *In vivo* flux through PDH was measured, along with ^{13}C label incorporation into lactate and alanine at each time point – PDH flux significantly correlated with ejection fraction at the 22 week time point. Flux into lactate and alanine was unaffected by reductions in ejection fraction.

Hyperpolarised ^{13}C label incorporation into [1-^{13}C]lactate and [1-^{13}C]alanine was also evaluated in these experiments. No correlation between ejection fraction and ^{13}C-label incorporation from pyruvate into [1-^{13}C]lactate or [1-^{13}C]alanine was observed at any time point, indicating no alteration in the non-oxidative fates of glycolytically derived pyruvate following myocardial infarction surgery (Figure 4.3, centre and right columns).

To further evaluate the effects of MI on TCA cycle metabolism, the conversion of [2-^{13}C]pyruvate into a number of downstream products, namely [5-^{13}C]glutamate, [1-^{13}C]citrate and [1-^{13}C]acetylcarnitine, was also evaluated. ^{13}C-label incorporation into these three metabolites showed no correlation with ejection fraction at 1 week post-surgery, but demonstrated significant reductions with ejection fraction at 6 and 22 weeks (Figure 4.4). Such results may reflect a number of different perturbations in these hearts, namely reductions in the pool sizes of these metabolites and/or a reduction in the activity of the enzymes required to synthesise these products. In addition, at 22 weeks, the observed differences may be partially due to decreases in the amount of ^{13}C-label reaching the TCA cycle due to reduced PDH flux.

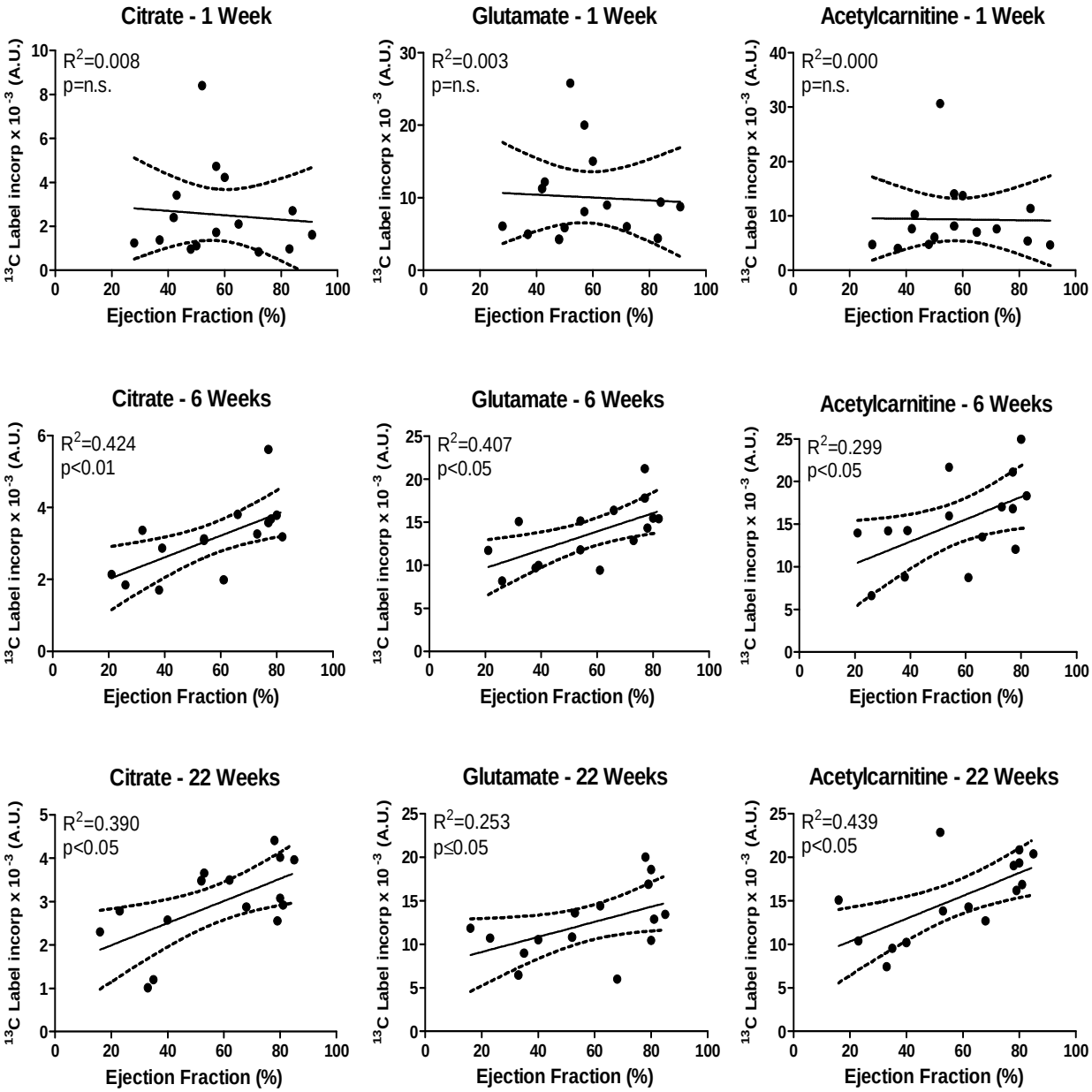

Figure 4.4 – *In vivo* ^{13}C label incorporation into citrate, glutamate and acetylcarnitine 1, 6 and 22 weeks post-MI – At 6 and 22 weeks ^{13}C label incorporation into the TCA cycle and acetylcarnitine correlated with ejection fraction.

4.4.3 Metabolomic analysis of the infarcted heart

To better characterise the metabolic abnormalities observed at 22 weeks, metabolomic analysis using ^{1}H-NMR spectroscopy was used to assess the concentrations of several relevant metabolites. Consistent with the *in vivo* data, no alterations in the concentration of alanine and lactate were detected in the infarcted hearts. Also, the concentration of citrate did not correlate with ejection fraction thereby demonstrating that the reduced ^{13}C-label incorporation into [1-^{13}C]citrate was not caused by a reduction in the intracellular concentration of this metabolite in infarcted hearts. In contrast to this, a positive correlation was observed between ejection fraction and the content of glutamate ($P < 0.01$) and malate ($P < 0.001$) but not succinate (Figure 4.5). This possibly indicates that there is altered content of metabolites downstream of citrate post MI injury. A positive correlation was also seen between creatine and ejection fraction, potentially highlighting an alteration in energy handling ($p<0.001$).

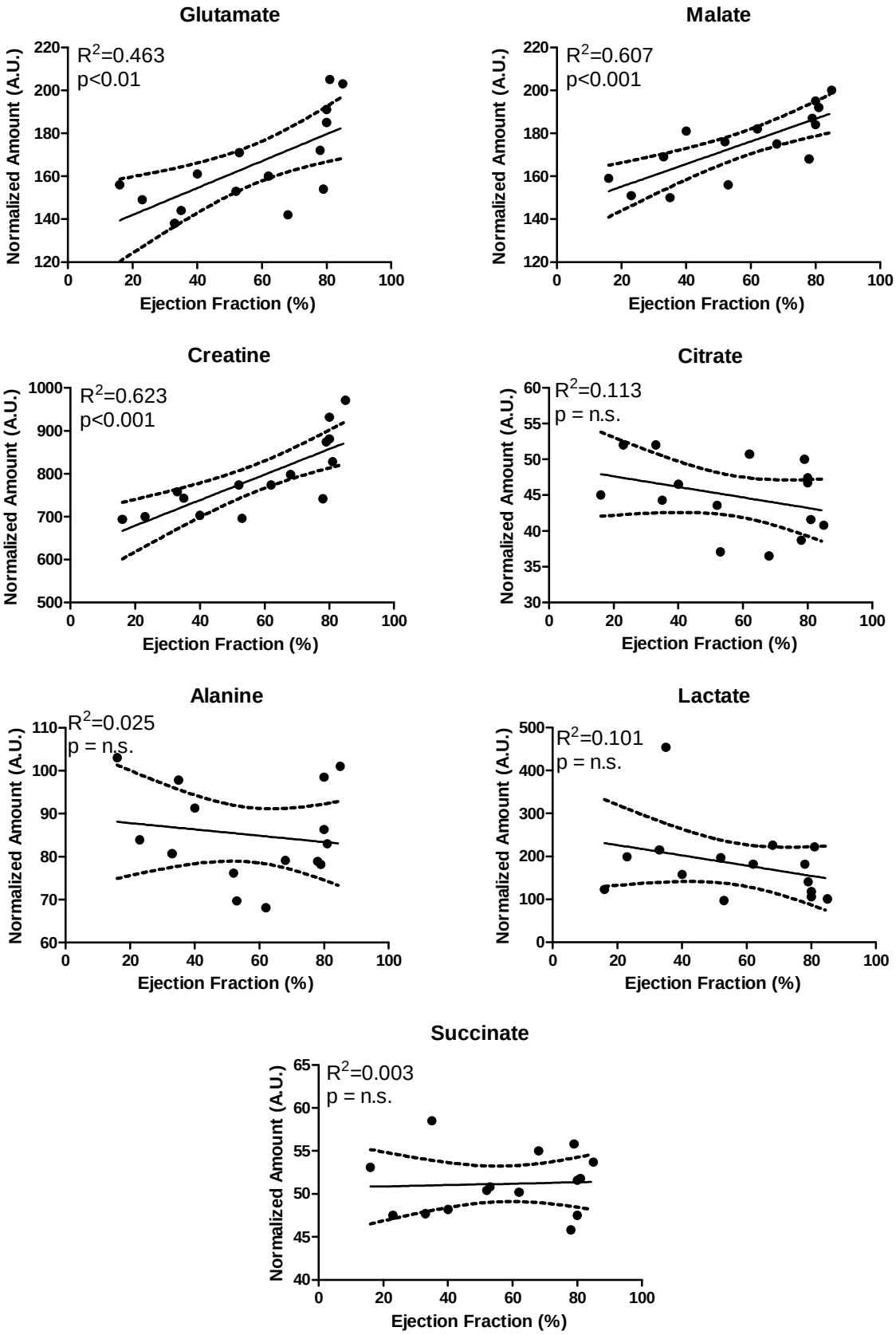

Figure 4.5 – *In vitro* metabolomic analysis of TCA cycle intermediates and other relevant cellular metabolites showed alterations in the infarcted heart – Malate, glutamate and creatine levels correlated positively with ejection fraction. Lactate, alanine, succinate and citrate levels were unaltered with ejection fraction.

The acylcarnitine: free carnitine ratio was calculated *ex vivo* using a direct infusion mass spectrometry (DI-MS) approach. The results of this study revealed that there was a significant negative correlation between the acylcarnitine: free carnitine ratio and ejection fraction (Figure 4.6). Further scrutiny of the data revealed that this was largely driven by a significant reduction in free carnitine in the infarcted hearts (Figure 4.6).

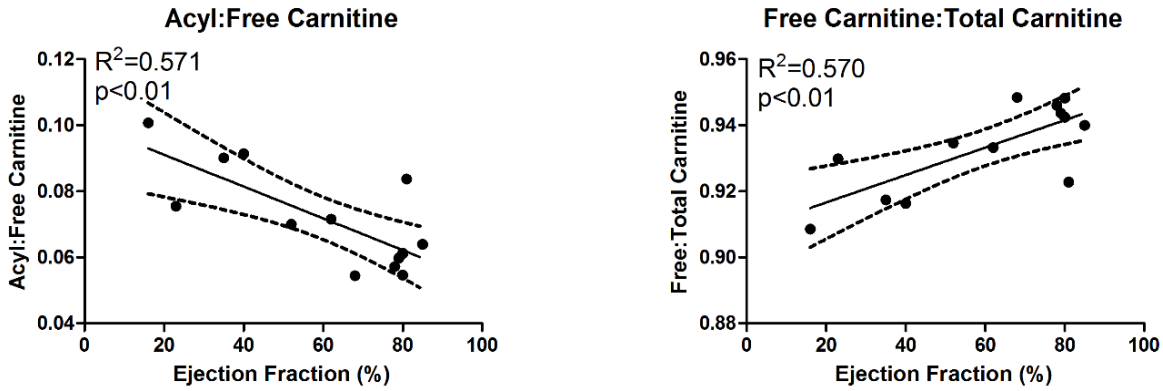

Figure 4.6 – Relative carnitine concentrations were assayed using GC-MS – The ratio of carnitine in the acylcarnitine to free carnitine, negatively correlated with ejection fraction. This was driven by decreases in the free carnitine to total carnitine levels, which is indicative of carnitine deficiency.

4.4.4 Myocardial infarction affects the activity of TCA cycle enzymes

To determine whether the observed alterations in energy metabolism were attributable to alterations in key mitochondrial enzymes (CS, ICDH, PDH and CAT) enzyme activity assays were performed (Figure 4.7). There was a significant positive correlation between ejection fraction and CS, ICDH, PDH and CAT activity. These results therefore indicate that the activity of all of these enzymes was impaired 22 weeks post myocardial infarction. Changes in PDH activity (which reflects the percentage of PDH in the active form relative to total) were not due to an increase in total PDH activity, which did not correlate with ejection fraction.

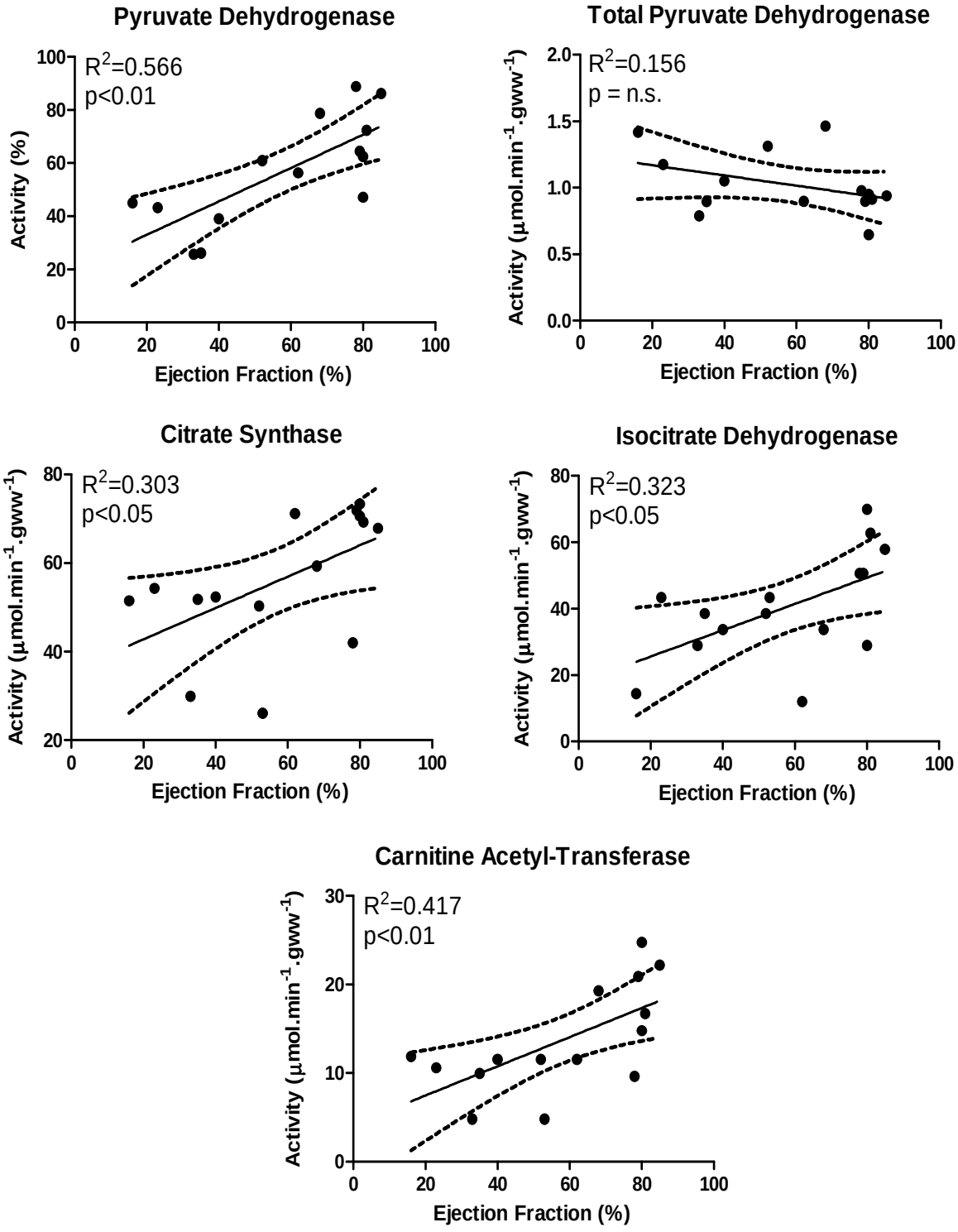

Figure 4.7 – *In vitro* analysis of key metabolic enzymes reveals reduced activity in the failing heart – Consistent with *in vivo* data, PDH, CS and CAT activity positively correlate with ejection fraction. ICDH also shows reduced activity. Highlighting abnormalities in key enzymes involved in processing of glycolytic products and TCA cycle flux with reducing ejection fraction.

4.4.5 The expression of PDK-4 positively correlates with ejection fraction

Western blots were used to assess the expression of the key inhibitor of PDH, PDK4. Interestingly, PDK4 correlated positively with ejection fraction ($p < 0.05$, Figure 4.8), suggesting it was not responsible for the decrease in PDH activity.

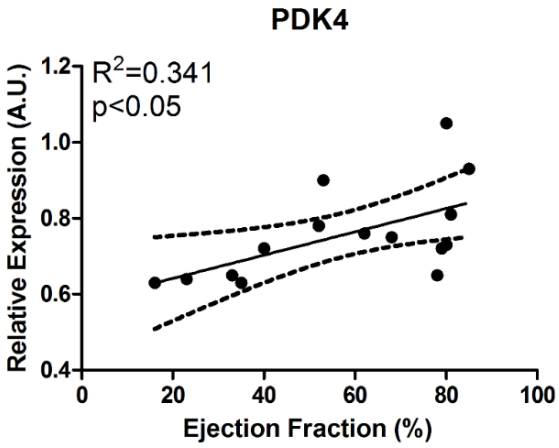

Figure 4.8 – Pyruvate dehydrogenase kinase 4 protein expression correlates with ejection fraction – Interestingly the key inhibitory regulator of PDH activity was also decreased in the failing heart.

4.5 Discussion

An increasing body of evidence suggests that the progression of heart failure is inextricably linked to alterations in cardiac metabolism [3]. In this study, using the recently developed technique of hyperpolarized ^{13}C DNP MRS, an *in vivo* assessment of metabolism following a myocardial infarction was performed. One week post-MI, animals displayed a range of ejection fractions between 28-81%. At this timepoint there was no detectable correlation between the measured ejection fraction and metabolic changes as assessed by PDH flux, ^{13}C label incorporation into lactate and alanine or ^{13}C label incorporation into the TCA cycle and acetylcarnitine. One week post-surgery represented an early timepoint where the heart was potentially recovering from the acute surgical insult [161,162]. Previous work has shown that by two weeks post-MI, there was no change in the activity of key TCA cycle enzymes; citrate synthase and α-ketoglutarate dehydrogenase [163]. However, defects in the electron transport chain have been observed in the infarcted heart at two weeks, with a reduction in the activity of complex III, highlighting possible early energy defects [163].

4.5.1 Reduced capacity to oxidise acetyl-CoA at six weeks post MI

Six weeks post-MI, no change in PDH flux was seen over the range of ejection fractions observed. In parallel, no alterations in flux into lactate and alanine were seen, suggesting no evidence for a switch to a more glucose oxidative-phenotype by 6 weeks, with altered ejection fractions. Consistent with the *in vivo* data, a 5-6 weeks post-MI canine model, has showed no change in glucose oxidation at this point of moderate heart failure [151]. However, a novel finding here was the detection of *in vivo* cardiac metabolic alterations in ^{13}C label incorporation into the TCA cycle and acetylcarnitine, which correlated with ejection fraction. ^{13}C label incorporation into citrate, glutamate and acetylcarnitine displayed a significant positive correlation with the 6 week ejection fraction. Consistent with previous clinical and experimental findings in MI, that showed that PDH activity was unaltered, whilst there was a

significant reduction in citrate synthase activity and expression [148,149]. Reduction in citrate synthase activity has previously been attributed to a decrease in mitochondrial density [48]. A decrease in *in vivo* flux into citrate might represent a decrease in mitochondrial function in heart failure and energy starvation.

At the 6 week timepoint, as ejection fraction decreases, there is a reduced capacity for acetyl-CoA oxidation in the TCA cycle, which is not related to reduced PDH flux. The reduction into acetylcarnitine may be more likely indicative of a reduction in available carnitine for the activity of carnitine acetyl-transferase [158,164]. The decreases in citrate and acetylcarnitine may provide a useful clinical marker of metabolic alterations consistent with moderate heart failure.

Energy defects are detected in high energy phosphates by 8 weeks in both pig and rat models of MI [165,166]. In the pig model, in failing hearts, there was a significant reduction in the mRNA expression of the β_{F1}-ATPase subunit, which might indicate a reduced capacity for ATPase to produce ATP [166]. Although decreases in ATP were not detected at 8 weeks post-MI in rats, there was a significant reduction in PCr and therefore a reduction in the PCr to ATP ratio, indicating an energetic defect [55,166].

4.5.2 Progression into heart failure at 22 weeks

Cardiac structural and functional parameters were assessed at this timepoint using cine-MRI. Ejection fraction measured by echocardiography at 22 weeks, tightly correlated with that measured by cine-MRI (Figure 4.1). This provided validity to the use of echo at each timepoint, which was necessary due to licencing constraints. With decreasing ejection fraction, the cardiac output and stroke volume also decreased, whilst scar size and end diastolic volume significantly increased. These data are consistent with a model of heart

failure, with significant dilatation of the left ventricle and a reduced capacity to pump blood [2]. The developed scar would also impede normal contraction of the heart, as this tissue is relatively inflexible. The infarcted heart does not display overt hypertrophy, likely indicating it's progression into heart failure.

Consistent with the progression into heart failure, at 22 weeks post MI, reduced ejection fraction lead to significant reductions in metabolic flux into the TCA cycle. PDH flux and ^{13}C label incorporation into the TCA cycle/acetylcarnitine all positively correlated with ejection fraction. This would indicate a reduction in carbohydrate-derived flux into the TCA cycle through PDH in the infarcted heart at 22 weeks post-MI. Supporting these *in vivo* findings, *in vitro* biochemical analysis of enzyme activity, revealed a similar pattern of reduced PDH, CAT and CS activity with decreasing ejection fraction (Figure 4.9). Taken with other 22 week post-MI rat data, which showed a significant positive correlation between MCAD activity and cardiac function [48], a generalised decrease in energy generation occurs in the infarcted heart. These data support the hypothesis that the failing heart has reduced mitochondrial function in glucose oxidation and β-oxidation, consistent with an energy starvation model [3,148,151].

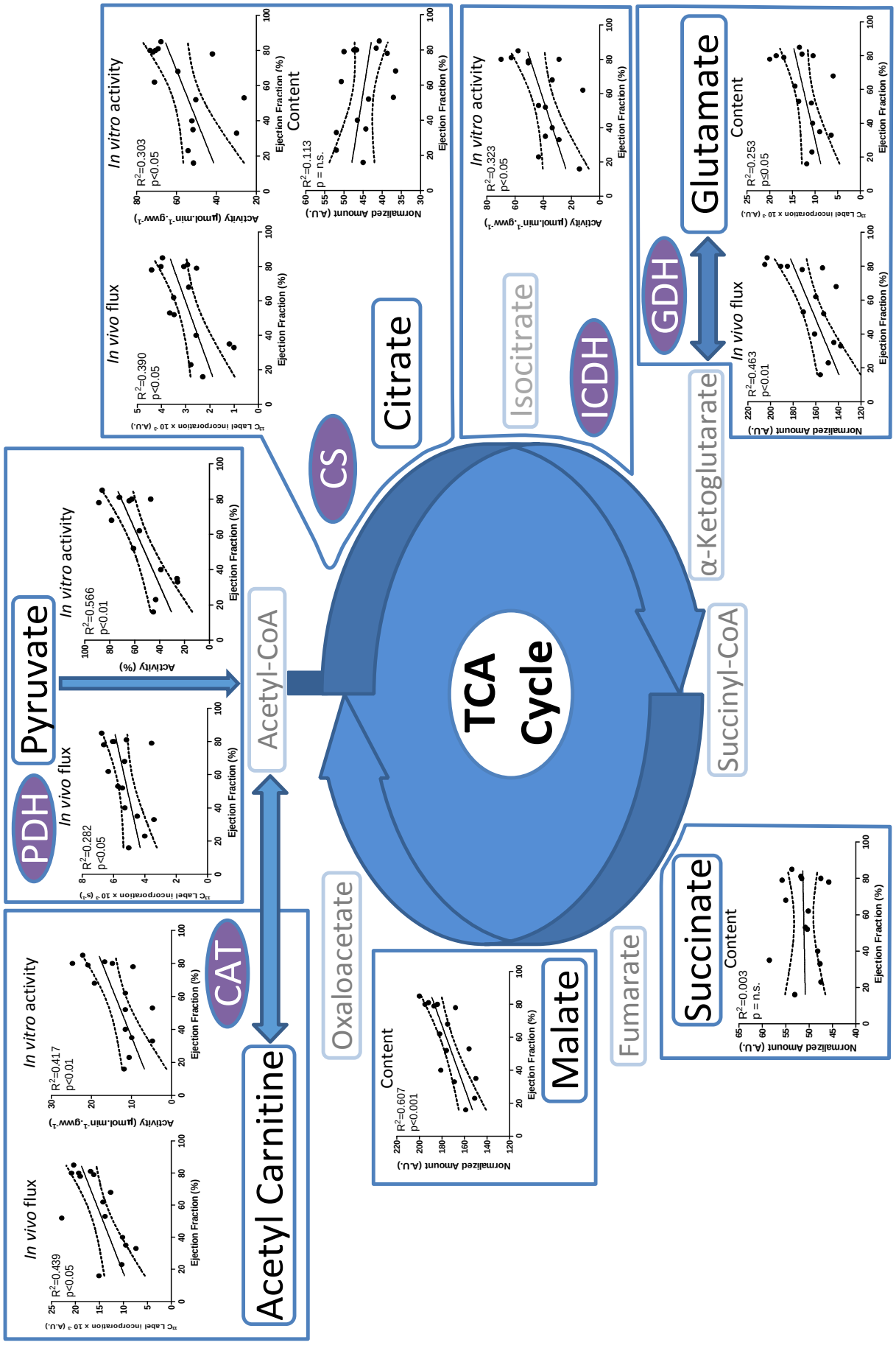

Figure 4.9 – Summary of 22 week data – Alterations are seen in TCA cycle intermediates, as well as changes in flux and activity of key enzymes. TCA cycle intermediates that are grey, have not been assessed.

In vitro analysis of heart tissue at 22 weeks post MI strengthened the *in vivo* analysis of metabolic alterations. Metabolomic analysis of the heart highlighted that consistent with a reduced ^{13}C label flux into glutamate, there was a positive correlation in glutamate pool size in the failing heart. Along with a positive correlation in malate, these data highlight a reduction in TCA cycle oxidative capacity. Interestingly, there was no correlation between the citrate concentration and ejection fraction. Chandler *et al* reported that at an early stage of heart failure, there were no changes in citrate and succinate levels, but changes in CS activity consistent with our data [48,151]. As ICDH activity also positively correlated with ejection fraction, it is possible that there was a reduced capacity to metabolise citrate and isocitrate in the infarcted heart. This therefore means that lower CS activity would be required to maintain a normal citrate concentration.

4.5.3 Mechanisms of pyruvate dehydrogenase inhibition

The mechanism by which PDH was inactivated in the failing heart is unclear. One of the key inhibitory enzymes of PDH, PDK4 correlated positively with ejection fraction. This has also been observed previously in a dog model of heart failure, where both PDK4 and PDK2 were significantly reduced in the failing heart [148]. This implies that PDK4 does not play a role in modulating the decrease in PDH activity seen in the failing heart. Other mechanisms responsible for the regulation of PDH activity exist, such as O-palmitoylation of the β-E1 subunit, which has been shown to potentially reduce PDH activity following ischemic injury [167]. Due to an increase in FA uptake in the infarcted heart but reduced β-oxidation, PDH activity could be directly inhibited by enhanced palmitate concentrations. Although it is unclear over what length of time this modification remains in place and whether this has occurred [167].

PDH activity can also be affected by the ratio of NADH/NAD+ and acetyl-CoA/CoA, where increases in these ratios inhibit PDH activity [28,29,31,43,133]. Several factors influence these ratios such as TCA cycle flux, carnitine availability, the ETC and flux between pyruvate and lactate. In the failing heart several ETC defects have been reported in complex I, II and III in clinical and experimental studies [163,168–171]. Complex I oxidizes NADH to liberate a free electron for the ETC whilst pumping protons from the mitochondrial matrix. Defects in complex I have been reported in canine models of heart failure, where after 4 weeks of pacing, complex I activity was reduced by approximately 50% [170]. Complex I defects would be associated with decreased NADH oxidation in the failing heart, possibly leading to an increased NADH/NAD+ ratio, if NADH producing steps are not halted. It might take time for the levels of NADH to build up to a point to enable the inhibition of PDH, possibly explaining why PDH flux did not correlate with ejection fraction at 6 weeks.

As previously mentioned the ratio of acetyl-CoA/CoA can alter PDH activity, and the ratio is affected by TCA cycle flux and carnitine availability [172]. Flux into citrate and glutamate have been shown to correlate with ejection fraction, possibly implicating decreased TCA cycle flux and reduced acetyl-CoA oxidation, in PDH inhibition. Another mechanism is reductions in the availability of free carnitine, which trap CoA in acetyl-CoA, resulting in increased levels of acetyl-CoA and end-product inhibition of PDH [27,173]. In this study, the negative correlation of acylcarnitine: free carnitine ratio with ejection fraction potentially indicates a “trapping” of carnitine in the acyl groups. L-carnitine is an essential component of β-oxidation as it facilitates fatty acid transport into the mitochondria. Alterations in the ratio of acylated to free carnitine in the heart may be indicative of perturbations in fatty acid metabolism, which in turn could impact negatively upon cardiac energetics. These data are further strengthened by positive correlations with cardiac function in CAT activity and *in vivo* flux into acetylcarnitine. Clinical and experimental studies have report trapping of carnitine within acylcarnitine [150,164,174175]. Trapping leads to a free carnitine deficiency which has been

reported to affect β-oxidation and glucose oxidation in the hypertrophied rat heart and the chronically infarcted rat heart [173,175,176]. Consistent with our data, clinical data from patients in heart failure showed no difference in total carnitine between groups, but a significant reduction in free carnitine [164]. This was due to increased short and long chain acylcarnitine and it was suggested that myocardial carnitine deficiency accompanied chronic heart failure [164], strengthening the link for translational studies. Myocardial carnitine deficiency supports the *in vivo* and *in vitro* data on carnitine handling seen in these animals. A reduction in the availability of carnitine would lead to a decrease in CAT activity. This could suggest that changes in *in vivo* flux into acetylcarnitine assessed by DNP MRS could be used as a marker of alterations in carnitine handling.

Consistent with previous clinical and experimental studies , we observed that creatine levels significantly decreased with decreasing ejection fraction [3,177,178]. This has previously been attributed to reductions in creatine transporter function in the failing heart, which leads to reductions in phosphocreatine. The result of this is a decline in ATP transfer rate and compromised energy generation [3,177,178].

These data are further strengthened by the work of Lei *et al* which suggests that in the failing heart there is a depression of both β-oxidation and glucose oxidation [148]. Similar to our study, a significant reduction was observed in CS activity and the protein expression of PDK4. However, unlike here, their study showed no difference in PDH activity between failing and control hearts, possibly due to the model/techniques used [148].

It is unclear at 22 weeks whether there is a loss of mitochondrial number, which contributes to the reduction in enzyme activities per gww that we have observed. The total stimulated PDH was not significantly different across the range of ejection fractions investigated, suggesting that a reduction in total PDH activity was not responsible for the

reduced PDH activity. This would suggest that mitochondrial number was unaltered in our experiments.

The data presented here would appear to contradict several other studies that identified reductions in β-oxidation or fatty acid uptake as the energy defect in the failing heart [25,142,179,180].Whilst β-oxidation was not measured in this model, it has previously been shown in this lab to be reduced by the 22 week timepoint. In this model, it would appear that there is a general energy defect, where both glucose oxidation and β-oxidation are decreased. In support of this, decreases in citrate synthase activity, reported here and elsewhere [48,148], and altered ^{13}C flux into citrate, suggest that mitochondrial function is impaired in the failing heart.

4.5.4 Conclusions

In conclusion, we have seen significant decreases in *in vivo* flux into the TCA cycle and into acetylcarnitine at 6 weeks after a myocardial infarction. The early six week alterations in flux into acetylcarnitine, might suggest a reduction in carnitine which is indicative of the development of heart failure [150,164,174,175]. By 22 weeks there were also significant reductions in PDH flux and activity, and along with signs of carnitine deficiency. These results have been strengthened by *in vitro* assessment of CS, CAT and ICDH activity and alterations in TCA cycle intermediates, which are reduced in the failing heart. Hyperpolarized DNP has allowed us to gain an insight into the *in vivo* metabolic state of the heart through its progression from myocardial infarction and into failure. The combination of changes in flux into citrate, glutamate and acetylcarnitine at 6 weeks, could be used as an *in vivo* clinical marker of metabolic alterations during the progression of heart failure. During the progression into heart failure there appears to be decreased glucose oxidation and a reduction in TCA cycle efficiency, which is proportional to the degree of contractile impairment.

Chapter 5

In Vivo Mouse Cardiac Hyperpolarized Magnetic Resonance Spectroscopy with Application in the Fumarate Hydratase Knockout Mouse

5.1 Overview

As has been shown in the previous chapters, alterations in cardiac metabolism and substrate selection accompany many diseases of the heart. The advent of cardiac hyperpolarized MRS, via DNP, has enabled a greater understanding of the *in vivo* metabolic changes seen as a consequence of myocardial infarction, hypertrophy and diabetes. However, all cardiac studies performed to date have focused on rats and larger animals, whereas more information could be gained through the study of transgenic mouse models of heart disease. Translation from the rat to the mouse is challenging, due in part to the reduction in heart size ($1/10^{th}$) and the 50% increase in heart rate. In this study, we demonstrate an approach to investigate the *in vivo* metabolism of hyperpolarized pyruvate in the mouse heart. To assess the sensitivity of the method to detect alterations in PDH flux, two well characterised methods of PDH modulation were performed; fasting overnight and infusion of sodium dichloroacetate. This technique was then used to assess the *in vivo* metabolic state of the transgenic cardiac specific fumarate hydratase knockout (FH-KO) mouse. The FH-KO mouse displayed significant alterations in PDH flux at 12-14 weeks of age compared to controls. This was accompanied by left ventricular dysfunction, compared to controls and younger, 6 weeks old FH-KO mice.

5.2 Background

The use of genetic mouse models to assess the metabolic basis of heart disease is important, because transgenic and knockout lines provide models to probe individual metabolic pathways that are disturbed during the development of heart disease and can yield valuable insights into the etiology of human diseases. Studying models, such as the LCAD-KO [16,181], PPARα-KO [182] and GLUT 1 [183] transgenic models, have increased our knowledge of the development and pathology of human diseases. The ability to probe individual enzymes or complexes has allowed a greater understanding of their role in the metabolic phenotype of heart disease and may provide possible targets for treatments. Such work has mainly been performed in the mouse, as the genetic manipulation required to create transgenic rats has proved extremely challenging. As mentioned in the introduction, recent advances with SAGE have opened the possibility of transgenic rats, however these are still very expensive and limited work has been performed using them. Therefore mice still offer the best option for the genetic study of cardiac metabolism.

All cardiac studies with DNP performed to date have focused on rats or larger animals, whereas more information could be gained through the study of transgenic mouse models of heart disease. However, translation from the rat to the mouse is challenging, due in part to the smaller heart size (~80 mg [99] vs ~600 mg [184]) and the higher heart rate (600 bpm vs 450 bpm[15]). This also means that RF coils previously used and optimized for rats, have to be either modified or new, smaller and more sensitive coils created.

This chapter demonstrates an approach to investigate the *in vivo* metabolism of [1-^{13}C] and [2-^{13}C]pyruvate in the mouse heart. This required the creation and testing of a new mouse surface coil, which was sensitive enough to encompass the whole mouse heart. Spectra of [1-^{13}C]pyruvate acquired from C57BL/6 mice were compared to those from the Wistar rat, to investigate whether there are differences in temporal kinetics or peak heights between

species. To define the sensitivity of the method to detect alterations in PDH flux, three sets of mice were scanned. Mice were scanned in either the fed state, the fasted state (removal of food for ~19 hours) or following an infusion of DCA. Both fasting and DCA have previously been shown to modulate *in vivo* PDH flux in rats [8,79].

Fasting increases plasma free fatty acid levels, which partially through the action of PPARα, mediate an increase in β-oxidation [8,185,186]. Increased expression and activity of PDK means that PDH activity is significantly decreased (Figure 5.1) [29,31,35,37,43,187]. This is an integral part of the Randle cycle, where an increase in β-oxidation inhibits oxidation of glycolytically derived pyruvate, therefore preserving glucose [6]. Conversely, DCA activates PDH through inhibition of all isoforms of PDK [31,79,80,188], by binding to the N-terminal pyruvate

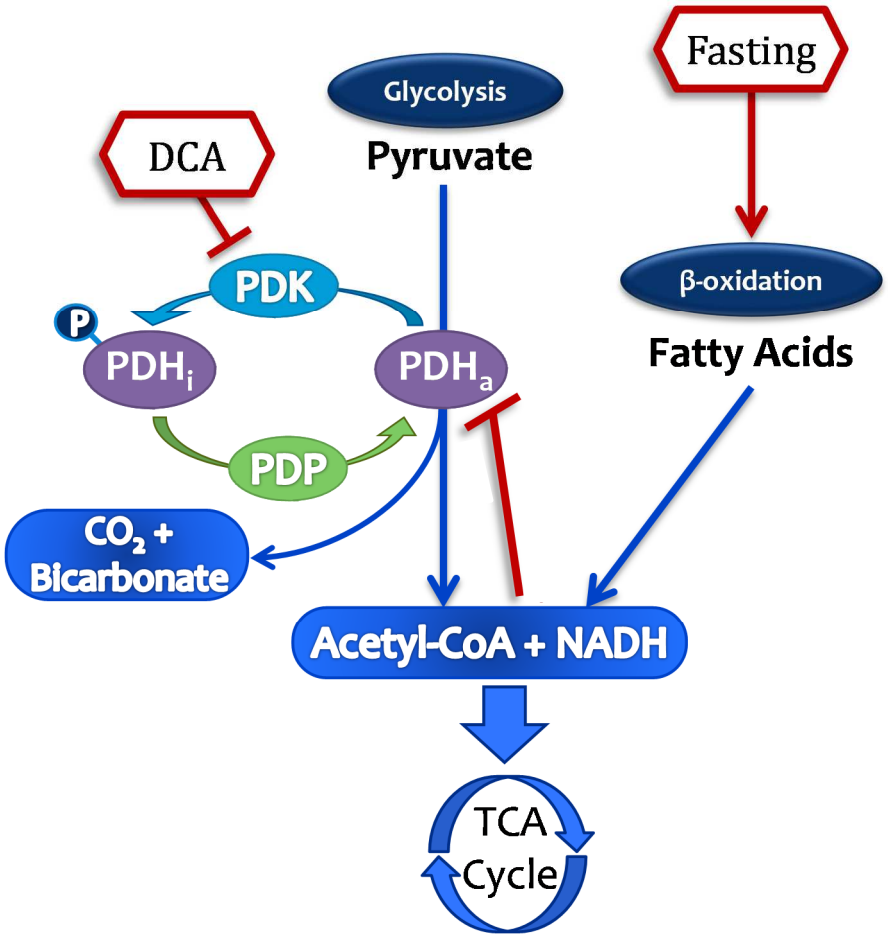

Figure 5.1 – PDH regulation – A diagrammatic representation of PDH regulation. A decrease in PDH activity is seen due to increased β-oxidation, increased acetyl-CoA/NADH and increased PDK activity/content. PDH activity is increased by PDP, inhibition of PDK and low levels of NADH.

binding site of PDK, mimicking high pyruvate concentrations within the cell [189–191]. This activation would allow cells to decrease PDK activity during times of plentiful energy supply or increased glycolytic rate [191].

Following validation of the technique, it was applied to characterize the metabolic profile of several control mice strains (C57BL/6, 129 SvEv and balb/c mice) that are commonly used as breeding backgrounds for transgenic mouse lines [192,193]. Differences in metabolic profiles in mouse models of heart disease can be influenced by the background strain used to generate the mouse [194,195]. The aim was to better understand the metabolic phenotype of injected [1-^{13}C]pyruvate in the mouse heart.

Finally the developed technique was applied to transgenic cardiac specific FH-KO mice. These mice were evaluated at 6 weeks and 12-14 weeks of age to assess their *in vivo* metabolic phenotype. The FH-KO mice were generated by Pollard *et al* [196] and Ashrafian *et al* [197], to investigate the role of increased fumarate in protection from ischemic injury. The model was created by *loxP* sequences that were introduced to flank exons 2 and 3 of the *fumarate hydratase* (*Fh*) gene, to produce mice termed *Fh1*$^{fl/fl}$. These mice were crossed with mice containing Cre recombinase which was under the control of the myosin light chain promoter (MLC2v) [197]. Upon induction of the cre-system with tamoxifen, *Fh* was knocked out in the mouse heart. A cre-system was necessary, as non-conditional knockout of *Fh* was embryonic lethal [196]. Ashrafian *et al* demonstrated that this mouse had a significant 71% reduction in FH protein expression within the cell, the remaining protein reflected FH from nonmyocyte compartments, which do not express the Cre recombinase [197].

Ashrafian *et al* further showed that 6 week old FH-KO mice were protected from cardiac ischemia/reperfusion injury and they proposed that this was due to the accumulation of fumarate [197]. Cardiac structure and function was unaltered between FH-KO mice and their

controls. This was particularly interesting as it may be expected that these animals would suffer from an energetic imbalance, due to the knockout of a TCA cycle enzyme. ^{31}P MRS of the perfused heart also showed that there was no difference in the PCr/ATP ratio between FH-KO and controls.

The surprising fact that FH-KO mice are able to maintain normal cardiac function and high energy phosphorous energetics indicates a level of metabolic remodelling. Computer simulations combined with metabolomics in FH-KO cells, have suggested that there is an increased reliance on anaplerotic pathways to supplement the loss of malate production from fumarate [197,198]. This was observed as an increased use of amino acids for malate and oxaloacetate production, thereby keeping the TCA cycle flowing [197,198]. The malate-aspartate shuttle normally functions to transport NADH from the intermembrane space of the mitochondria, into the matrix, as can be seen in Figure 5.2. However in the FH-KO mouse it is proposed that this system acts as a mechanism to produce malate and oxaloacetate from aspartate and α-ketoglutarate [197]. This system would generate α-ketoglutarate from the first portion of the TCA cycle and aspartate from amino acids, e.g. alanine. The net result is the production of malate and oxaloacetate and a normally functioning TCA cycle.

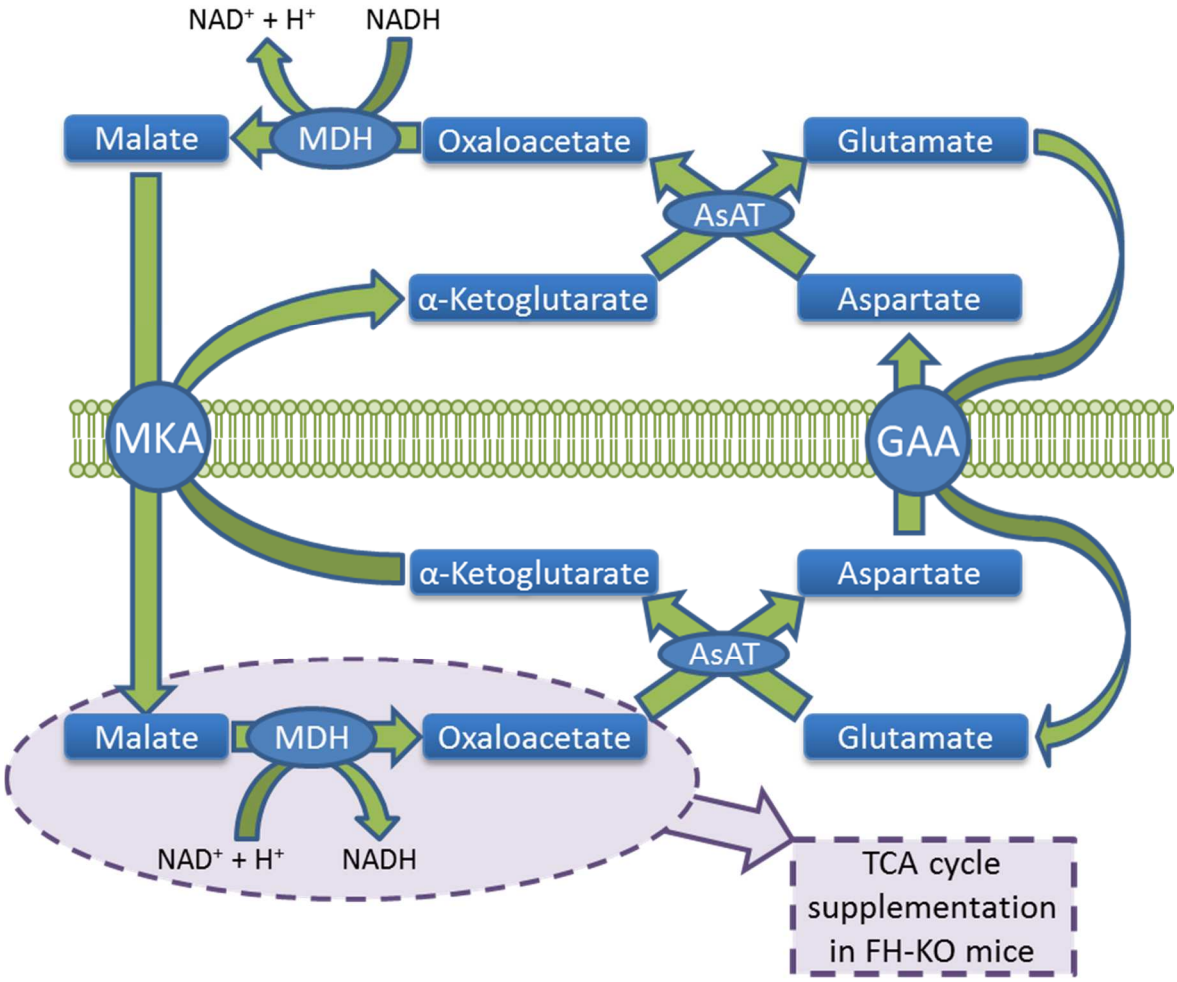

Figure 5.2 – The Malate-aspartate shuttle – The purpose of this shuttle is to transport NADH from the intermembrane space (IMS), to the mitochondrial matrix. This is done by the creation of malate in the IMS (consuming NADH), which is transported through to the matrix and converted back to oxaloacetate, generating NADH. AsAT: Aspartate aminotransferase, GAA: Glutamate-aspartate antiporter, MDH: Malate dehydrogenase and MKA: Malate-α-ketoglutarate antiporter.

However, upon stress with dobutamine, which increases cardiac workload and has been shown to increase TCA cycle flux [95], there was a significant decrease in LV end-diastolic pressure in 6 week old FH-KO mice [197]. Potentially highlighting a, stress-inducible, effect on cardiac workload, possibly due to an inability to increase TCA cycle flux in the FH-KO mouse.

Beyond 6 weeks of age these mice start to develop a severe impairment of cardiac function and die at around 12-14 weeks of age [197]. The reason for this transition is unclear,

although it is likely to be due to an inability of the anaplerotic pathways to maintain normal TCA cycle function.

The aim of the studies performed here was to assess the *in vivo* metabolic phenotype of the FH-KO mouse at 6 weeks of age, before the onset of cardiac complications and again at the later time point of 12-14 weeks. Such application demonstrated that the development of hyperpolarized MRS for cardiac mouse studies offers the potential to provide a novel tool to assess *in vivo* genetic alterations in the diseased heart.

5.3 Methods

5.3.1 *Animal handling*

Nineteen C57BL/6 mice (~25 g, 15 week old), five Balb/c (~25 g, 15 week old), six 129 SvEv (~25 g, 15 week old) and four Wistar rats (~250 g) were obtained from Harlan UK. *Fh11*$^{fl/fl}$ MLC2v-Cre (termed FH-KO, n = 17), *Fh11*$^{fl/+}$ MLC2v-Cre and *Fh11*$^{fl/fl}$ (termed controls and indistinguishable from wild-type, n = 14) were provided by Dr Houman Ashrafian, University of Oxford, UK.

Animal handling was carried out as set out in section – 2.1. However, the MR animal-handling system was modified to fit mice, by adding a plastic insert and a smaller anaesthetic nose cone, this set up can be seen in Figure 5.3.

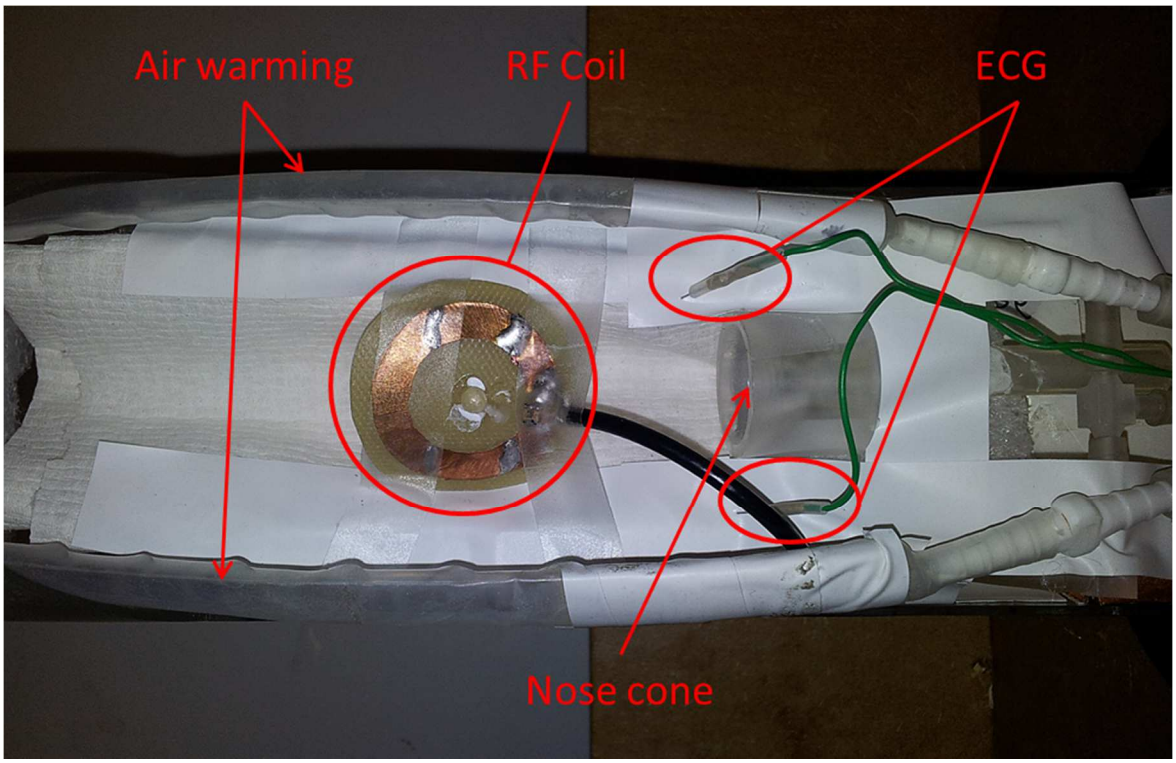

Figure 5.3 – MR animal handling system showing mouse insert, air warming, ECG leads, anaesthetic nose cone and mouse RF coil.

5.3.2 *Development of a mouse hyperpolarized ^{13}C MR protocol*

Animals received either a [1-^{13}C] or [2-^{13}C]pyruvate scan depending on the study. The basic hyperpolarized protocol and pyruvate dissolution were as set out in sections 2.2.3 and 2.2.1. For the delivery of the hyperpolarized compound a specially designed cannula was required. In the mouse, intravenous injection volume is limited to approximately 200 µl (for a 20 g mouse) [15]. However the original cannula used for rat studies has a 'dead' volume of 160 ± 3 µl (Figure 5.4), which would mean that only 40 µl of hyperpolarized compound could be delivered [199]. To overcome this, a new cannula was designed specifically for mouse use, this cannula consisted of a 30 gauge insulin needle, 60 cm portex tubing (0.28 mm ID, 0.61 mm OD, 800/100/100, Smiths medical international Ltd. Hythe, UK) and the needle hub from a 30 gauge insulin needle (Monoject, Tyco Healthcare Ltd, Hampshire, UK), as can be seen in Figure 5.5. This new cannula allowed the delivery of ~140 µl of hyperpolarized solution for a 200 µl injection, i.e. a dead volume of 60 µl.

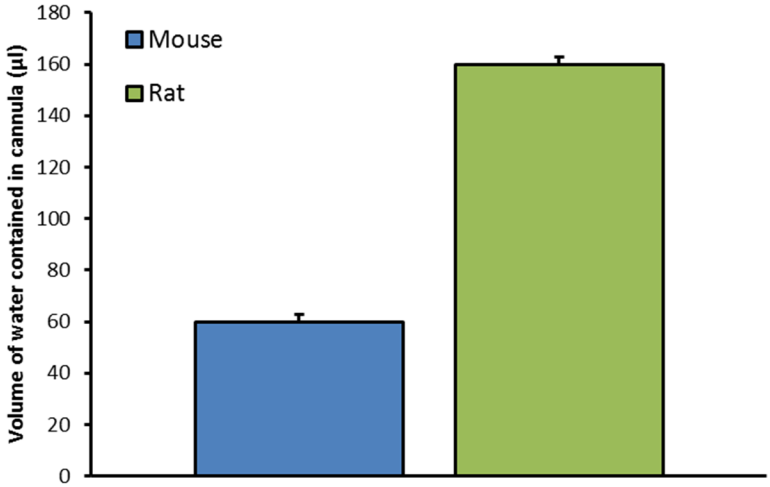

Figure 5.4 – Volume of water contained in rat and new mouse cannula – Water was inserted into the cannula and then ejected on to a balance to determine the weight of water, and therefore volume of water, contained within each cannula. This was performed 10 times to provide a mean volume and standard error of the mean, (error bars)

Figure 5.5 – Mouse cannula shown to scale against a 2 pence coin.

The next challenge was to develop a sensitive ^{13}C surface RF coil for the mouse. This was achieved using a 2 cm diameter circular coil (Figure 5.7), designed to have a penetration depth of ~10 mm (Figure 5.8). The non-magnetic capacitors were arranged in parallel and had the following capacitances: 82 pF + 27 pF = 99 pF. The coil was linked to a homebuilt tuning and matching circuit through the coaxial cable. The positional point phantom was a small glass vial containing water. It was designed to be visible during scout imaging of the mouse, to ensure that the centre of the coil was accurately positioned over the centre of the mouse heart. This ensured that signal originating from other organs, i.e. the liver, were minimized by being outside the sensitive volume of the coil.

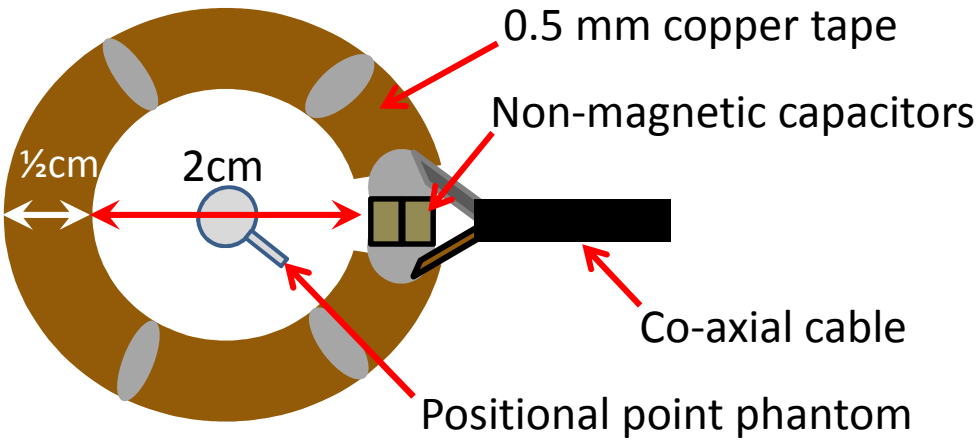

Figure 5.6 – Coil schematic of the mouse coil

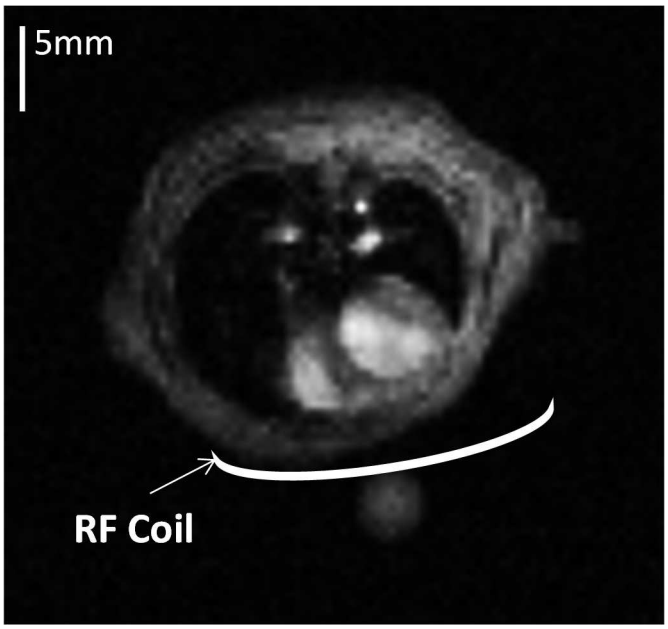

Figure 5.8 – Axial image of mouse to show depth that RF coil would need to penetrate to reach back wall of the heart.

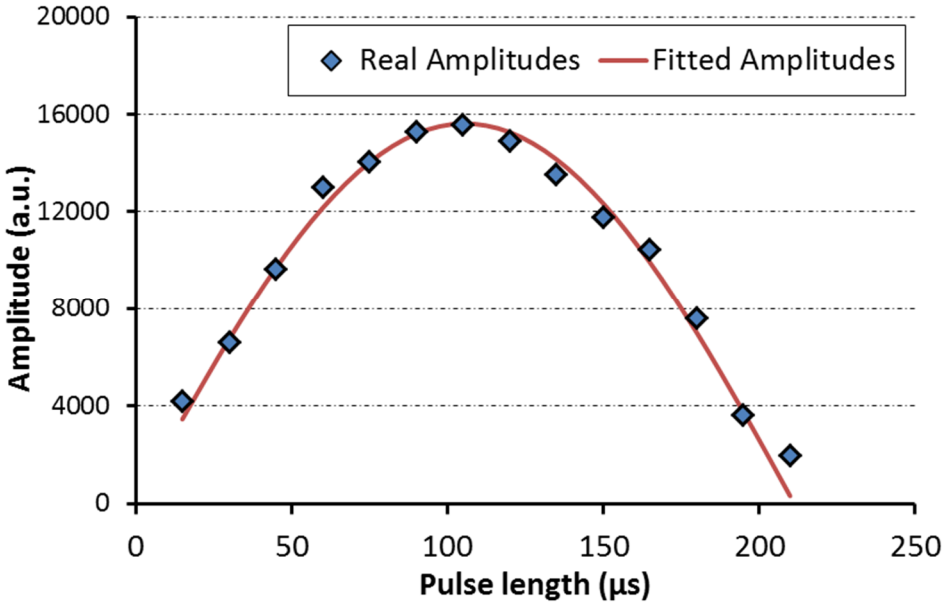

Figure 5.9 – Flip angle calculation for the mouse coil – Max amplitude was found at a pulse length of 105 µs for 57 dB, this was set as 90°.

A flip angle calibration was performed on an acetone phantom to find the pulse length required to obtain a 90° flip angle at 57 dB transmission power. A simple pulse acquire protocol was used, TR = 300 s, 32 averages, arrayed pulse length. The pulse length was arrayed from 15 to 210 µs, in increments of 15 µs. The peak area of the acetone resonance, at

each pulse length was entered in to Excel (Microsoft, Washington USA) (Figure 5.9). A simulated amplitude at each pulse length was calculated using the following equation:

$$x = M_0 * \sin(pw * F)$$

Where x was the fitted amplitude, pw was pulse length (μs), F was the flip angle constant ($°.\mu s^{-1}$), and M_0 was the net magnetization. The Solver function in Excel was used to optimize the values of F and M_0 so that the sum of squares error of the fit compared to the real data was minimized. This calculated a 90° flip angle, at a pulse length of 105 μs at 57dB.

To test the sensitivity profile of the coil, a field map was generated using an acetone phantom and then overlaid on to an axial proton mouse image. The field map was calculated using a chemical shift imaging acquisition at multiple flip angle values (TR/TE, 1000/1.01 ms; flip angle, arrayed from 10 - 180°; 32 averages, 20 mm slice thickness; matrix 8 x 8 x 512; field of view 64 x 64 mm; zero-filled 32 x 32 x 512). This showed that the coil was sensitive to the back wall of the heart (Figure 5.10).

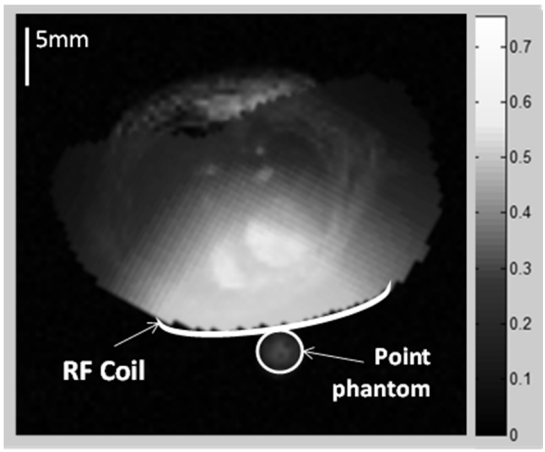

Figure 5.10 – Field map of mouse coil, overlaid on an axial proton mouse image

5.3.3 MRS data analysis

MRS data analysis was carried out as described in section 2.2.4.

5.3.4 *Comparison with rats*

Wistar rats have previously been used as control animals for hyperpolarized cardiac studies [199]. To perform a comparison between fed C57BL/6 mice and Wistar rats, four rats were also scanned using the methods set out in section 2.2.2. Briefly, rats were anesthetised using 2.5-3% isoflurane and maintained at 2%. A catheter was introduced into the tail vein for i.v. delivery of hyperpolarized [1-^{13}C]pyruvate solution. Following dissolution, 1 ml of hyperpolarized pyruvate was injected over 10 s into the anesthetised rat. Sixty individual ECG-gated ^{13}C MR pulse-acquire cardiac spectra were acquired over 1 min after injection, using a custom built ^{13}C loop butterfly RF coil (20 mm)[199].

5.3.5 *Validation with C57BL/6 mice*

Male C57BL/6 mice received [1-^{13}C]pyruvate scans, in either the fed state (n=7) or after fasting overnight for a minimum of 19 hours (n = 7). In the fasted animals, food was removed at 16:00 h on the day before experiments, resulting in a ~10% loss of body weight. Another group of C57BL/6 mice (n = 5) received [1-^{13}C]pyruvate scans after an infusion of DCA (30 mg/ml, in saline at pH 7.4). DCA (0.2 ml) was injected as a bolus into the tail vein cannula, followed by an infusion of 0.1 ml over 10 minutes. The end of the infusion was timed to allow immediate injection of hyperpolarized [1-^{13}C]pyruvate. Due to the increased volume injected, mice were sacrificed immediately following the acquisition of spectroscopic data.

5.3.6 *Comparing different control strains*

It is well known that the correct background strain of control animals is vital for a valid study. To compare the metabolic phenotype of frequently used control strains, male balb/c (n = 5, BW = ~25 g) and 129 SvEv (n = 6, BW = ~25g) received [1-^{13}C]pyruvate scans in the fed state, and were compared to the data from the fed C57BL/6 mice.

5.3.7 *Testing of [2-^{13}C]pyruvate in C57BL/6*

Five C57BL/6 mice were injected with [2-^{13}C]pyruvate to test the sensitivity of the technique to detect downstream metabolites. This was performed on fed mice and spectra were summed over 30 s, to provide a pyruvate to metabolite ratio. The SNR was low, but citrate, glutamate and acetylcarnitine peaks were visible in the summed spectra. This was then used to assess metabolic alterations in the FH-KO mouse.

5.3.8 *Fumarate hydratase knockout mouse*

To perform the first transgenic cardiac mouse DNP experiments we used a recently developed cardiac specific FH-KO mouse. This mouse line has recently been characterized by Ashrafian *et al* 2012, where some of this work is presented [197]. FH-KO and controls were observed at 6 weeks (healthy) and 12-14 weeks (diseased). At 12-14 weeks of age these mice develop progressive left ventricular dysfunction and this time point was chosen to assess the metabolic state of the diseased animals [197].

At the 6 week timepoint, nine controls and eight FH-KO mice were scanned with [1-^{13}C]pyruvate. Of this group, four controls and five FH-KO also received a [2-^{13}C]pyruvate scan on a separate day. At 12-14 weeks five controls and six FH-KO mice were scanned with [1-^{13}C]pyruvate and, with the exception of one FH-KO mouse, all received a [2-^{13}C]pyruvate scan on a separate day.

5.3.9 *Cine magnetic resonance imaging*

Following hyperpolarized scans, a set of animals (in the FH-KO study) were imaged to assess left ventricular mass and cardiac function (6 weeks n = 5 (for FH-KO and WT) and 12-14 weeks n = 4 (for FH-KO and WT)). Cine MRI was performed as set out in section 2.2.8.

5.3.10 Statistics

All results are expressed as mean ± SEM. Significant differences between mean values were determined by a one-way analysis of variance (ANOVA) followed by Bonferroni's multiple comparison post hoc test. Differences between groups were considered significant if $p < 0.05$.

5.4 Results

5.4.1 *Acquisition of [1-^{13}C]pyruvate spectra in the in vivo mouse heart*

A typical set of spectra from a control fed mouse is shown in Figure 5.11 (C57BL/6). Along with the injected [1-^{13}C]pyruvate, its metabolites, [1-^{13}C]lactate, [1-^{13}C]alanine and [^{13}C]bicarbonate can be visualized with 1 second temporal resolution (Figure 5.11 A). [^{13}C]bicarbonate is produced from the conversion of $^{13}CO_2$ by the carbonic anhydrase enzyme. Due to the low SNR of the peak and a rapid exchange into [^{13}C]bicarbonate, $^{13}CO_2$ is only visible in the summed spectrum (Figure 5.11 B)

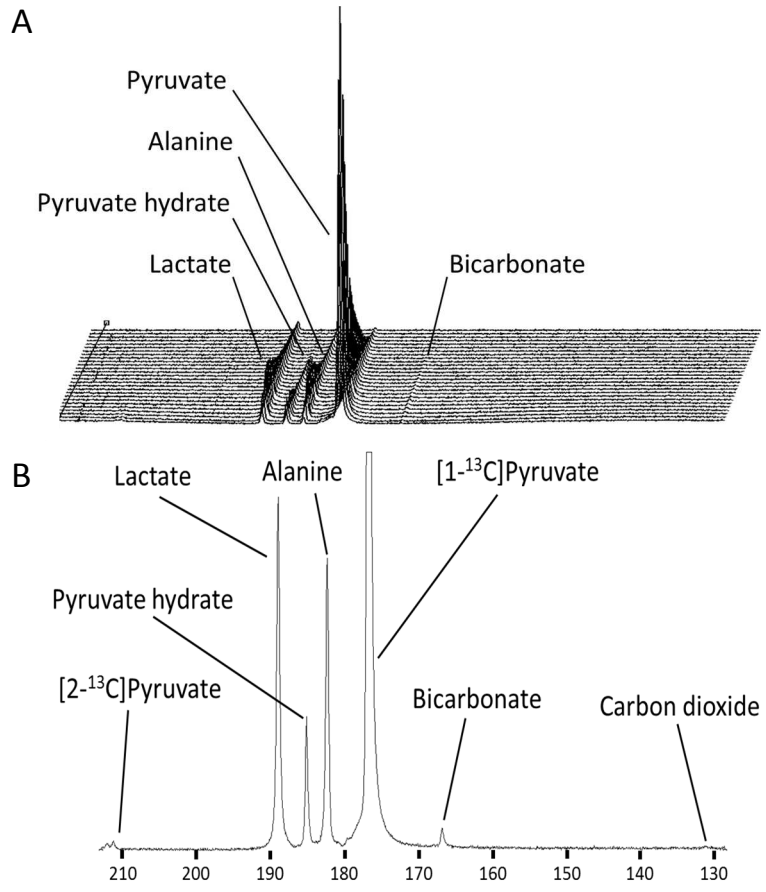

Figure 5.11 – Example mouse spectra – A) Example spectra in a fed wild type C57BL/6 mouse. B) Summed spectrum of 40 individual spectra from a fed wild type C57BL/6 mouse. N.B. [2-^{13}C]pyruvate is derived from ^{13}C natural abundance pyruvate

5.4.2 *Appearance of pyruvate and lactate peaks follow a similar time course to the rat*

An averaged time course of the fitted peak areas of pyruvate, lactate, alanine and bicarbonate from the fed rat heart (n = 4) and the fed C57BL/6 mouse heart (n = 5) are shown in Figure 5.12. Curves are normalized to the peak pyruvate signal intensity to account for any differences in the initial polarization and coil sensitivity. Alanine appeared significantly earlier in the mouse heart, compared to the rat heart (2.6 ± 0.8 s vs 6 ± 1 s, time of arrival normalized to pyruvate arrival, $p < 0.05$), bicarbonate also appeared significantly earlier in the mouse heart (1.4 ± 0.2 s vs 2.3 ± 0.3 s, time of arrival normalized to pyruvate arrival, $p < 0.05$). Maximum bicarbonate signal was reduced 7-fold in the mouse heart compared to the rat (0.023 ± 0.001 a.u. vs 0.165 ± 0.008 a.u., bicarbonate normalized to peak pyruvate signal),

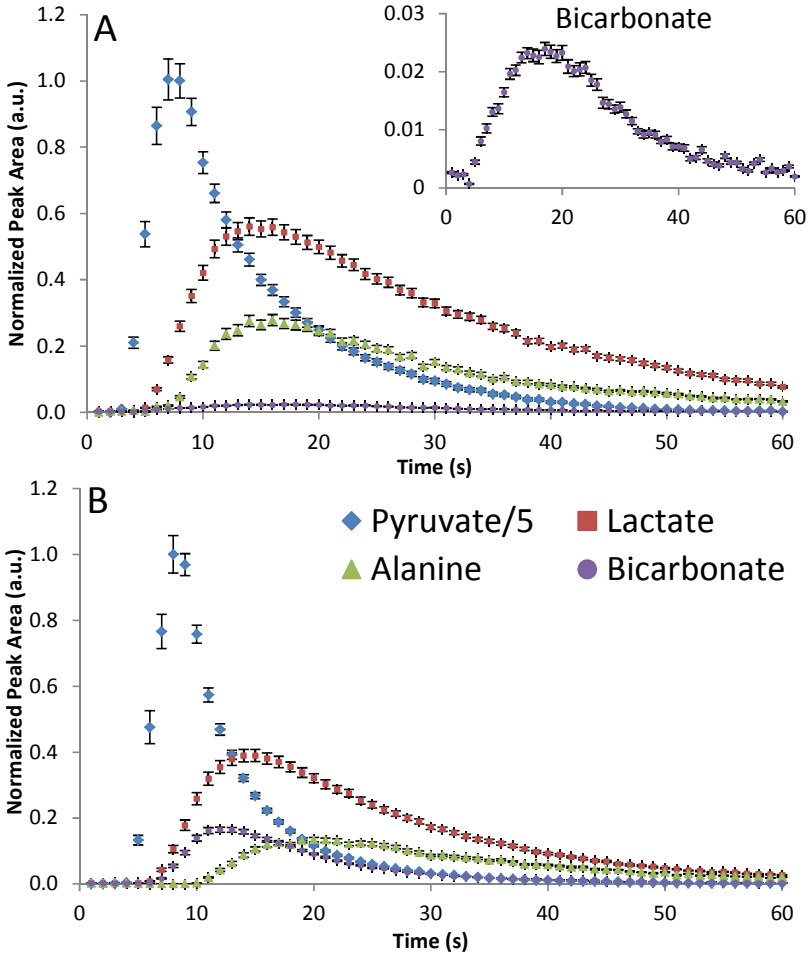

Figure 5.12 – Example mouse and rat time course – A) Shows a combined time course in control mice (C57BL/6), bicarbonate signal is reduced compared to the rat and the insert shows the bicarbonate time course expanded. B) Shows a combined time course in the rat (Wistar) for pyruvate and the three main metabolites lactate, alanine and bicarbonate (n=4).

potentially representing a difference in PDH activity in the mouse heart compared to the rat heart.

5.4.3 Overnight fasting and dichloroacetate modulate PDH flux in vivo

To define the sensitivity of the DNP technique in mice, two well characterized models of PDH flux modulation were employed (Figure 5.13). Overnight fasting led to a significant 80% reduction in ^{13}C label incorporation into bicarbonate compared to fed controls (from 11 ± 2 x 10^{-4} s^{-1} to 2.5 x ± 0.5 10^{-4} s^{-1}, $p < 0.05$). No significant change was observed in the ^{13}C label incorporation into lactate (from 300 ± 50 x 10^{-4} s^{-1} to 250 ± 20 x 10^{-4} s^{-1}) or ^{13}C label incorporation into alanine (from 90 ± 20 x 10^{-4} s^{-1} to 130 ± 30 x 10^{-4} s^{-1}). Infusion of 0.3 ml of 30 mg/kg DCA significantly increased PDH flux by 145% (from 11 ± 2 x 10^{-4} s^{-1} to 29 ± 6 x 10^{-4} s^{-1}, $p < 0.001$). Again no difference in ^{13}C label incorporation into either lactate or alanine was observed.

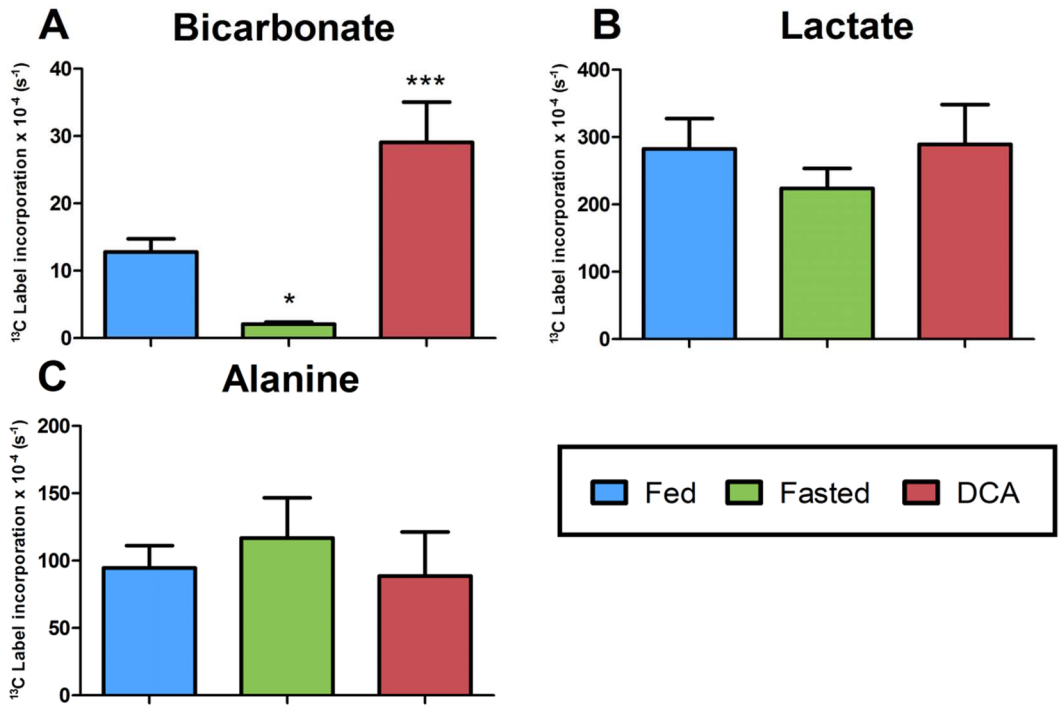

Figure 5.13 – Assessing the sensitivity of hyperpolarized [1-^{13}C]pyruvate in mouse heart – A) Fasting in control mice led to a significant decrease in ^{13}C label incorporation into bicarbonate in the C57BL/6 mouse, compared to fed controls. Infusion of DCA led to a significant increase in 13C label incorporation compared to fed mice. B) No difference was found in ^{13}C label incorporation of lactate between fed, fasting and DCA infusion. C) No significant difference was found between ^{13}C label incorporation into alanine in the fed, fasted or DCA state.

* $p < 0.05$ and *** $p < 0.001$ compared to fed controls.

5.4.4 *Comparison of frequently used mouse strains*

Following the successful demonstration of the sensitivity of the mouse DNP technique, comparison of the metabolic profiles of the commonly used control strains, balb/c and 129 SvEv were compared to the data from fed C57BL/6 mice (Figure 5.14). ^{13}C label incorporation into bicarbonate was significantly higher in the 129 SvEv, compared to both balb/c and C57BL/6 mice. Label incorporation into lactate was significantly lower in the balb/c mice compared to C57BL/6. ^{13}C label incorporation into alanine appears elevated in the C57BL/6 mice, although there was no statistical difference between groups, (C57BL/6 verses 129 SvEv p=0.06).

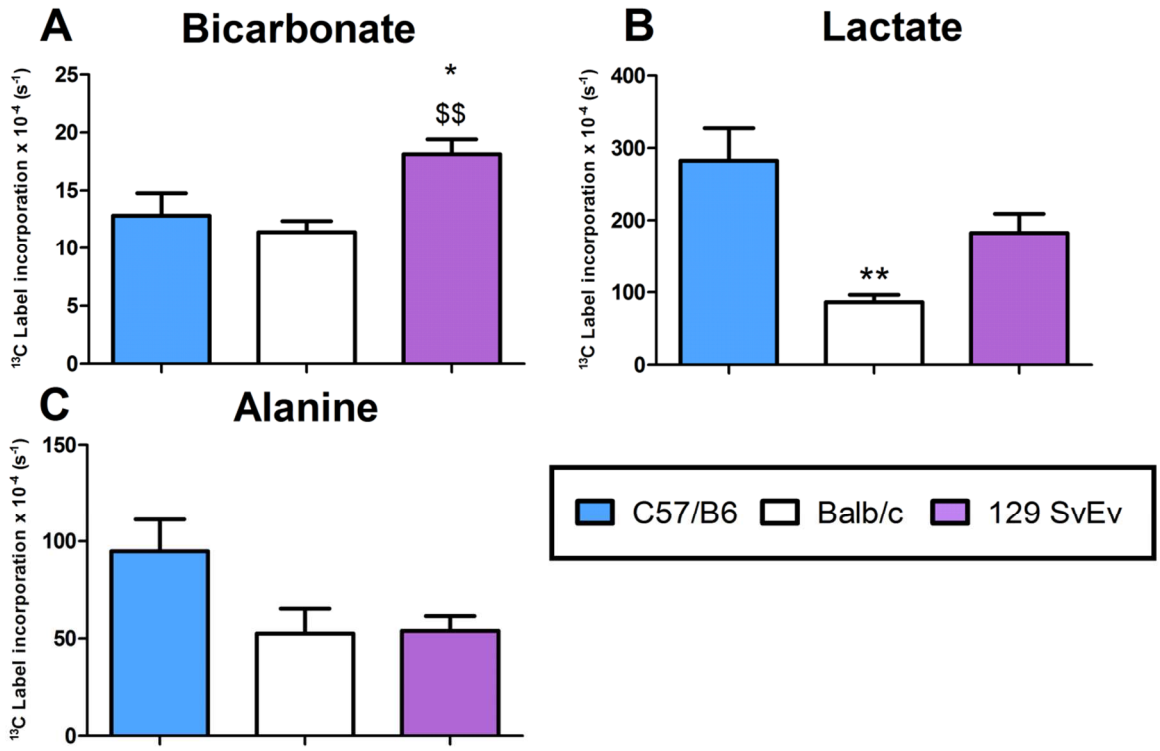

Figure 5.14 – Comparison between different mouse strains – Several commonly used mouse strains (C57BL/6, Balb/c and 129 SvEv) were compared using [1-^{13}C]pyruvate. A) Label incorporation into bicarbonate was found to be similar between the C57BL/6 and balb/c, it was however significantly elevated in the 129 SvEv. B) Label incorporation into lactate was significantly reduced in the balb/c mouse, compared to C57BL/6. C) No difference was seen in alanine.

* $p < 0.05$ and ** $p < 0.01$ vs C57BL/6 and $$ $p < 0.01$ compared to Balb/c.

5.4.5 *[2-^{13}C]Pyruvate metabolism in the C57BL/6 mouse*

To test the ability of the hyperpolarized mouse protocol to detect TCA cycle metabolites downstream of pyruvate, five control mice (C57BL/6) were injected with [2-^{13}C]pyruvate. In the rat the following peaks are observed: Lactate, alanine, glutamate, acetylcarnitine and citrate [95]. These peaks were also reproducibly detected in the mouse enabling the use of this technique to probe cardiac metabolic alterations in transgenic animals (Figure 5.15).

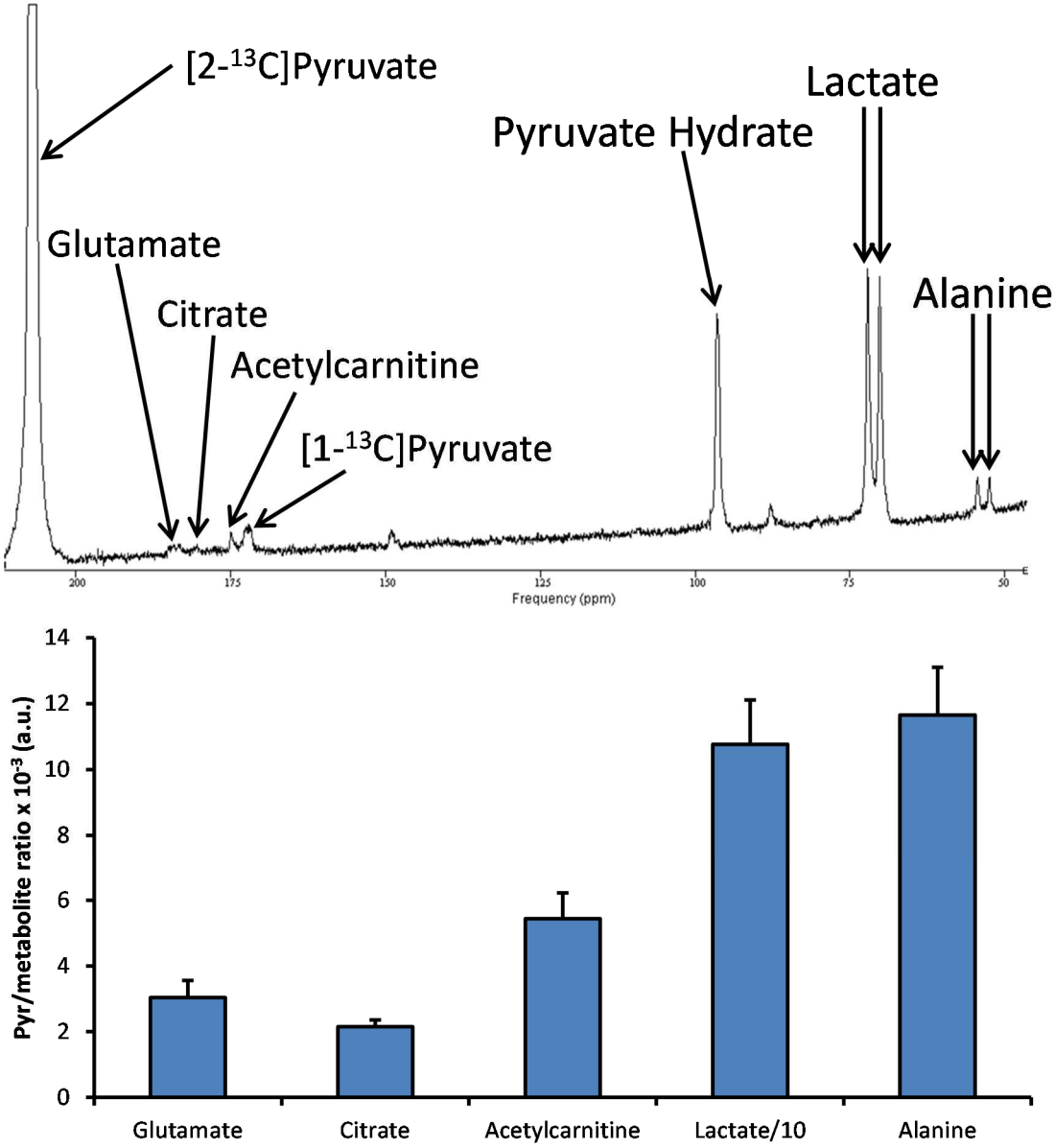

Figure 5.15 – [2-^{13}C]pyruvate spectra from a C57BL/6 mouse – This spectrum is the sum of 30 individual spectra from t = 4 sec until t = 33 sec. The graph shows repoducible results from the analysis of [2-^{13}C]pyruvate in the mouse.

5.4.6 *Aged FH-KO mice display abnormal cardiac structure*

At 6 weeks of age the controls and FH-KO mice are indistinguishable in terms of their cardiac function or LV mass (Figure 5.16). At 12-14 weeks of age, control animals display no difference from 6 weeks, however the FH-KO mice start to display hallmarks of heart failure. FH-KO mice displayed elevated left ventricular mass compared to 12-14 weeks old controls (270 ± 30 mg compared to 150 ± 7 mg) and 6 week FH-KO (270 ± 30 mg compared to 200 ± 10 mg), although the LV mass was highly variable within the 12-14 week FH-KO group. End diastolic volume was also significantly elevated in the 12-14 week old FH-KO mice compared to 12-14 week old controls (150 ± 20 µl compared to 79 ± 6 µl), and to 6 week old FH-KO

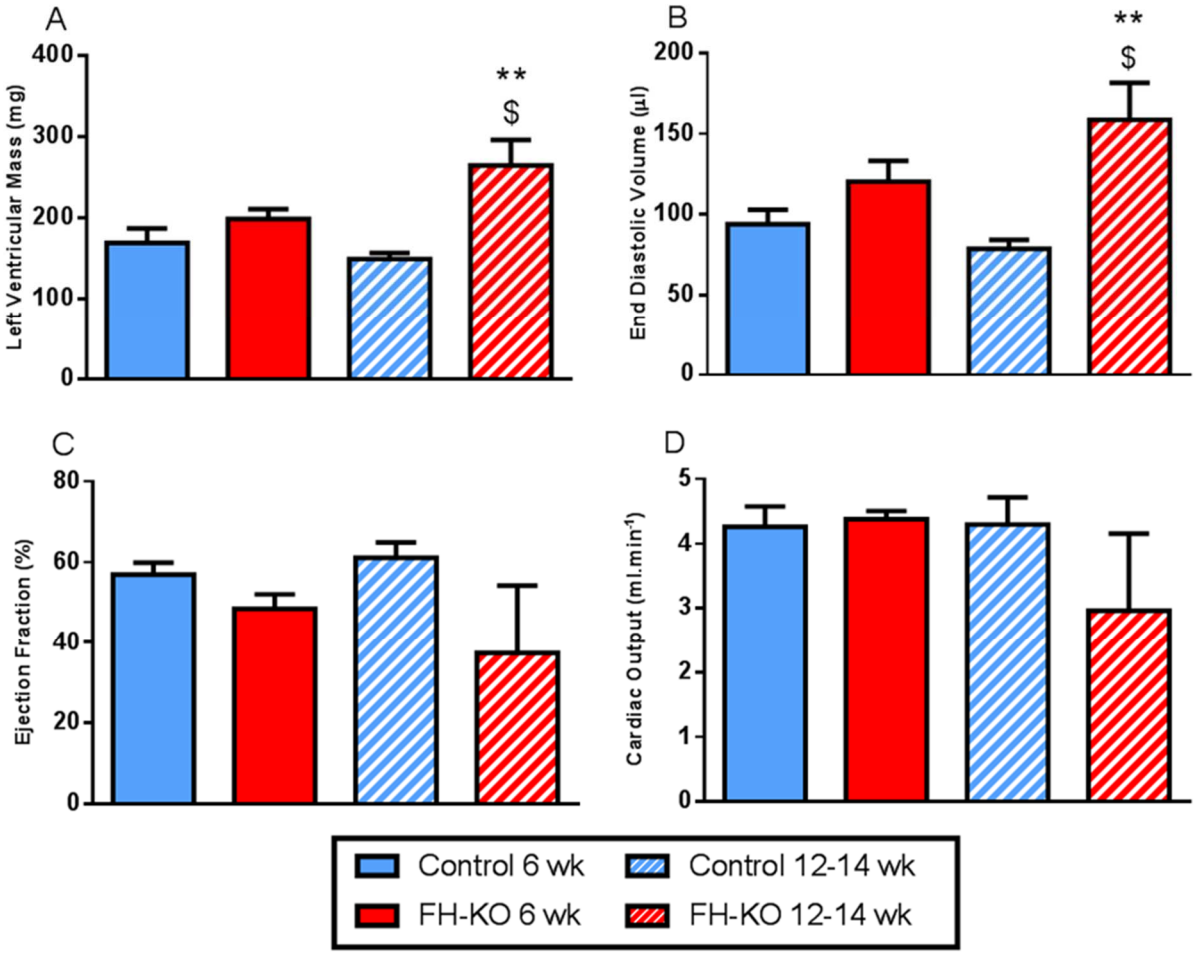

Figure 5.16 – Cine-MRI analysis of the 6 and 3-4 month old FH-KO mice – At 6 weeks of age, there is no difference in cardiac function or structure between the groups. But by 12-14 weeks of age, the FH-KO displayed significant increase in left ventricular mass and end diastolic volume. Ejection fraction was highly variable in the FH-KO, with 2 displaying normal (~60%) and the two displaying a failing heart phenotype (below 30%).

** $p<0.01$ vs control 12-14 weeks of age, $ $p<0.05$ vs FH-KO 6 weeks of age.

mice (120 ± 10 µl). Finally ejection fraction and cardiac output were not significantly different between groups, however this was again highly variable, as two 12-14 week old FH-KO mice had a normal ejection fraction of 65 and 68%, whilst the other two were failing with ejection fractions of 7 and 10% (one FH-KO mouse was not scanned due to technique issues). Figure 5.17 shows the 4 chamber view of a 12-14week old control and a failing 12-14 week old FH-KO, to display the elevation in LV volume and hypertrophy.

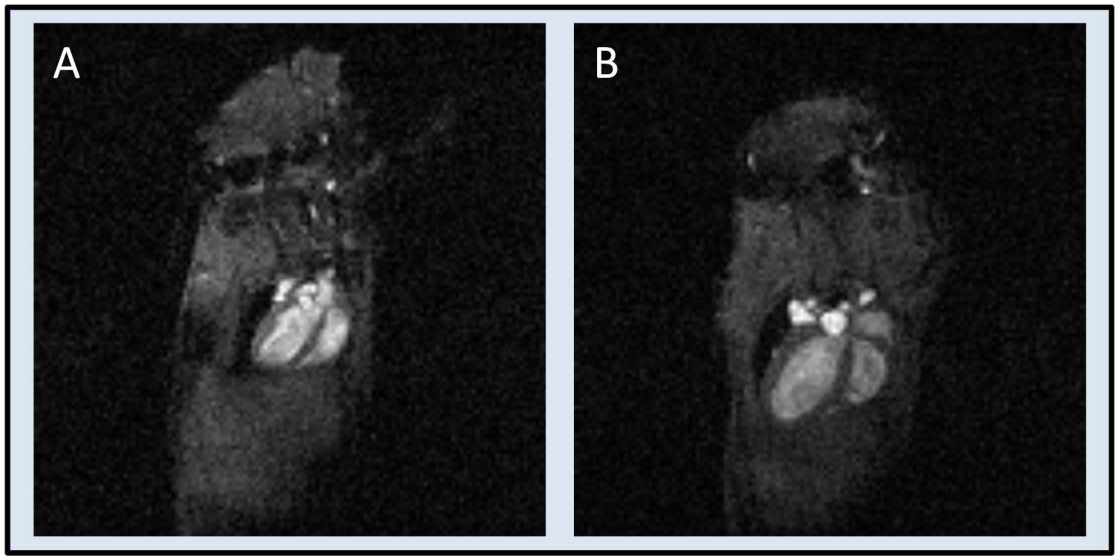

Figure 5.17 – 4 chamber image of 12-14 week old animals – A) A typical control animal (ejection fraction: 69%) **B**) A failing FH-KO (ejection fraction: 7%).

5.4.7 PDH flux in the FH-KO mouse

At 6 weeks of age there was no significant difference in lactate, alanine or bicarbonate signal levels between the controls and FH-KO mice (Figure 5.18). Indicating no metabolic abnormality in glucose derived carbohydrate metabolism at this early time point. By 12-14 weeks of age, there was a significant reduction in ^{13}C label incorporation into bicarbonate between the FH-KO and controls ($p < 0.05$), controls were significantly elevated compared to 6 week old animals ($p < 0.01$). Label incorporation into lactate in the 12-14 week old FH-KO mice remained unchanged compared to controls and was unaltered by age. Label incorporation into alanine was significantly reduced within the 12-14 week old FH-KO mice compared to 12-14 week old controls ($p < 0.05$).

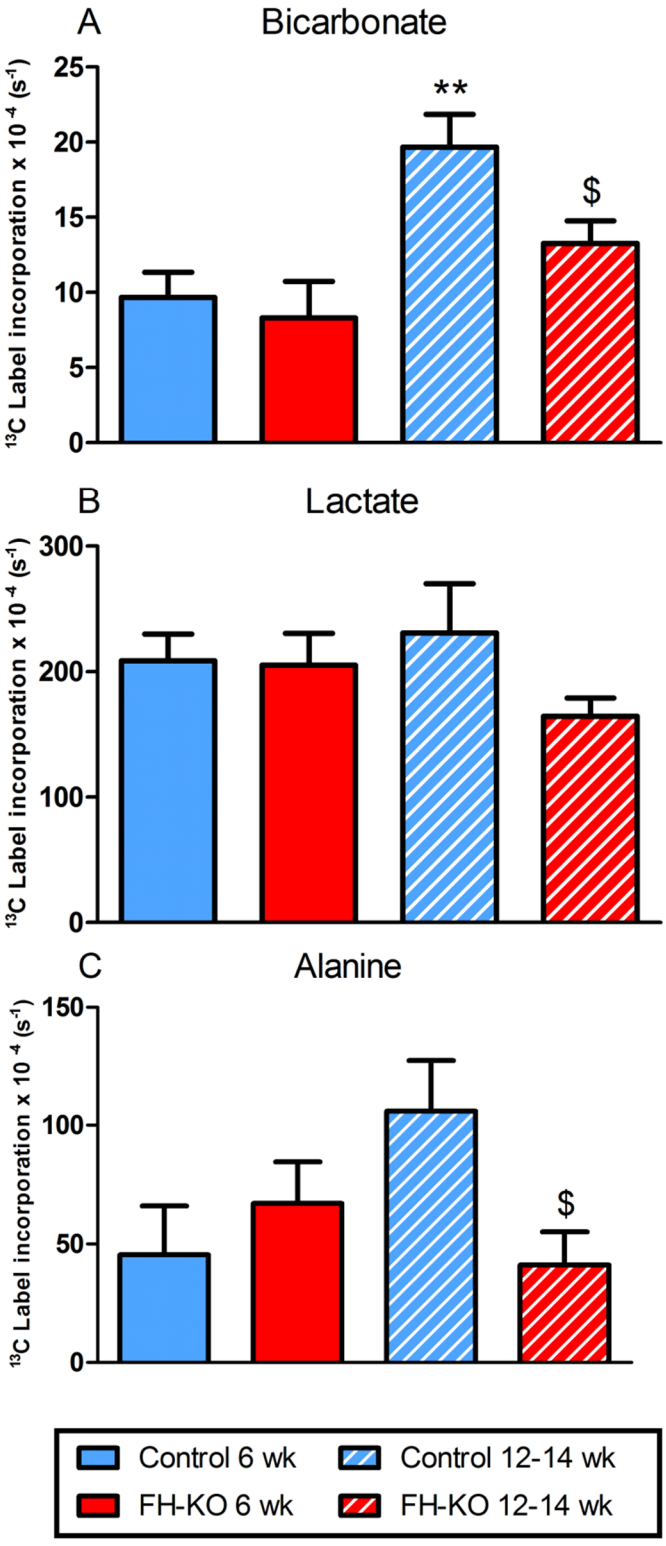

Figure 5.18 – Assessement of [1-^{13}C]pyruvate flux into bicarbonate, lactate and alanine – A) An age related increase was observed in the flux into bicarbonate in controls, 12-14week old FH-KO were significantly reduced compared to controls, but were not changed compared to young mice. B) No significant difference was seen in flux into lactate. C) Alanine label incorportation was significantly reduced in the 12-14 week FH-KO compared to controls

$ $p < 0.05$ vs. 12-14 week contols, ** $p < 0.01$ v.s 6 week contols

5.4.8 Normal TCA cycle flux in the FH-KO mouse

Flux into the TCA cycle and accessory pathways was assessed using [2-^{13}C]pyruvate (Figure 5.19). This technique was technically challenging in the mouse due to the decrease in size, compared to rats, and the decreased polarization that [2-^{13}C]pyruvate can achieve, compared to [1-^{13}C]pyruvate [95]. No statistically significant differences were observed between groups or related to age.

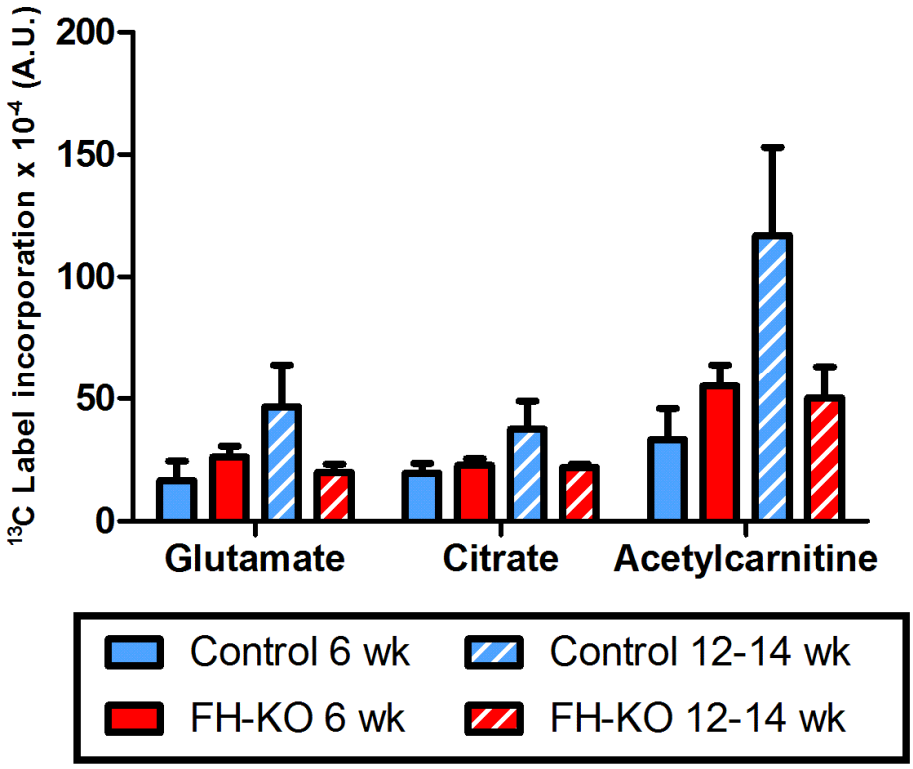

Figure 5.19 – Assessment of TCA cycle flux by the use of [2-^{13}C]pyruavte – No alterations were seen between the metabolites, when compared to age or transgenic status.

5.5 Discussion

In this chapter, hyperpolarized MRS was used to assess cardiac metabolism in the *in vivo* mouse heart. The chapter has detailed the development, testing and subsequent employment of the technique in the study of the FH-KO mouse. Using a custom built ^{13}C surface transmit/receive coil, the first mouse cardiac hyperpolarized [1-^{13}C]pyruvate spectra were collected. The field-map generated from the coil, illustrated that the coil was sensitive to the back wall of the mouse heart, with a penetration depth of ~10 mm. The next challenge was the development of an effective cannula for delivery of hyperpolarized solutions. As mentioned in the methods, there is an i.v. limit of 0.2 ml that can be injected into a mouse [15]. The rat cannula used in several previous studies and this thesis, was found to have a dead volume of ~0.16 ml, which would allow only 0.04 ml of hyperpolarized solution to be delivered [8,79,95]. Using ultrafine portex tubing and insulin needles, a new cannula with a 0.06 ml dead volume was created.

The first spectra in wild type mice (C57BL/6) showed similar resonances to the rat heart. However, carbon dioxide was only occasionally visible. Carbon dioxide was present in summed spectra, indicating that its absence was due to a lower SNR when compared to the rat. Pyruvate and lactate appearance mirrored that of rats, whilst alanine signals were slightly elevated when compared to the time evolution in the rat and also showed significant differences in the time of appearance. However, the major difference was the relative levels of bicarbonate, which were 7-fold lower in the mouse heart compared to the rat heart when normalized to maximum pyruvate signal, which may represent a species difference in PDH expression/activity due to differences in cardiac work load. It could also be the result of increased pyruvate signal from the larger lumen of the rat heart, when compared to the mouse heart. Due to the normalization to pyruvate, it is difficult to distinguish between increased detection of pyruvate or decreased bicarbonate, due to reduced PDH flux. However, as alanine and lactate normalized peak heights were unaltered in the mouse heart,

compared to the rat heart, increased pyruvate signal would not seem to be responsible for this difference. It is however difficult to make a realistic comparison between the rat and mouse without extensive kinetic modelling to yield a true measure of metabolic flux.

Mouse cardiac hyperpolarized MRS technique was assessed by demonstrating the sensitivity of the technique to alterations in PDH flux. Previously, using hyperpolarized [1-^{13}C]pyruvate in the rat, a significant reduction in cardiac PDH flux was observed in the fasted state [8]. Further, infusing 30 mg/kg of DCA significantly increased PDH flux in Wistar rat hearts [79]. Both methods of PDH modulation rely on alterations to PDK [188,189] (reviewed in [29]). In fasted rats, this leads to a significant 74% reduction in PDH flux, seen as a drop in the total [^{13}C]bicarbonate/[1-^{13}C]pyruvate ratio [8]. In this study, mice fasted overnight for a minimum of 19 hours, had an 80% decrease in PDH flux compared to controls in the fed state group ($p < 0.05$).

The third group of mice received a DCA infusion, prior to the hyperpolarized injection. DCA has a broad inhibitory action on all 4 isoforms of PDK, thereby increasing the proportion of PDH in the active form [31,188,189]. In rats, DCA infusion resulted in a 160% increase in PDH flux in control animals [79]. In mice the infusion of DCA significantly increased PDH flux by 145%, compared to control mice ($p < 0.001$). This validation proved that the technique was sensitive to alterations in PDH flux within the mouse heart and demonstrated the potential to use hyperpolarized MRS to investigate transgenic mouse models of cardiac diseases in the future.

Following validation of the technique, we characterized the metabolic profile of other commonly used control mice strains. C57BL/6, 129 SvEv and balb/c mice are inbred mice strains commonly used for metabolic studies and are breeding backgrounds for many transgenic mice lines [192,193]. In mouse models of heart disease, observed differences in

metabolic profiles are influenced by the background strain used to generate the mouse [194,195]. In the study by Gavaghan *et al* [195], nuclear magnetic resonance analysis of control strain urine found that there were differences in metabolite composition between healthy mouse strains. In our study several differences were observed in cardiac ^{13}C label incorporation into metabolite pools between these control strains. The 129 SvEv strain had elevated ^{13}C label incorporation into bicarbonate, suggesting a difference in PDH flux, compared to C57BL/6 and balb/c mice. ^{13}C label incorporation into lactate was reduced in the balb/c strain compared to C57BL/6, but not compared to 129 SvEv. These differences highlight an important requirement in selecting both the correct mouse background and appropriate control animals for metabolic studies.

Due to low SNR, the kinetic model, that is normally applied to [1-^{13}C] and [2-^{13}C]pyruvate, was not applied to mouse [2-^{13}C]pyruvate data. Instead 30 spectra, selected from the first spectrum that contained pyruvate, were summed and the relative peak areas of each metabolite were normalized to pyruvate. This provided a pyruvate to metabolite ratio, which has previously been used, before the implementation of the kinetic model used in this thesis [8]. Injection of [2-^{13}C]pyruvate into the control mouse, showed the same resonances as in the rat, which could be reproducibly measured in the fed state. The evaluation of [2-^{13}C]pyruvate as a hyperpolarized compound in mice, provided another technique for the assessment of *in vivo* cardiac metabolism.

The development of this technique demonstrated the potential of hyperpolarized MRS to investigate transgenic mouse models of cardiac diseases, e.g. the FH-KO mouse. The cardiac specific FH-KO mouse was generated to investigate the effect of fumarate on the heart during ischemia-reperfusion [197]. At 6 weeks of age the FH-KO mouse has previously been shown to have normal cardiac function and structure [197], this was confirmed in this study through the use of cine-MRI. No difference was seen between the controls and FH-KO at this timepoint.

This was interesting as the mice present with significantly elevated levels of intracellular fumarate, succinate and a non-functional TCA cycle, yet this does not alter resting cardiac function [197]. Pyruvate flux into the TCA cycle was also unaffected in the FH-KO at 6 weeks, as there was no change in PDH flux, or ^{13}C-label incorporation into citrate, acetylcarnitine or glutamate. This highlights an inability of increased fumarate to feedback to slow flux into the TCA at acetyl-CoA. To maintain normal TCA cycle flux, several pathways are likely to be upregulated, including increases in the activity of pyruvate carboxylase or altered processing of aspartate to maintain normal production of malate. These accessory pathways are able to produce malate, which can no longer be produced by TCA cycle in the FH-KO mouse. Computer simulated modelling of metabolism in FH-KO cells, suggest that there is an increased use of amino acids to supplement the TCA cycle [198,200].

One such mechanism for production of malate or oxaloacetate is through the deamination of aspartate, through the malate-aspartate shuttle, which normally functions to effectively transport NADH from the IMS into the mitochondria. It is likely that in the FH-KO mice this shuttle acts to generate malate and oxaloacetate, at the expense of aspartate to maintain normal cardiac energy metabolism. Our data on normal flux into the TCA cycle suggests that the cell is still able to maintain normal levels of oxaloacetate for conversion into citrate, through adaptive mechanisms [197,198,200].

At 12-14 weeks of age, FH-KO mice develop severe left ventricular dysfunction. This has been seen previously with increased heart mass and LV dilation [197]. Cine-MRI showed that the 12-14 week FH-KO mice had a significant elevation in LV mass, indicative of LV hypertrophy. They also displayed LV dilation, with a significant increase in end diastolic and end systolic lumen volume. Although ejection fraction and cardiac output appeared unaltered between the FH-KO and controls, this was due to highly variable ejection fractions within the FH-KO group and a low n number (not all mice could be scanned using cine-MRI). Some FH-

KO mice showed normal ejection fractions in the >60% range, whilst others had entered end stage heart failure with ejection fractions below ~10% and cardiac outputs of ~1 ml/min (compared to ~5 ml/min for other mice).

By this late time point there were significant metabolic differences between FH-KO and controls. Controls animals demonstrated a significant elevation in PDH flux between 6 weeks and 12-14 weeks. This increase was age related, with the 12-14 week PDH flux, being consistent with 129 SvEv control animals of a similar age and genetic background (see section on strain comparison). This age related increase in PDH flux was not observed in the 12-14 week FH-KO mice, with no significant difference compared to the 6 weeks FH-KO mice. This was also accompanied by a significant reduction in ^{13}C label incorporation into alanine in the FH-KO mice, compared to age matched controls. Whilst lactate was not significantly altered, there was a potential reduction in ^{13}C label incorporation in the 12-14 week FH-KO, compared to controls (P =0.09). Flux into the TCA cycle was unaltered between groups, but due to the reduction in PDH flux in the aged FH-KO mice, it is unclear whether TCA cycle flux was still normal or elevated in the FH-KO mice. As mentioned in chapter 3, flux into the TCA cycle, using [2-^{13}C]pyruvate, can be normalized to PDH flux. This accounts for any alterations in the availability of labelled [1-^{13}C]acetyl-CoA, which might be altered due to changes to PDH flux/activity. Unfortunately as the kinetic model could not be applied to [2-^{13}C]pyruvate mouse data, this normalization could not be performed.

5.5.1 Limitations

The major limitation within the FH-KO study was an increased lumen volume at the 12-14 week timepoint, it is unclear whether changes in metabolism were exacerbated by this factor. The majority of the pyruvate signal observed in the hyperpolarized study originates from the heart lumen, this can be seen in imaging studies in the pig heart [10]. This means that a

larger lumen, could result in a larger pyruvate signal within the spectrum. The kinetic model uses the pyruvate input signal to model the rate of ^{13}C label flux from pyruvate into its metabolites. The peak areas of the metabolites would be smaller in comparison to pyruvate in the FH-KO mice, when compared to control. The overall result being, an under-estimation of ^{13}C label incorporation into metabolites. It is possible that this has occurred in the 12-14 week FH-KO mice.

In conclusion, a mouse hyperpolarized DNP protocol has been successfully developed to understand *in vivo* alterations within the diseased mouse heart. The use of fasting and DCA, demonstrated the sensitivity of the technique to detect alterations in PDH activity. Finally the use of the FH-KO mouse has shown the ability to monitor the metabolic phenotype of a cardiac specific transgenic mouse at two different time points. This offers a significant advantage over existing techniques that require invasive *in vitro* assessment. This technique enables reduced animal numbers and decreased biological variability. It has also shown that both [1-^{13}C] and [2-^{13}C]pyruvate can be used to monitor the *in vivo* metabolic phenotype of mice.

Chapter 6

Assessment of In Vivo Cardiac Metabolism in Mouse Models of β-Oxidation Modulation

6.1 Overview

Alterations in β-oxidation underlie many conditions of the heart. Following the development of the mouse cardiac DNP techniques described in the previous chapter, the work in this chapter aims to demonstrate the information that can be obtained through application in three mouse models of β-oxidation defects.

Many childhood diseases related to β-oxidation defects have been linked to altered function in the acyl-CoA dehydrogenases, the enzymes responsible for the first step in β-oxidation. The genetic knockout of the long chain acyl-CoA dehydrogenase (LCAD) enzyme in mice has provided a model in which to study the etiology of such diseases. In the work described in the first part of this chapter, application of hyperpolarized MRS in the fed LCAD-KO mouse showed no difference in PDH flux when compared to controls. However, the LCAD-KO mouse did display a stunted PDH response to fasting when compared with the reduction in PDH flux observed in fasted, control animals.

The transcription factor PPARα is, in part, responsible for the upregulation of β-oxidation genes during periods of elevated plasma free fatty acid levels, such as occurs during fasting. The PPARα knockout mouse was therefore developed to allow further understanding of the role of PPARα in the control of physiological and pathological changes in metabolic substrate selection. In the second part of this chapter, the response of the PPARα-KO mouse to fasting was investigated in both young (3 months of age) and aged (12-14 months of age) PPARα

knockout mice. Interestingly, the knockout of PPARα was seen to have an age related cardiac metabolic phenotype. Fasted 3 month old PPARα-KO mice did not show any difference in PDH flux when compared to controls. There was, however, a significant reduction in flux from pyruvate into lactate, which may indicate an increase in the reverse reaction (i.e. oxidation of lactate) in the young fasted PPARα-KO heart. When the PPARα-KO mice were aged (12-14 months) they showed significant alterations in PDH flux. During both the fed and fasted state, there were significant elevations in PDH flux compared to controls. Further, whilst there was still a fasting induced decrease in PDH flux, when compared to fed PPARα-KO mice, the response was stunted, in a similar manner to that observed in the fasted LCAD-KO mouse.

In the final part of this chapter a mouse model of type 1 diabetes was used to assess the metabolic alterations that occur in the diabetic heart following treatment. The K_{ATP} mutant mouse, has a cre inducible, pancreatic specific gain-of-function in the K_{ATP} channel. Upon induction of this mutation, the channel remains constantly open, preventing insulin release from pancreatic β-cells, inducing type 1 diabetes. As expected in the diabetic heart, a significant reduction in cardiac PDH flux was observed in the K_{ATP} channel mutant mice. These mice displayed severely impaired glucose handling, a significant elevation in fasted plasma glucose concentrations and hypoinsulinemia. When K_{ATP} channel mutant mice were treated with the sulfonylurea, glibenciamide there was a significant reduction in fasted plasma glucose levels and an increase in insulin levels. However, glucose tolerance was still impaired and PDH flux was still significantly reduced. These data, in combination with results from western blotting and real-time PCR techniques, appear to demonstrate that the treated animals may be displaying a type 2 diabetic phenotype.

6.2 Background

Defects in β-oxidation have been shown in many diseases of the heart [3]. Decreases in β-oxidation have been reported in myocardial infarction and cardiac pressure overload hypertrophy [27,48,201], whilst increased β-oxidation has also been observed in diabetes, where PPARα may play a role in the pathogenesis. The aim of the work in this chapter was to characterize *in vivo* substrate alterations in three different mouse models of β-oxidation disorders. The results should help to provide a greater understanding of the influences of such alterations. PPARα- and LCAD-KO mice have proven to be invaluable in helping to develop our understanding of the pathogenesis of a group of inherited childhood β-oxidation disorders, such as very long-chain acyl-CoA dehydrogenase deficiency (VLCADD) [16,185]. Both models represent deficits in β-oxidation, but from two different control points. One represents a single enzyme deletion and the other a knockout of a transcription factor, which controls multiple enzymes in the β-oxidation pathway. In addition to the LCAD- and PPARα-KO mouse models, a model of type 1 diabetes generated through a gain in function mutation of the pancreatic K_{ATP} channel was also studied.

6.2.1 The role of the knockout of LCAD in disorders of β-oxidation

As shown in Figure 6.1, the acyl-CoA dehydrogenases (ACDs) are responsible for the initial oxidation of fatty acyl-CoA and the reduction of FAD to $FADH_2$ in the first step of β-oxidation. There are 4 main ACD enzymes, short chain acyl-CoA dehydrogenase (SCAD), medium chain acyl-CoA dehydrogenase (MCAD), long chain acyl-CoA dehydrogenase (LCAD) and very-long chain acyl-CoA dehydrogenase (VLCAD). Each differs in its specificity to the chain length of the fatty acyl-CoAs upon which it acts.

Mutations in the ACDs have been associated with inherited childhood β-oxidation disorders such as VLCADD [185]. Following a period of fasting a young patient with VLCADD can

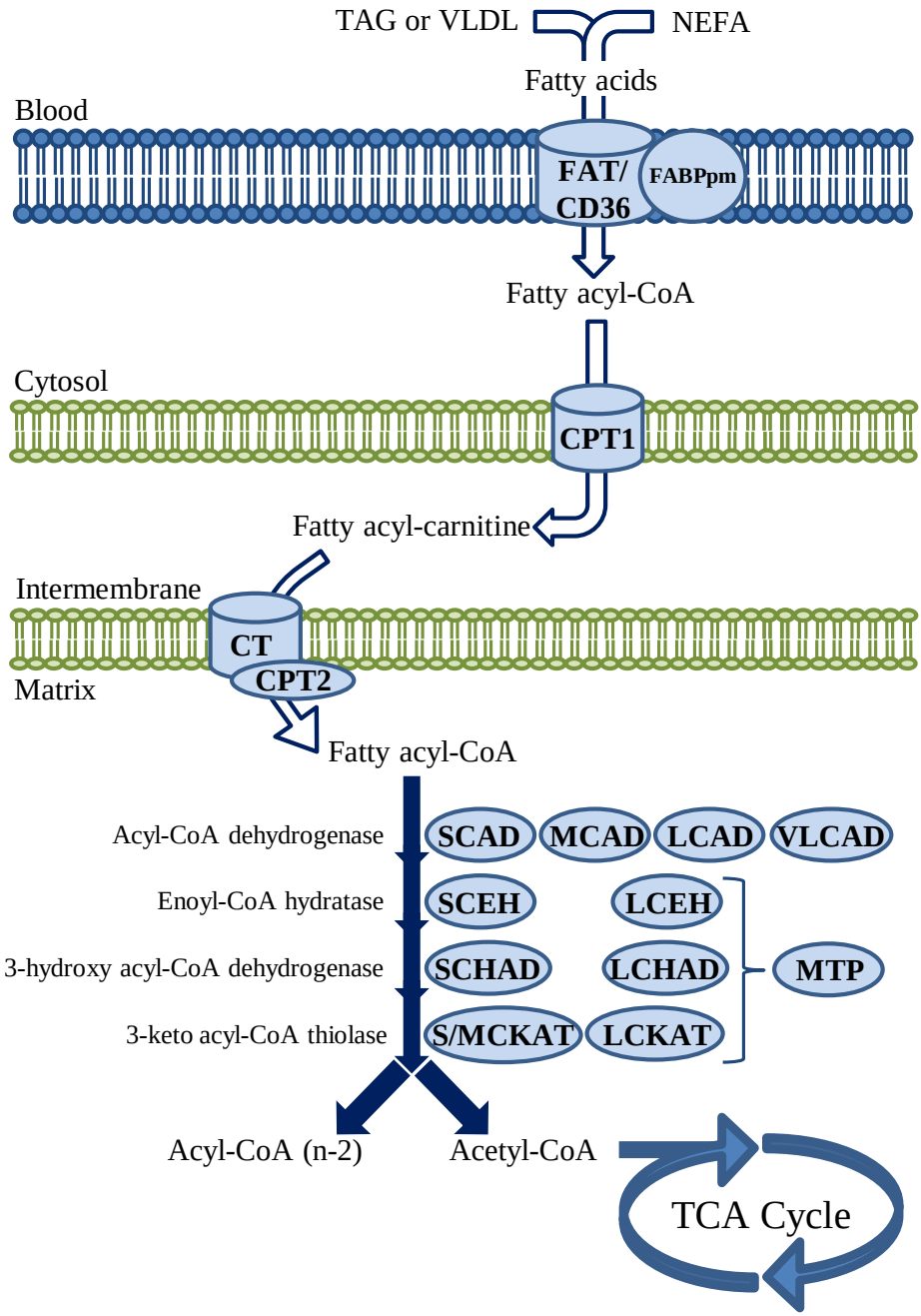

Figure 6.1 – β-oxidation in the rat heart – As described previously in chapter 1, fatty acids are transported into the cell and then into the mitochondria as fatty acyl-CoA molecules. These then enter β-oxidation, where depending on the chain length a specific acyl-CoA dehydrogenase will act upon the acyl-CoA, before it is then passed to the mitochondrial trifunctional protein, which contains an enoyl-CoA hydratase, 3-hydroxy acyl-CoA dehydrogenase and 3-keto acyl-CoA thiolase. For each pass through β-oxidation an acetyl-CoA molecule is produced, which is passed on to the TCA cycle along with a acyl-CoA molecule, two carbon shorter, which will re-enter β-oxidation.

SCAD-Short chain acyl-CoA dehydrogenase, MCAD-Medium chain acyl-CoA dehydrogenase, LCAD-Long chain acyl-CoA dehydrogenase, VLCAD-Very-long chain acyl-CoA dehydrogenase, MTP-Mitochondrial trifunctional protein, which can be made up of the following enzymes: SCEH-Short chain Enoyl-CoA hydratase, LCEH-Long chain Enoyl-CoA hydratase, SCHAD-Short chain 3-hydroxy acyl-CoA dehydrogenase, LCHAD-Long chain 3-hydroxy acyl-CoA dehydrogenase, S/MCKAT-Short/medium chain 3-keto acyl-CoA thiolase, LCKAT-Long chain 3-keto acyl-CoA thiolase. [205]

develop a severe phenotype of hypoketosis and hypoglycaemia, which can be potentially fatal [202]. Several mouse models have been generated in an attempt to better understand the metabolic consequences of VLCADD. The knockout of VLCAD in mice, leads to a relatively mild phenotype, even following periods of fasting, and as such, VLCAD-KO models do not correlate closely to the human VLCADD condition [202]. There is a level of overlap in the substrate specificity in the ACD enzymes (Figure 6.2). In rodents this leads to a level of redundancy in the oxidation of LCFAs. The overlap of LCAD and VLCAD might explain the relatively mild phenotype observed in the VLCAD-KO mice, where LCAD would compensate for the loss of VLCAD. The same level of overlap is not found in humans, where although all ACD genes are present, expression of LCAD in the heart appears very low [202–205]. Although not as severe as the human condition, the knockout of LCAD in mice does closely mimic VLCADD [181,202]. Where fasted LCAD-KO mice display severe cardiac metabolic and functional abnormalities [16]. The LCAD-KO mouse therefore provides a suitable animal model to help our understanding of this human disease.

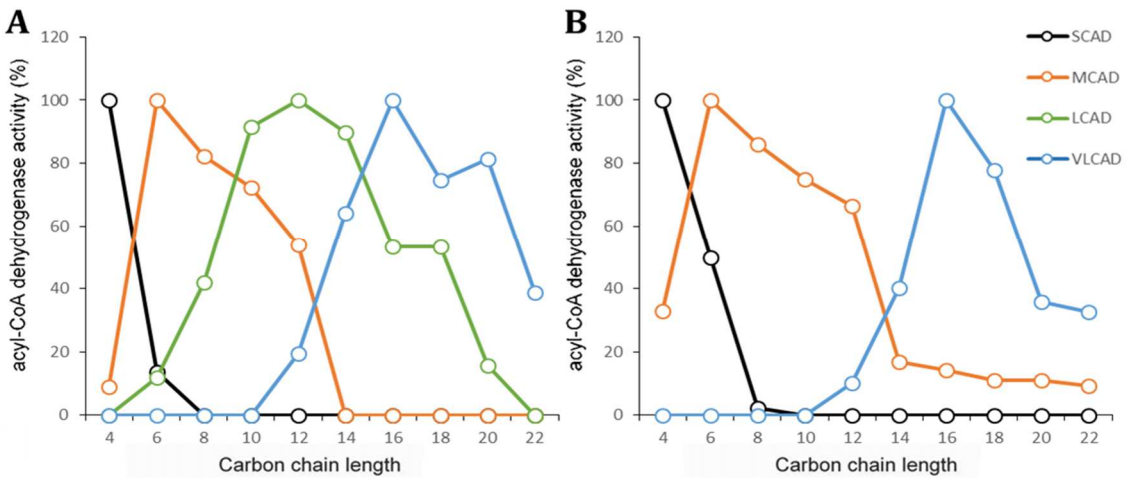

Figure 6.2 – Enzyme complex activity of acyl-CoA dehydrogenases (ACD) in the rat liver and human heart – A) Enzyme activity of the ACDs within the rat liver, a similar profile is found within the rat heart [203]. Data were modified from Modre-Osprian *et al* 2009 [204] and were normalized to 100% of total activity, for each isoform. B) The enzyme profile of ACDs within the human heart, unlike the rat, LCAD is not present in the heart. Figure modified from Wanders *et al* 2010 [205].

VLCADD in patients, can be detected using mass spectrometry or NMR analysis of the lipid composition of fasted blood plasma [206]. Plasma analysis of patients with VLCAD deficiency shows an excess of C14:1, C16:0 and C18:1 LCFAs [16,202]. Although β-oxidation of

the LCFAs isn't completely halted because of the overlap of ACDs, there is still a reduction in the processing of LCFAs, causing the accumulation of fatty acids longer than C14 [202]. This fasted phenotype is also observed in LCAD-KO mice, using *in vivo* ^{1}H MRS, an accumulation of C14:1 fatty acids has been detected in the hearts of these mice [16]. The livers of fasted LCAD-KO mice also show a significant increase in lipid accumulation similar to the heart and plasma, with increased C18:1 and C16:1 LCFAs [202]. Bakermans *et al* (2011) [16] have shown that due to an accumulation of cardiac LCFAs, there is potentially a phenotype of lipotoxicity in the hearts of fasted LCAD-KO mice. This lipotoxicity in fasted LCAD-KO mice, presents as an increase in cardiac mass and diastolic dysfunction [16]. The diastolic dysfunction manifested as a significant reduction in ejection fraction and diastolic filling rate, following fasting.

The aim of using the mouse DNP technique in this model was to assess the extent to which a substrate switch occurs in both the fed and fasted state. The DNP technique offers a unique opportunity to characterise *in vivo* metabolic alterations in the same mice in different physiological states.

6.2.2 Cardiac metabolism in the PPARα-KO mouse

During fasting, plasma free fatty acids increase and stimulate their own catabolism through increased β-oxidation. This is mediated in part by the activation of the nuclear response elements peroxisome proliferator-activated receptors (PPARs), which regulate the expression of a number of genes responsible for fatty acid and carbohydrate metabolism. There are three PPAR isoforms: PPARα, PPARβ/δ and PPARγ. PPARα has a high binding affinity for fatty acids and functions to transcriptionally regulate the expression of a range of β-oxidation genes and to regulate carbohydrate metabolism (Figure 6.3) [36,39,43,156]. During times of increased fatty acid availability, such as during fasting, PPARα controls expression of several ACDs, thereby increasing β-oxidation. The PPARα knockout mouse was previously

generated to improve our understanding of the role that PPARα plays in the metabolic switches that underlie many conditions of the heart, i.e. myocardial infarction [207]. Further evidence suggests that PPARα is also important in regulating increased β-oxidation in conditions such as diabetes.

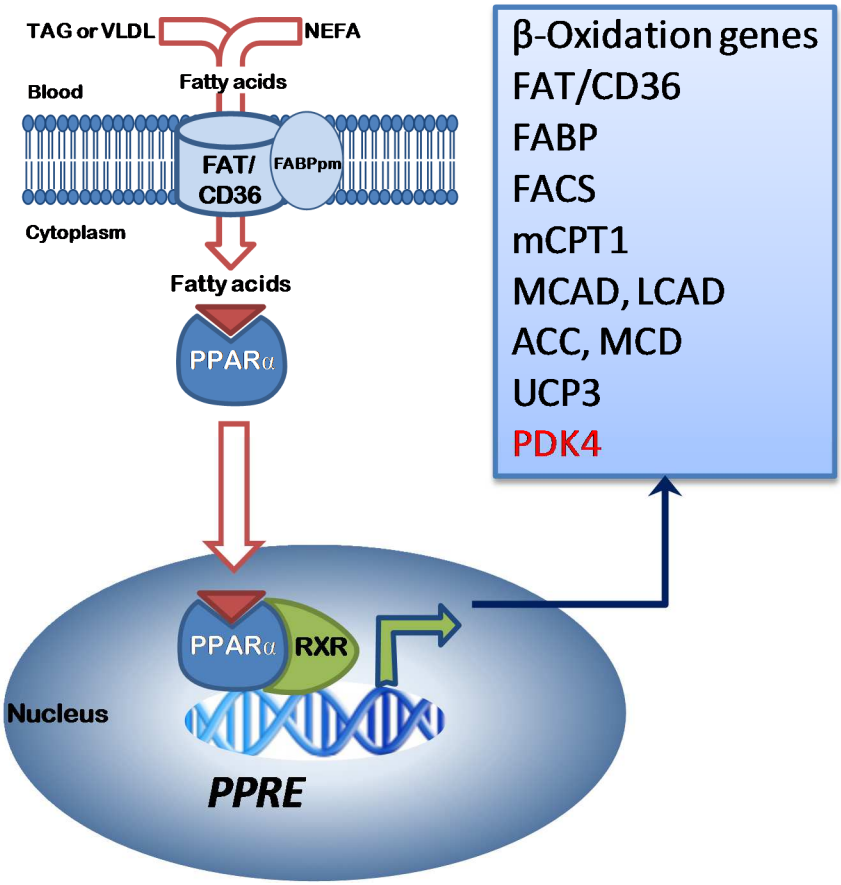

Figure 6.3 – The action of PPARα on gene expression – Free fatty acids in the blood are absorbed into the cells, and are one of the substrates for PPARα. Upon binding of fatty acids, the fatty acid/PPARα complex translocates to the nucleus, along with the retinal-X-receptor and leads to the transcription of genes under the control of the PPARα-response elements. These include several transporters and enzymes involved in β-oxidation and an inhibitor of PDH, PDK4.

Although PPARα-KO mice do not display an overt phenotype in the fed state, evidence suggests that they still display several hepatic and cardiac phenotypes, particularly during times of stress [185]. Fed PPARα-KO mice have reduced β-oxidation genes, as demonstrated by reduced VLCAD, MCAD, SCAD and CPT2 protein expression in the heart [208]. In contrast, in the liver, whilst LCAD and VLCAD levels are also reduced, MCAD, SCAD and CPT2 levels are the

same as in controls [209]. *Ex vivo* working heart models show that this leads to an increase in cardiac glucose oxidation within PPARα-KO mice [36]. However, these hearts fail to respond normally to an increase in preload, which mimics the pressure increase generated during exercise [36]. Cardiac efficiency has also been shown to decrease, due to an increased MVO_2, indicating an underlying energy defect in these mice that is only seen during times of stress. This is accompanied by a modest increase in myocardial fibrosis, which could compromise cardiac efficiency [208]. Possible myocardial damage has also been highlighted by an increased release of LDH in the stressed PPARα-KO mouse, indicating potential loss of membrane integrity [36].

However, similar to LCAD-KO mice, fasted PPARα-KO mice display hypoketosis, hypoglycaemia, hyperlipidaemia, and an inability to upregulate β-oxidation and decrease glycolysis [36,39,185,186,210]. The livers and hearts of these mice are characterized by a severe depletion of glycogen stores and a reduction in intracellular glucose concentrations [156,186,211,212]. There is also increased cardiac and hepatic lipid accumulation, leading to possible lipotoxicity. The livers of fasted PPARα-KO mice (at 4 months of age) show increases in hepatic gluconeogenesis, which is not suppressed by insulin or after refeeding [210]. This however, is not driven by an increased usage of lactate, where a significant reduction in lactate-derived glucose has been seen in the PPARα-KO mice [156]. There is evidence that the substrate for hepatic gluconeogenesis in the PPARα-KO mice is glycerol [156,210]. The fasted PPARα-KO mouse has an 80% increase in glycerol production and 50% of the hepatic production of glucose, is derived from glycerol, compared to normal levels of 10% [210]. This increase in glycerol production and usage is likely due to increased adipocyte lipolysis and circulating LPL levels, leading to the well characterized increase in plasma free fatty acid levels in the PPARα-KO mouse [210].

Fed PPARα-KO mice also appear to display hepatic insulin resistance, as insulin is unable to regulate gluconeogenesis even during the fed state [210,213]. It is believed that the hypoglycaemia in fasted PPARα-KO mice, is due to the increased usage of glucose (in glucose oxidation) [214]. Insulin resistance is further highlighted by a stunted increase in PDK4 expression in the liver of fasted PPARα-KO mice [212]. This stunted fasting response of PDK4 expression, is also seen in the hearts of fasted PPARα-KO mice [186]. In healthy mice, increased PDK4 expression, leads to inhibition of PDH and a decrease in glucose oxidation. This thus "spares" pyruvate for oxaloacetate production and gluconeogenesis [43,212].

After long term starvation (48 hours), there was shown to be a significant reduction in ATP in PPARα-KO mice from 240±20 to 160±40 μmol.100 g.w.w^{-1}, this was not seen in control mice, where ATP levels were maintained [208]. There was also a significant increase in myocardial Ca^{2+} following starvation, which would affect contractility and PDH activity [208]. Increases in Ca^{2+} have been shown to activate PDP, which dephosphorylates PDH, thereby increasing glucose oxidation in the PPARα-KO mouse [30,208]. This evidence points to a switch in the PPARα-KO mouse away from β-oxidation, towards glycolysis and increased glucose oxidation.

Age also appears to play an important role in the phenotype of PPARα-KO mice. Older mice (12-13 months of age) show an increase in myocardial creatine and a decrease in lactate, alanine and the ketone body, β-hydroxybutyrate. This would suggest increased flux through PDH and a more efficient use of glucose, through glucose oxidation and away from anaerobic glycolysis [156]. This would also suggest a mild hypoketosis within the fed state, evidence by the reduced ketone bodies.

These older mice also show increased lipid peroxidation in the livers, compared to controls, indicating a decrease in cell integrity [208,215]. There is also evidence of a significant

increase in myocardial fibrosis compared to the younger mice and aged matched controls [208]. The aim of the work described in this chapter was to use DNP to increase our understanding of the *in vivo* metabolic alterations that occur in the PPARα-KO mouse, during times of stress (fasting) and with age.

6.2.3 The pancreatic specific potassium ATP channel gain-of-function mouse model

In contrast to VLCADD patients during periods of fasting, type 1 diabetics are hyperglycaemic, hyperlipidaemic and hyperketotic. Type 1 diabetes is characterized by an autoimmune destruction of pancreatic β cells, which leads to hypoinsulinemia. This means that postprandial increases in blood glucose concentrations are not suppressed by insulin, resulting in hyperglycaemia. Blood glucose concentrations can exceed 20 mmol/L and glucose is also found in the urine.

Low levels of insulin, lead to severe alterations in plasma metabolites, and hepatic and cardiac metabolism. Low insulin levels lead to an increase in lipolysis within adipocytes, causing an increase in plasma free fatty acids. Due to low insulin stimulation there is also a significant reduction in cell surface presentation of GLUT4 and therefore a reduction in glucose uptake. There is also a reduction in glycolysis due to inhibition of phosphofructokinase, from increased β-oxidation derived citrate and NADH [216,217]. The PDH activator, PDP is stimulated by insulin, and during diabetes there is a reduction in activity resulting in a reduced PDH activity and glucose oxidation [35].

Increased plasma free fatty acid levels lead to an increase in fatty acid uptake and β-oxidation. This increased fatty acid uptake induces PPARα expression, which further increases β-oxidation [207]. As already discussed PPARα activation leads to increased expression of β-oxidation genes, along with PDK4 [37]. PDK4 expression, decreases PDH

activity and reduces glucose oxidation [29,218]. Increased β-oxidation also stimulates PDK2 activity, due to an increase in acetyl-CoA and NADH. The overall effect is a decrease in PDH activity and glucose oxidation in the diabetic heart.

To study the metabolic alterations that follow the development of diabetes, we used a transgenic inducible model of type 1 diabetes [18,219]. This model used a cre inducible pancreatic specific potassium ATP (K_{ATP}) channel overexpression model. The K_{ATP} channel is a voltage gated channel, which is sensitive to inhibition by increased concentrations of ATP. The K_{ATP} channel effectively "senses" blood glucose concentrations allowing pancreatic β cells to control the release of insulin. This is summarized in Figure 6.4, adapted from Ashcroft 2005 [220]. Briefly, during low glucose levels, the K_{ATP} channel is opened, pumping K^+ out of the cell, hyperpolarising the membrane, and preventing Ca^{2+} influx and insulin release. Postprandially, glucose enters the β cells, is metabolised and the ATP concentration increases, closing the K_{ATP} channels. This leads to depolarization of the membrane, increased Ca^{2+} influx and the mobilization of insulin-containing vesicles. The K_{ATP} mutant is a gain-of-function in the Kir6.2 subunit, which forces the channel to constantly remain open, making the β-cells insensitive to glucose concentrations and leading to failure of insulin release [18]. The benefit of using this model is that mice can be scanned before the induction of diabetes and again after the development of type 1 diabetes using non-invasive techniques such as DNP and MRI.

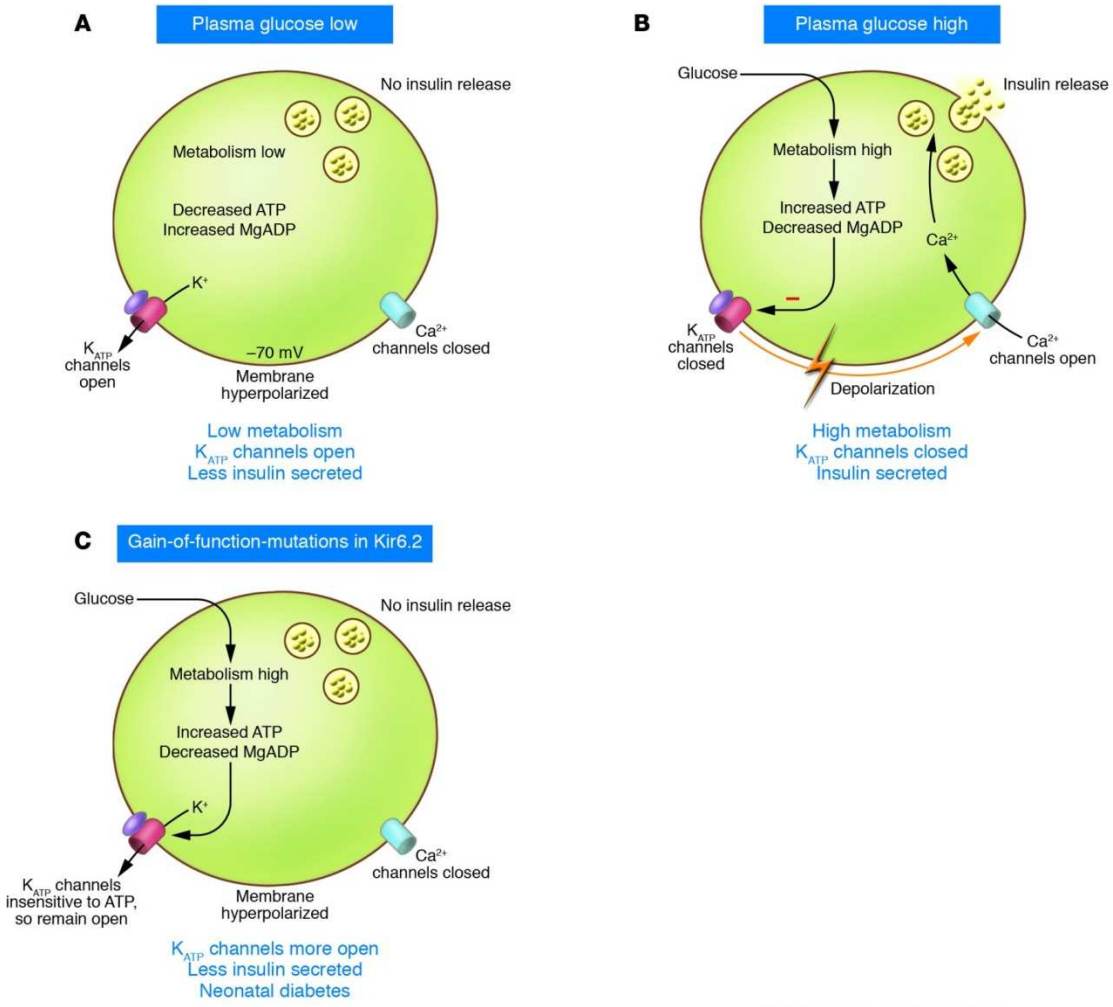

Figure 6.4 – The K_{ATP} channel and its function in insulin release in pancreatic β cells – A) Low glucose levels lead to an open K_{ATP} channel and no release of insulin. B) Post meal, when glucose rises, the K_{ATP} channel is shut and insulin is released into the blood. C) A gain-of-function in the Kir6.2 subunit leads to the channel being insensitive to ATP and no insulin release. Ashcroft 2005 [220]. Permission to reproduce this figure has been granted by The Journal of Clinical Investigation.

This gain-of-function in the K_{ATP} channel is also susceptible to treatment using sulfonylureas. These drugs are able to bind to the sulfonylurea receptor (SUR) subunit of the K_{ATP} channel. This subunit is responsible for sensing the increase in ATP, as it has nucleotide-binding domains on the cytoplasmic side of the membrane, which lead to the closure of the K_{ATP} channel [221–224]. Treatment with the sulfonylurea, glibenclimide, leads to closure of the K_{ATP} channel, depolarizing the membrane and stimulating the release of insulin [222]. This should reverse the metabolic abnormalities associated with this model of type 1 diabetes.

The aim of the work in this chapter was therefore to study these metabolic alterations before and after initiation of type 1 diabetes and also during treatment.

6.2.4 Aim

As these three models demonstrate, there is clearly a need to understand the *in vivo* metabolic alterations that underlie many conditions of β-oxidation dysfunction. Therefore, the overall aim of the work in this chapter was to offer some new insights into the importance of alterations to β-oxidation in the diseased heart.

6.3 Methods

6.3.1 *Animal handling*

Eight LCAD-KO mice (3 months old) and seven non-transgenic (NTg) littermate controls (3 months old) were obtained from Dr Jeanine J. Prompers' laboratory, TUE, Eindhoven, Netherlands [16]. Five (3 month old) and five (12-14 month old) PPARα-KO mice, and six (3 month old) and five (12-14 month old) NTg controls, were bred in-house at the University of Oxford [207]. Twenty three (2 ½ month old) ER-ROSA K_{ATP} channel mutant mice were obtained from Prof. F. Ashcroft, University of Oxford [225].

Animal handling was carried out as set out in section 2.1. Both the LCAD-KO and PPARα-KO mice were scanned in both the fed state and following an overnight fast of approximately 19 hours. Seventeen K_{ATP} mice were scanned at baseline, then given an injection of tamoxifen, which lead to the development of diabetes in these mice [18]. The following day mice were randomly assigned to either a treated or an untreated group. The treated group were subcutaneously implanted with a glibenclamide 21-day release pellet. The untreated group were implanted with a placebo pellet. These mice were then scanned eleven days later.

6.3.2 *Hyperpolarized ^{13}C MRS protocol*

All animals received a [1-^{13}C]pyruvate scan, the hyperpolarized protocol and pyruvate dissolution were as set out in sections 2.2.3 and 2.2.1.

6.3.3 *MRS data analysis*

MRS data analysis was carried out as set out in section 2.2.4.

6.3.4 *Cine magnetic resonance imaging*

On a separate day to the hyperpolarized scan, cardiac structure and function were assessed in the K_{ATP} mice as described in section 2.2.9.

6.3.5 *Intraperitoneal glucose tolerance test*

An intraperitoneal glucose tolerance test (IPGTT) was used to analyse the systemic response to a glucose load in the K_{ATP} mice, both at baseline and 10 days after tomoxifen induction of diabetes. After an overnight fast, mice were injected IP with 2 g/kg body weight of glucose [226]. Blood plasma was taken via the tail vein at 0 (pre-glucose injection), 30, 60, and 120 min post injection. Glucose concentrations were assessed using a blood glucose meter. This test was performed by a trained technician in the University animal facility.

6.3.6 *Tissue and blood collection*

All animals were sacrificed at least one day after their final DNP examination as described in section 2.2.11. Blood from all mice was collected immediately in heparinised tubes, after sacrifice and spun down in a centrifuge to collect the plasma (375 x g for 10 min at 4°C). To provide control tissue and plasma for the K_{ATP} mice, six ER-ROSA mice, from the same breeding pairs as the K_{ATP} mutant mice, were also sacrificed. This tissue and plasma was subsequently used for western blotting and blood insulin analysis comparison.

6.3.7 *Insulin ELISAs*

10µl blood plasma samples were used, in triplicate, for the insulin ELISA (Mercodia, Sweden). The samples were pipetted into wells containing anti-insulin antibodies. 100µl of enzyme-conjugate was added and the samples were left to incubate for 2 hours. During incubation insulin in the sample reacts with the peroxidase-conjugated anti-insulin

antibodies and the anti-insulin antibodies bound to the microplate wells. A washing step after the incubation removed the unbound enzyme labelled antibody. 200µl 3,3',5,5'-tetramethylbenzidine (substrate TMB) was then added to detect the bound conjugate and the reaction was stopped by adding acid to give a colorimetric endpoint that was read spectrophotometrically (450nm). Results were analysed using a standard curve of known insulin concentrations.

6.3.8 Western blotting

Protein expression levels of key metabolic pathways were assessed in total heart homogenates using SDS-PAGE western blotting (section 2.4). Proteins, primary and secondary antibodies are set out in Table 6.1. All samples were run in duplicate on separate gels to confirm results.

Table 6.1 – Antibodies used to probe key metabolic pathways in the K_{ATP} mutant mouse heart.

Protein	*Antibody*	*Dilution*	*Company*	*Secondary*	*Dilution*
PDK 1	Rabbit anti-PDK1	1:2000	Cell Signalling Technology	Goat anti-rabbit	1:3000
PDK 2	Rabbit anti-PDK2	1:10000	Abgent	Goat anti-rabbit	1:3000
PDK 4	Rabbit anti-PDK4	1:500	Abgent	Goat anti-rabbit	1:2000
PDP 1	Mouse anti-PDP1	1:1000	Abcam	Goat anti-mouse	1:2000
PDP 2	Mouse anti-PDP2	1:1000	Abcam	Goat anti-mouse	1:2000

6.3.9 Realtime PCR analysis

Heart tissue was lysed and total RNA purification was obtained using the RNeasy Fibrous Tissue Mini Kit (Qiagen, West Sussex, UK). RNA concentration for each sample was calculated using a nano-drop. Total RNA was converted to cDNA for stable usage and storage. 10µl reaction samples were prepared in duplicate for use in an Applied Biosystems StepOnePlus Real-Time PCR System (AB International, CA) [227] containing the appropriate forward and

reverse primers for either β-actin or PPARα, SYBR green PCR Master Mix (AB International, CA), cDNA and nuclease free water. Data analysis was performed using the ΔΔCT method, normalising to the housekeeping gene of β-actin.

6.3.10 Statistics

All results are expressed as mean ± SEM. For the LCAD-KO and PPARα-KO mouse experiments, significant differences between mean values were determined by a two-way ANOVA followed by Bonferroni's multiple comparison post hoc test. For the K_{ATP} mutant mouse, a significant difference between mean values was determined by a one-way ANOVA followed by Bonferroni's multiple comparison post hoc test. Differences between groups were considered significant if $p < 0.05$.

6.4 Results

6.4.1 *Alterations in metabolism in the fasted LCAD-KO mouse*

During the fed state, the knockout of LCAD did not lead to any alteration in PDH flux (Figure 6.5). However, following an overnight fast (~19 hours) there was a significant reduction in PDH flux in both the controls and LCAD-KO mice. The reduction in PDH flux in the LCAD-KO mice was not as severe as in fasted controls and PDH was therefore significantly higher than in fasted controls. ^{13}C label incorporation into lactate and alanine

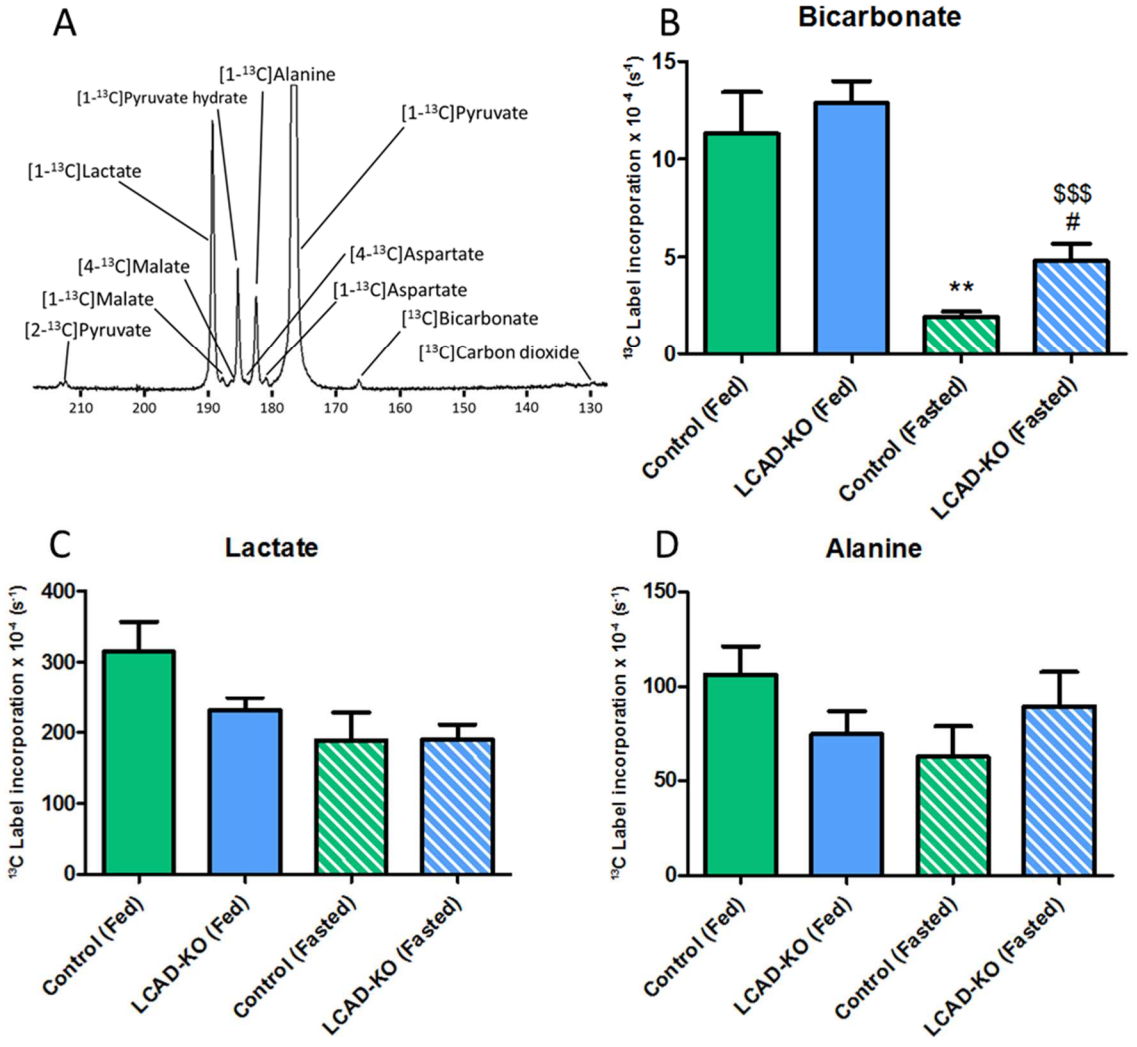

Figure 6.5 – Fasted LCAD-KO mice have altered PDH flux – A) An example summed spectra from a fasted LCAD-KO mouse. Extra peaks are visible in the fasted LCAD-KO mouse, compared to controls. B) ^{13}C Label incorporation into bicarbonate was significantly decreased due to fasting in both controls and LCAD-KO mice. However, this reduction was stunted in the LCAD-KO mouse. C) Flux into lactate was not altered between groups. D) Alanine flux was unchanged between groups. ** $p < 0.01$ vs. control fed, $$$ $p < 0.001$ vs. LCAD-KO fed, # $p < 0.05$.

was not different between groups in either the fed or fasted state. Interestingly, additional resonances were detected in the fasted LCAD-KO mice (Figure 6.5 A), these peaks shared similar frequencies to those detected by Merritt and colleagues in the liver [228], being aspartate ([1-^{13}C]aspartate 175.1 ppm and [4-^{13}C]aspartate 178.2) and malate ([1-^{13}C]malate 181.5 ppm and [4-^{13}C]malate 180.2). These peaks were only detected in the LCAD-KO fasted mice and not in the controls or fed LCAD-KO mice. Merritt *et al* proposed that these resonances were derived from anaplerotic processing of [1-^{13}C]pyruvate through pyruvate carboxylase. The linewidth of these peaks, however, was too broad to allow for accurate quantification.

6.4.2 A PPARα-independent response to fasting

Three month old PPARα-KO mice were assessed for alterations in metabolism during the fed and fasted state (Figure 6.6). During the fed state there were no differences in PDH flux or flux into lactate and alanine between groups. To test the ability of the PPARα-KO mice to respond to a metabolic stress, PPARα-KO and controls were fasted overnight for a minimum of 19 hours. Upon fasting a significant decrease in PDH flux was observed in both groups, but no difference was seen between controls and KO mice. Interestingly, there was a significant reduction in flux into lactate within the fasted PPARα-KO mice compared to fed PPARα-KO mice ($p < 0.05$). This decrease was not significantly different to fasted control flux into lactate, meaning that it is possible that this was simply a response to fasting, independent of PPARα. No significant difference was seen in flux into alanine between groups.

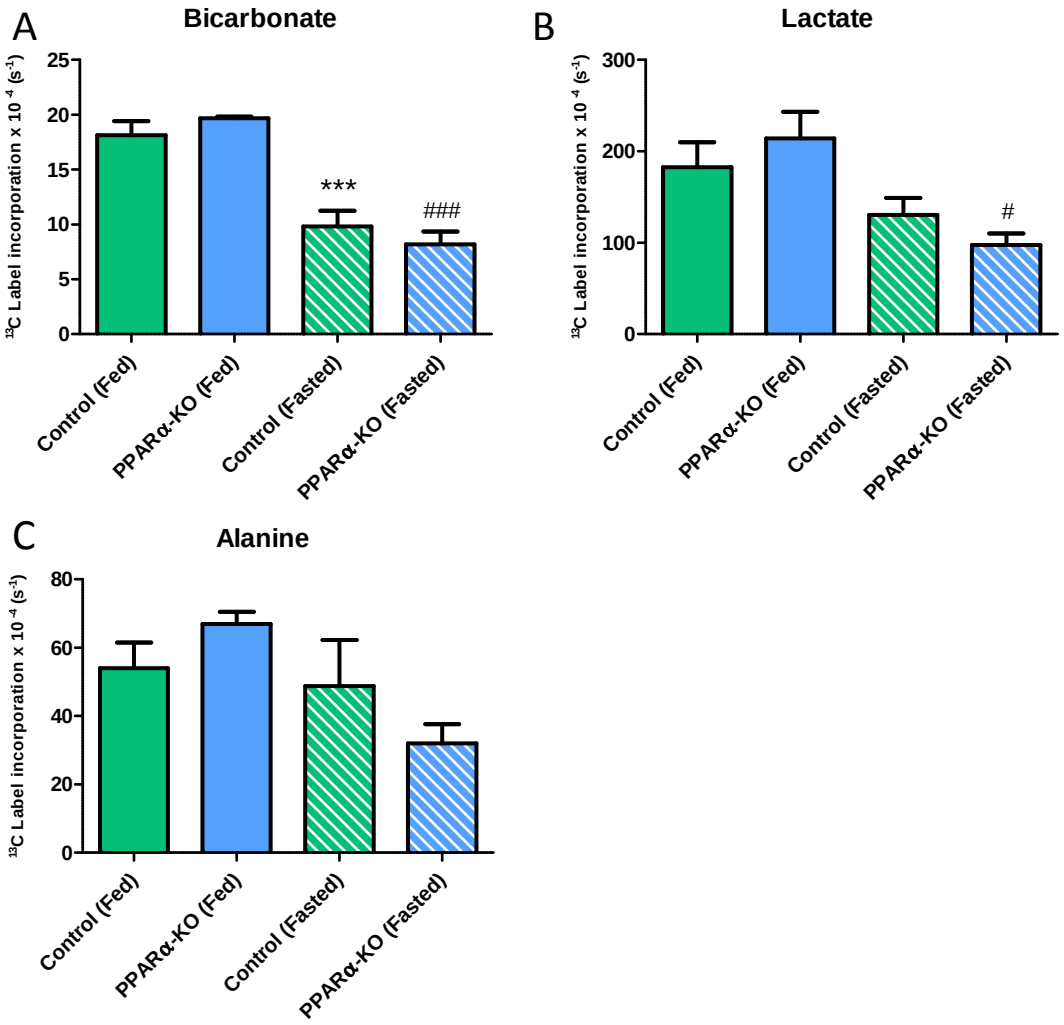

Figure 6.6 – Young PPARα-KO mice display a normal response to fasting – A) In the fed state there was no change in ^{13}C label incorporation into bicarbonate between groups. During the fasted state, control and PPARα-KO mice displayed a significant decrease in ^{13}C label incorporation compared to fed mice, but no difference was seen between groups. B) ^{13}C label incorporation into lactate was unaltered between fed groups, but significantly reduced in the fasted PPARα-KO mice, compared to the fed PPARα-KO mice. C) ^{13}C label incorporation into alanine was unaltered between groups. *** $p < 0.001$ and compared to fed controls, # $p < 0.05$ and ###$p < 0.001$ compared to PPARα-KO fed.

6.4.3 The effects of age on the metabolic state of PPARα-KO mice

Twelve-fourteen month old PPARα-KO mice showed a significant 41% increase in PDH flux compared to controls (Figure 6.7, control 17 ± 3 x10^{-4} s^{-1}, PPARα-KO 24 ± 1 x10^{-4} s^{-1}, $p < 0.05$). Flux into lactate and alanine were unchanged between groups. During an overnight fast, whilst the controls lost on average 3.4 ± 0.5 g (~9% of fed body weight), the PPARα-KO mice only lost 2.0 ± 0.3 g (~6%), which was significantly less than controls ($p < 0.05$). As expected, fasting in the controls resulted in a significant 56% reduction in ^{13}C label

incorporation into bicarbonate (8 ± 1 x10^{-4} s^{-1}, $p < 0.05$), whilst lactate and alanine were unchanged. Interestingly, there was also a highly significant 45% decrease in ^{13}C label incorporation into bicarbonate in the fasted PPARα-KO mice (14 ± 1 x10^{-4} s^{-1}, $p < 0.01$). However this was still significantly elevated when compared to fasted controls animals (76%, $p < 0.05$). Flux into lactate and alanine was unchanged between groups.

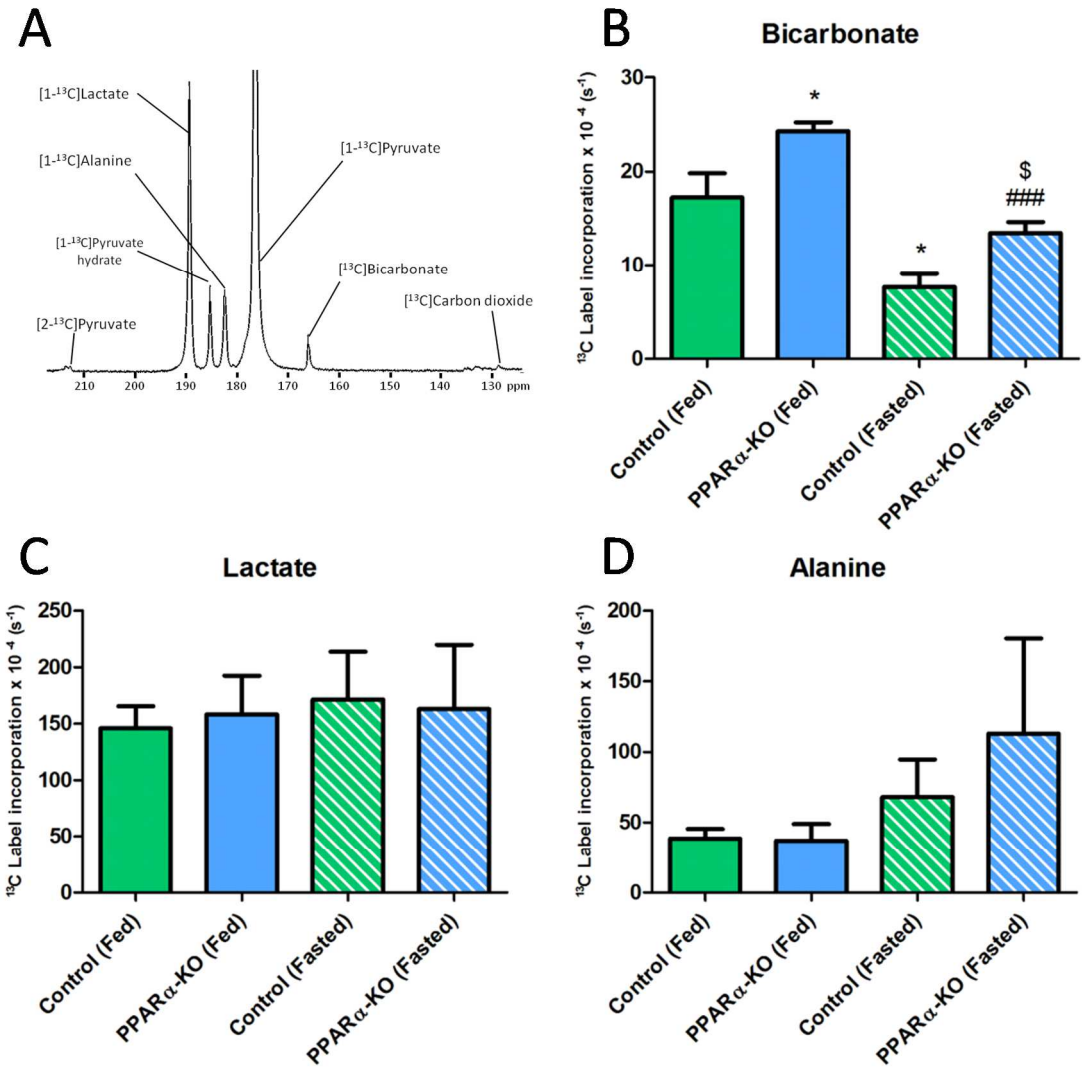

Figure 6.7 – Aged PPARα-KO mice display altered flux into bicarbonate compared to control mice – A) Fed PPARα-KO mice had a significant increase in ^{13}C label incorporation into bicarbonate, compared to controls. During the fasted state, PPARα-KO mice still display a significant increase in ^{13}C label incorporation compared to fasted controls. B) Flux into lactate was unaltered between groups. C) Flux was also unaltered into alanine. D) An example summed spectra from a PPARα-KO mouse.

* $p < 0.05$ and compared to fed controls, ### $p < 0.001$ compared to PPARα-KO fed and $ $p < 0.05$ compared to fasted controls.

6.4.4 *Assessment of the K_{ATP} mutant model*

The final mouse model to be assessed within this chapter was the K_{ATP} transgenic mouse model of type 1 diabetes. As mentioned within the background, one of the characteristic phenotypes of diabetes as a whole, is an inability to utilize glucose. In type 1 diabetes, postprandially, there is a lack of insulin release in response to increased plasma glucose concentrations. This can be assessed using an IPGT test. Figure 6.8 shows results from baseline (healthy) and K_{ATP} TG (following induction of diabetes) IPGT tests. The fasting blood glucose concentration was already significantly elevated within the diabetic mice (time = 0, $p < 0.001$). Upon IP glucose challenge, blood glucose concentrations increased in both baseline and diabetic mice. In the baseline mice, insulin was released and blood glucose concentrations returned to normal between 60 and 120 min. Due to a lack of insulin release, diabetic blood glucose concentrations still remained above time = 0, even after 120 mins. These data confirmed the diabetic phenotype of the K_{ATP} mice.

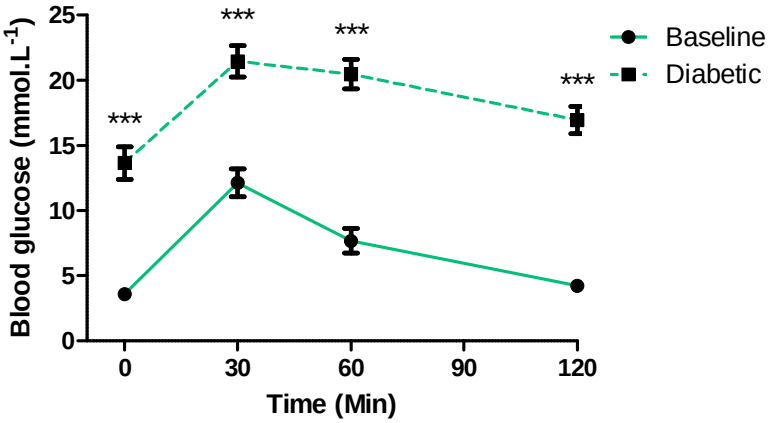

Figure 6.8 – IPGT test in the baseline and diabetic mice – Glucose concentration was measured at the start of the test (t=0), before the mice are administrated IP glucose. Blood glucose concentrations increased until insulin release led to storage or utilization of excess glucose. Diabetic mice started with a higher blood glucose concentration and respond poorly to the glucose challenge. *** $p < 0.001$ compared to Baseline

Implantation of glibenclamide pellets into diabetic mice lead to a significant reduction in fasting blood glucose concentrations one day post pellet implantation (22 ± 1 to 8 ± 1 mmol.L^{-1}), this was maintained throughout the study (Figure 6.9).

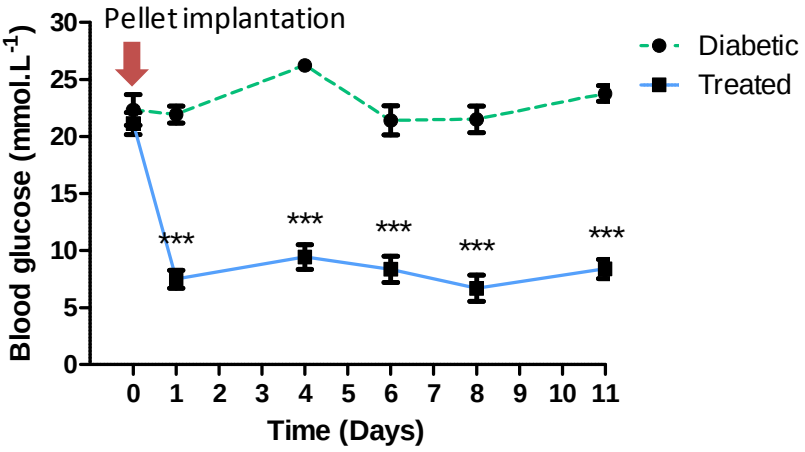

Figure 6.9 – Fasted blood glucose concentrations following glibenclamide pellet implantation – Treated animals had a significant reduction in blood glucose concentration after 1 day, which was maintained for the entire study.

*** $p < 0.001$ compared to diabetic mice.

Interestingly, even though implantation of the glibenclamide pellet lead to a significant reduction in blood glucose concentration, the IPGT test revealed that glucose handling was still affected after 10 days (Figure 6.10). Despite normal fasting blood glucose levels, there was a significant increase in blood glucose after 30 min which stayed elevated throughout the IPGT test.

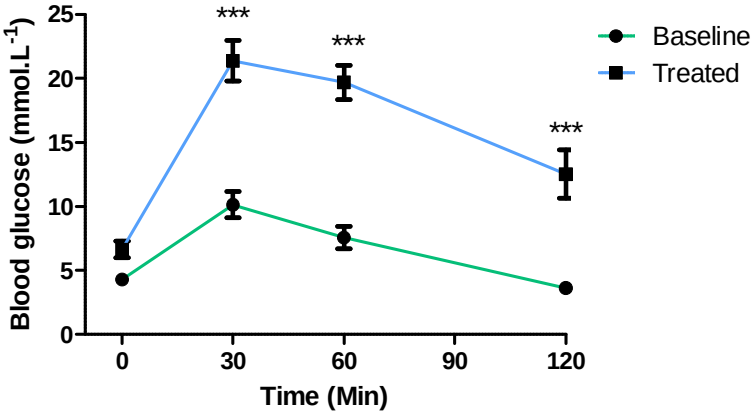

Figure 6.10 – IPGT test in the baseline and treated mice – Treated mice start with a normal blood glucose concentration, but respond poorly to a glucose challenge.

*** $p < 0.001$ compared to Baseline

6.4.5 *Treatment leads to a significant elevation in plasma insulin*

To confirm that the diabetic mice had a reduced blood insulin concentration, an insulin ELISA was performed. Induction of the K_{ATP} channel mutation led to a significant reduction in blood insulin (Figure 6.11). Treatment with glibenclamide led to a restoration of insulin levels and a significant increase over controls.

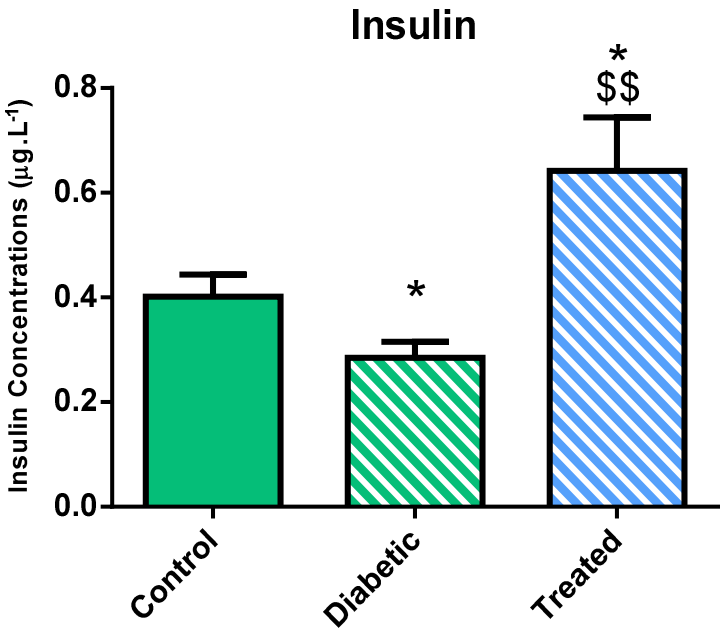

Figure 6.11 – Insulin concentrations in the diabetic and treated animals are altered – An ELISA for the content of insulin within the blood plasma of diabetic, treated and control animals. A significant reduction was seen in diabetic animals. Treatment returned insulin levels over that of control animals.

* $p \leq 0.05$ vs control and $$ $p < 0.01$ vs diabetic.

6.4.6 *In vivo metabolism of diabetic and treated mice*

Diabetes led to a significant reduction in *in vivo* PDH flux compared to baseline (Figure 6.12, baseline 11 ± 2 $x10^{-4}$ s^{-1}, diabetic 4 ± 2 $x10^{-4}$ s^{-1}, $p < 0.001$). Treatment with glibenclamide did not return PDH flux back to normal and was not different between diabetics and treated (treated 4 ± 2 $x10^{-4}$ s^{-1} compared to baseline, $p < 0.001$). Flux into lactate and alanine was not altered between groups.

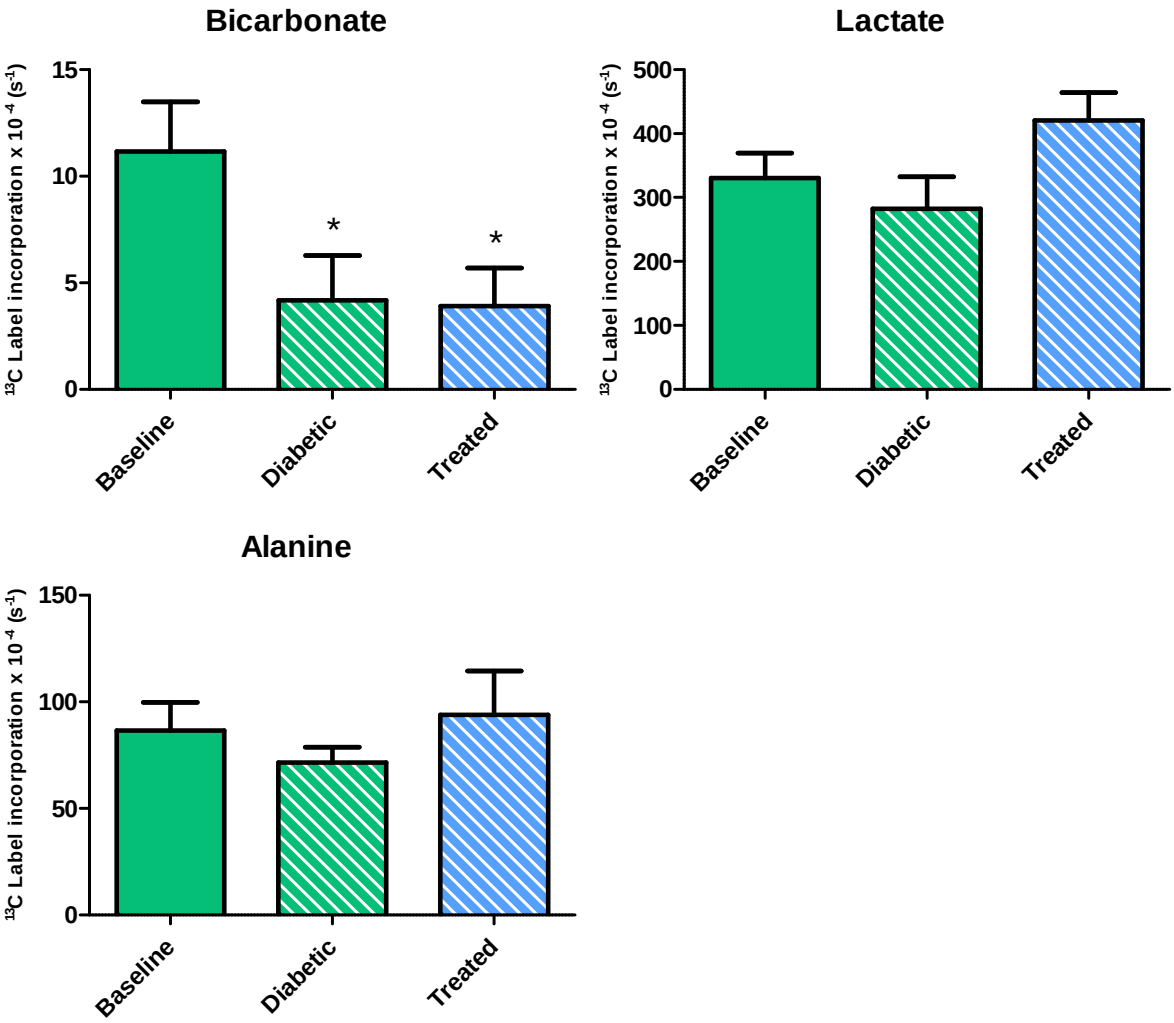

Figure 6.12 – Reduced PDH flux in diabetic and treated mice – ^{13}C label incorporation into bicarbonate was significantly decreased in the diabetic mouse. Interestingly, even though their blood glucose concentration was normal, treated animals still showed a significant reduction in flux into bicarbonate. Lactate and alanine were unaltered between groups.

* $p < 0.05$ compared to Baseline

6.4.7 Assessment of cardiac function in diabetes

Cardiac structure and function were assessed in all K_{ATP} mice using cine-MRI. Cardiac function was found to be unaltered in the diabetic and treated mice. All markers of cardiac function were normal, including ejection fraction and cardiac output (Figure 6.13). No hypertrophy was detected in any of the groups. Interestingly no evidence of any diabetic cardiomyopathy was detected in either group, assessed as a normal diastolic function (Figure 6.14).

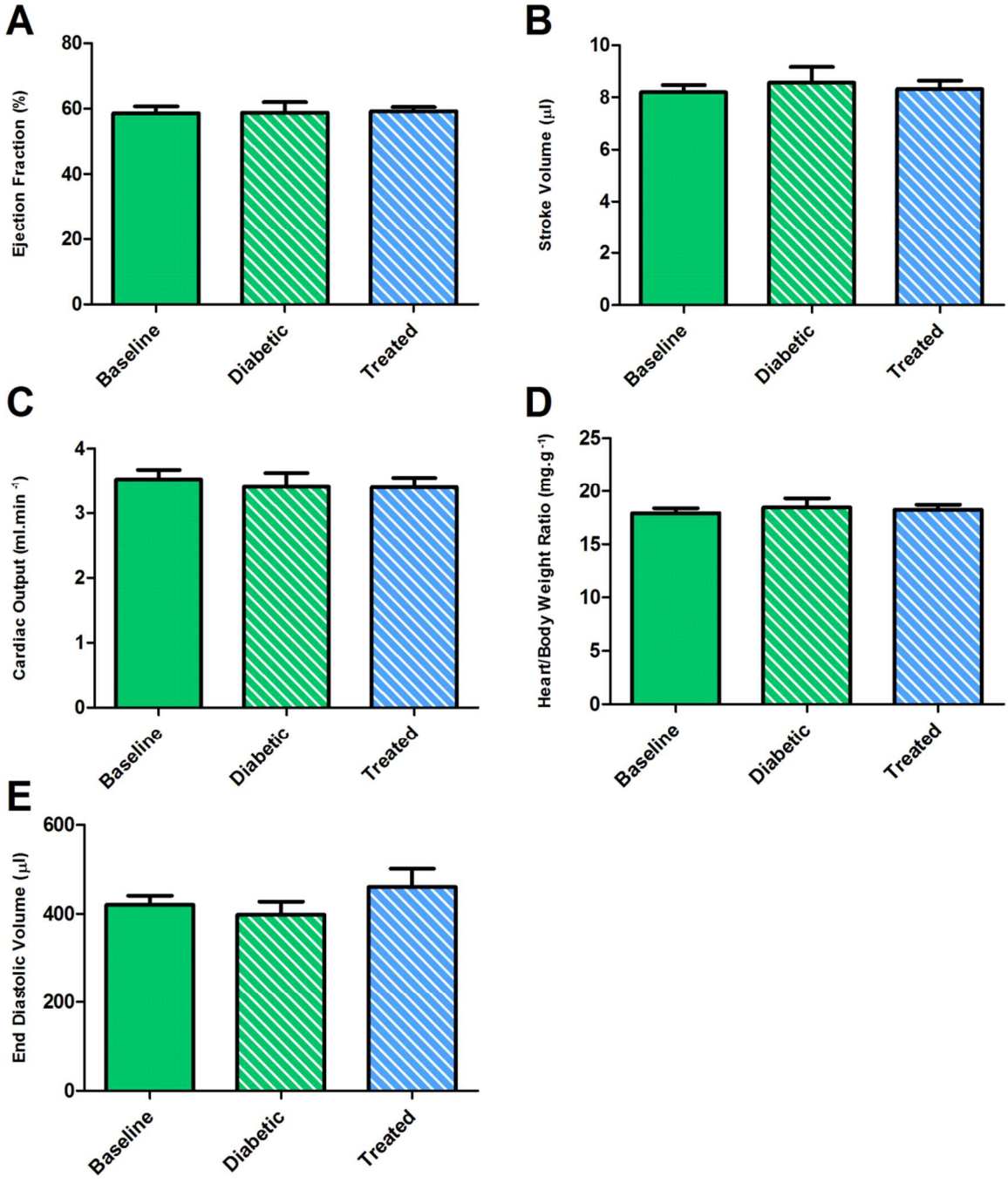

Figure 6.13 – Cardiac function and structure was assessed using cine-MRI – No differences were seen in any of the parameters of cardiac function or structural remodelling.

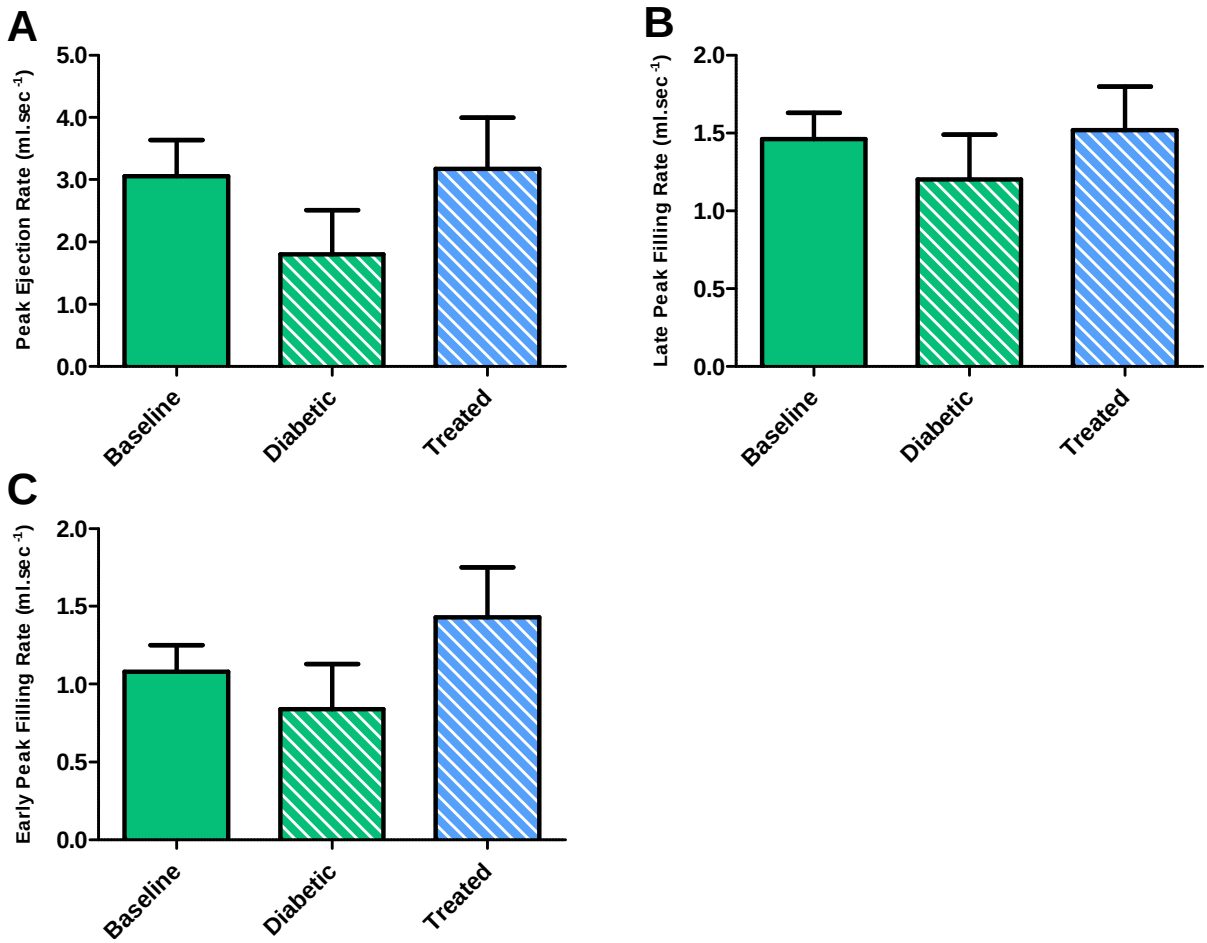

Figure 6.14 – Diastolic function was assessed using HTR cine-MRI – No significant differences were found in diastolic function in between the groups.

6.4.8 Biochemical analysis of cardiac tissue

RT-PCR was performed on extracted heart tissue to measure mRNA expression of PPARα. As mentioned previously in this chapter, this gene is partially responsible for controlling β-oxidation in periods of high free fatty acids. PPARα was significantly elevated by 29% in the diabetic and 54% in the treated hearts (Figure 6.15).

Protein expression of key PDH regulatory genes were measured to assess their contribution to the alterations in PDH flux. The inhibitor of PDH, PDK2 was found to be significantly elevated by 136% and 107% in the diabetic and treated hearts, respectively (figure 6.15). PDK1, PDK4, PDP1, and PDP2 were not different between groups.

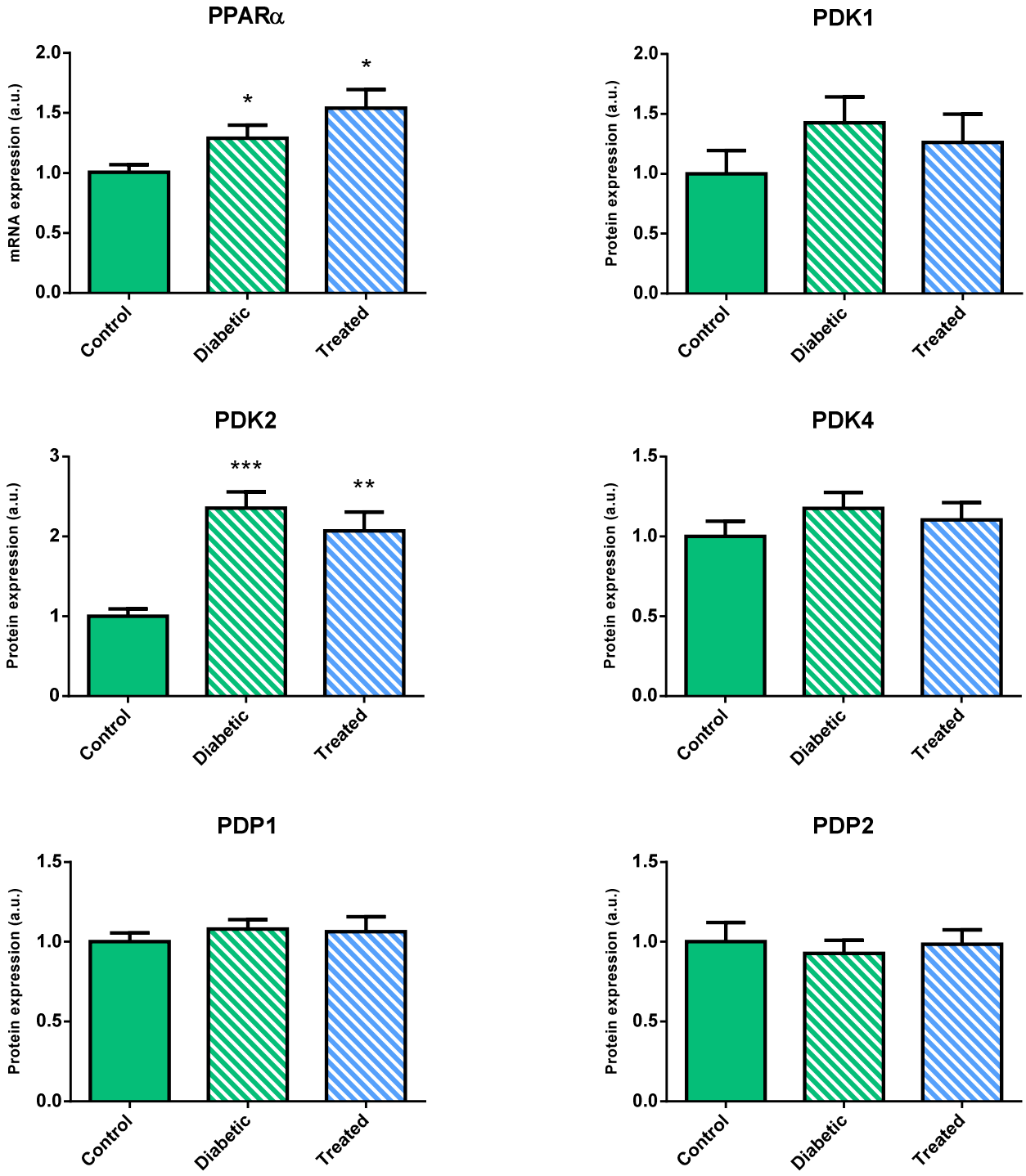

Figure 6.15 – Biochemical analysis of cardiac tissue homogenates – RT-PCR analysis showed that PPARα was significantly elevated in the treated group. Western blotting analysis of the regulators of PDH, showed a significant elevation in PDK2 in the diabetic and treated animals and no change in any other protein expression. ** $p < 0.01$, *** $p < 0.001$ verses control

6.5 Discussion

In this chapter, the mouse DNP technique developed in the previous chapter has been employed to assess *in vivo* cardiac metabolism in three different mouse models of β-oxidation modulations. PPARα-KO and LCAD-KO mice represent reductions in β-oxidation, whilst type 1 diabetes has been used here as a model of increased β-oxidation. Substrate selection is tightly regulated in the heart, but this balance is significantly altered within the diseased heart. By understanding more about what causes this relationship to breakdown, we may highlight therapeutic targets.

6.5.1 In vivo assessment of cardiac metabolism in the LCAD-KO mouse

The fed LCAD-KO mouse maintains a normal myocardial PDH flux compared to control mice. Following a period of fasting there was a significant reduction in PDH flux in both the controls and the knockout mice. However, this reduction was blunted in the LCAD-KO mice, when compared to controls. In the fasted LCAD-KO mice, additional resonances were also observed, which based on the work by Merritt and colleagues [228], have been assigned as aspartate and malate. These resonances were only present in the fasted LCAD-KO mouse but due to the broad linewidths of these peaks, they could not be quantified. The appearance of these peaks, suggests an increase in anaplerotic pathways in the LCAD-KO mouse, which would likely "top up" the TCA cycle during fasting. These data suggest that these mice have a phenotype of compensatory glucose metabolism in the fasted state, in an attempt to maintain myocardial energy homeostasis.

The normal cardiac response to fasting is a greater reliance on fatty acids and a shift away from glucose oxidation. The breakdown of fatty acid stores (circulating triglycerides or lipolysis in adipocytes) results in elevated plasma fatty acid levels, which stimulate their own catabolism through increased β-oxidation. However, in the LCAD-KO mice, there is an

inability to upregulate β-oxidation during a fast [16,202]. This leads to the observed stunted reduction in PDH flux. Previously in the PPARα-KO mouse, it has been shown that there is a stunted fasting-induced PDK4 increase, which will lead to a stunted reduction in PDH activity [187,212]. Whether this reduction is also observed in the LCAD-KO is currently unclear.

Another possible mechanism for the observed alterations in PDH flux is a reduction in β-oxidation derived acetyl-CoA and NADH. Due to the reduction in β-oxidation, there will be a reduction in the end products of this pathway. As previously mentioned in chapter 3, acetyl-CoA and NADH play an important role in regulating PDH activity, through the modulation of the PDKs and direct end product inhibition [29,187]. Acetyl-CoA and NADH accumulation leads to decreased PDH activity and therefore decreased glucose oxidation [229]. A reduction in acetyl-CoA and NADH derived from β-oxidation would therefore partially remove any inhibition on PDH.

6.5.2 Alterations to cardiac metabolism in the PPARα-KO mouse with aging

Interestingly the young PPARα-KO mice do not show any difference in PDH flux compared to controls, in either the fed or fasted state. Consistent with the data here, young PPARα-KO mice have previously been reported to have increased glycolytic flux without a concomitant increase in PDH activity [36]. Flux into lactate was significantly reduced in the fasted PPARα-KO mouse, compared to the fed PPARα-KO mouse. It is possible that this was due to an increased consumption of lactate in the fasted PPARα-KO heart, to compensate for a lack of β-oxidation [36,230]. This is supported by evidence from Gélinas *et al*, who showed that there was a significant increase in ^{13}C label incorporation into the TCA cycle from lactate [36]. Although this was seen in the fed state, further evidence from the fasted PPARα-KO mouse, shows that they have a significantly lower blood lactate concentrations, compared to controls and the fed state, possibly indicating increased lactate uptake and utilization [186].

Myocardial PDH flux in the 3 month old fasted PPARα-KO mice was decreased by the same amount as controls, it could be assumed that this portion of PDH flux reduction was not mediated by PPARα, indicating a PPARα-independent response to fasting in these young mice. This likely highlights redundancy within the regulatory pathways in an attempt to minimize glucose usage, during a time of fasting [202,231]. Other PPAR isoforms, namely PPARβ/δ, have also been shown to be responsible for regulation of β-oxidation in the heart. Both PPARα and PPARβ/δ display distinct metabolic regulation of β-oxidation, but there is some overlap in target genes [232,233]. It is important to note that cardiomyocyte specific knockout of PPARδ also leads to downregulation of PDK4 [234,235]. In the skeletal muscle of PPARα-KO mice, an increase in PPARδ has been proposed to compensate for the lack of PPARα [186]. It is possible that in this model there is also a compensatory increase in PPARδ in the heart, which upon fasting results in an increase in PDK4 expression.

Whilst the young PPARα-KO mice showed no alterations in PDH flux when compared to controls, aged PPARα-KO mice showed an altered phenotype in both the fed and fasted state. At 12-14 months of age, the PPARα-KO mouse had a significant increase in PDH flux during the fed state. This was accompanied by a similar reduction in the fasting induced decrease in PDH flux as was seen in the LCAD-KO mouse. It would be interesting to study older LCAD-KO mice to see if differences might have also been visible in the fed state too. Previously, a significant decrease in cardiac glycogen and glucose was seen with ageing within the fed PPARα-KO mouse (3 vs 13 months) [156]. This might imply a shift towards greater utilization of glucose in glycolysis/glucose oxidation in the fed aged mice. This is driven by the lack of PPARα to upregulate β-oxidation under conditions of low glucose. This ultimately results in an observed energy deficit in the mouse [214]. It is likely that a similar mechanism is working as discussed in the LCAD-KO mice, where reductions in β-oxidation will relieve the inhibitory action of acetyl-CoA and NADH on PDH.

6.5.3 Assessing the effects of treatment of type 1 diabetes on cardiac metabolism

PPARα has also been implicated in type 1 diabetes, where increases in β-oxidation are observed [236,237]. The type 1 diabetic heart switches away from glucose oxidation due to a lack of insulin production from the pancreatic β-cells. The diabetic heart has an increased myocardial fatty acid uptake and reliance on β-oxidation, this switch leads to an increased myocardial oxygen consumption [238]. In this work, type 1 diabetes was successfully induced in a pancreatic-specific kir6.2 K_{ATP} gain-of-function transgenic mouse. The diabetic phenotype was demonstrated through a significant increase in fasting blood glucose and a compromised ability of the mice to restore blood glucose levels following an infusion of glucose (IPGT test). Consistent with a type 1 diabetic model, these mice also had a significant reduction in plasma insulin concentrations. Further, due to the increase in β-oxidation, the diabetic hearts had a significant decrease in PDH flux. This was accompanied by increases in the protein expression of the PDH inhibitor, PDK2. The diabetic mice also showed a significant increase in PPARα mRNA expression.

Treatment with the sulfonylurea, glibenclamide led to a significant reduction in fasting blood glucose concentrations. However, the IPGT test revealed that these mice still had impaired glucose handling. This was reflected in a significant reduction in PDH flux and a significant increase in PDK2 protein expression. This was however, despite an increase in blood insulin concentrations, significantly above control levels.

As explored earlier, the induction of PPARα leads to a significant increase in expression of β-oxidation genes and a shift away from glucose oxidation. This is consistent with the decrease in PDH flux observed here. There are striking similarities between the hearts of diabetic mice and cardiac specific MHC-PPARα overexpression mice, which show increased β-oxidation genes and impaired glucose uptake and oxidation [236,237]. High fat fed MHC-PPARα and diabetic mice also display lipotoxcitiy, with stenosis and increased reactive oxygen

species [231]. There is also evidence of cardiomyopathic remodelling in both the diabetic and MHC-PPARα mice [231]. This might imply that alterations in PPARα or β-oxidation handling, might play an important role in the cardiac pathogensis of diabetes.

Interestingly, treatment with glibenclamide did not prevent the significant increase in PPARα expression seen in untreated animals, when compared to control animals. This could explain the apparent underlying diabetic phenotype that is still expressed in the treated animals. Even though fasting blood glucose levels had been returned to normal, there was still a defect in glucose handling. The insulin ELISA, highlighted that as expected there was a significant reduction in insulin in the diabetic mice, but that treatment led to a large increase in insulin release, significantly above control levels. One explanation for the apparent diabetic-phenotype following treatment is that the treatment causes the animals to develop insulin-insensitivity. The increase in PPARα, decreased PDH flux and increased expression of β-oxidation stimulated PDK proteins, is consistent with a reduced glucose uptake and reduced glucose oxidation. This is consistent with the insulin insensitive phenotype of type 2 diabetes. The mechanism for this apparent insulin insensitivity is unclear, it is possible that the treatment leads to a partially uncontrolled insulin release or that there is myocardial fatty acid accumulation, which alters insulin signalling [239].

In this work, no cardiomyopathy was detected, it is likely that, due to the relatively short period of diabetes that the animals were subjected to, any functional differences were subtle. The HTR-cine MRI technique, has previously identified the presence of a diabetic cardiomyopathy within the *Db/Db* mouse model of type 2 diabetes. However, this was at 12 weeks of age, where metabolic abnormalities would have impacted myocardial efficiency. Even at 3 weeks, following induction of type 1 diabetes, only a mild cardiomyopathy has been detected in streptozotocin-injected mice [240,241]. This study also required the use of an *ex vivo* working heart model to detect a difference. It is also possible that any subtle differences

would possibly be lost using *in vivo* HTR-cine MRI. Unlike echocardiography, which measures the flow of blood through the mitral value, HTR-cine MRI only provides a measure of changes in LV diameter during blood ejection and filling. Although this provides a very useful tool whilst mice are undergoing cine-MRI examination, it is not as sensitive as echocardiography at detecting subtle alterations in diastolic filling.

6.5.4 Conclusion

In conclusion all three mouse models have shown metabolic inflexibility during a period of stress, either during fasting or diabetes. Of particular interest, the young PPARα-KO mouse did not show any discernible phenotype in PDH flux; whilst 9 months later there were significant increases in PDH flux in both the fed and fasted state, relative to controls. This has highlighted that age can be an important factor in the development of metabolic alterations in these genetic models. Another interesting finding was that the K_{ATP} mutant mice, which were treated, still showed significant decreases in PDH flux and exhibited a type 2 diabetic-like phenotype. The DNP technique has been a useful tool in highlighting the metabolic switches that are characteristic of all these mouse models. It does however over simplify the contribution of both β-oxidation and glucose oxidation to metabolism. Flux through PDH provides a measure of metabolic switches, but cannot fully characterise its exact nature. Molecular biology techniques, which were explored within the K_{ATP} mutant mouse, add weight to the *in vivo* DNP findings. This chapter has however, provided interesting insights into the response of genetic mouse models to metabolic stress.

7. General Discussion

Hyperpolarized ^{13}C MRS has been used in this work to improve our understanding of the alterations in cardiac metabolism which underlie many diseases of the heart. Cardiac application of the DNP technique for hyperpolarization has allowed real time, *in vivo* assessment of ^{13}C label flux through a number of key enzymes. The applications in this thesis have demonstrated some of the possibilities that hyperpolarization offers to probe a range of models of heart disease and follow disease progression. The ability to monitor the same animals at multiple timepoints and in different pathological and physiological states has reduced the number of animals needed in each study, compared to traditional *in vitro* experiments.

Initially a model of hypertension, the spontaneously hypertensive rat (SHR), was used to understand changes to the metabolic balance between fatty acids and glucose caused by hypertension induced hypertrophy. A highly significant increase was observed in pyruvate dehydrogenase (PDH) flux in the SHR heart, along with a significant increase in PDH activity. This was likely due to a reduction in the inhibitors of PDH, PDK1 and PDK4. Taken together this data supports a move away from classical, predominantly fatty acid oxidation driven cardiac metabolism, matching evidence from previous *in vitro* data [13].

The second model to be studied was a model of myocardial infarction (MI). Following a myocardial infarction and during the progression into heart failure, metabolic substrate selection has been shown to alter [141]. The 4th chapter of this thesis explored the *in vivo* metabolic alterations that followed a MI and progression into heart failure. One week post MI, no significant differences were seen in *in vivo* cardiac metabolism despite a range of ejection fractions being generated by the MI surgery.

Six weeks following MI, there were significant alterations in the flux of ^{13}C labelled metabolite within the TCA cycle. There was a significant positive correlation between citrate, glutamate and acetylcarnitine label incorporation and ejection fraction, indicating impaired TCA cycle flux in the infarcted heart. Despite these alterations in the TCA cycle, no change in PDH flux was seen over the range of ejection fractions observed. However, by 22 weeks post-MI, there was a significant correlation between flux through PDH and ejection fraction in addition to alterations in label flux into the TCA cycle. The observed changes in *in vivo* PDH flux were supported by decreases in PDH activity in the infarcted heart. Coupled with these *in vivo* changes, *in vitro* biochemical analysis showed that there were significant positive correlations between citrate synthase, carnitine acetyl-transferase and isocitrate dehydrogenase activity and ejection fraction. There was also a significant negative correlation with acylcarnitine: free carnitine, and a positive correlation with free carnitine: total carnitine, indicating a reduction in free carnitine in the infarcted heart due to the "trapping" of carnitine in its acyl derivatives. The early alterations in acetylcarnitine at the 6 week timepoint, possibly suggests an early reduction in carnitine, which could be used as a metabolic marker of heart disease. In conclusion, this work has shown that during the progression into heart failure there appears to be a reduction in glucose oxidation and also impairment in TCA cycle efficiency.

The use of hyperpolarized ^{13}C MRS has provided a unique opportunity to monitor the *in vivo* flux through PDH and into the TCA cycle. This has enabled a smaller number of animals to be used to make serial measurements at 3 timepoints along the progression towards heart failure, thereby reducing biological variability and animal usage. At the final timepoint, the use of biochemical analysis strengthened the *in vivo* data and provided key information on enzyme activity and metabolite concentrations.

The use of rat models in these first two studies provided a wealth of information on the changes to metabolic substrate utilization that occur in cardiovascular disease. However there is also a need to probe individual metabolic pathways to better understand the cause and effect of such changes. This led to the development of mouse cardiac DNP in chapter 5, where two well characterized modulations of PDH flux, namely overnight fasting and infusion of sodium dichloroacetate, were used to successfully assess the sensitivity of the DNP technique in the mouse heart. The correct selection of control animals for metabolic studies is undoubtedly important, and it has previously been shown that there are metabolic differences between commonly used mouse strains. This was further highlighted in Chapter 5 where the use of DNP revealed significant differences in *in vivo* cardiac metabolism between C57BL/6, Balb/c and 129 SvEv mice.

Following these successful demonstrations of the sensitivity of mouse DNP to detect altered cardiac metabolism, a cardiac specific FH-KO mouse was studied. FH-KO mice were studied at 6 weeks and 12-14 weeks of age in an attempt to understand the *in vivo* metabolic alterations which occur in response to a genetic disruption of the TCA cycle. At 6 weeks of age, when fumarate hydratase knockout (FH-KO) mice have previously been shown to be protected from ischemia-reperfusion injury [197], there were no differences observed in *in vivo* pyruvate metabolism between controls and FH-KO mice. However, after this time the mice develop severe cardiac dysfunction, with heart failure and alterations in cardiac metabolism. This was observed as a reduced PDH flux and an impaired flux into alanine in the 12-14 week old FH-KO mice.

Alterations in β-oxidation underlie many diseases of the heart. Using the DNP technique, the contribution of PDH flux to cardiac metabolism was assessed in three different transgenic mouse models. The knockout of long chain acyl dehydrogenase (LCAD) led to a stunted decrease in PDH flux following an overnight fast. There was also an appearance of

anaplerotic intermediates, indicating that the TCA cycle was being "topped up" to compensate for the knockout of LCAD.

Young peroxisome proliferator-activated receptor α knockout (PPARα-KO) mice (3 months old) did not show any differences in PDH flux in the fed or fasted state. Flux into lactate, however was significantly lower in the fasted PPARα-KO mouse, compared to fed mice. This could suggest an increased usage of lactate in the fasted PPARα-KO mouse, to compensate for the lack of PPARα induced β-oxidation. When PPARα-KO mice were aged to 12-14 months of age, there were significant alterations in PDH flux in both the fed and fasted state. PDH flux was significantly elevated in the fed state and similar to the LCAD-KO mouse, there was a stunted decrease in PDH flux following an overnight fast.

Finally, DNP was used to assess the *in vivo* cardiac metabolic alterations that occur in the diabetic heart in response to treatment. The K_{ATP} mutant mouse is a model of type 1 diabetes that can be treated with the sulfonylurea, glibenclamide. Sulfonylurea treatment reverses the lack of insulin that occurs with type 1 diabetes. As expected, there was a significant reduction in PDH flux in the diabetic heart. However, despite a significant increase in insulin levels in the treated animals, the reduction in PDH flux remained. Biochemical analysis of the treated heart showed that there was increased PPARα mRNA expression and increased PDK2 protein expression, possibly indicating that excess insulin release in response to treatment had generated a 'type 2 diabetic' like phenotype.

In summary the aim of this thesis was to provide a greater understanding of the *in vivo* metabolic alterations that occur in the diseased heart. Rat models have provided key findings such as significant increases in PDH flux in the heart of the 15 week old SHR and metabolic alterations in the TCA cycle during the progression into heart failure. Both could prove to be useful markers in non-invasively identifying metabolic alterations associated with

hypertrophy and heart failure in patients. Subsequently, the novel challenges that underlie the development of mouse cardiac DNP were undertaken. The development of this technique will allow for interesting insights in to the *in vivo* metabolic phenotype of many genetic models of heart disease. In addition in the LCAD-KO mouse revealed that hyperpolarized [1-^{13}C]pyruvate could be used to monitor anaplerotic pathways in the stressed mouse heart, increasing its power for clinical use. In combination with cine-MRI and ^{31}P MRS, this work has highlighted that DNP could play an important role in the diagnosis, prognosis and monitoring of treatment response in many cardiovascular diseases.

8. References

1. Scarborough P, Bhatnagar P, Wickramasinghe K, Smolina K, Mitchell C. Coronary heart disease statistics. Oxford: 2010.

2. Opie LH. Heart physiology: from cell to circulation. 4th ed. Philadelphia: Lippincott Williams & Wilkins; 2004.

3. Neubauer S. The failing heart--an engine out of fuel. *The New England Journal of Medicine*. 2007; 356:1140–1151.

4. Visscher MB, Mulder AG. The carbohydrate metabolism of the heart. *American Journal of Physiology*. 1930; 94:630–640.

5. Bing RJ, Siegel A, Ungar I, Gilbert M. Metabolism of the Human heart II. Studies on Fat, Ketone and Amino Acid Metabolism. *American Journal of Medicine*. 1954; 16:504 – 515.

6. Randle PJ, Garland PB, Hales CN, Newsholme EA. The glucose fatty-acid cycle. Its role in insulin sensitivity and the metabolic disturbances of diabetes mellitus. *The Lancet*. 1963; 1:785.

7. Bailey IA, Gadian DG, Matthews PM, Radda GK, Seeley PJ. Studies of metabolism in the isolated, perfused rat heart using 13C NMR. *FEBS Letter*. 1981; 123:315–318.

8. Schroeder MA, Cochlin LE, Heather LC, Clarke K, Radda GK, Tyler DJ. In vivo assessment of pyruvate dehydrogenase flux in the heart using hyperpolarized carbon-13 magnetic resonance. *Proc. Natl. Acad. Sci. USA*. 2008; 105:12051–6.

9. Ardenkjaer-Larsen JH, Fridlund B, Gram A, Hansson G, Hansson L, Lerche MH, Servin R, Thaning M, Golman K. Increase in signal-to-noise ratio of > 10,000 times in liquid-state NMR. *Proc. Natl. Acad. Sci. USA*. 2003; 100:10158–10163.

10. Lau AZ, Chen AP, Ghugre NR, Ramanan V, Lam WW, Connelly K a, Wright G a, Cunningham CH. Rapid multislice imaging of hyperpolarized 13C pyruvate and bicarbonate in the heart. *Magnetic Resonance in Medicine*. 2010; 64:1323–31.

11. Iemitsu M, Shimojo N, Maeda S, Irukayama-Tomobe Y, Sakai S, Ohkubo T, Tanaka Y, Miyauchi T. The benefit of medium-chain triglyceride therapy on the cardiac function of SHRs is associated with a reversal of metabolic and signaling alterations. *Am J Physiol Heart Circ Physiol*. 2008; 295:H136–44.

12. Shimamoto N, Goto N, Tanabe M, Imamoto T, Fujiwara S, Hirata M. Myocardial energy metabolism in the hypertrophied hearts of spontaneously hypertensive rats. *Basic Research in Cardiology*. 1982; 77:359–7.

13. Labarthe F, Khairallah M, Bouchard B, Stanley WC, Des Rosiers C. Fatty acid oxidation and its impact on response of spontaneously hypertensive rat hearts to an adrenergic stress: benefits of a medium-chain fatty acid. *Am J Physiol Heart Circ Physiol*. 2005; 288:1425–1436.

14. Maher B. Knockout rats made to order [Internet]. Nature. 2009;Available from: http://www.nature.com/news/2009/090901/full/news.2009.876.html

15. Wolfensohn S, Lloyd M. Handbook of Laboratory Animal Management and Welfare. John Wiley & Sons; 2008.

16. Bakermans AJ, Geraedts TR, van Weeghel M, Denis S, João Ferraz M, Aerts JMFG, Aten J, Nicolay K, Houten SM, Prompers JJ. Fasting-induced myocardial lipid accumulation in long-chain acyl-CoA dehydrogenase knockout mice is accompanied by impaired left ventricular function. *Circulation. Cardiovascular Imaging*. 2011; 4:558–65.

17. Lee SS, Pineau T, Drago J, Lee EJ, Owens JW, Kroetz DL, Fernandez-Salguero PM, Westphal H, Gonzalez FJ. Targeted disruption of the alpha isoform of the peroxisome proliferator-activated receptor gene in mice results in abolishment of the pleiotropic effects of peroxisome proliferators. *Molecular and Cellular Biology*. 1995; 15:3012–22.

18. Girard CA, Wunderlich FT, Shimomura K, Collins S, Kaizik S, Proks P, Abdulkader F, Clark A, Ball V, Zubcevic L, Bentley L, Clark R, Church C, Hugill A, Galvanovskis J, Cox R, Rorsman P, Brüning JC, Ashcroft FM. Expression of an activating mutation in the gene encoding the K ATP channel subunit Kir6.2 in mouse pancreatic β cells recapitulates neonatal diabetes. *The Journal of Clinical Investigation*. 2009; 119:80–90.

19. Jungas RL. Hormonal regulation of pyruvate dehydrogenase. *Metabolism*. 1971; 20:43–53.

20. Mueckler M, Hresko RC, Sato M. Structure, function and regulation of glucose transporters. *Biochem. Soc. Trans*. 1997; 25:951–4.

21. Young LH, Coven DL, Russell III RR. Cellular and molecular regulation of cardiac glucose transport. *Journal of Nuclear Cardiology*. 2000; 7:267–276.

22. Young LH, Renfu Y, Russell R, Hu X, Caplan M, Ren J, Shulman GI, Sinusas AJ. Low-Flow Ischemia Leads to Translocation of Canine Heart GLUT-4 and GLUT-1 Glucose Transporters to the Sarcolemma In Vivo. *Circulation*. 1997; 95:415–422.

23. James DE, Brown R, Navarro J, Pilch PF. Insulin-regulatable tissues express a unique insulin-sensitive glucose transport protein. *Nature*. 1988; 333:183–185.

24. Fischer Y, Thomas J, Sevilla L, Becker C, Holman G, Kozka IJ, Palacı M, Testar X, Kammermeier H, Zorzano A. Insulin-induced Recruitment of Glucose Transporter 4 (GLUT4) and GLUT1 in Isolated Rat Cardiac Myocytes. *The Journal of Biological Chemistry*. 1997; 272:7085–7092.

25. Stanley WC, Lopaschuk GD, Hall JL, McCormack JG. Regulation of myocardial carbohydrate metabolism under normal and ischaemic conditions. Potential for pharmacological interventions. *Cardiovascular research*. 1997; 33:243–57.

26. Frayn KN. Metabolic Regulation: A Human Prespective. 3rd ed. Wiley-Blackwell; 2010.

27. Stanley WC, Recchia FA, Lopaschuk GD. Myocardial substrate metabolism in the normal and failing heart. *Physiological Reviews*. 2005; 85:1093–1129.

28. Randle PJ. Phosphorylation-dephosphorylation cycles and the regulation of fuel selection in mammals. *Curr Top Cell Regul*. 1981; 18:107–129.

29. Holness MJ, Sugden MC. Regulation of pyruvate dehydrogenase complex activity by reversible phosphorylation. *Biochemical Society Transactions*. 2003; 31:1143–51.

30. Denton RMM, Randle PJ, Martin B. R. Stimulation by Calcium Ions of Pyruvate Dehydrogenase Phosphate Phosphatase. *Biochemical Journal*. 1972; 128:161–163.

31. Bowker-Kinley MM, Davis WI, Wu P, Harris RA, Popov KM. Evidence for existence of tissue-specific regulation of the mammalian pyruvate dehydrogenase complex. *Biochemical Journal*. 1998; 329:191–196.

32. Linn TC, Pettit FH, Hucho F, Reed LJ. α-Keto acid dehydrogenase complexes, XI. comparative studies of regulatory properties of the pyruvate dehydrogenase complexes from kidney, heart, and liver mitochondria. *Proc. Natl. Acad. Sci. USA*. 1969; 64:227–234.

33. Wieland O, Jagow-Westermann B v. ATP-dependent inactivation of heart muscle pyruvate dehydrogenase and reactivation by Mg++. *FEBS letters*. 1969; 3:271–274.

34. Huang B, Gudi R, Wu P, Harris RA, Hamilton J, Popov KM. Isoenzymes of Pyruvate Dehydrogenase Phosphatase DNA-derived Amino Acid Sequences, Expression, And Regulation. *The Journal of Biological Chemistry*. 1998; 273:17680–17688.

35. Huang B, Wu P, Popov KM, Harris RA. Starvation and diabetes reduce the amount of pyruvate dehydrogenase phosphatase in rat heart and kidney. *Diabetes*. 2003; 52:1371–6.

36. Gélinas R, Labarthe F, Bouchard B, Mc Duff J, Charron G, Young ME, Des Rosiers C. Alterations in carbohydrate metabolism and its regulation in PPARalpha null mouse hearts. *Am J Physiol Heart Circ Physiol*. 2008; 294:H1571–80.

37. Wu P, Sato J, Zhao Y, Jaskiewicz J, Popov KM, Harris RA. Starvation and diabetes increase the amount of pyruvate dehydrogenase kinase isoenzyme 4 in rat heart. *Biochemical Journal*. 1998; 329:197–201.

38. Issemann I, Green S. Activation of a member of the steroid hormone receptor superfamily by peroxisome proliferators. *Nature*. 1990; 347:645 – 650.

39. Djouadi F, Brandt J., Weinheimer C., Leone T., Gonzalez F., Kelly D. The role of the peroxisome proliferator-activated receptor α (PPARα) in the control of cardiac lipid metabolism. *Prostaglandins, Leukotrienes and Essential Fatty Acids*. 1999; 60:339–343.

40. Gulick T, Cresci S, Caira T, Moore DD, Kelly DP. The peroxisome proliferator-activated receptor regulates mitochondrial fatty acid oxidative enzyme gene expression. *Proceedings of the National Academy of Sciences of the United States of America*. 1994; 91:11012–6.

41. Yu GS, Lu YC, Gulick T. Co-regulation of tissue-specific alternative human carnitine palmitoyltransferase Ibeta gene promoters by fatty acid enzyme substrate. *The Journal of Biological Chemistry*. 1998; 273:32901–9.

42. Disch DL, Rader TA, Cresci S, Leone TC, Barger PM, Vega R, Wood P a, Kelly DP. Transcriptional control of a nuclear gene encoding a mitochondrial fatty acid oxidation enzyme in transgenic mice: role for nuclear receptors in cardiac and brown adipose expression. *Molecular and Cellular Biology*. 1996; 16:4043–51.

43. Huang B, Wu P, Bowker-Kinley MM, Harris RA. Regulation of pyruvate dehydrogenase kinase expression by peroxisome proliferator-activated receptor-alpha ligands, glucocorticoids, and insulin. *Diabetes*. 2002; 51:276–83.

44. Panagia M, Gibbons GF, Radda GK, Clarke K. PPAR-alpha activation required for decreased glucose uptake and increased susceptibility to injury during ischemia. *Am J Physiol Heart Circ Physiol*. 2005; 288:H2677–83.

45. Cary HH, Beckman AO. A quartz photoelectric spectrophotometer. *J Opt Soc Am*. 1941; 31:682–689.

46. Kim HY, Wang TC, Ma YC. Liquid chromatography/mass spectrometry of phospholipids using electrospray ionization. *Analytical Chemistry*. 1994; 66:3977–82.

47. Griffin JL, Atherton H, Shockcor J, Atzori L. Metabolomics as a tool for cardiac research. *Nature Reviews. Cardiology*. 2011; 8:630–43.

48. Heather LC, Cole MA, Lygate CA, Evans RD, Stuckey DJ, Murray AJ, Neubauer S, Clarke K. Fatty acid transporter levels and palmitate oxidation rate correlate with ejection fraction in the infarcted rat heart. *Cardiovascular Research*. 2006; 72:430–7.

49. Obrzut S, Jamshidi N, Karimi A, Birgersdotter-Green U, Hoh C. Imaging and modeling of myocardial metabolism. *Journal of Cardiovascular Translational Research*. 2010; 3:384–96.

50. Maddahi J, Schelbert H, Brunken R, Carli MD. Role of Thallium-201 and PET Imaging in Evaluation of Myocardial Viability and Management of Patients with Coronary Artery Disease and Left Ventricular Dysfunction metabolism. *Cardiovascular Nuclear Medicine*. 1994; 35:707–715.

51. Vitale GD, DeKemp R a, Ruddy TD, Williams K, Beanlands RS. Myocardial glucose utilization and optimization of (18)F-FDG PET imaging in patients with non-insulin-dependent diabetes mellitus, coronary artery disease, and left ventricular dysfunction. *Journal of Nuclear Medicine*. 2001; 42:1730–6.

52. Ten Hove M, Neubauer S. MR spectroscopy in heart failure--clinical and experimental findings. *Heart Fail Rev*. 2007; 12:48–57.

53. Jacobus W, Taylor G, HOLLIS D. Phosphorus nuclear magnetic resonance of perfused working rat hearts. *Nature*. 1977; 265:756–758.

54. Garlick P, Radda G, Seeley P, Chance B. Phosphorus NMR studies on perfused heart. *Biochemical and Biophysical Research Communications*. 1977; 74:1256–1262.

55. Neubauer S, Horn M, Cramer M, Harre K, Newell JB, Peters W, Pabst T, Ertl G, Hahn D, Ingwall JS, Kochsiek K. Myocardial Phosphocreatine-to-ATP Ratio Is a Predictor of Mortality in Patients With Dilated Cardiomyopathy. *Circulation*. 1997; 96:2190–2196.

56. Bottomley PA, Weiss RG. Non-invasive magnetic-resonance detection of creatine depletion in non-viable infarcted myocardium. *The Lancet*. 1998; 351:714–718.

57. Walecki J, Michalak MJ, Michalak E, Bilinska ZT, Ruzyllo W. Usefulness of 1H MR spectroscopy in the evaluation of myocardial metabolism in patients with dilated idiopathic cardiomyopathy. *Academic Radiology*. 2003; 10:1187–1192.

58. Evanochko W, Reeves R, Canby R, McMillin J, Pohost G. Proton NMR Spectroscopic Studies of "Stunned" Myocardium. *Annals New York Academy of Sciences*. 1987; 508:460–462.

59. Schneider JE, Tyler DJ, ten Hove M, Sang a E, Cassidy PJ, Fischer A, Wallis J, Sebag-Montefiore LM, Watkins H, Isbrandt D, Clarke K, Neubauer S. In vivo cardiac 1H-MRS in the mouse. *Magnetic Resonance in Medicine*. 2004; 52:1029–35.

60. Ugurbil K, Petein M, Maidan R, Michurski S, Cohn JN, From a H. High resolution proton NMR studies of perfused rat hearts. *FEBS letters*. 1984; 167:73–8.

61. Malloy CR, Thompson JR, Jeffrey FM, Sherry AD. Contribution of exogenous substrates to acetyl coenzyme A: measurement by 13C NMR under non-steady-state conditions. *Biochemistry*. 1990; 29:6756–6761.

62. O'Donnell JM, Fields AD, Sorokina N, Lewandowski ED. The Absence of Endogenous Lipid Oxidation in Early Stage Heart Failure Exposes Limits in Lipid Storage and Turnover. *J Mol Cell Cardiol*. 2008; 44:315–322.

63. Neurohr KJ, Barrett EJ, Shulman RG. In vivo carbon-13 nuclear magnetic resonance studies of heart metabolism. *Proc. Natl. Acad. Sci. USA*. 1983; 80:1603–1607.

64. Laughlin MR, Taylor J, Chesnick AS, DeGroot M, Balaban RS. Pyruvate and lactate metabolism in the in vivo dog heart. *Am J Physiol*. 1993; 264:H2068–79.

65. Golman K, Ardenkjaer-Larsen JH, Petersson JS, Mansson S, Leunbach I. Molecular imaging with endogenous substances. *Proc. Natl. Acad. Sci. USA*. 2003; 100:10435–10439.

66. Golman K, Olsson LE, Axelsson O, Mansson S, Karlsson M, Petersson JS. Molecular imaging using hyperpolarized 13C. *Br J Radiol*. 2003; 76:S118–S127.

67. Overhauser AW. Polarization of nuclei in metals. *Physical Review*. 1953; 92:411–415.

68. Comment A, van den Brandt B, Uffmann K, Kurdzesau F, Jannin S, Konter J a., Hautle P, Wenckebach WT, Gruetter R, van der Klink JJ. Design and performance of a DNP prepolarizer coupled to a rodent MRI scanner. *Concepts in Magnetic Resonance Part B: Magnetic Resonance Engineering*. 2007; 31B:255–269.

69. Abragam A, Goldman M. Principles of dynamic nuclear polarisation. *Reports on Progress in Physics*. 1978; 41:395–467.

70. Maly T, Debelouchina GT, Bajaj VS, Hu K-N, Joo C-G, Mak-Jurkauskas ML, Sirigiri JR, van der Wel PCA, Herzfeld J, Temkin RJ, Griffin RG. Dynamic nuclear polarization at high magnetic fields. *The Journal of Chemical Physics*. 2008; 128:052211.

71. Farrar CT, Hall DA, Gerfen GJ, Inati SJ, Griffin RG. Mechanism of dynamic nuclear polarization in high magnetic fields. *The Journal of Chemical Physics*. 2001; 114:4922.

72. Wind RA, Duljvestljn MJ, van der Lugt C, Manenschijn A, Vriend J. APPLICATIONS OF DYNAMIC NUCLEAR IN 13C NMR IN SOLIDS. *Progress in NMR Spectroscopy*. 1985; 17:33–67.

73. Golman K, in 't Zandt R, Thaning M. Real-time metabolic imaging. *Proc. Natl. Acad. Sci. USA*. 2006; 103:11270–5.

74. Sigma Aldrich. http://chemicalland21.com/industrialchem/IUH/SODIUM%20PYRUVATE.htm.

75. Golman K, Petersson JS. Metabolic imaging and other applications of hyperpolarized 13C1. *Acad Radiol*. 2006; 13:932–942.

76. Golman K, Petersson JS, Magnusson P, Johansson E, Akeson P, Chai C-M, Hansson G, Månsson S. Cardiac metabolism measured noninvasively by hyperpolarized 13C MRI. *Magnetic Resonance in Medicine*. 2008; 59:1005–13.

77. Schroeder MA, Clarke K, Neubauer S, Tyler DJ. Hyperpolarized magnetic resonance: a novel technique for the in vivo assessment of cardiovascular disease. *Circulation*. 2011; 124:1580–94.

78. Merritt ME, Harrison C, Storey C, Jeffrey FM, Sherry AD, Malloy CR. Hyperpolarized 13C allows a direct measure of flux through a single enzyme-catalyzed step by NMR. *Proc. Natl. Acad. Sci. USA*. 2007; 104:19773–19777.

79. Atherton HJ, Schroeder MA, Dodd MS, Heather LC, Carter EE, Cochlin LE, Nagel S, Sibson NR, Radda GK, Clarke K, Tyler DJ. Validation of the in vivo assessment of pyruvate dehydrogenase activity using hyperpolarised (13)C MRS. *NMR in Biomedicine*. 2011; 24:201–8.

80. Atherton HJ, Dodd MS, Heather LC, Schroeder MA, Griffin JL, Radda GK, Clarke K, Tyler DJ. Role of pyruvate dehydrogenase inhibition in the development of hypertrophy in the hyperthyroid rat heart: a combined magnetic resonance imaging and hyperpolarized magnetic resonance spectroscopy study. *Circulation*. 2011; 123:2552–61.

81. Bohndiek SE, Kettunen MI, Hu DE, Witney TH, Kennedy BW, Gallagher FA, Brindle KM. Detection of tumor response to a vascular disrupting agent by hyperpolarized 13C magnetic resonance spectroscopy. *Mol Cancer Ther*. 2010; 9:3278–3288.

82. Day SE, Kettunen MI, Gallagher FA, Hu DE, Lerche M, Wolber J, Golman K, Ardenkjaer-Larsen JH, Brindle KM. Detecting tumor response to treatment using hyperpolarized 13C magnetic resonance imaging and spectroscopy. *Nature Medicine*. 2007; 13:1382–1387.

83. Warburg O. On the Origin of Cancer Cells. *Science*. 1956; 123:309–314.

84. Zhou M, Zhao Y, Ding Y, Liu H, Liu Z, Fodstad O, Riker AI, Kamarajugadda S, Lu J, Owen LB, Ledoux SP, Tan M. Warburg effect in chemosensitivity: targeting lactate

dehydrogenase-A re-sensitizes taxol-resistant cancer cells to taxol. *Molecular Cancer*. 2010; 9:1–12.

85. Hu S, Balakrishnan A, Bok R a, Anderton B, Larson PEZ, Nelson SJ, Kurhanewicz J, Vigneron DB, Goga A. (13)C-Pyruvate Imaging Reveals Alterations in Glycolysis that Precede c-Myc-Induced Tumor Formation and Regression. *Cell Metabolism*. 2011; 14:131–42.

86. Witney TH, Kettunen MI, Hu D-E, Gallagher FA, Bohndiek SE, Napolitano R, Brindle KM. Detecting treatment response in a model of human breast adenocarcinoma using hyperpolarised [1-13C]pyruvate and [1,4-13C2]fumarate. *British Journal of Cancer*. 2010; 103:1400–6.

87. Gallagher FA, Kettunen MI, Hu D-E, Jensen PR, in 't Zandt R, Karlsson M, Gisselsson A, Nelson SK, Witney TH, Bohndiek SE, Hansson G, Peitersen T, Lerche MH, Brindle KM. Production of hyperpolarized [1,4-13C2]malate from [1,4-13C2]fumarate is a marker of cell necrosis and treatment response in tumors. *PNAS*. 2009; 106:19801–19806.

88. Hu S, Zhu M, Yoshihara H a I, Wilson DM, Keshari KR, Shin P, Reed G, von Morze C, Bok R, Larson PEZ, Kurhanewicz J, Vigneron DB. In vivo measurement of normal rat intracellular pyruvate and lactate levels after injection of hyperpolarized [1-(13)C]alanine. *Magnetic Resonance Imaging*. 2011; 29:1035–40.

89. Harzstark A. Hyperpolarized Pyruvate Injection in Subjects With Prostate Cancer - Full Text View - ClinicalTrials.gov [Internet]. 2010 [cited 2012 Apr 10];Available from: http://clinicaltrials.gov/ct2/show/NCT01229618

90. UCSF. New Prostate Cancer Imaging Shows Real-Time Tumor Metabolism | News | UCSF Medical Center [Internet]. 2010 [cited 2012 Apr 10];Available from: http://www.ucsfhealth.org/news/2010/11/new_prostate_cancer_imaging_shows_real_time_tumor_metabolism.html

91. Schroeder MA, Swietach P, Atherton HJ, Gallagher FA, Lee P, Radda GK, Clarke K, Tyler DJ. Measuring intracellular pH in the heart using hyperpolarized carbon dioxide and bicarbonate: a 13C and 31P magnetic resonance spectroscopy study. *Cardiovascular Research*. 2010; 86:82–91.

92. Gallagher FA, Kettunen MI, Day SE, Hu D-EE, Ardenkjaer-Larsen JH, Zandt R in 'T, Jensen PR, Karlsson M, Golman K, Lerche MH, Brindle KM. Magnetic resonance imaging of pH in vivo using hyperpolarized 13C-labelled bicarbonate. *Nature*. 2008; 453:940–943.

93. Jennings R, Reimer K. The cell biology of acute myocardial ischemia. *Annual review of medicine*. 1991; 42:225–246.

94. Schroeder MA, Atherton HJ, Ball DR, Cole MA, Heather LC, Griffin JL, Clarke K, Radda GK, Tyler DJ. Real-time assessment of Krebs cycle metabolism using hyperpolarized 13C magnetic resonance spectroscopy. *The FASEB journal*. 2009; 23:2529–38.

95. Schroeder MA, Atherton HJ, Dodd MS, Lee P, Cochlin LE, Radda GK, Clarke K, Tyler DJ. The Cycling of Acetyl-CoA through Acetylcarnitine Buffers Cardiac Substrate Supply: A Hyperpolarised 13C Magnetic Resonance Study. *Circulation. Cardiovascular imaging*. 2012; 5:201–9.

96. Cassidy PJ, Schneider JE, Grieve SM, Lygate CA, Tyler DJ, Neubauer S, Clarke K. An animal handling system for small animals in vivo MR. In: ISMRM (Abstract). 2005. p. 488.

97. Naressi A, Couturier C, Castang I, de Beer R, Graveron-Demilly D. Java-based graphical user interface for MRUI, a software package for quantitation of in vivo/medical magnetic resonance spectroscopy signals. *Comput Biol Med*. 2001; 31:269–286.

98. Zierhut ML, Yen Y-FF, Chen AP, Bok R, Albers MJ, Zhang V, Tropp J, Park I, Vigneron DB, Kurhanewicz J, Hurd RE, Nelson SJ. Kinetic modeling of hyperpolarized 13C1-pyruvate metabolism in normal rats and TRAMP mice. *J Magn Reson*. 2010; 202:85–92.

99. Tyler D, Lygate C, Schneider J, Cassidy P, Neubauer S, Clarke K. CINE-MR Imaging of the Normal and Infarcted Rat Heart Using an 11.7 T Vertical Bore MR System. *Journal of Cardiovascular Magnetic Resonance*. 2006; 8:327–333.

100. Stuckey D, Carr C, Tyler D, Aasum E, Clarke K. Novel MRI method to detect altered left ventricular ejection and filling patterns in rodent models of disease. *Magnetic Resonance in Medicine*. 2008; 60:582–7.

101. Cross HR, Clarke K, Opie LH, Radda GK, Heart I, Town C. Is Lactate-induced Myocardial Ischaemic Injury Mediated by Decreased pH or Increased Intracellular Lactate ? *J Mol Cell Cardiol*. 1995; 27:1369–1381.

102. Murray AJ, Lygate CA, Cole MA, Carr CA, Radda GK, Neubauer S, Clarke K. Insulin resistance, abnormal energy metabolism and increased ischemic damage in the chronically infarcted rat heart. *Cardiovascular Research*. 2006; 71:149–57.

103. Seymour AM, Chatham JC. The effects of hypertrophy and diabetes on cardiac pyruvate dehydrogenase activity. *J Mol Cell Cardiol*. 1997; 29:2771–2778.

104. Bergmeyer HU. Methods of Enzymatic Analysis: Poly-,Oligo- and Disaccharides. 3rd ed. New York, NY: Academic Press Inc; 1983.

105. Cross HR, Opie LH, Radda GK, Clarke K. Is a High Glycogen Content Beneficial or Detrimental to the Ischemic Rat Heart? : A Controversy Resolved. *Circulation Research*. 1996; 78:482–491.

106. WHO | Global Health Observatory Data Repository [Internet]. [cited 2012 Feb 17];Available from: http://apps.who.int/ghodata/

107. NICE. Clinical management of primary hypertension in adults. 2011;:NICE clinical guideline 127.

108. Ashrafian H, Redwood C, Blair E, Watkins H. Hypertrophic cardiomyopathy:a paradigm for myocardial energy depletion. *Trends Genet*. 2003; 19:263–268.

109. Jameel MN, Zhang J. Myocardial energetics in left ventricular hypertrophy. *Current Cardiology Reviews*. 2009; 5:243–50.

110. Pound KM, Sorokina N, Ballal K, Berkich D a, Fasano M, Lanoue KF, Taegtmeyer H, O'Donnell JM, Lewandowski ED. Substrate-enzyme competition attenuates

upregulated anaplerotic flux through malic enzyme in hypertrophied rat heart and restores triacylglyceride content: attenuating upregulated anaplerosis in hypertrophy. *Circulation Research*. 2009; 104:805–12.

111. Allard MF, Parsons HL, Saeedi R, Wambolt RB, Brownsey R. AMPK and metabolic adaptation by the heart to pressure overload. *Am J Physiol Heart Circ Physiol*. 2007; 292:H140–8.

112. Leong HS, Brownsey RW, Kulpa JE, Allard MF. Glycolysis and pyruvate oxidation in cardiac hypertrophy—Why so unbalanced? *Comparative Biochemistry and Physiology - Part A: Molecular & Integrative Physiology*. 2003; 135:499–513.

113. Lydell CP, Chan A, Wambolt RB, Sambandam N, Parsons H, Bondy GP, Rodrigues B, Popov KM, Harris R a, Brownsey RW, Allard MF. Pyruvate dehydrogenase and the regulation of glucose oxidation in hypertrophied rat hearts. *Cardiovascular Research*. 2002; 53:841–51.

114. Rockman H a, Ross RS, Harris a N, Knowlton KU, Steinhelper ME, Field LJ, Ross J, Chien KR. Segregation of atrial-specific and inducible expression of an atrial natriuretic factor transgene in an in vivo murine model of cardiac hypertrophy. *Proc. Natl. Acad. Sci. USA*. 1991; 88:8277–81.

115. Charles River UK. SHR Rats [Internet]. 2000 [cited 2012 May 25];Available from: http://www.criver.com/SiteCollectionDocuments/SHR Rat.pdf

116. Beevers DG. Epidemiological, pathophysiological and clinical significance of systolic, diastolic and pulse pressure. *Journal of Human Hypertension*. 2004; 18:531–3.

117. McCarron DA, Lucas PA, Shneidman RJ, LaCour B, Drueke T. Blood Pressure Development of the Spontaneously Hypertensive Rat after Concurrent Manipulations of Dietary Ca2+ and Na+. *J Clin Invest*. 1985; 76:1147–1154.

118. McGuire PG, Twietmeyer TA. Aortic endothelial junctions in developing hypertension. *Hypertension*. 1985; 7:483–490.

119. Aitman TJ, Glazier AM, Wallace CA, Cooper LD, Norsworthy PJ, Wahid FN, Al-Majali KM, Trembling PM, Mann CJ, Shoulders CC, Graf D, St Lezin E, Kurtz TW, Kren V, Pravenec M, Ibrahimi A, Abumrad N a, Stanton LW, Scott J. Identification of Cd36 (Fat) as an insulin-resistance gene causing defective fatty acid and glucose metabolism in hypertensive rats. *Nature Genetics*. 1999; 21:76–83.

120. Hajri T, Han XX, Bonen A, Abumrad NA. Defective fatty acid uptake modulates insulin responsiveness and metabolic responses to diet in CD36-null mice. *J Clin Invest*. 2002; 109:1381–1389.

121. Hajri T, Ibrahimi A, Coburn CT, Knapp FF, Kurtz T, Pravenec M, Abumrad NA, Knapp Jr. FF. Defective fatty acid uptake in the spontaneously hypertensive rat is a primary determinant of altered glucose metabolism, hyperinsulinemia, and myocardial hypertrophy. *The Journal of Biological Chemistry*. 2001; 276:23661–6.

122. Rimbaud S, Sanchez H, Garnier A, Fortin D, Bigard X, Veksler V, Ventura-Clapier R. Stimulus specific changes of energy metabolism in hypertrophied heart. *Journal of Molecular and Cellular Cardiology*. 2009; 46:952–959.

123. Paternostro G, Clarke K, Heath J, Seymour AM, Radda GK. Decreased GLUT-4 mRNA content and insulin-sensitive deoxyglucose uptake show insulin resistance in the hypertensive rat heart. *Cardiovascular Research*. 1995; 30:205–11.

124. Cuneo ME, Grassi de Gende AO. Cardiac sarcoplasmic reticulum characteristics in hypertrophic hearts from spontaneously hypertensive rats. *Basic Research in Cardiology*. 1988; 83:286–95.

125. Meerson FZ. Compensatory Hyperfunction of the Heart and Cardiac Insufficiency. *Circulation Research*. 1962; X:250–258.

126. Doggrell S a, Brown L. Rat models of hypertension, cardiac hypertrophy and failure. *Cardiovascular Research*. 1998; 39:89–105.

127. Louis W, Howes L. Genealogy of the spontaneously hypertensive rat and Wistar-Kyoto rat strains: implications for studies of inherited hypertension. *J Cardiovasc Pharmacol*. 1990; 16:S1–5.

128. Aiello EA, Villa-Abrille MC, Escudero EM, Portiansky EL, Pérez NG, de Hurtado MCC, Cingolani HE. Myocardial hypertrophy of normotensive Wistar-Kyoto rats. *Am J Physiol Heart Circ Physiol*. 2004; 286:H1229–35.

129. Felig P, Pozefsky T, Marliss E, Cahill GF. Alanine: Key Role in Gluconeogenesis. *Science*. 1970; 167:1003–1004.

130. Conlay LA, Maher TJ, Wurtman RJ. Alanine increases blood pressure during hypotension. *Pharmacology & Toxicology*. 1990; 66:415–6.

131. Holmes E, Loo RL, Stamler J, Bictash M, Yap IKS, Chan Q, Ebbels T, De Iorio M, Brown IJ, Veselkov KA, Daviglus ML, Kesteloot H, Ueshima H, Zhao L, Nicholson JK, Elliott P. Human metabolic phenotype diversity and its association with diet and blood pressure. *Nature*. 2008; 453:396–400.

132. Lauzier B, Merlen C, Vaillant F, McDuff J, Bouchard B, Beguin PC, Dolinsky VW, Foisy S, Villeneuve LR, Labarthe F, Dyck JRB, Allen BG, Charron G, Des Rosiers C. Post-translational modifications, a key process in CD36 function: lessons from the spontaneously hypertensive rat heart. *Journal of Molecular and Cellular Cardiology*. 2011; 51:99–108.

133. Kim J, Tchernyshyov I, Semenza GL, Dang CV. HIF-1-mediated expression of pyruvate dehydrogenase kinase: a metabolic switch required for cellular adaptation to hypoxia. *Cell Metabolism*. 2006; 3:177–85.

134. Stephens JM, Pilch PF. The Metabolic Regulation and Vesicular Transport of GLUT4, the Major Insulin-Responsive Glucose Transporter. *Endocrine Reviews*. 1995; 16:529–546.

135. Bing RJ. Myocardial ischemia and infarction: growth of ideas. *Cardiovascular Research*. 2001; 51:13–20.

136. Ambrosio G, Zweier JL, Duilio C, Kuppusamy P, Santoro G, Elia PP, Tritto I, Cirillo P, Condorelli M, Chiariello M, Flaherty JT. Evidence that mitochondrial respiration is a

source of potentially toxic oxygen free radicals in intact rabbit hearts subjected to ischemia and reflow. *The Journal of Biological Chemistry*. 1993; 268:18532–41.

137. Lesnefsky EJ, Moghaddas S, Tandler B, Kerner J, Hoppel CL. Mitochondrial dysfunction in cardiac disease: ischemia--reperfusion, aging, and heart failure. *Journal of Molecular and Cellular Cardiology*. 2001; 33:1065–89.

138. Whelan RS, Kaplinskiy V, Kitsis RN. Cell death in the pathogenesis of heart disease: mechanisms and significance. *Proc. Natl. Acad. Sci. USA*. 2010; 72:19–44.

139. Hearse DJ, Humphrey SM, Chain EB. Abrupt Reoxygenation of the Anoxic Potassium-arrested Perfused Rat Heart: A study of Myocardial Enzyme Release. *Journal of Molecular and Cellular Cardiology*. 1973; 5:395–407.

140. Yellon DM, Hausenloy DJ. Myocardial reperfusion injury. *The New England Journal of Medicine*. 2007; 357:1121–35.

141. Lopaschuk GD, Ussher JR, Folmes CDL, Jaswal JS, Stanley WC. Myocardial Fatty Acid Metabolism in Health and Disease. *Physiological Reviews*. 2010; 90:207–258.

142. Lionetti V, Stanley WC, Recchia F a. Modulating fatty acid oxidation in heart failure. *Cardiovascular Research*. 2011; 90:202–9.

143. Wellner M, Dechend R, Park J-K, Shagdarsuren E, Al-Saadi N, Kirsch T, Gratze P, Schneider W, Meiners S, Fiebeler A, Haller H, Luft FC, Muller DN. Cardiac gene expression profile in rats with terminal heart failure and cachexia. *Physiological genomics*. 2005; 20:256–67.

144. Nahrendorf M, Hiller K-H, Hu K, Ertl G, Haase A, Bauer WR. Cardiac magnetic resonance imaging in small animal models of human heart failure. *Medical Image Analysis*. 2003; 7:369–75.

145. Waller C, Hiller K, Kahler E, Hu K, Nahrendorf M, Voll S, Haase A, Ertl G, Bauer WR. Serial Magnetic Resonance Imaging of Microvascular Remodeling in the Infarcted Rat Heart. *Circulation*. 2001; 103:1564–1569.

146. Dutka DP, Camici PG. The contribution of positron emission tomography to the study of ischemic heart failure. *Progress in Cardiovascular Diseases*. 2001; 43:399–418.

147. Schelbert HR. Measurements of Myocardial Ischemic Heart Disease. *The American Journal of Cardiology*. 1998; 82:61K–67K.

148. Lei B, Lionetti V, Young ME, Chandler MP, D'Agostino C, Kang E, Altarejos M, Matsuo K, Hintze TH, Stanley WC, Recchia F a. Paradoxical downregulation of the glucose oxidation pathway despite enhanced flux in severe heart failure. *Journal of Molecular and Cellular Cardiology*. 2004; 36:567–76.

149. Razeghi P, Young ME, Alcorn JL, Moravec CS, Frazier OH, Taegtmeyer H. Metabolic Gene Expression in Fetal and Failing Human Heart. *Circulation*. 2001; 104:2923–2931.

150. Wittels B, Spann JF. Defective lipid metabolism in the failing heart. *J Clin Invest*. 1968; 47:1787–94.

151. Chandler MP, Kerner J, Huang H, Vazquez E, Reszko A, Martini WZ, Hoppel CL, Imai M, Rastogi S, Sabbah HN, Stanley WC. Moderate severity heart failure does not involve a downregulation of myocardial fatty acid oxidation. *Am J Physiol Heart Circ Physiol*. 2004; 287:H1538–43.

152. Osorio JC, Stanley WC, Linke A, Castellari M, Diep QN, Panchal AR, Hintze TH, Lopaschuk GD, Recchia FA. Impaired Myocardial Fatty Acid Oxidation and Reduced Protein Expression of Retinoid X Receptor-alpha in Pacing-Induced Heart Failure. *Circulation*. 2002; 106:606–612.

153. Seymour AL. Imaging Cardiac Metabolism in Heart Failure: The Potential of NMR Spectroscopy in the Era of Metabolism Revisited. *Heart, Lung and Circulation*. 2003; 12:25–30.

154. Stuckey DJ, Carr CA, Tyler DJ, Clarke K. Cine-MRI versus two-dimensional echocardiography to measure in vivo left ventricular function in rat heart. *NMR in Biomedicine*. 2008; 21:765–772.

155. Hale SL, Kloner RA. Effect of early coronary artery reperfusion on infarct development in a model of low collateral flow. *Cardiovascular Research*. 1987; 21:668–73.

156. Atherton HJ, Gulston MK, Bailey NJ, Cheng K-K, Zhang W, Clarke K, Griffin JL. Metabolomics of the interaction between PPAR-alpha and age in the PPAR-alpha-null mouse. *Molecular Systems Biology*. 2009; 5:259.

157. Srere PA, Brazil H, Gonen L. The Citrate Condensing Enzyme of Pidgeon Breast Muscle and Moth Flight Muscle. *Acta Chem. Scand.* 1963; 17:S129 – 134.

158. Marquis NR, Fritz IB. The Distribution of Carnitine, Acetylcarnitine, and Carnitine Acetyltransferase in Rat Tissues. *The Journal of Biological Chemistry*. 1965; 240:2193–6.

159. Pearson DJ, Tubbs PK, Chase FA. Carnitine and acylcarnitine. In: Bergmeyer HU, editor. Methods of Enzymatic Analysis. Weinheim : New York :: Verlag Chemie ; Academic Press; 1974. p. 1758–1771.

160. Grizard G, Lombard-Vignon N, Boucher D. Changes in carnitine and acetylcarnitine in human semen during cryopreservation. *Hum Reprod*. 1992; 7:1245–1248.

161. Sanbe A, Tanonaka K, Hanaoka Y, Katoh T, Takeo S. Regional energy metabolism of failing hearts following myocardial infarction. *Journal of Molecular and Cellular Cardiology*. 1993; 25:995–1013.

162. Braunwald E, Kloner R a. The stunned myocardium: prolonged, postischemic ventricular dysfunction. *Circulation*. 1982; 66:1146–1149.

163. Heather LC, Carr C a, Stuckey DJ, Pope S, Morten KJ, Carter EE, Edwards LM, Clarke K. Critical role of complex III in the early metabolic changes following myocardial infarction. *Cardiovascular Research*. 2010; 85:127–36.

164. Suzuki Y, Masumura Y, Kobayashi A, Yamazaki N. Myocardial carnitine deficiency in chronic heart failure. *Lancet*. 1982;:116.

165. Ning XH, Zhang J, Liu J, Ye Y, Chen SH, From a H, Bache RJ, Portman M a. Signaling and expression for mitochondrial membrane proteins during left ventricular remodeling and contractile failure after myocardial infarction. *Journal of the American College of Cardiology*. 2000; 36:282–7.

166. Horn M, Remkes H, Stromer H, Dienesch C, Neubauer S. Chronic Phosphocreatine Depletion by the Creatine Analogue b-Guanidinopropionate Is Associated With Increased Mortality and Loss of ATP in Rats After Myocardial Infarction. *Circulation*. 2001; 104:1844–1849.

167. Folmes CD, Sawicki G, Cadete VJ, Masson G, Barr AJ, Lopaschuk GD. Novel O-palmitolylated beta-E1 subunit of pyruvate dehydrogenase is phosphorylated during ischemia/reperfusion injury. *Proteome Science*. 2010; 8:38.

168. Chen Q, Vazquez EJ, Moghaddas S, Hoppel CL, Lesnefsky EJ. Production of reactive oxygen species by mitochondria: central role of complex III. *The Journal of Biological Chemistry*. 2003; 278:36027–31.

169. Scheubel RJ, Tostlebe M, Simm A, Rohrbach S, Prondzinsky R, Gellerich FN, Silber RE, Holtz J. Dysfunction of mitochondrial respiratory chain complex I in human failing myocardium is not due to disturbed mitochondrial gene expression. *Journal of the American College of Cardiology*. 2002; 40:2174–81.

170. Ide T, Tsutsui H, Kinugawa S, Utsumi H, Kang D, Hattori N, Uchida K, Arimura K -i., Egashira K, Takeshita a. Mitochondrial Electron Transport Complex I Is a Potential Source of Oxygen Free Radicals in the Failing Myocardium. *Circulation Research*. 1999; 85:357–363.

171. Chen Y-R, Chen C-L, Pfeiffer DR, Zweier JL. Mitochondrial complex II in the post-ischemic heart: oxidative injury and the role of protein S-glutathionylation. *The Journal of Biological Chemistry*. 2007; 282:32640–54.

172. Wall BT, Stephens FB, Marimuthu K, Constantin-Teodosiu D, Macdonald I a, Greenhaff PL. Acute pantothenic acid and cysteine supplementation does not affect muscle coenzyme A content, fuel selection, or exercise performance in healthy humans. *Journal of Applied Physiology*. 2012; 112:272–8.

173. Sambandam N, Lopaschuk GD, Brownsey RW, Allard MF. Energy metabolism in the hypertrophied heart. *Heart Failure Reviews*. 2002; 7:161–73.

174. Calvani M, Reda E, Arrigoni-Martelli E. Regulation by carnitine of myocardial fatty acid and carbohydrate metabolism under normal and pathological conditions. *Basic Research in Cardiology*. 2000; 95:75–83.

175. Rennison JH, McElfresh T a, Okere IC, Patel HV, Foster AB, Patel KK, Stoll MS, Minkler PE, Fujioka H, Hoit BD, Young ME, Hoppel CL, Chandler MP. Enhanced acyl-CoA dehydrogenase activity is associated with improved mitochondrial and contractile function in heart failure. *Cardiovascular Research*. 2008; 79:331–40.

176. Allard MF, Schonekess BO, Henning SL, English DR, Lopaschuk GD. Contribution of oxidative metabolism and glycolysis to ATP production in hypertrophied hearts. *Am J Physiol Heart Circ Physiol*. 1994; 267:H742–H750.

177. Ten Hove M, Chan S, Lygate C, Monfared M, Boehm E, Hulbert K, Watkins H, Clarke K, Neubauer S. Mechanisms of creatine depletion in chronically failing rat heart. *Journal of Molecular and Cellular Cardiology*. 2005; 38:309–13.

178. Neubauer S, Hu K, Horn M, Remkes H, Hoffmann KD, Schmidt C, Schmidt TJ, Schnackerz K, Ertl G. Functional and energetic consequences of chronic myocardial creatine depletion by beta-guanidinopropionate in perfused hearts and in intact rats. *Journal of Molecular and Cellular Cardiology*. 1999; 31:1845–55.

179. Russell LK, Finck BN, Kelly DP. Mouse models of mitochondrial dysfunction and heart failure. *Journal of Molecular and Cellular Cardiology*. 2005; 38:81–91.

180. Huss JM, Kelly DP. Mitochondrial energy metabolism in heart failure : a question of balance. *J Clin Invest*. 2005; 115:547–555.

181. Kurtz DM, Rinaldo P, Rhead WJ, Tian L, Millington DS, Vockley J, Hamm DA, Brix AE, Lindsey JR, Pinkert CA, O'Brien WE, Wood PA. Targeted disruption of mouse long-chain acyl-CoA dehydrogenase gene reveals crucial roles for fatty acid oxidation. *Proc. Natl. Acad. Sci. USA*. 1998; 95:15592–7.

182. Guellich A, Damy T, Lecarpentier Y, Conti M, Claes V, Samuel J-L, Quillard J, Hébert J-L, Pineau T, Coirault C. Role of oxidative stress in cardiac dysfunction of PPARalpha-/- mice. *Am J Physiol Heart Circ Physiol*. 2007; 293:H93–H102.

183. Liao R, Jain M, Cui L, D'Agostino J, Aieollo F, Luptak I, Ngoy S, Mortensen RM, Tian R. Cardiac-Specific Overexpression of GLUT1 Prevents the Development of Heart Failure Attributable to Pressure Overload in Mice. *Circulation*. 2002; 106:2125–2131.

184. Schneider JE, Cassidy PJ, Lygate C, Tyler DJ, Wiesmann F, Grieve SM, Hulbert K, Clarke K, Neubauer S. Fast, high-resolution in vivo cine magnetic resonance imaging in normal and failing mouse hearts on a vertical 11.7 T system. *JMRI*. 2003; 18:691–701.

185. Leone TC, Weinheimer CJ, Kelly DP. A critical role for the peroxisome proliferator-activated receptor α (PPAR alpha) in the cellular fasting response : The PPAR α -null mouse as a model of fatty acid oxidation disorders. *Proc. Natl. Acad. Sci. USA*. 1999; 96:7473–7478.

186. Muoio DM, MacLean PS, Lang DB, Li S, Houmard J a, Way JM, Winegar D a, Corton JC, Dohm GL, Kraus WE. Fatty acid homeostasis and induction of lipid regulatory genes in skeletal muscles of peroxisome proliferator-activated receptor (PPAR) alpha knock-out mice. Evidence for compensatory regulation by PPAR delta. *The Journal of Biological Chemistry*. 2002; 277:26089–97.

187. Hopkins T a, Sugden MC, Holness MJ, Kozak R, Dyck JRB, Lopaschuk GD. Control of cardiac pyruvate dehydrogenase activity in peroxisome proliferator-activated receptor-alpha transgenic mice. *Am J Physiol Heart Circ Physiol*. 2003; 285:H270–6.

188. Kato-Weinstein J, Lingohr MK, Orner G a, Thrall BD, Bull RJ. Effects of dichloroacetate on glycogen metabolism in B6C3F1 mice. *Toxicology*. 1998; 130:141–54.

189. Whitehouse S, Cooper RH, Randle PJ. Mechanism of activation of pyruvate dehydrogenase by dichloroacetate and other halogenated carboxylic acids. *Biochemical Journal*. 1974; 141:761–774.

190. Pratt ML, Roche TE. Mechanism of Pyruvate Kinase and Synergistic Inhibition Inhibition of Kidney Pyruvate by Pyruvate and ADP. *The Journal of Biological Chemistry*. 1979; 254:7191–6.

191. Roche TE, Hiromasa Y. Pyruvate dehydrogenase kinase regulatory mechanisms and inhibition in treating diabetes, heart ischemia, and cancer. *Cellular and Molecular Life Sciences*. 2007; 64:830–49.

192. Gurley SB, Clare SE, Snow KP, Hu A, Meyer TW, Coffman TM. Impact of genetic background on nephropathy in diabetic mice. *Am J Physiol Renal Physiol*. 2006; 290:F214–222.

193. Berglund E, Li C, Poffenberger G, Ayala J. Glucose metabolism in vivo in four commonly used inbred mouse strains. *Diabetes*. 2008; 57:1790–1799.

194. Jones GL a H, Sang E, Goddard C, Mortishire-Smith RJ, Sweatman BC, Haselden JN, Davies K, Grace A a, Clarke K, Griffin JL. A functional analysis of mouse models of cardiac disease through metabolic profiling. *The Journal of Biological Chemistry*. 2005; 280:7530–9.

195. Gavaghan CL, Holmes E, Lenz E, Wilson ID, Nicholson JK. An NMR-based metabonomic approach to investigate the biochemical consequences of genetic strain differences: application to the C57BL10J and Alpk:ApfCD mouse. *FEBS letters*. 2000; 484:169–74.

196. Pollard PJ, Spencer-Dene B, Shukla D, Howarth K, Nye E, El-Bahrawy M, Deheragoda M, Joannou M, McDonald S, Martin A, Igarashi P, Varsani-Brown S, Rosewell I, Poulsom R, Maxwell P, Stamp GW, Tomlinson IPM. Targeted inactivation of fh1 causes proliferative renal cyst development and activation of the hypoxia pathway. *Cancer Cell*. 2007; 11:311–9.

197. Ashrafian H, Czibik G, Bellahcene M, Aksentijević D, Smith AC, Mitchell SJ, Dodd MS, Kirwan J, Byrne JJ, Ludwig C, Isackson H, Yavari A, Støttrup NB, Contractor H, Cahill TJ, Sahgal N, Ball DR, Birkler RID, Hargreaves I, Tennant DA, Land J, Lygate CA, Johannsen M, Kharbanda RK, Neubauer S, Redwood C, de Cabo R, Ahmet I, Talan M, Günther UL, Robinson AJ, Viant MR, Pollard PJ, Tyler DJ, Watkins H. Fumarate Is Cardioprotective via Activation of the Nrf2 Antioxidant Pathway. *Cell Metabolism*. 2012; 15:361–371.

198. Frezza C, Zheng L, Folger O, Rajagopalan KN, MacKenzie ED, Jerby L, Micaroni M, Chaneton B, Adam J, Hedley A, Kalna G, Tomlinson IPM, Pollard PJ, Watson DG, Deberardinis RJ, Shlomi T, Ruppin E, Gottlieb E. Haem oxygenase is synthetically lethal with the tumour suppressor fumarate hydratase. *Nature*. 2011; 477:225–8.

199. Dodd MS, Ball DR, Schroeder MA, Le Page LM, Atherton HJ, Heather LC, Seymour A, Ashrafian H, Watkins H, Clarke K, Tyler DJ. In Vivo Alterations in Cardiac Metabolism and Function in the Spontaneously Hypertensive Rat Heart. *Cardiovascular Research*. 2012; EPub.

200. McCarthy N. Haem is where the heart is. *Nat Rev Cancer*. 2011; 11:692.

201. Sack MN, Rader TA, Park S, Bastin J, Mccune A, Kelly DP. Fatty Acid Oxidation Enzyme Gene Expression Is Downregulated in the Failing Heart. *Circulation*. 1996; 94:2837–2842.

202. Chegary M, Brinke HT, Ruiter JPNN, Wijburg FA, Stoll MSKK, Minkler PE, van Weeghel M, Schulz H, Hoppel CL, Wanders RJA, Houten SM. Mitochondrial long chain fatty acid beta-oxidation in man and mouse. *Biochimica et biophysica acta*. 2009; 1791:806–15.

203. Ikeda Y, Okamura-Ikeda K. Purification and characterization of short-chain, medium-chain, and long-chain acyl-CoA dehydrogenases from rat liver mitochondria. Isolation of the holo-and. *Journal of Biological Chemistry*. 1985; 260:1311–1325.

204. Modre-Osprian R, Osprian I, Tilg B, Schreier G, Weinberger KM, Graber A. Dynamic simulations on the mitochondrial fatty acid beta-oxidation network. *BMC Systems Biology*. 2009; 3:2.

205. Wanders RJA, Ruiter JPN, IJlst L, Waterham HR, Houten SM. The enzymology of mitochondrial fatty acid beta-oxidation and its application to follow-up analysis of positive neonatal screening results. *Journal of Inherited Metabolic Disease*. 2010; 33:479–494.

206. Wanders R, Vreken P, den Boer M, Wijburg FA, van Gennip A, Ijlst L. Disorders of mitochondrial fatty acyl-CoA b-oxidation. *J Inher Metab Dis*. 1999; 22:442–487.

207. Murray A, Panagia M, Hauton D, Gibbons G, Clarke K. Plasma free fatty acids and peroxisome proliferator-activated receptor alpha in the control of myocardial uncoupling protein levels. *Diabetes*. 2005; 54:3496–3502.

208. Watanabe K, Fujii H, Takahashi T, Kodama M, Aizawa Y, Ohta Y, Ono T, Hasegawa G, Naito M, Nakajima T, Kamijo Y, Gonzalez FJ, Aoyama T. Constitutive Regulation of Cardiac Fatty Acid Metabolism through Peroxisome Proliferator-activated Receptor alpha Associated with Age-dependent Cardiac Toxicity. *Journal of Biological Chemistry*. 2000; 275:22293–22299.

209. Aoyama T, Peters JM, Iritani N, Nakajima T, Furihata K, Hashimoto T, Gonzalez FJ. Altered Constitutive Expression of Fatty Acid-metabolizing Enzymes in Mice Lacking the Peroxisome Proliferator-activated Receptor ␣ (PPAR ␣)*. *The Journal of Biological Chemistry*. 1998; 273:5678–5684.

210. Xu J, Xiao G, Trujillo C, Chang V, Blanco L, Joseph SB, Bassilian S, Saad MF, Tontonoz P, Lee WNP, Kurland IJ. Peroxisome proliferator-activated receptor alpha (PPARalpha) influences substrate utilization for hepatic glucose production. *The Journal of Biological Chemistry*. 2002; 277:50237–44.

211. Djouadi F, Weinheimer CJ, Saffitz JE, Pitchford C, Bastin J, Gonzalez FJ, Kelly DP. A gender-related defect in lipid metabolism and glucose homeostasis in peroxisome proliferator- activated receptor alpha- deficient mice. *J Clin Invest*. 1998; 102:1083–91.

212. Sugden MC, Bulmer K, Gibbons GF, Knight BL, Holness MJ. Peroxisome-proliferator-activated receptor-α (PPARα) deficiency leads to dysregulation of hepatic lipid and carbohydrate metabolism by fatty acids and insulin. *Biochemical Journal*. 2002; 364:361–368.

213. Xu J, Chang V, Joseph SB, Trujillo C, Bassilian S, Saad MF, Lee WNP, Kurland IJ. Peroxisomal proliferator-activated receptor alpha deficiency diminishes insulin-responsiveness of gluconeogenic/glycolytic/pentose gene expression and substrate cycle flux. *Endocrinology*. 2004; 145:1087–95.

214. Le May C, Pineau T, Bigot K, Kohl C, Girard J, Pégorier JP. Reduced hepatic fatty acid oxidation in fasting PPARalpha null mice is due to impaired mitochondrial hydroxymethylglutaryl-CoA synthase gene expression. *FEBS letters*. 2000; 475:163–6.

215. Poynter ME, Daynes R a. Peroxisome proliferator-activated receptor alpha activation modulates cellular redox status, represses nuclear factor-kappaB signaling, and reduces inflammatory cytokine production in aging. *The Journal of Biological Chemistry*. 1998; 273:32833–41.

216. Stanley WC, Lopaschuk GD, McCormack JG. Regulation of energy substrate metabolism in the diabetic heart. *Cardiovascular Research*. 1997; 34:25–33.

217. Brock DJ. Purification and properties of sheep liver phosphofructokinase. *The Biochemical Journal*. 1969; 113:235–42.

218. Sugden MC. PDK4: A factor in fatness? *Obesity Research*. 2003; 11:167–9.

219. Shimomura K, Flanagan SE, Zadek B, Lethby M, Zubcevic L, Girard C a J, Petz O, Mannikko R, Kapoor RR, Hussain K, Skae M, Clayton P, Hattersley A, Ellard S, Ashcroft FM. Adjacent mutations in the gating loop of Kir6.2 produce neonatal diabetes and hyperinsulinism. *EMBO Molecular Medicine*. 2009; 1:166–77.

220. Ashcroft FM. ATP-sensitive potassium channelopathies : focus on insulin secretion. *J Clin Invest*. 2005; 115:2047–2058.

221. Nichols CG, Shyng SL, Nestorowicz A, Glaser B, Clement JP, Gonzalez G, Aguilar-Bryan L, Permutt M a, Bryan J. Adenosine diphosphate as an intracellular regulator of insulin secretion. *Science*. 1996; 272:1785–1787.

222. Proks P, de Wet H, Ashcroft FM. Activation of the K(ATP) channel by Mg-nucleotide interaction with SUR1. *The Journal of General Physiology*. 2010; 136:389–405.

223. Gribble FM, Tucker SJ, Haug T, Ashcroft FM. MgATP activates the beta cell KATP channel by interaction with its SUR1 subunit. *Proc. Natl. Acad. Sci. USA*. 1998; 95:7185–90.

224. Gribble FM, Tucker SJ, Ashcroft FM. The essential role of the Walker A motifs of SUR1 in K-ATP channel activation by Mg-ADP and diazoxide. *The EMBO journal*. 1997; 16:1145–52.

225. Clark R, Männikkö R, Stuckey DJ, Iberl M, Clarke K, Ashcroft FM. Mice expressing a human K(ATP) channel mutation have altered channel ATP sensitivity but no cardiac abnormalities. *Diabetologia*. 2012; 55:1195–1204.

226. Church C, Moir L, McMurray F, Girard C, Banks G, Teboul L, Wells S, Bruning J, Nolan P, Ashcroft FM, Cox RD. Overexpression of Fto leads to increased food intake and results in obesity. *Nature genetics*. 2010; 42:1086–1092.

227. Tan SC, Carr CA, Yeoh KK, Schofield CJ, Davies KE, Clarke K. Identification of valid housekeeping genes for quantitative RT-PCR analysis of cardiosphere-derived cells preconditioned under hypoxia or with prolyl-4-hydroxylase inhibitors. *Molecular Biology Reports*. 2012; 39:4857–67.

228. Merritt ME, Harrison C, Sherry AD, Malloy CR, Burgess SC. Flux through hepatic pyruvate carboxylase and phosphoenolpyruvate carboxykinase detected by hyperpolarized 13C magnetic resonance. *Proc. Natl. Acad. Sci. USA*. 2011; 108:19084–9.

229. Randle PJ. Fuel selection in animals. *Biochemical Society Transactions*. 1986; 14:799–806.

230. Francis GA, Annicotte J-S, Auwerx J. PPAR-alpha effects on the heart and other vascular tissues. *Am J Physiol Heart Circ Physiol*. 2003; 285:H1–9.

231. Finck BN. The PPAR regulatory system in cardiac physiology and disease. *Cardiovascular Research*. 2007; 73:269–77.

232. Burkart EM, Sambandam N, Han X, Gross RW, Courtois M, Gierasch CM, Shoghi K, Welch MJ, Kelly DP. Nuclear receptors PPARβ / δ and PPARα direct distinct metabolic regulatory programs in the mouse heart. *The Journal of Clinical Investigation*. 2007; 117:3930–3939.

233. Yang Q, Li Y. Roles of PPARs on regulating myocardial energy and lipid homeostasis. *Journal of Molecular Medicine*. 2007; 85:697–706.

234. Cheng L, Ding G, Qin Q, Huang Y, Lewis W, He N, Evans RM, Schneider MD, Brako F a, Xiao Y, Chen YE, Yang Q. Cardiomyocyte-restricted peroxisome proliferator-activated receptor-delta deletion perturbs myocardial fatty acid oxidation and leads to cardiomyopathy. *Nature Medicine*. 2004; 10:1245–50.

235. Wang Y-X. PPARs: diverse regulators in energy metabolism and metabolic diseases. *Cell Research*. 2010; 20:124–37.

236. Finck BN, Lehman JJ, Leone TC, Welch MJ, Bennett MJ, Kovacs A, Han X, Gross RW, Kozak R, Lopaschuk GD, Kelly DP. The cardiac phenotype induced by PPARα overexpression mimics that caused by diabetes mellitus. *J Clin Invest*. 2002; 109:121–130.

237. Park S, Cho Y, Finck BN, Kim H, Higashimori T, Hong E-G, Lee M-K, Danton C, Deshmukh S, Cline GW, Wu JJ, Bennett AM, Rothermel B, Kalinowski A, Russell KS, Kim Y-B, Kelly DP, Kim JK. Cardiac-Specific Overexpression of Peroxisome Proliferator-Activated Receptor-alpha Causes Insulin Resistance in Heart and Liver. *Diabetes*. 2005; 54:2514–2524.

238. Hafstad AD, Khalid AM, How O-J, Larsen TS, Aasum E. Glucose and insulin improve cardiac efficiency and postischemic functional recovery in perfused hearts from type 2 diabetic (db/db) mice. *Am J Physiol Endocrinol Metab*. 2007; 292:E1288–94.

239. An D, Rodrigues B. Role of changes in cardiac metabolism in development of diabetic cardiomyopathy. *Am J Physiol Heart Circ Physiol*. 2006; 291:H1489–H1506.

240. Trost SU, Belke DD, Bluhm WF, Meyer M, Swanson E, Dillmann WH. Overexpression of the sarcoplasmic reticulum Ca(2+)-ATPase improves myocardial contractility in diabetic cardiomyopathy. *Diabetes*. 2002; 51:1166–71.

241. Severson DL. Diabetic cardiomyopathy : recent evidence from mouse models of type 1 and type 2 diabetes 1. *Can. J. Physiol. Pharmacol.* 2004; 823:813–823.